Development of clumped isotope techniques and their application to palaeoclimate studies

A thesis submitted to the University of East Anglia for the degree of Doctor of Philosophy

by

Ruth Kirk

School of Environmental Sciences

April 2017

Abstract

The aims of this research were to firstly help development of clumped isotope measurements of carbonate samples at UEA, and to then explore whether the technique could be used to retrieve robust environmental signals from geological material. This specifically looks at the Hirnantian glaciation at the boundary between the Ordovician and Silurian periods. Using the MIRA instrument, it is possible to make high precision measurements to enable the assessment of Earth surface temperatures. Long term precision of standard material is comparable to existing studies. MIRA is also absent of any non-linearity issues. Removal of contaminants and the identification of samples displaying contamination is stringent, as we find contamination has a serious effect on the Δ_{47} signal.

Using modern biogenic carbonates and controlled temperature precipitates, the relationship between the clumped isotope signatures represented by the Δ_{47} value and temperature is:

$$\Delta_{47(ARF)} = \frac{3.5 \times 10^4}{T^2} + 0.2416$$

The relationship lies within measurement error of the theoretical estimate of temperature sensitivity.

Applying this temperature calibration to fossil material collected from across the Ordovician/Silurian boundary found that the clumped isotope signal had been overprinted during diagenesis, and it has not been possible to extract an original Earth Surface temperature. However, the isotopic signal does show how the basin has developed during diagenesis under closed system conditions. As a result, the bulk $\delta^{18}O$ and $\delta^{13}C$ values have not been altered and record an original environmental signal.

Contents

List of Figures and Tables

Acknowledgements

Firstly, I would like to thank my supervisors Paul Dennis, Alina Marca and Julian Andrews for providing me with this opportunity, and for always supporting and encouraging me. Particular thanks go to Paul for help with Section 2.3 of Chapter 2. This project was funded by the National Environmental Research Council; without this it would not have been possible.

I would also like to thank the external collaborators who have helped with this project. Huge thanks go to André Desrochers for help and expertise completing fieldwork and providing knowledge of the Anticosti sequence, and for your comments on Chapter 5. Many thanks go to Juraj Farkas and Elizabeth Harper for the kind donation of brachiopod shell material for use in the temperature calibration. I would also like to thank Jisuo Jin of the University of Western Ontario for the identification of brachiopod samples from Anticosti.

I have had much help with this project along the way, including support from technical staff at UEA. Many thanks go to Graham Chilvers for LA-ICPMS analysis of trace elements, John Brindle for making thin sections and blocks, Bertrand Leze for help with microscopes and XRD analysis, and Paul Disdle for your support and supplying of cake.

I am extremely lucky to have some wonderful friends who have supported me through all of the ups and downs of this PhD. First of all, huge thanks go to Emily Peckover, for your constant support, proof-reading and scientific discussion skills, and for always having a listening ear. I would also like to thank Amelia Frizell-Armitage, Tahmeena Aslam and Louise Biddle for always having time for me, along with encouragement and a cup of tea, and thanks go to Osgur McDermott Long for always dancing along with me. Special thanks also go to Kate Fraser, Keith Brown and Alex Howat for your support, encouragement and always having a glass of wine ready. Many thanks go to Georgia Isom for her support from afar.

I would also like to thank John Aldridge, for being a wonderful geological inspiration and introducing me to the best beers.

Finally, I would like to thank my family. Completing a PhD is no easy task, and you have all been on the other end of the phone with love, help and encouragement. Thank you to Dad, for your help with figures in this thesis, and for always sending the best jokes, and thank you to Mum for always knowing what to say. Finally, thank you to Holly, for being the best big sister whichever side of the world you are on.

Chapter 1 - Introduction and Literature Review

1.1 Overview

1.1.1 Aims and Objectives

The purpose of this research is to evaluate if clumped isotopes can contribute to understanding environmental conditions, notably Earth surface temperature during periods in the geologic past. The specific objectives were:

- To aid in the development and improvement of the MIRA mass spectrometer and gas preparation line in order to improve the accuracy and precision of measurements of clumped isotopes at UEA.

- To produce a temperature calibration using modern materials to identifying the relationship between growth/precipitation temperature of calcium carbonate and the clumped isotope signal recorded in the material. This temperature calibration will then be applied to geological material.

- To obtain clumped isotope, stable isotope and trace element data on Ordovician/Silurian aged rocks from Anticosti Island (E. Canada) and to use this in conjunction with a sedimentary petrography study to identify if original environmental signals are recorded in the fossil material, and if not to hypothesise the burial history and conditions for the sampled area.

1.1.2 Structure of the thesis

Chapter 1 covers the background to this study. The study of clumped isotopes is a rapidly evolving area of research and holds great promise as a potential new proxy for understanding marine palaeoenvironmental conditions. The literature review in Chapter 1 will outline the theory behind clumped isotopes and a brief overview of present understanding and methods at the time of writing. Chapter 2 describes the methodological challenges faced by laboratories making measurements in terms of the capabilities of mass spectrometers. It also introduces and describes the MIRA mass spectrometer, with some comparison of its design with others currently in use. Chapter 3 explains how we prepare and clean samples at UEA, in particular carbonate material. The modern temperature calibration produced for MIRA is outlined in Chapter 4, along with a

comparison and discussion of many of the other published temperature calibrations. Chapter 5 presents the investigation of the Ordovician material collected from Anticosti Island as a case study for the applicability of the clumped isotope technique for understanding palaeoenvironmental conditions. Final thoughts and a brief discussion on the future direction of the development of clumped isotope methodologies and research application will be outlined in chapter 6, along with the key conclusions from this research.

1.2 A review of the current understanding of clumped isotopes

1.2.1 Conventional carbonate-water oxygen isotope thermometer - theory and application

Measurement of the variations in oxygen isotopes recorded in carbonates has been used for many years as a method to determine palaeotemperatures (e.g. McCrea (1950); Urey et al. (1951); Epstein et al. (1953)). The carbonate-water oxygen isotope thermometer determines the isotopic equilibrium of carbonate ions and water as they partition between the solid and liquid phases. The abundance of the ^{18}O isotope incorporated in carbonate material varies according to the temperature of the water from which the carbonate precipitated. The ^{18}O and ^{16}O ratio described by the $\delta^{18}O$ measurement is a function of the temperature at which the carbonate ion and the water are in equilibrium.

As the isotopes are exchanged between phases, there is a slight change in the $^{18}O/^{16}O$ ratio (fractionation) of the oxygen isotopes that is dependent on the temperature of formation (McCrea, 1950). Many studies have been published where the authors have tried to define the oxygen isotope fractionation between calcite and water (see Chapter 4 for a discussion on this). The fractionation factor is defined by α in Equation 1.1 for the calcite-water palaeothermometer (Kim & O'Neil 1997):

$$\propto = \left(\frac{1000+\delta^{18}OCaCO_3}{1000+\delta^{18}OH_2O}\right) \qquad \text{Equation 1.1}$$

In order to calculate the fractionation factor, the oxygen isotopic composition of the fluid from which the calcite has precipitated must be known. This is a disadvantage for the carbonate-water thermometer as, for geological samples, we do not know the precise composition of the fluid from which they formed.

The relationship between the oxygen isotopes in calcite and water can be used as a palaeothermometer. The $\delta^{18}O$ (and $\delta^{13}C$) values describe the relationship between two isotopes compared to a standard (for example see Equation 1.2):

$$\delta^{18}O = \left[\frac{\left(\frac{^{18}O}{^{16}O} sample\right)}{\left(\frac{^{18}O}{^{16}O} reference\right)} - 1 \right] \times 1000 \qquad \text{Equation 1.2}$$

Various carbonate materials have been successfully analysed for their bulk isotope composition and are regularly used for palaeothermometry. Marine limestone and fossil material is now routinely analysed to understand past marine environments (e.g. (Urey et al. (1951); Veizer & Hoefs (1976); Veizer et al. (1986)). Foraminifers also contain a record of palaeoenvironmental conditions (e.g. Emiliani (1955)). Speleothem carbonates can also have their bulk isotopic signal measured (e.g. Hendy & Wilson (1968)), and can be used to either identify a groundwater oxygen isotope signal, or to identify climatic signals, such as glacial events. However, there remains a key issue with the conventional carbonate-water oxygen isotope thermometer in terms of understanding past geological environments, as the technique requires knowledge of the oxygen isotope composition of the fluid from which the carbonate formed.

For many carbonate systems, it remains impossible to determine if the changes recorded in the carbonate material are a product of changes in temperature of the fluid or changes in the oxygen isotope composition of the fluid, or a combination of both. There are marked variations in the isotopic composition of meteoric waters, and there are also problems with interpretation of marine carbonates. Major glacial events alter both the oxygen isotope composition of the fluid, and the temperature.

Measurements of carbonate rocks and fossils have been completed on material throughout geological time (Veizer & Hoefs (1976); Veizer et al. (1986); Veizer & Prokoph (2015)). The carbonate material preserved throughout the Phanerozoic shows a rise in $\delta^{18}O$ value from the Cambrian to the Quaternary from approximately -8 ‰ to 0 ‰. As we cannot know the fluid isotope composition of the ocean at the time of the carbonate formation, there is no way to determine whether this trend is caused by changing marine temperatures, changing marine oxygen isotope composition or even whether there is a diagenetic effect where the oxygen isotope composition has been altered. The clumped isotope thermometer provides a way to partially overcome this issue, as the technique allows determination of a formation temperature from within a single phase, the carbonate crystal, and knowledge of the formation fluid composition is not required (see Section 1.2.3) (Ghosh et al. 2006).

1.2.2 Clumped isotopes

In some of the earliest stable isotope studies, it was found that there can be isotopic substitution within compounds affecting their thermodynamic properties (Urey 1947). After a

review of experimental and theoretical studies, Urey (1947) found that these variations caused by the substitution of heavier isotopes for lighter isotopes altered the properties of the compounds and could potentially act as a method to determine the temperatures of geological formations. The bond between two heavy isotopes has a slower vibration, and is lower in energy (zero-point energy) than the bond between two light isotopes. A commonly used example is clumping within the hydrogen system. H_2, H-D and D_2 progressively show lower zero point energies with addition of each heavier isotope. There is a drive for bonding between the heavier isotopes at the expense of bonding between the lighter isotopes (Eiler 2007).

Where a molecule contains isotopic variation of its constituent atom, this is termed an isotopologue. There can be two or more variations within the molecule (Eiler 2007). If there is only one rare (heavier) isotope contained within the molecule, it is referred to as a singly substituted isotopologue. Where there is more than one heavier isotope included within the molecule, it becomes a multiply substituted isotopologue (Wang et al. 2004).

This suggests that a population of isotopologues under a stochastic (random) distribution would have fewer multiply substituted isotopologues than a population that is equilibrated to Earth surface temperatures (Eiler & Schauble 2004). As multiply substituted isotopologue is an unwieldy term, the community refers to them as "clumped isotopes". Clumped isotope geochemistry is the study of clumped isotopes within natural systems. It is essentially the study of the ordering of isotopes within a population of isotopologues independent of the bulk isotope composition (Eiler 2007).

1.2.3 Clumped isotopes and the carbonate molecule – developing the thermometer

The study of clumped isotopes can be applied to the carbonate anion, as clumped isotopes have the potential to act as palaeothermometer and identify the temperature of mineral formation. Carbonate minerals are already known to preserve an isotopic signal. Clumped isotopes provide a way to study the internal isotopic ordering of the crystal. The carbonate mineral contains C-O bonds, and there is exchange of ^{13}C, ^{18}O and ^{17}O within the crystal lattice (Schauble et al. 2006). Equation 1.3 shows the order/disorder equation for the formation of the carbonate mineral.

$$Ca^{12}C^{18}O^{16}O_2 + Ca^{13}C^{16}O_3 \leftrightarrow Ca^{13}C^{18}O^{16}O_2 + Ca^{12}C^{16}O_3 \qquad \text{Equation 1.3}$$

All of the components are present within the mineral phase, and so the equilibrium constant of the equation is not dependent on the bulk isotopic composition of the crystal nor the isotopic

composition of the fluid. This makes it ideal as a palaeothermometer, as the traditional bulk isotope carbonate-water thermometer is dependent on the temperature sensitivity of the carbonate exchanging with the formation fluid (Schauble et al. 2006).

The equilibrium constant in Equation 1.3 is only dependent on temperature. The lower the temperature, the more the reaction favours the right hand side of Equation 1.3, where the zero-point energy is lower. This means that the system will have a greater abundance of the multiply substituted isotopologues, such as $Ca^{13}C^{18}O^{16}O_2$ when compared to a system where the carbon and oxygen have a stochastic distribution (Schauble et al. 2006). Measuring the abundance of isotopologues from both sides of Equation 1.3 allows us to calculate a temperature at which the carbonate mineral formed (if it grew in equilibrium) (Eiler 2007). The most common multiply substituted isotopologue of carbonate within calcite is the $^{13}C^{18}O^{16}O_2$ isotopologue with a mass of 63 (see Table 1.1 and Figure 1.1).

Isotopologue	Mass	Abundance
$^{13}C^{18}O^{16}O^{16}O$	63	67 ppm
$^{12}C^{17}O^{18}O^{16}O$	63	4.4 ppm
$^{13}C^{17}O^{17}O^{16}O$	63	4.54 ppb
$^{12}C^{17}O^{17}O^{17}O$	63	50 ppt

Table 1. 1 Carbonate isotopologues of mass 63 (re-drawn from Ghosh et al. (2006)).

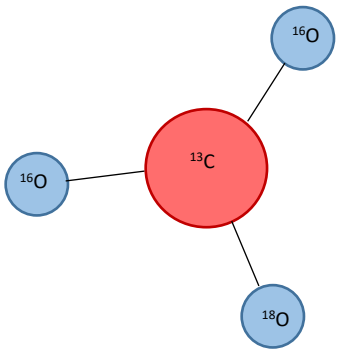

Figure 1.1 Carbonate anion made up of the mass 63 isotopologue.

There is currently no analytical method that can measure the isotopic composition of a carbonate mineral in the solid state, therefore the calcite is reacted with ortho-phophoric acid to release carbon dioxide. This is done with ortho-phosphoric acid greater than 100 %, based on the original method used by McCrea (1950). Reaction of the carbonate anion produces carbon dioxide (CO_2) of mass 44 to mass 49 (See Chapter 2 Table 2.1 for a full list of CO_2 isotopologues).

Digestion of the carbonate releases CO_2 as shown in Equation 1.4:

$$CaCO_3 + H_3PO_4 \leftrightarrow CaHPO_4 + CO_2 + H_2O \qquad \text{Equation 1.4}$$

We aim to measure the mass 47 CO_2 isotopologue, which reflects the abundance of the mass 63 carbonate anion. Masses 48 and 49 are of such low abundance they are generally not measured save as an indicator for contamination. The $^{13}C^{18}O^{16}O$ isotopologue is the most abundant in the mass 47 group, therefore a clumped isotope measurement is predominantly a measurement of this isotopologue (Eiler 2007).

As there can more than one isotopic species of an element that is common within each of the compounds, there is potential for fractionation between the carbonate anion and the CO_2. This was first proposed by Urey (1947) through theoretical statistics, and was then experimentally confirmed by McCrea (1950) for the carbonate system. As in Section 1.2.1, this fractionation factor (α) is defined as the ratio of the two isotopes in one phase divided by the same ratio in the other phases (McCrea 1950). For clumped isotopes, this is between the carbonate and CO_2 phases. It is considered that carbon is completely converted to CO_2 during the digestion of calcite, but there is a small enrichment in the CO_2 relative to the proportions of the most abundant multiply substituted isotopologue (Ghosh et al. 2006). This is due to the breaking of the C-O bond during the reaction. The fractionation factor is considered to be constant, and to depend on the temperature at which digestion of the calcite occurs (Urey 1947; McCrea 1950; Swart et al. 1991). It is possible that a kinetic isotope effect reorders the bonds between the carbon and oxygen atoms. We know that temperature controls the fractionation between oxygen isotopes, therefore it is expected that the clumped isotope value would alter with the digestion temperature (Ghosh et al. 2006). Therefore, if not reacting at 25 °C it is vital that the acid fractionation is accurately applied during clumped isotope analysis. A full outline of how clumped isotope values are calculated and standardised is outlined in Chapter 2.

1.2.5 Introduction to analytical techniques

Cleaning of the product CO_2

The product CO_2 undergoes cleaning to an ultra-pure standard before being introduced to the mass spectrometer. This includes the removal of water through cryogenic separation from the CO_2, and the removal of organic compounds by a packed U-shaped trap or GC column. The preparation lines can either be offline (such as the system at UEA, Ghosh et al. (2006); Wacker et al. (2013)) or online automated systems (such as Schmid & Bernasconi (2010)). There is still some

variation and debate within the community as to the best methods of CO_2 cleaning. The temperature of the water traps varies between laboratories, from -77 °C to -115 °C. There is also much variability in the length of time, temperature and length of packing of the U-shaped trap or GC column used to remove organic material. The effects of contamination are still not fully understood. This is further covered in Chapter 3.

Mass spectrometry

The mass 47 isotopologues make up a small fraction of CO_2 gas, therefore the method used to measure them must be capable of high sensitivity and precision. Gas source isotope ratio mass spectrometry is considered to meet those demands. A full discussion of the requirements of mass spectrometry for clumped isotope analysis is outlined in Chapter 2. The instruments currently in use have multiple Faraday collectors that can achieve the high precision required to analyse clumped isotopes. They also complete the analysis on molecular ions, which retain a record of the distribution of isotopologues (Eiler 2007).

There are four types of mass spectrometer currently used to analyse clumped isotopes. The majority of published data has been produced by the Thermo-Finnegan MAT 253, but other measurements have been completed on the 5kV Isoprime (Rosenheim et al. 2013) and the Thermo-Finnegan Delta XP (Yoshida et al. 2013). In this thesis data was produced using the MIRA mass spectrometer at UEA for clumped isotope measurements.

The Thermo- Finnegan MAT 253 is the most commonly used instrument. This is a dual-inlet system with a changeover valve that analyses a sample gas in comparison to a reference gas (Eiler 2007). The MAT 253 is reconfigured to measure ion beams 44 to 49, and registers the ion beam for mass 47 through a $10^{12}\Omega$ resistor. It is in use in a variety of laboratories including the California Institute of Technology (CALTECH), Yale University, Johns Hopkins University, ETH in Zurich, UCLA, Goethe University in Frankfurt, Harvard University and Imperial College London.

Tulane University (New Orleans) has performed clumped isotope analysis on 5 kV Isoprime mass spectrometer which is produced by Elementar Analysensysteme GmbH. This instrument uses a different ion source than the MAT 253. The mass spectrometer has been fitted with Faraday cups that enable measurement of beams 44-49. They are not able to measure on the mass 48 and 49 cups. The measuring time is slightly longer, but produces external precision of reference carbonates that is comparable to other labs (Rosenheim et al. 2013). The Isoprime has been used in several instances of published work. This includes analysis of siderite (Fernandez et al. 2014), aragonitic freshwater gastropods (Hren et al. 2013) and inorganic calcite precipitates (Tang et al. 2014).

Clumped isotope analysis has also been successfully completed on a Thermo-Finnegan 3kV Delta XP at the Tokyo Institute of Engineering. The XP does not show any issues with linearity and has comparable internal precisions to the MAT 253 (± 0.006 ‰). It is a dual-inlet system that is configured to collect ion beams from 44 to 49. This required the original triple collector to be modified to nine collectors (Yoshida et al. 2013).

1.2.6 Applications of clumped isotope thermometry

To be able to use clumped isotopes as in palaeothermometry, the relationship between Δ_{47} and temperature must be fully understood. Many laboratories measuring clumped isotopes have produced temperature calibrations. The calibration line is a linear regression between the Δ_{47} value recorded in these modern materials and the inverse of the temperature squared. There is one theoretically calculated example of the relationship between clumped isotopes and temperature (Guo et al. 2009) and the other calibrations have all been empirically determined in the laboratory. There is a wide variation between the temperature calibrations, and the cause of this remains a topic of discussion amongst the research groups. At this point all calibrations are generally used locally and are laboratory dependent. These differences are likely caused by the variations in preparation methodology that still need to be resolved. This is why one aim of my thesis was to produce a temperature calibration for use at UEA (Chapter 4).

Reconstruction of growth temperatures of a speleothem was completed by Affek et al. (2008). They were able to extract a growth temperature during glacial periods that was comparable to other records, but suggest that for speleothems, there must be a correction applied to the clumped isotope data to account for non-equilibrium growth effects. Clumped isotope body temperatures have been extracted from the carbonate component of bio-apatite (Eagle et al. 2010). These were body temperatures for extinct species, where previous studies using the conventional carbonate-water oxygen isotope thermometer were limited. Foraminifer and coccoliths also preserve clumped isotope records that can be used to determine palaeo-ocean temperature and compositions (Tripati et al. 2010). More recently, there has been application of the clumped isotope thermometer to natural inorganic calcite formations. The connectivity between fractures within a geothermal reservoir was characterised using clumped isotopes. It has been found that the layering of trace elements and clumped isotope variation within a single vein suggests episodic opening and multiple generations of fluids and fractures. Both hot and cold temperatures were identified at different locations within a geothermal reservoir suggested that some of the fractures could be used to transport cold meteoric water down from the surface to be heated at depth, before returning to the surface (Sumner et al. 2015). Further applications of the

clumped isotope thermometer have included travertines and tufas (Kele et al. 2015) and paleosols (e.g. Ghosh 2013).

There have been key studies which have applied the clumped isotope palaeothermometer to marine macro-fossil material. Silurian and Carboniferous age brachiopods and molluscs that showed good preservation were analysed in Came et al. (2007). Their data suggested that the marine surface temperature changes are driven by atmospheric CO_2 level changes, and tried to exclude samples that showed signs of alteration. They also suggest that their data supported the argument that $\delta^{18}O$ of the ocean did not vary throughout the Phanerozic. Finnegan et al. (2011) completed a study on material from the end-Ordovician to early Silurian. The samples included brachiopods, trilobites and rugose corals, but some analyses were excluded on the basis that they showed diagenetic alteration. For the final Hirnantian glaciation event, they used material collected from the sequence exposed on Anticosti Island, which was at a subtropical location during this time. They found that there was a clear temperature and ocean fluid variation recorded in the material at this point of maximum glaciation. In light of the difficulties in making clumped isotope measurements that remains a source of discussion in the community, this thesis will revisit material from Anticosti Island to see if the early conclusions by Finnegan et al. (2011) are robust (see Chapter 5). Anticosti Island displays an accessible and well-studied early Palaeozoic sequence, that appears to be well-preserved.

Chapter 2 - Clumped Isotope Mass Spectrometry

2.1 Introduction

Clumped isotope measurements with isotope ratio mass spectrometers are very challenging because the target isotopologues are low in abundance (Table 2.1; Eiler & Schauble (2004); Eiler (2007)) but must be measured to a very high precision. This chapter will identify the criteria that mass spectrometers need to meet in order to successfully measure clumped isotopes of carbon dioxide (CO_2). To date, the majority of measurements have been made on the Thermo-Finnegan 253 gas source ratio mass spectrometer; for example Ghosh et al. (2006), Came et al. (2007), Huntington et al. (2009). In addition, some studies have been made on the Thermo-Finnegan Delta XP and the Elementa IsoPRIME mass spectrometers. This chapter outlines required key performance specifications of mass spectrometers making clumped isotope measurements, and demonstrates how MIRA is suitable for these high precision measurements. The results, methodology and discussions outlined here have arisen from work contributed by all members of the research group at UEA.

Mass of CO_2	**Isotopologue**	**Relative abundance**
44	$^{12}C^{16}O_2$	98.4 %
45	$^{13}C^{16}O_2$	1.11 %
	$^{12}C^{17}O^{16}O$	748 ppm
46	$^{12}C^{18}O^{16}O$	0.4 %
	$^{13}C^{17}O^{16}O$	8.4 ppm
	$^{12}C^{17}O_2$	0.142 ppm
47	$^{13}C^{18}O^{16}O$	44.4 ppm
	$^{12}C^{17}O^{18}O$	1.5 ppm
	$^{13}C^{17}O_2$	1.6 ppb
48	$^{12}C^{18}O_2$	3.96 ppm
	$^{13}C^{17}O^{18}O$	16.8 ppb
49	$^{13}C^{18}O_2$	44.5 ppb

Table 2.1 Relative abundances of isotopologues of CO2 from masses 44 to masses 49. Redrawn from Eiler (2007).

2.2 Definition of Δ value

The abundance of a multiply-substituted isotopologue is expressed as a Δ value with respect to the theoretical stochastic abundance:

$$\Delta_i = \left(\frac{R_i}{R_i^*} - 1\right) \times 1000 \qquad \text{Equation 2.1}$$

where R_i represents the measured abundance ratio of isotopologue *i* relative to the non-isotopically substituted isotopologue (containing no rare isotopes), and R_i* represents the abundance ratio for the isotopologue when the isotopes are stochastically (randomly) distributed. This stochastic abundance is calculated from the bulk isotope composition of the sample (Wang et al. 2004; Eiler & Schauble 2004).

For carbon dioxide (CO_2), we are mostly concerned with the isotopologue $^{13}C^{18}O^{16}O$, with mass 47 (*i* = 47), which is the most abundant multiply substituted isotopologue at this mass. R_i is considered to be the sample mass 47 isotopologue relative to mass 44, and R_i* is the calculated stochastic distribution of 47/44. We can also determine values for the dominant isotopologues at mass 48 ($^{13}C^{18}O^{17}C$) and mass 49 ($^{13}C^{18}O^{18}O$). It is important to note that there is a contribution of ^{17}O towards the measured and calculated ratios of isotopologues at mass 47 and mass 48, but the mass resolution of the mass spectrometer is unable to define the separate isotopologues as the abundance is so low. Table 2.1 shows the relative abundances of the isotopologues at each CO_2 mass. The contribution of ^{17}O is small (Wang et al. 2004) and therefore:

$$\Delta^{13}C^{18}O^{16}O \approx \Delta_{47} \qquad \text{Equation 2.2}$$

Wang et al. (2004) state that Δ_{47} is equal to the weighted sum of the three isotopologues. For example:

$$\Delta_{47} = a.\Delta_{^{13}C^{18}O^{16}O} + b.\Delta_{^{13}C^{17}O^{17}O} + c.\Delta_{^{12}C^{17}O^{16}O} \qquad \text{Equation 2.3}$$

where a, b and c are weightings determined by the relative concentrations of the isotopologues. For Δ_{47}, the total concentration is equal to approximately 46 ppm, therefore:

$$a \cong \frac{44.4ppm}{46ppm} = 97\ \% \qquad b \cong \frac{1.6\times10^{-3}ppm}{46ppm} = 0.003\ \% \qquad c \cong \frac{1.5ppm}{46ppm} = 3.3\ \%$$

indicating that ^{17}O has very little impact on the whole of the measured Δ_{47}.

Δ_{47} is expressed as in Equation 2.3. Deriving Δ_{48} and Δ_{49} is completed in a similar manner:

$$\Delta_{47} = \left(\frac{R_{47}}{R_{47}^{*}} - 1\right) \times 1000 \approx \Delta^{13}C^{18}O^{16}O = \left(\frac{\left[\frac{^{13}C^{18}O^{16}O}{^{12}C^{16}O_2}\right]}{\left[\frac{^{13}C^{18}O^{16}O}{^{12}C^{16}O_2}\right]} - 1\right) \times 1000 \qquad \text{Equation 2.4}$$

The ratios for R_i and R_i* are calculated from the measured bulk isotope values ($\delta^{13}C$ and $\delta^{18}O$) and δ^i. For R_{47}:

$$R_{47} = \left(\frac{\delta^{47}_{sam-wrg}}{1000} - 1\right) \times R_{47(wrg)} \qquad \text{Equation 2.5}$$

where δ^{47}sam-wrg represents the 47/44 signal of the sample with respect to the working reference gas (wrg) (see full description in Section 2.6). $R_{47(wrg)}$ is determined from its bulk isotope composition as in Equation 2.6:

$$R_{47(wrg)} = 2 \times R_{13(wrg)} \times R_{18(wrg)} + 2 \times R_{18(wrg)} \times R_{17(wrg)} + R_{13(wrg)} \times \left(R_{17(wrg)}\right)^2$$

Equation 2.6

There is an additional assumption that the working reference gas has a stochastic composition. The UEA working reference gas is in equilibrium at (or close to) the lab room temperature. This is corrected for with a linear transformation of the data that takes into account the actual mass spectrometer working reference gas R^{47} value.

2.3 Requirements of mass spectrometry

The technique for measuring clumped isotopes in any laboratory worldwide is still evolving rapidly due to various issues that prevent high precision measurements. These include things such as non-linearity in the majority of mass spectrometers, and identifying the key sources of contamination. This section reviews key issues that the community is currently attempting to overcome.

2.3.1 Precision

To ascertain the precision at which Δ_{47} can be measured, the precision of the δ^{47} measurement has to be understood. This precision is limited by the random error associated with ion detection and counting statistics: the 'shot-noise' limit (Merritt & Hayes 1994). For the shot-noise limit on MIRA see Section 2.8. If we ignore noise from electronic components such as the thermal noise of the high gain amplifier resistors ($10^{12}\,\Omega$) then the shot-noise limit is determined by statistical fluctuations in the arrival frequency of ions into the faraday cups. Sampling statistics of the ion beam is then the only source of error. This beam of discrete particles is produced by an ion current, and randomly distributed over time. When analysing at the shot-noise limit, the collected number of ions will vary, giving a measurable variation over time (Schmid & Bernasconi 2010).

The random fluctuations in the arrival frequency are described by a Poisson distribution. This distribution describes the probability of a number of independent events occurring during a fixed time period. The ionised molecules are summed over a finite period of time (t). P is the probability of a measurement interval containing N events, therefore $P_{(N)}$ represents the probability of N ions per second when applied to mass spectrometry (Bevington & Robinson 1992):

$$P_{(N)} = \frac{\mu^N \times e^{-\mu}}{N!} \qquad \text{Equation 2.7}$$

If the measurement is repeated a large number of times (e.g. 1600 measurements of reference and sample gas with each measurement consisting of a one second integration of the signal) and the values of N are averaged, the mean value of N approaches the mean of the sampling distribution (μ), therefore:

$$P = \frac{N^N \times e^{-N}}{N!} \qquad \text{Equation 2.8}$$

and has a standard deviation of:

$$\sigma = \sqrt{N}$$ Equation 2.9

The relative precision (σ_N) is given by:

$$\sigma_N = \frac{\sigma}{N} = \frac{\sqrt{N}}{N}$$ Equation 2.10

For Δ_{47} measurements with a precision of 0.01 ‰, δ^{47} needs to be measured to a precision better than this. Noting that:

$$\delta^{47} = \left(\frac{\frac{47}{44}sample}{\frac{47}{44}wrg} - 1 \right) \times 1000$$ Equation 2.11

it is clear that we need to measure 47/44 of the sample and reference gas to better than 0.01 ‰/√2 (approximately ±0.007 ‰, or $7x10^{-6}$). If we set σ_N to $7x10^{-6}$ in Equation 2.9, we find:

$$7x10^{-6} = \frac{\sqrt{N}}{N} = \frac{1}{\sqrt{N}}$$ Equation 2.12

therefore:

$\sqrt{N} = 1.43 \times 10^5$, therefore $N = 2.04 \times 10^{10}$ Equation 2.13

This indicates that it is necessary to collect $2.04x10^{10}$ mass 47 ions for both the sample and working reference gas in order to achieve a precision of 0.01 ‰. Using the MIRA mass spectrometer at UEA, we typically measure with a m/z signal of approximately 3.3 x 10^{-12} A. This corresponds to an average ion flux of (Equation 2.14):

$$\frac{3.3\times10^{-12} coulombs.s^{-1}}{1.6\times10^{-19} coulombs.ion^{-1}} = 2.06 \times 10^7 ions.s^{-1}$$ Equation 2.14

To achieve the adequate precision, we are required to count for minimum of 1000 seconds each for the sample and working reference gas:

$$\frac{2.04\times10^{10} ions}{2.06\times10^{7} ions.s^{-1}} = 990.29\ seconds$$ Equation 2.15

MIRA measures δ^{47} at a precision limited by the shot-noise only (Section 2.7). It is therefore reasonable to assume that electronic noise can be excluded in consideration of the present practical limits to measurement precision of clumped isotopes of CO_2.

2.3.2 Sensitivity

The minimum integrated ion signal required to achieve the desired precision for clumped isotope measurements is outlined in Section 2.3.1. However, we also need to consider the minimum gas amount that is necessary to meet requirements. This is controlled by the instrument sensitivity. Sensitivity is conventionally defined as the number of molecules of analyte gas needed for the detection of a single ion of the major isotopologue (Merritt & Hayes 1994). For CO_2, this is the non-isotopically substituted $^{12}C^{16}O_2$ isotopologue. To complete clumped isotope analyses on isotopologues of CO_2, the mass spectrometer requires a high sensitivity. This is due to the target species being only small fractions of the analysed gas (approximately 44 ppm or 10^{-5} of the analyte CO_2) (Eiler 2007).

The IRMS instruments used to measure clumped isotopes contain a Nier-type ion source. These have typical sensitivities of between 600 and 2000 molecules per ion (typical specification of commercial IRMS instruments). If 1000 molecules.ion^{-1} is a typical sensitivity, when scaled for the mass 47 $^{13}C^{18}O^{16}O$ isotopologue, the sensitivity required is 2.3×10^7 molecules.ion^{-1}. It was calculated that we need to detect a minimum of 2.04×10^7 ions of the $^{13}C^{18}O^{16}O$ isotopologue (Section 2.3.1). Therefore, we require approximately 5×10^{17} molecules of CO_2, approximately 1 µmole.

When the instrument is in dual-inlet mode, there are several allowances that also have to be made when calculating the gas amount required for a high-precision measurements. Firstly, the measurement time of both the sample and working reference gas has to be taken into account. There is also dead time after switching of the changeover valve, and additional setting up time including tasks such as balancing of the beams. Allowing for all these, a typical measurement time approaches 90 minutes. This is greater than the minimum 2000 seconds identified in Section 2.3.1. (1000 seconds each for sample and working reference gas), therefore the total sample required as a minimum is defined by:

$$2.06 \times 10^7 ions.s^{-1} \times 90 mins \times 60 secs.min^{-1} \times 2.5 \times 10^7 molecules.ion^{-1} = 2.7 \times 10^{18}\ molecules\ of\ CO_2 \qquad \text{Equation 2.16}$$

This equates to $4.5x10^{-6}$ mole of CO_2. The absolute lower limit of sample size is 5 µmols of CO_2. This is 500 micrograms of carbonate sample (0.5 milligrams).

In practise this size of sample is difficult to achieve. The bellows configuration of dual-inlet systems typically necessitates a minimum factor of 2 increase in sample size to account for a reasonable level of sample depletion during a measurement whilst maintaining an adequate signal. This means that a final estimate for a minimum samples size is 10-20 µmoles of CO_2, or 1-2 mg.

2.3.3 Linearity

The problem of linearity is present within other isotope systems, and is a major artefact of clumped isotope analysis. The derived Δ_{47} value varies as a function of the bulk isotope composition of the sample. It is observed as a linear trend between the Δ_{47} as a function of the δ^{47} of the sample with respect to the working reference gas. The δ^{47} of a sample is approximately equal to $\delta^{13}C$ and $\delta^{18}O$, thereby representative of the bulk isotope composition. This relationship is most clearly seen within gases of varying bulk isotope composition but with identical Δ_{47} values as the gas is equilibrated at a common temperature (e.g. 1000 °C).

This non-linearity appears to be a feature of the Thermo-Finnegan MAT 253, the instrument that has yielded most published clumped isotope data (for example Huntington et al. (2009)). Figure 2.1 shows a selection of published non-linear trends showing a range of gradients when plotting Δ_{47} and δ^{47} of 1000 °C heated gases. Figure 2.1 caption contains the equations of linear regressions. For the Thermo-Finnegan MAT 253, the gradients range from 0.004 to 0.027. Only two mass spectrometers appear to be non-linear in this regard, the MIRA instrument at UEA (discussed later) and the Thermo-Finnegan Delta XP at the Tokyo Institute of Technology (Yoshida et al. 2013). In this study they found that there was no significant relationship between Δ_{47} and δ^{47}. Their regression line is plotted in Figure 2.1 with a gradient value of 0.0011.

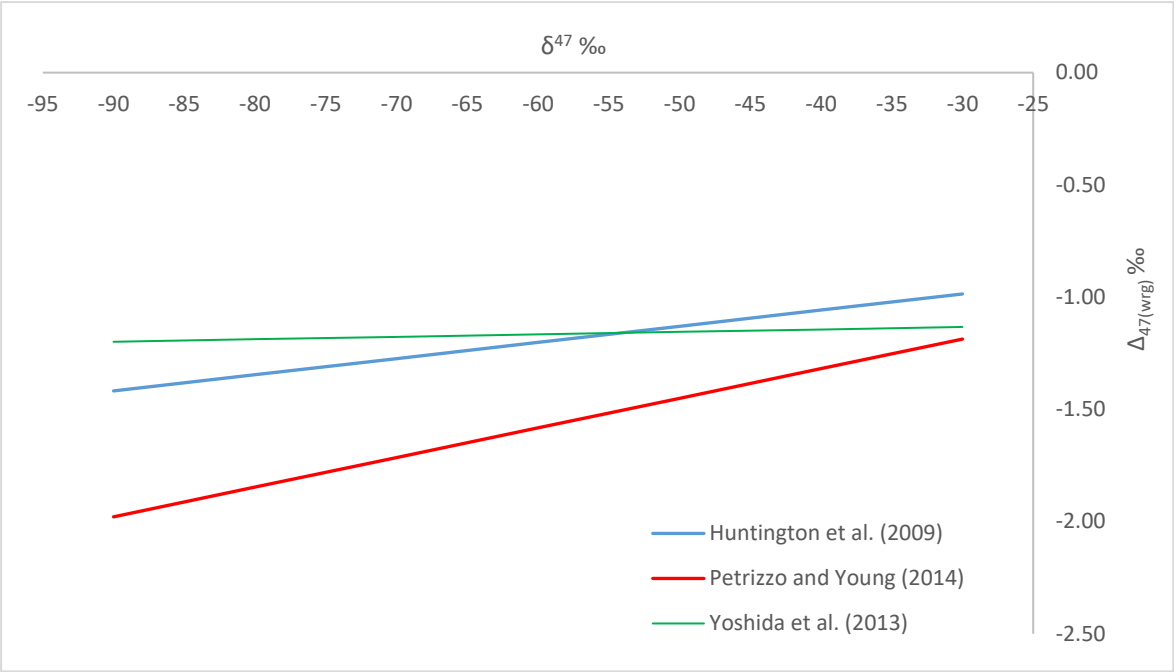

Figure 2.1 Published 'heated gas lines' showing the relationship between Δ47 and δ47. Huntington et al. (2009) equation is Δ47 = 0.0072(δ47) – 0.77, Petrizzo & Young (2014) equation is Δ47 = 0.0132(δ47) – 0.791, Yoshida et al. (2013) equation is Δ47 = 0.0011(δ47)-1.

Huntington et al. (2009) suggested that the correlation between Δ_{47} and δ^{47} represented a non-linear relationship between the R^{47} (calculated isotope ratios) values and the current intensity ratio between mass 47 and 44 ion beams. They also suggested that this non-linear feature develops over time and is individual to each mass spectrometer. Rosenheim et al. (2013) also noted that there was a large change in linearity directly after a filament change, which suggests there can be slow drift, and step changes when conditions vary in mass spectrometers.

The drivers of this covariation are not fully understood. It has been observed that there is also a negative offset in the baselines of the minor isotopologue peaks. When analyte gas is in the mass spectrometer, there is a negative offset in the faraday cup amplifier. This has been noted by multiple research groups (He et al. 2012; Bernasconi et al. 2013). The magnitude of the offset varies between instruments, reflected in the varying slopes of the heated gas lines. From this observation, the pressure baseline correction was developed, which is one way to correct clumped isotope measurements for non-linearity (He et al. 2012). Yoshida et al. (2013) indicate that a key difference between the MAT 253 and the Delta XP is the geometry of the ionisation chamber which affects the width of the beam. Yoshida et al. (2013) do not need to correct for non-linearity, and I show later that the MIRA instrument at UEA also requires no correction.

2.3.4 Scrambling and scale compression

Scale compression is an issue that is perhaps less well understood, and consequently has been much less discussed in the clumped isotope literature. When a sample gas is analysed, there is potential for the isotopes to be reordered amongst the molecules in the ion source. Huntington et al. (2009) noted that this reduces the difference in Δ_{47} between the analyte gas and the working reference gas. This 'scrambling' produces a scale compression in clumped isotope measurements (Huntington et al. 2009; Dennis et al. 2011). Scrambling of the analyte gas may be through dissociative fragmentation-recombination reactions requiring a threshold energy of 10-20 eV, such as,

$$CO_2 + e^- = CO_2 + 2e^- \qquad \text{Equation 2.17}$$

or through ion-molecule interactions, for example,

$$CO_2^+ + 2CO_2 = C_2O_4^+ + CO_2 \qquad \text{Equation 2.18}$$

These reactions could go in either direction, producing a large number of combinations and driving the gases towards a stochastic distribution (Dennis et al. 2011). Scale compression can be identified when the theoretical Δ_{47} composition of heated gases and gases equilibrated with water at a range of temperatures are plotted against the measured Δ_{47} compositions with respect to the working reference gas. An example of this is shown in Figure 2.10 using MIRA data. The theoretical values are attained using the data of Wang et al. (2004). The gases analysed in Figure 2.10 are the compositions of the heated gases and water equilibrated gases described in Section 2.4, and represent temperatures of 21 °C and 1000 °C. Scrambling and scale compression on MIRA will be discussed fully in Section 2.5.1.3.

The processes that cause scrambling are yet to be definitively identified. Huntington et al. (2009) suggested that a long residence time of the analyte gas in the source, or high gas pressure in the source promotes scrambling of the isotopes. It is also noted that the degree of scale compression changes over time, which could be related to variations in source tuning that subsequently affect the gas residence time and source pressure. As different instruments display varying amounts of scale compression, it therefore needs to be corrected for in order to compare data between mass spectrometers.

2.3.5 Normalisation to absolute reference frame

In light of the non-linearity and scrambling issues outlined above, clumped isotope measurements need to be standardised between laboratories in order to compare the data. Dennis et al. (2011) suggested that projecting data onto an absolute reference frame has advantages over using a calibration of inter-laboratory carbonates as all laboratories can use a common scale tied to theoretical predictions of the behaviour of clumped isotopes. Each individual mass spectrometer measures a Δ_{47} value that is on a "local reference frame"; a Δ_{47} calculated directly from the isotope ratios measured with respect to a working reference gas by the mass spectrometer. Different mass spectrometers suffer from varying degrees of source scrambling and other instrumental problems at different times (Dennis et al. 2011).

To project data onto the absolute reference frame, CO_2 gases of differing bulk isotope composition that have been equilibrated at the same temperatures are measured. These are the 1000 °C heated gases, and lower temperature water equilibrated CO_2, representing the likely range of temperatures to be measured. From these measurements, firstly a "heated gas line" is constructed, showing the linear regression between the measured Δ_{47} and δ^{47} values. This is used to correct for non-linearity within each mass spectrometer. We can then construct a transfer function by comparing the measured Δ_{47} values with the thermodynamic predictions of the isotopic compositions at these temperatures. The linear trend (transfer function) defined allows us to project unknown samples onto the absolute reference frame. Finally, if reaction of the sample has occurred at a temperature greater than 25 °C, an acid correction also needs to be applied.

2.3.6 Contamination

Clumped isotope measurements are done on isotopologue species that are present at very low natural abundances (Table 2.1), therefore even a ppb-level contaminant can cause apparent changes in the clumped isotope composition. Mass 47 should be present at about 40 ppm in CO_2, and we require a measurement precision of <0.01 ‰. A contaminant present at 0.4 ppb can alter the Δ_{47} value by an amount equal to the measurement precision (see Section 2.5.1.4). Because of the low abundance of the target multiply substituted isotopologue and the need for high measurement precision, it is necessary to use a rigorous gas cleaning procedure that effectively removes contaminants. For example, a typical sample amount is $5x10^{-5}$ mols. A contaminant at mass 47 of just $2x10^{-14}$ mols will lead to a systematic measurement error equal to or greater than the measurement precision required.

Due to the low mass resolution of isotope ratio mass spectrometry, any isobaric interferences from contaminant species of a similar mass cannot be resolved during analyses. Possible sources for contamination include impure samples, contaminated reagents, gas leaks during sample reaction and gas handling and background impurities in the mass spectrometer. Whilst it is necessary to use a rigorous cleaning procedure, it is also useful to identify diagnostic characteristics indicative of the presence of contamination. Eiler & Schauble (2004) suggested that the mass-48 and 49 signals should be routinely analysed and used as an identifier for contaminants. This is because there are relationships between contaminant species and the effects they have on isotopologues of m/z = 44 to 49 (Eiler & Schauble 2004).

The likely contaminants for CO_2 have not yet been fully identified, but are likely to include halocarbons, hydrocarbons and sulphur compounds. These have characteristic fragmentation patterns and mass spectra. For example, chlorinated compounds such as CH_2Cl_2 (methylene chloride) have strong peaks at mass 47, 48 and 49. Therefore we may see covariation amongst the measured Δ_{47}, Δ_{48} and Δ_{49}. Masses 48 and 49 are present at only 4000 and 40 ppb amongst the CO_2 isotopolgues. It is for this reason that Eiler & Schauble (2004) suggested monitoring of these masses for identifiers of potential contamination. As a test, they added dichloromethane (CH_2Cl_2) to pure CO_2. They found that this produced a linear trend between Δ_{47}, Δ_{48} and the intensity of the mass 49 ion beam. The trends are described by two equations:

$$\Delta_{47} = 0.735 \times [(mV\ mass49\ sample) - (mV\ mass\ 49\ reference)] \quad \text{Equation 2.19}$$

$$\Delta_{48} = 3.47 \times [(mV\ mass49\ sample) - (mV\ mass\ 49\ reference)] \quad \text{Equation 2.20}$$

The interfering masses are produced by fragmentation of the methylene chloride in the ion source, along with dissociation and recombination of C-H-Cl components under electron bombardment. They also found a similar covariation in samples with contamination from halocarbon and hydrocarbons, and therefore suggest using this relationship to identify contaminated samples (Eiler & Schauble 2004).

Eiler & Schauble (2004) also worked with atmospheric CO_2 and identified species of nitrous oxide (N_2O), fragments of halocarbons and hydrocarbons as contaminants. The vapour pressures of these compounds are low and so the contaminant (excluding N_2O) should remain in an ethanol-dry ice trap (Eiler & Schauble 2004). However, it is also necessary to reduce the relative partial pressure of contaminant species to very small values, and so it is unlikely that cryo-trapping alone would be successful in removing all contaminants. Ghosh et al. (2006) further cleaned their gases

by passing them through a GC column packed with divinyl benzene polymer and held at -10 °C, which was baked between samples. Yoshida et al. (2013) also noted that cleaning of samples using a packed GC column is a more efficient way of removing hydrocarbons and halocarbons. Within the published literature, it appears that every gas preparation procedure involves either a GC column for separation of CO_2 from contaminants, or trapping the gas on a static column packed with Porapak™ resin beads. Further discussions on contamination and sample preparation methods are included in Chapter 3.

2.4 Procedures for clumped isotope analysis

On a typical day, three or four samples can be cleaned (for carbonates at UEA the reaction occurs overnight prior to gas clean-up) and then analysed on MIRA. A minimum of one carbonate standard and either a heated gas or water equilibrated gas are cleaned and analysed also. The frequency within a week of analyses is dependent on the stability of the mass spectrometer. For example, during the week after a major change such as a filament replacement we measure more standard materials and calibration gases to ensure there are no further issues arising. We have a large collection of data surrounding our carbonate standards and calibration gases, which means we can rapidly identify a problem as the standards show drift away from the norm.

2.4.1 Heated gases

Calibration gases used to define the transfer to the absolute reference frame are made from three different CO_2 gases with known and different bulk isotope composition. These are a BOC cylinder gas, room temperature phosphoric acid digestion of crushed BDH marble chips to produce CO_2, and an approximately 1:1 mixture of the two. These are all cleaned identically to the sample CO_2 preparation method (Chapter 3 Section 3.4.3). Table 2.2 describes the bulk isotopic composition of each gas and the average δ^{47} and Δ_{47} for the entire analysis period.

Gas	δ^{13}CSamp ‰$_{VPDB}$	δ^{18}OSamp ‰$_{VSMOW}$	δ^{47} ‰	Δ_{47} ‰	S.D. Δ_{47}	S.E. Δ_{47}	Number of samples (n)
HGBOC	-34.31	10.05	-59.087	-0.592	0.073	0.012	35
HGBDH	2.01	30.71	-4.837	-0.681	0.080	0.006	175
HGMIX	-17.46	23.07	-30.569	-0.602	0.072	0.014	25

Table 2. 2 Average values for composition of heated gases. Data from February 2013 to May 2016.

Heated gases are prepared by flame sealing a small aliquot of any of the gas types into a quartz tube. These tubes are pre-flamed at 1000 °C for a minimum of three hours prior to use to

remove any trace contaminants, such as chlorine-based gases or organic materials. Once the tube is sealed, the gases are heated in a muffle furnace to 1000 °C for a minimum of three hours to induce a stochastic isotope distribution. The tubes are quenched immediately by immersion into water at room temperature. The gases then undergo the same cleaning procedure on the same vacuum line as the samples prior to analysis on the mass spectrometer.

Heated gas analyses during October 2012 to December 2012 showed anomalous results. While the BOC gas was used as a reference gas in late 2012, the majority of calibration gas results showed apparent disequilibrium. There was no difference in results when identical samples were run with different trap currents, suggesting the source of the problem was not scrambling of the signal by the trap current. It was considered likely that the heated gases were equilibrating over time after heating. It was also thought that scale compression may have contributed to the issues. From this time onward the protocol was revised so that gases were heated as required – no gases are left for more than four hours at room temperature after heating, to minimise redistribution of the bonds.

2.4.2 Water equilibrated gases

The same CO_2 gas types are also used to prepare water equilibrated gases between 19 °C and 25 °C. The method used for the majority of my research was as follows. Approximately 0.1 ml of deionised water was syringed into the base of a 6 mm pyrex tube with a Louwers-Happert valve. These tubes are 20 cm in length. The water is frozen at the base of the tube and the tube is evacuated. An aliquot of CO_2 is loaded into the evacuated tube by freezing it in with liquid nitrogen. Once loaded, the tube is allowed to warm up and is left for a minimum of four days in a GC oven to reach thermal equilibration. The gas is then cleaned using the same methods and vacuum line as for a sample before analysis on MIRA.

Over a long time period, water equilibrated gases have varied around a zero value. This is due to their equilibration temperature being similar or very close to the water equilibrated reference gas values. The fact that there is fluctuation above and below zero would suggest that some of the measured water equilibrated gases may not have had enough time to fully equilibrate to the room temperature, or they may have fractionated during preparation. After loading into the vessel with water, leaving it for four days should be adequate time for the CO_2 to equilibrate with the water. It is therefore likely that there is some fractionation of the gas during sample preparation. There have been changes to the methodology of the water equilibrated gases since this thesis was started (Autumn 2015). One large batch is now prepared in a one litre flask in a similar manner to the working reference gas (see below). Each time a measurement is required, a

single aliquot is drawn from the flask. This means the bulk of the gas can remain at a constant equilibration at room temperature.

2.4.3 Preparation of working reference gas

At UEA we prepare our own working reference gas in-house. This means we can produce a gas which has a similar bulk isotope composition to the carbonate samples we analyse. Having a reference gas close in composition to the sample material means that any non-linearity corrections are less severe than if measuring with a reference gas that is different in composition. Approximately 5 g of BDH marble chips are reacted with 85 % phosphoric acid and 50 ml of deionised water in a 2 l flask. The flask is pumped to a high vacuum (approximately 10^{-5} mbar) prior to reaction, with the acid frozen under liquid nitrogen. The carbonate is kept in a separate but connected flask attached using a ball and joint clip. Once the acid is defrosted the carbonate is allowed to react with the acid. The ratio of acid to carbonate is calculated such that the acid is fully consumed by the reaction as there is a slight carbonate excess. This ensures the residual fluid is not acidic, as there is the potential for pH to affect the clumped isotope signature (see Chapter 4). The flask is kept at room temperature for a month on a shaker table so that the CO_2 will equilibrate with the excess of water and be at thermal equilibrium at room temperature.

After approximately a month of equilibration, the reference gas undergoes the same cleaning process as any sample or standard gas. The CO_2 is pre-cleaned by passing it through a large volume glass trap at -78 °C (using an ethanol-dry ice mixture) and then freezing into a 1 L flask (Figure 2.2). The flask is connected to a sequence of five 5 L gas flasks attached to the MIRA preparation line (Figure 2.3). These are evacuated to a high vacuum pressure, then the CO_2 can be expanded from the 1 L flask into this sequence. This step lowers the pressure of the CO_2 so that water vapour can be removed at -115 °C. The two spiral traps are maintained at -115 °C as the expanded contents of the 0.5 L flask are passed through the line in the same cleaning process as sample gas (see Chapter 3) and frozen into another 1 L flask. The Poropak™ trap was held between -20 °C and -30 °C. This process was completed over a period of approximately four days, moving the gas an aliquot at a time.

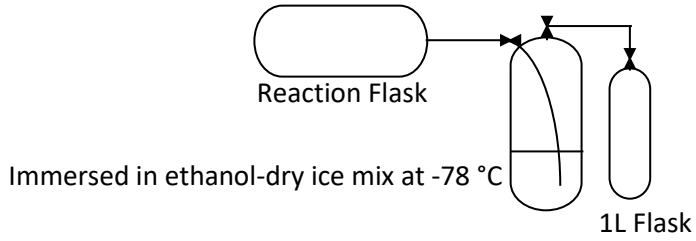

Figure 2.2 Schematic to show pre-cleaning steps taken during preparation of the working reference gas.

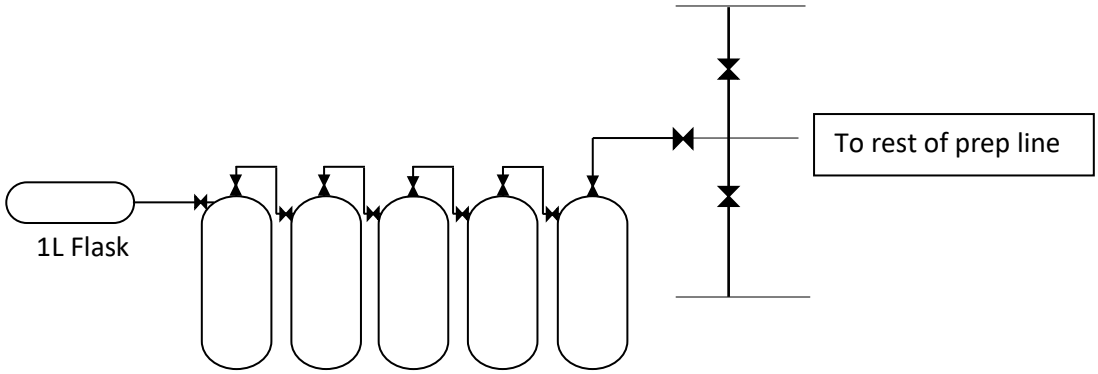

Figure 2.3 Schematic to show expansion into 25 L flasks prior to cleaning on vacuum line. The full vacuum line is shown in Chapter 3 Section 3.2.

Once the gas is cleaned, it is measured against an aliquot of the previous reference gas and against NIST-612 and UEACMST to fully characterise its isotopic composition. Table 2.3 shows when each reference gas was in use and these periods are colour coded. Gases are usually changed when taking multiple aliquots of gas cannot provide an adequate reference gas signal. Table 2.4 shows the average compositions of the heated gases each time the reference gas was changed.

1	**BOC**	**Oct 2012 - 29th Jan 2013**
2	**BDH 1 (A)**	**30th Jan 2013 - 19th May 2013**
3	**BDH 2 (B)**	**20th May 2013 - 25th Feb 2014**
4	**BDH C**	**26th Feb 2014 - 19th May 2015**
5	**BDH C (2)**	**20th May 2015 - present**

Table 2.3 Dates that each reference gas has been in use (colour coded).

Ref. Gas Periods	δ^{13}CSamp ‰$_{VPDB}$	δ^{18}OSamp ‰$_{VSMOW}$	δ^{47} ‰	Δ_{47} ‰	S.D. Δ_{47}	S.E. Δ_{47}	Number of analyses (n)
HGBOC	-37.04	7.83	-0.005	-0.535	0.037	0.026	2
HGBDH	-0.77	35.79	65.436	-0.538	0.019	0.014	2
HGBOC	-34.26	10.03	-58.679	-0.606	0.071	0.041	3
HGMIX	-17.46	23.40	-29.995	-0.604	0.053	0.022	6
HGBOC	-34.27	10.47	-58.346	-0.526	0.053	0.015	12
HGBDH	2.03	32.20	-2.856	-0.559	0.039	0.009	18
HGMIX	-17.44	23.78	-29.568	-0.545	0.041	0.014	9
HGBOC	-34.36	9.82	-59.695	-0.610	0.072	0.021	12
HGBDH	1.96	30.50	-5.306	-0.664	0.068	0.009	58
HGMIX	-17.54	22.78	-31.431	-0.657	0.079	0.030	7
HGBOC	-34.35	9.51	-59.662	-0.576	0.024	0.017	2
HGBDH	2.00	30.70	-4.813	-0.708	0.076	0.009	66

Table 2.4 Average heated gas composition for each period of different reference gas. Gases are colour coded to define the reference gas periods as in Table 2.3. It is possible to see that different reference gas types can alter the measured composition of the heated gases.

2.5 MIRA IRMS description

UEA owns a newly designed mass spectrometer that is purpose built for clumped isotope measurements. The MIRA (Multi-Isotopologue Ratio Analyser) is designed to optimise performance in terms of sensitivity and linearity. It has a 120 ° symmetric geometry and a Nier-type high sensitivity electron impact ion source. The 120 ° angle enables a shorter path between the source slit and magnet entrance, and magnet exit to resolving slit (288.7 mm each), reducing beam broadening to lower ion-molecule collisions and improving the beam profile. It also reduces the amount of ion scatter and secondary electron generation from interactions between the beam and the flight tube, the lenses and the resolving slits. The Nier-type source consists of a three element immersion lens along with a repeller plate located towards the rear of the ionisation cavity. We use a thoria-coated filament as the source for the electrons. The beam is located centrally with respect to the filament length, and is further focused by a magnetic field from two small magnets either side of the source.

There are six faraday cup collectors to enable measurements of the isotopologue masses of carbon dioxide. These have integral resolving slits, secondary electron suppression lenses and are individually screened. The inside of the cups are coated with a graphite deposit. Each cup and lens grouping are mounted on individual supports, and the base plate is etched with a graticule and mounting slots to ensure exact placement in relation to the CO_2 beams and resolving slits. The electromagnet is made from high purity iron plates with two 600 turn assemblies made from

polyester resin coated copper wire. The total coil resistance is 10 Ω and 125 W is required for a field of 0.35 T.

MIRA is a dual inlet system, with sample and reference gas variable bellows (including an additional external reference bellows), a cold finger volume, 50 cm stainless steel capillaries and a change-over valve. The standard reference bellow has been replaced in order to match the bellow volumes to 2-40x10^{-3} L. The external reference bellow has a variable volume between 10-200x10^{3} L. Sample and reference gas volumes deplete at the same rate due to the matching volumes in the bellows and balanced capillaries, ensuring there is no isotope drift during a run. The variable bellows are used to keep the pressure and signals balanced before and during an analysis. MIRA is kept under vacuum by three turbomolecular high vacuum pumps and two diaphragm pumps. This ensures a clean vacuum pressure of 1x10^{-9} hPa is easily achieved. The changeover valve is pumped with its own dedicated turbomolecular pump and diaphragm pump, whilst the other valves and inlets are pumped by two more diaphragm pumps and a turbomolecular pump.

2.5.1 Key performance indicators

2.5.1.1 Peak shapes and sensitivity

An example of peak shape and quality is shown in Figure 2.4. The peaks were recorded at a major beam intensity of 7.5x10^{-8} A and an analyser vacuum of 2x10^{-8} mb. The output from the six faraday collectors are recorded as the source high voltage is scanned over 60 volts at an acceleration voltage of 8 kV. The peaks all have broad, flat tops, with steep sides and flat baselines. The cardinal masses are in line with the beam centres and are within 4 volts of each other. This indicates that the resolving slits are correctly located on the focal plane. Figure 2.4 shows screenshots taken from MIRA during peak scans. Figure 2.4a displays a scan of the beams over a 60V range when there is gas in the source, indicating a flat topped peak. The magnified section shows the beam ratios (45/44, 46/44 and 47/44) scanned over a 10 V range. The three ratios are flat to within 2 ‰ over the voltage range. This indicates that the outer envelope of the beam is within the resolving slit width.

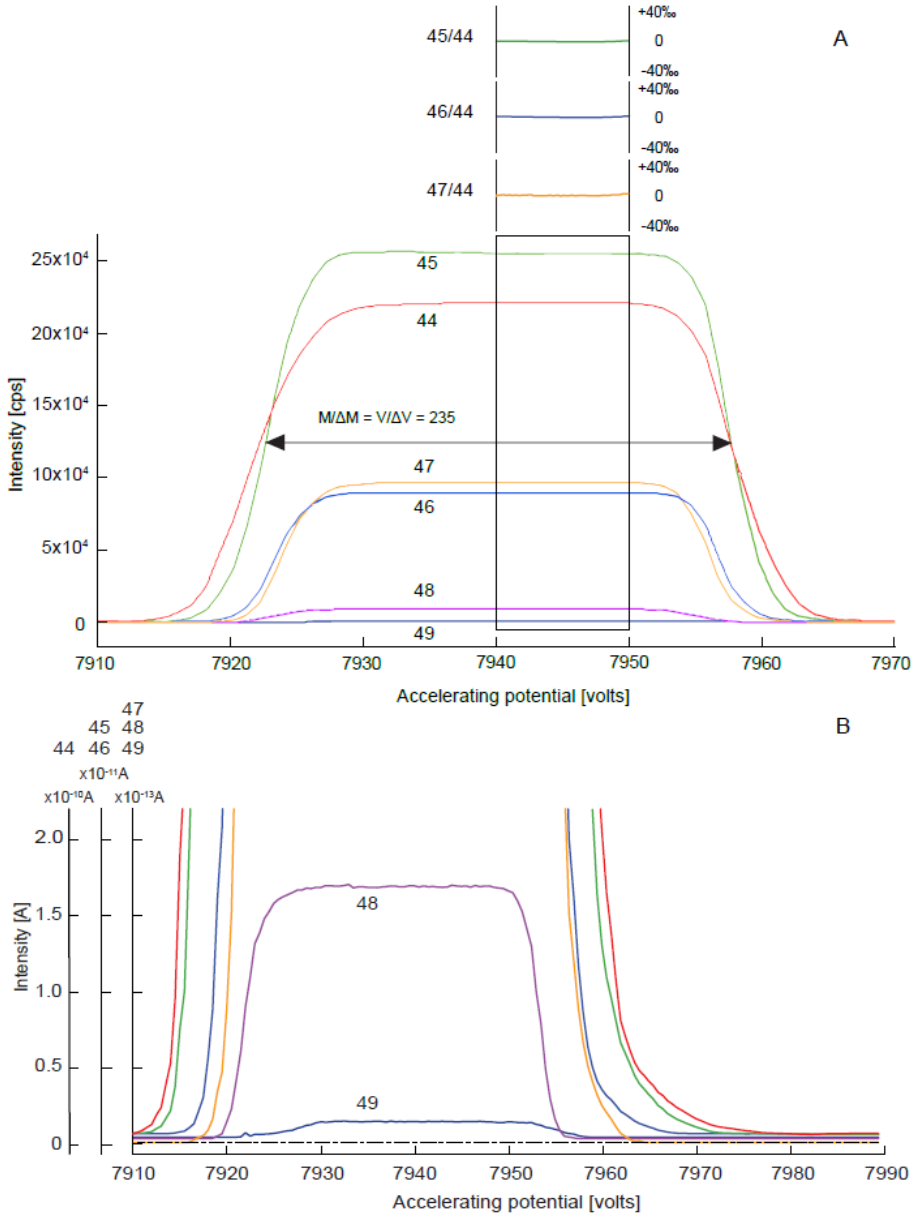

Figure 2.4 Image displaying the beam intensity as the peak is scanned over a 60 V range. Each beam colour is labelled along the peak. B is a close up section of A.

Figure 2.4b (bottom figure) is a highly magnified image of baseline and peaks of the top half of the figure. Here, it can be seen that there is no peak baseline shift when gas is put into the mass spectrometer. The dashed and dotted black line represents mass 47 baseline in absence of gas in the mass spectrometer. As the peaks return to baseline (and prior to peak scan on left hand side of the diagram) there is no offset, and each beam returns smoothly to the baseline.

2.5.1.2 Linearity

At UEA we measure three different heated gases, and we use a reference gas based on the composition of BDH marble chips. The preparation of these gases, and also the method with which we prepare a heated gas for analysis is covered in Section 2.4. Our reference gas has changed through time, which is outlined in Table 2.3. During the very early measurements, we used a BOC gas as a working reference gas. This is the same composition as the BOC gas used for heated gases. We later switched to a reference gas produced by reaction of BDH marble chips with ortho-phosphoric acid and equilibrated a room temperature. This provides a heated gas with isotopic values similar to the carbonates we predominantly measure.

MIRA is designed specifically for clumped isotope measurements, and has an ion source designed to minimise the measurement artefacts that cause problems for other laboratories, namely the non-linearity that others correct for, and scrambling in the source. The key way that non-linearity can be identified is by plotting the values of Δ_{47} and δ^{47} for each of the heated gas compositions to produce the 'heated gas line'. On MIRA, this linear regression has varied over time, but always remains close to zero, and has shown a negative gradient in the past rather than the positive one seen in the majority of published work.

Figure 2.5 shows four plots demonstrating the linear regression between Δ_{47} and δ^{47}. The same reference gas is in use throughout this time, but the design of the ion source was altered in December 2015. The data is split into a 'before' and 'after' the re-design groups. Figures 2.5A and 2.5B represent the data prior to the re-design. Figure 2.5A shows all of the data for BDH and BOC heated gas compositions measured during this time, excluding any analyses with high Δ_{48} and Δ_{49} values indicative of contamination (see Section 2.3.6). There were no MIX composition gases measured during this time. There is a large spread in the BDH data, with values ranging from -0.906 ‰ to -0.594 ‰ for Δ_{47}. There is a much narrower spread in δ^{47}, from -2.315 ‰ to -6.381 ‰. There are just two values for BOC gas composition, and these are close together. Figure 2.5B shows the gradient between the averaged values for these two gas compositions. The regression is stated on the graph, and the gradient is a shallow negative slope. This is quite different from the 'heated gas lines' identified on the Thermo-Finnegan MAT 253 instruments. A selection of these heated gas lines are also included in Figure 2.5B for comparison.

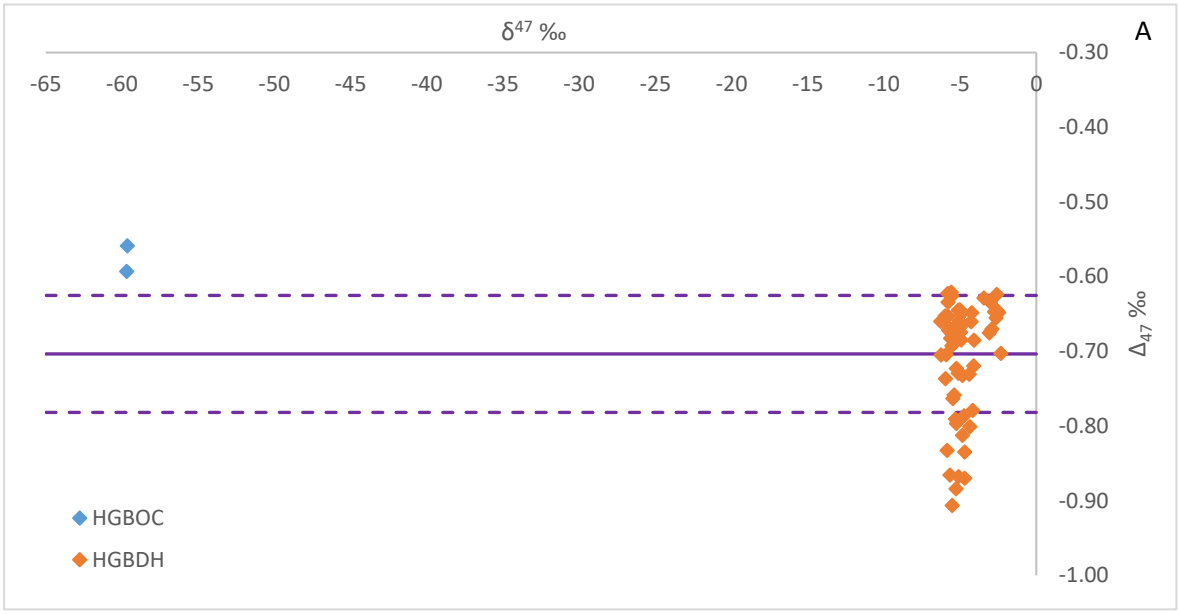
A
δ47 ‰
-65 -60 -55 -50 -45 -40 -35 -30 -25 -20 -15 -10 -5 0
-0.30 -0.40 -0.50 -0.60 -0.70 -0.80 -0.90 -1.00
Δ47 ‰
HGBOC
HGBDH

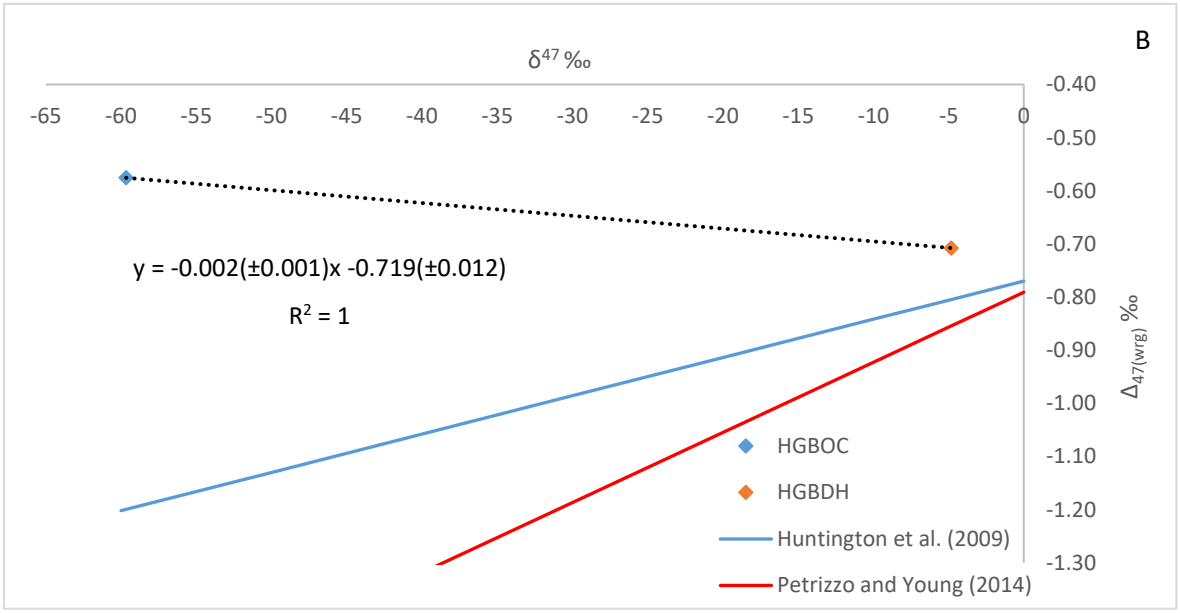
B
δ47 ‰
-65 -60 -55 -50 -45 -40 -35 -30 -25 -20 -15 -10 -5 0
-0.40 -0.50 -0.60 -0.70 -0.80 -0.90 -1.00 -1.10 -1.20 -1.30
Δ47(wrg) ‰
y = -0.002(±0.001)x -0.719(±0.012)
R2 = 1
HGBOC
HGBDH
Huntington et al. (2009)
Petrizzo and Young (2014)

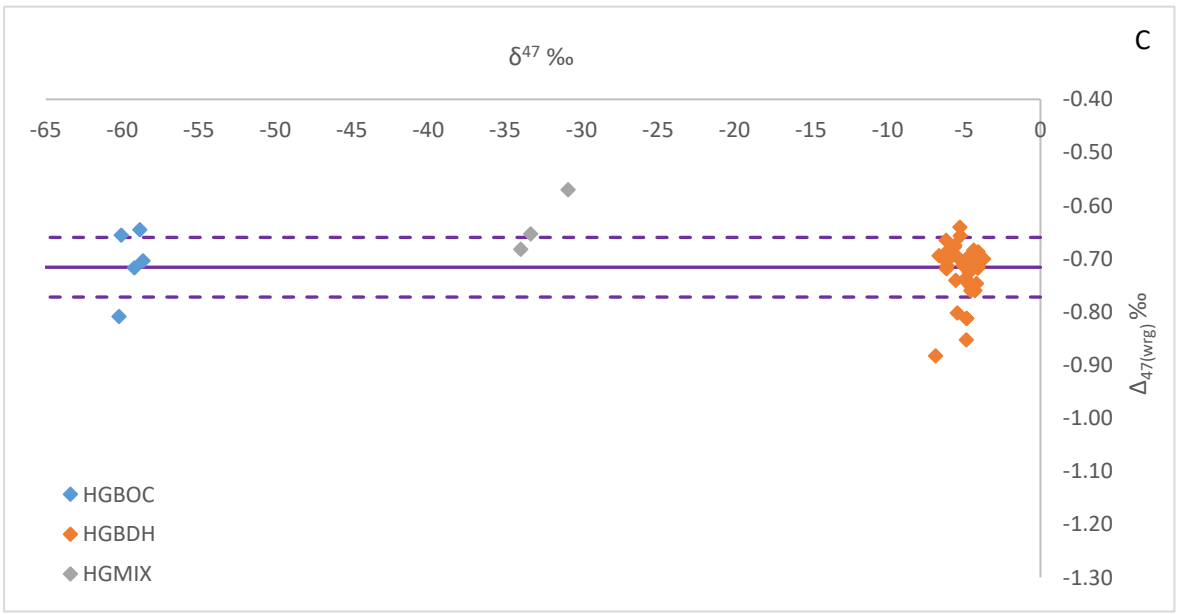
C
δ47 ‰
-65 -60 -55 -50 -45 -40 -35 -30 -25 -20 -15 -10 -5 0
-0.40 -0.50 -0.60 -0.70 -0.80 -0.90 -1.00 -1.10 -1.20 -1.30
Δ47(wrg) ‰
HGBOC
HGBDH
HGMIX

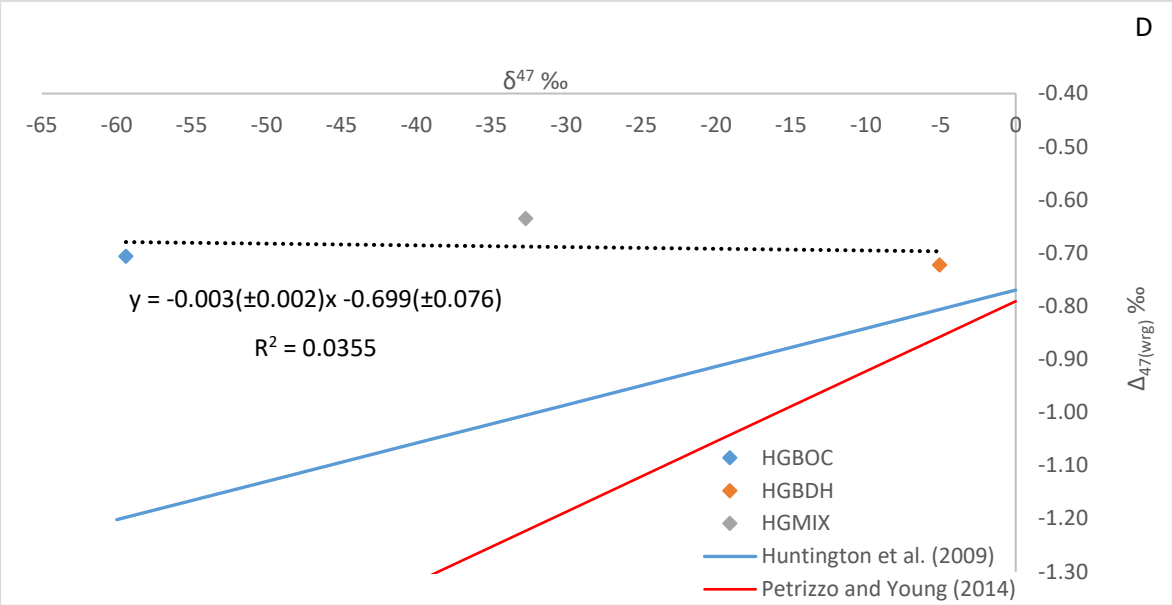

Figure 2.5 MIRA's linearity is indicated by plotting the δ47 value against the $\Delta_{47(wrg)}$ values for heated gases. Panels A and B display the linearity for the period 22nd May 2015 to 10th December 2015. Panels C and D display the heated gas lines between 11th December 2015 and 12th May 2016. These two groups are before and after a modification to the source. Panels A and C display the mean and standard deviation for the heated gases during this time period.

Figure 2.5C and 2.5D represent the heated gas data after the source design was altered. In mid-December 2016, the ion optics were altered and an extra plate was added in front of the filament. This was to encourage a lower pressure of CO_2 to be in contact with the filament. Figure 2.5C contains all three compositions of heated gas plotted to show the relationship between δ^{47} and Δ_{47}. The BOC heated gases have a greater spread in composition than in Figure 2.5A, ranging from -0.809 ‰ to -0.646 ‰ for Δ_{47}. The BDH gas ranges from -0.883 ‰ to -0.641 ‰ for Δ_{47}, which is a narrower range than before the source re-design. Figure 2.5D again shows the linear regression through the average value for each gas composition. The regression equation on the graph describes a slight negative slope of 0.0003. This source re-design has meant that the linearity of MIRA has been further improved. The slight negative slope has almost been removed, as (within error) the Δ_{47} and δ^{47} regression can be considered a linear relationship, much more so than some of the published 'heated gas lines' displayed on Figure 2.5D for comparison.

A feature of both figure 2.5A and 2.5C is the smearing of the BDH data towards a more negative value. During June 2015, we replaced the filament on MIRA. During the first few measurements of heated gases and carbonate standards, we noticed the data had shifted to much more negative values. This same pattern occurred again when the filament was replaced twice in mid-December, around the same time as the source re-design. Figure 2.6 shows the heated gas

data (all compositions) analysed during this period. The x-axis is numbered according to day 1, 2 and so on. There are sometimes multiple analyses each day, and some of the heated gas values are quite spread (for example on day 10). The time period covered by these measurements is from 7th December 2015 to the 11th January 2016. The two changes in filament (Fig 2.6) represent times when the mass spectrometer was opened up to air. Each time this occurred, the Δ_{47} value drops considerably, followed by a slow rise back to the norm, after which it appears to plateau. This rise and plateau typically takes a few days and probably records the change in vacuum as water vapour is removed and MIRA recovers optimum vacuum.

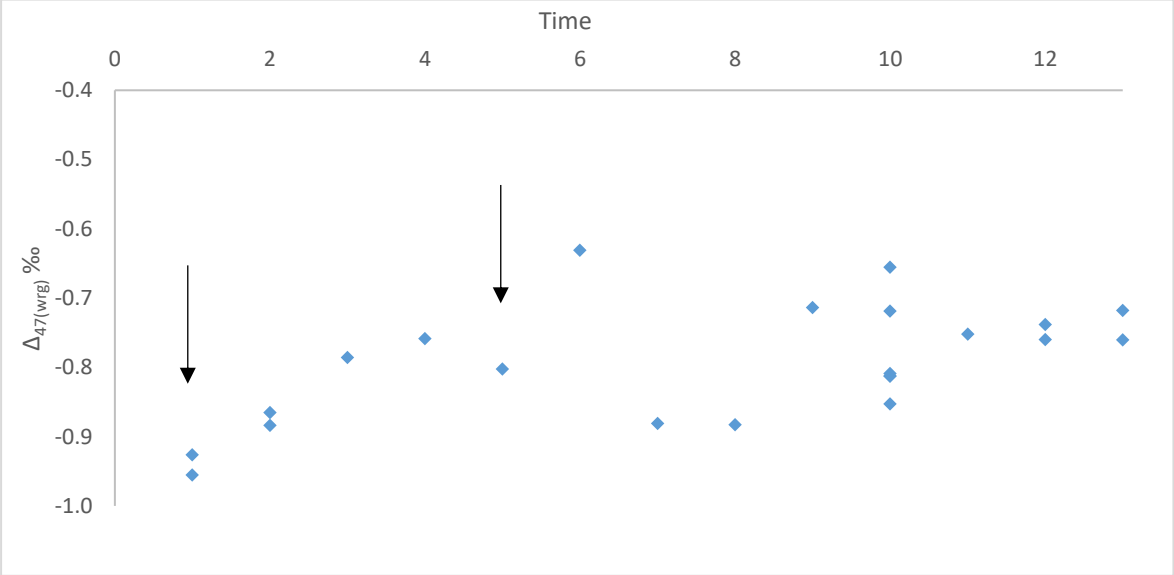

Figure 2.6 Heated gases analysed immediately after two filament changes. The black arrows indicate the first analysis after each filament change.

If the new filament or maintenance work affected data points are excluded (any datum more negative than -0.8 ‰), there is considerable improvement in the scatter of heated gas values (Figure 2.7). Figure 2.7A and 2.7B show the heated gas data before and after source re-design. There is a much tighter grouping within the BDH gas data, which has the highest number of analyses. Figure 2.7B shows the linear regression between the average gas composition values before the source re-design. The removal of the more negative data shows a heated gas line that is shallower than before, but still with a negative gradient. However, the very low gradient value of -0.0018 is much shallower than the majority of published calibrations. Figure 2.7D shows the linear regression between Δ_{47} and δ^{47} for the heated gases after source re-design, with the more negative data removed. There has been a negligible change to the gradient here, which suggests that the

combined removal of anomalous data and a source re-design produces a stable and linear heated gas relationship.

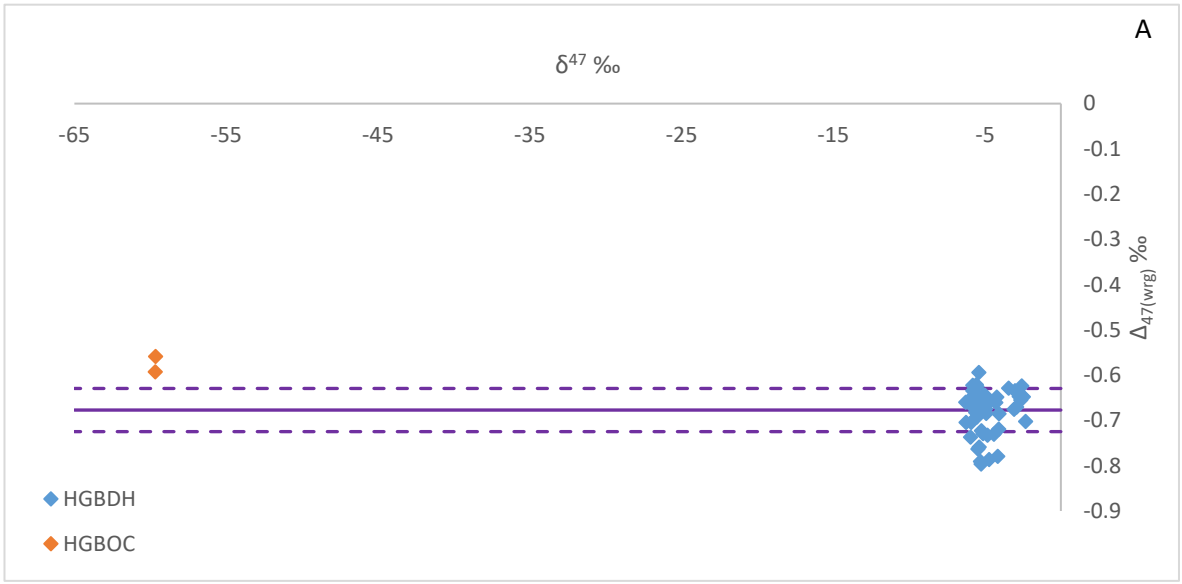

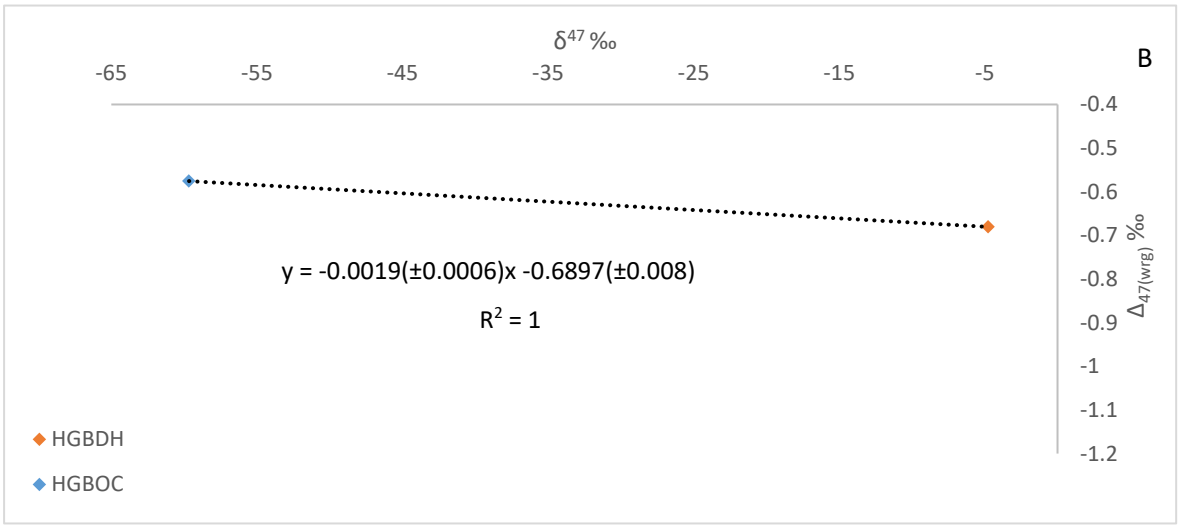

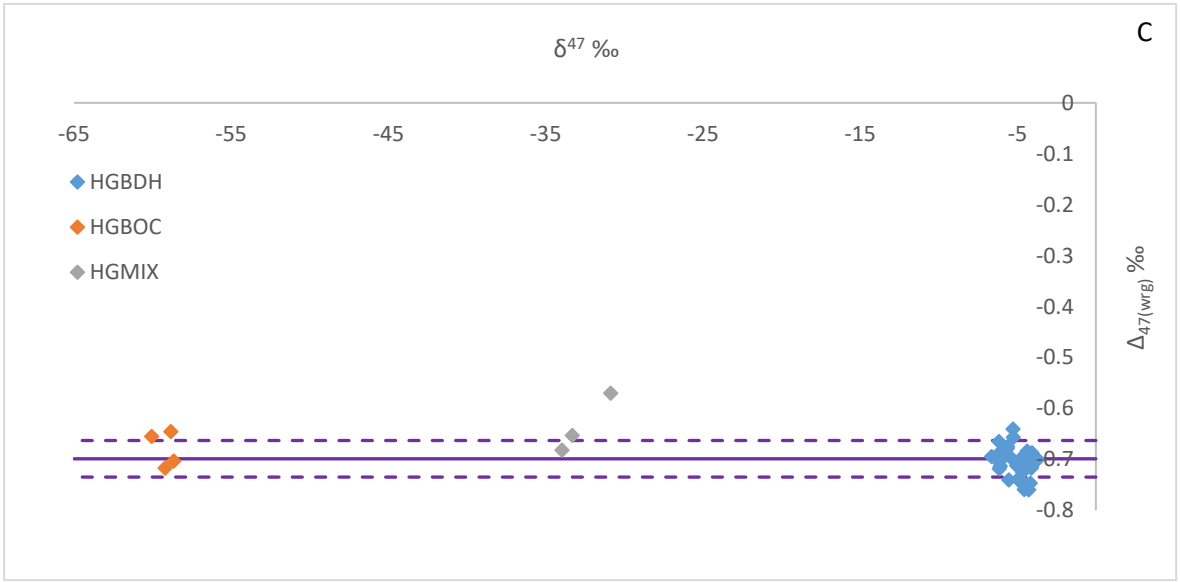

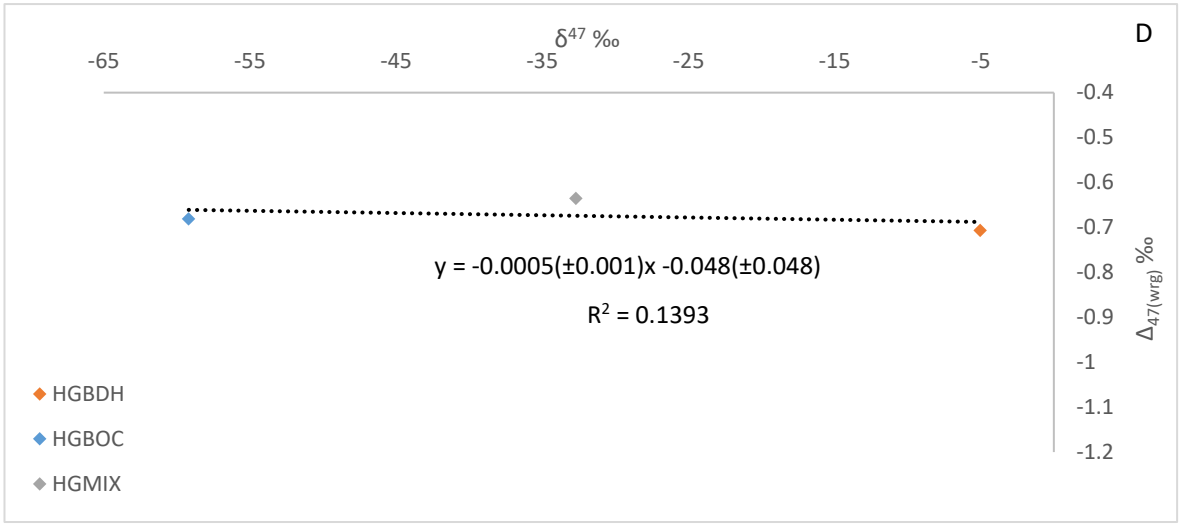

Figure 2.7 Linearity graphs for MIRA over the same time periods as Figure 2.5 (panels A and B are between 22nd May 2015 and 10th December 2015, and panels C and D are between 11th December 2015 and 12th May 2016). Low values in Δ47 after filament changes have been removed. Panels B and D show the heated gas lines for each period, using the average values for the measured heated gases.

MIRA can remain linear or close to linear for over a year, as indicated by the heated gas data between March 2014 and May 2015 (Figures 2.8A and 2.8B). This shows there is stability in MIRA throughout time. Figure 2.8B shows the average value for each of the three gas with a linear regression between Δ_{47} and δ^{47}. The slope is extremely shallow, negative at -0.001. This again shows that MIRA is a linear instrument, with a stable heated gas line showing minimal variation over time.

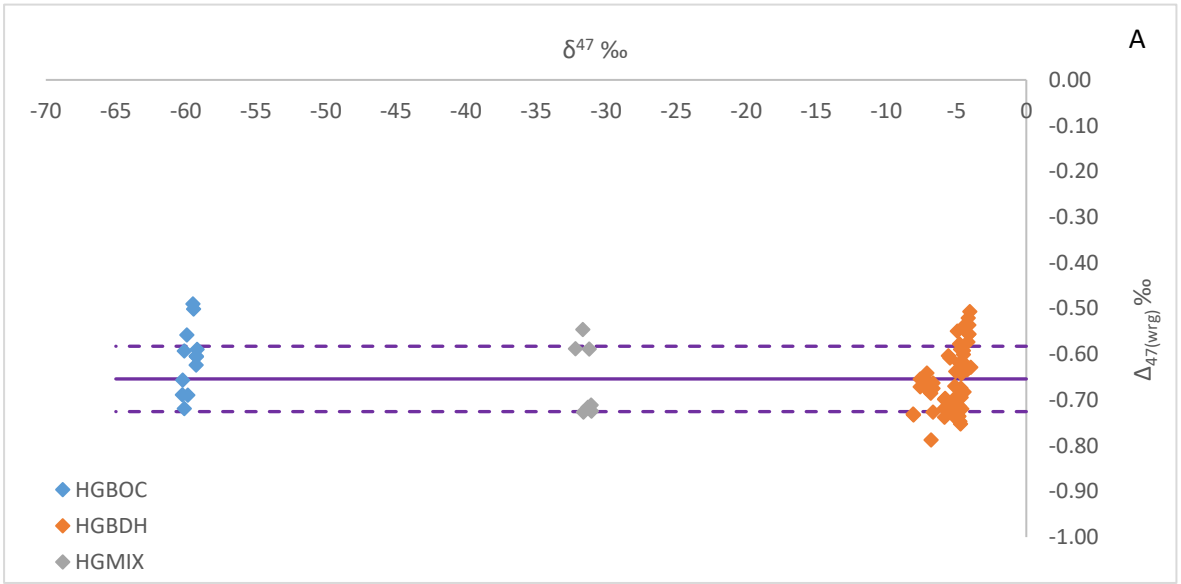

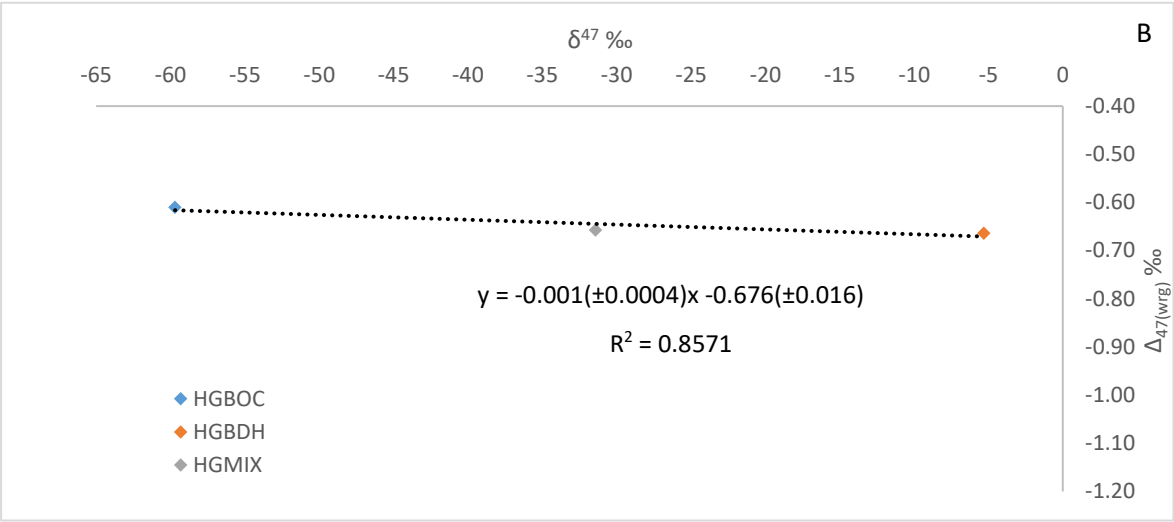

Figure 2.8 Linearity plot for heated gas data between 5th March 2014 and 15th May 2015. Panel A is all measurements, and the regression in plot B is based on the averaged values of these gases.

Finally, it is also possible to identify MIRA's linearity through the relationship between Δ_{47} and δ^{47} in the 20 °C water equilibrated gases. Figure 2.9A shows all of the water equilibrated Δ_{47} and δ^{47} data between September 2014 and April 2015. There is quite a large spread in Δ_{47} for all three gas compositions. Since the Autumn of 2015, we have improved our preparation and measurement of water equilibrated gases compared to the time these measurements were made. The average value for each gas composition is plotted in Figure 2.9B, and the linear regression between these values is identified on the graph. Despite the larger spread in data, the gradient of the line is similar to what is seen for the heated gases – a very shallow, slightly negative gradient. This is consistent with the overall statement that MIRA is a linear mass spectrometer.

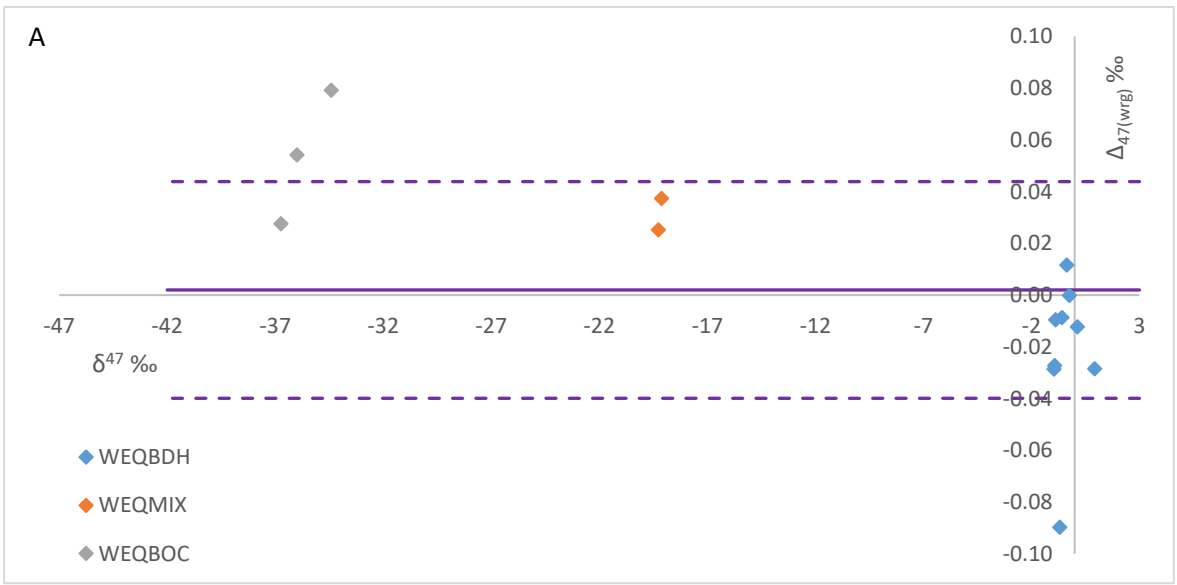

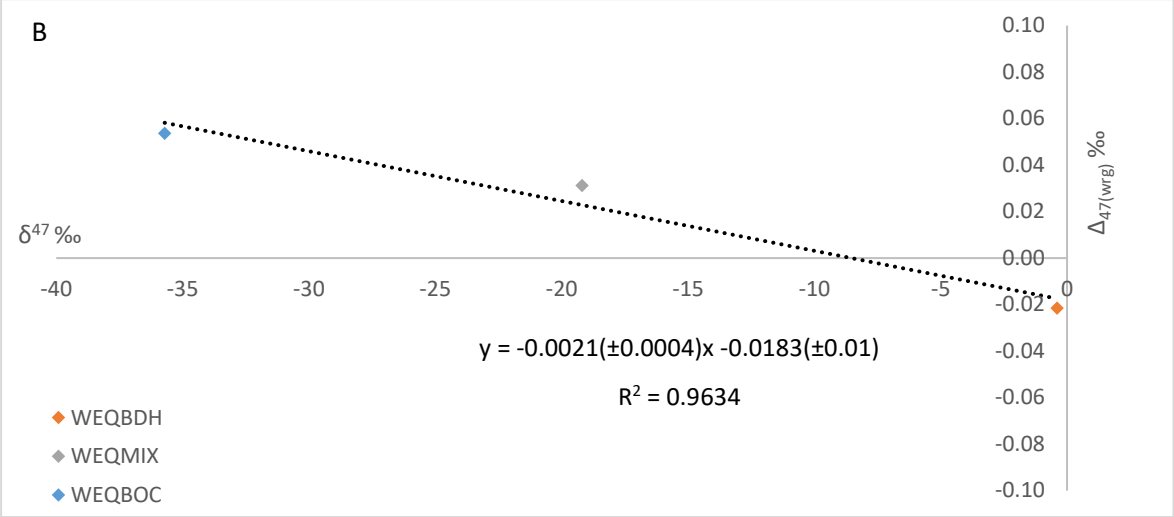

Figure 2. 9 Linearity plots using water equilibrated data between 24th September 2014 and 9th April 2015. Panel A shows all of the data, and B shows the heated gas line based on the average values for the three gases during this time.

There is debate in the literature as to what causes non-linearity in other mass spectrometers. The only published data showing a linear relationship comes from a Thermo-Finnegan Delta XP (Yoshida et al. 2013) who identify a near neutral gradient for their instrument of 0.0011. They suggest a key difference between their instrument and the MAT 253 is the ionisation chamber geometry which alters the width of the beam. Bernasconi et al. (2013) state that negative backgrounds on the Faraday cups, due to the presence of secondary electrons, cause the non-linearites in the measurements of CO_2 isotopologues. These are occurring in the cups recording the minor ion beams. They suggest that the background effects can be corrected when there is gas flowing into the source. He et al. (2012) also noted that this non-linearity is due to a change in the baseline signal when gas is admitted into the ion source. The negatively charged particles offset the residual background noise and this needs to be corrected. They suggest that the major mass-44 ion beam interacts with the flight tube, producing secondary electrons from the collisions. The secondary electrons, and the scattered beam, enters into the Faraday cups, producing the background offset (He et al. 2012).

MIRA is designed so that there is no interaction between the beam and the upper and lower surfaces of the flight tube. This is due to the flight tube and magnet fringing design. The arrangement of the Faraday cups and the resolving slits is such that only ions travelling along the faraday axis can pass through the resolving slit, and any off-axis ions are screened. There is no generation of secondary electrons and therefore no pressure baseline effect (Paul Dennis, Pers. Comm.).

2.5.1.3 Scale Compression

The severity of scale compression on MIRA has varied over time. There have been periods of stability, where our transfer function has remained similar on a week-to-week basis. At these times, the scale on MIRA is compressed by approximately a factor of 1.3. Some of the earliest data shows a scale compression of up to 1.5. We have tried several stratagems to reduce scale compression. The capillaries were crimped to reduce pressure in the source, which could reduce the chances of fragmentation and recombination of the analyte gas. The positioning of the filament was also changed to bring the ionisation region further back. Neither of these changes improved scale compression.

There have also been periods when scale compression has varied dramatically over a short space of time. An example plot using heated gas and water equilibrated data to plot the relationship between the measured and theoretical Δ_{47} values is shown in Figure 2.10. The data in Fig. 2.10 are from a three-day period (7th to 10th December 2015), the same data set used to demonstrate change in linearity after maintenance work (Figure 2.6). The blue data and linear regression represent gases measured immediately after changing the filament, and the orange data is when the filament has aged slightly and the values plateau back toward the average value. This rapid change in heated gas value after a filament change causes the scale to become temporarily extended, with minimal scale compression as heated gas values change to -0.8 ‰ or lower. This can be seen in the two quite different gradients labelled on Figure 2.10.

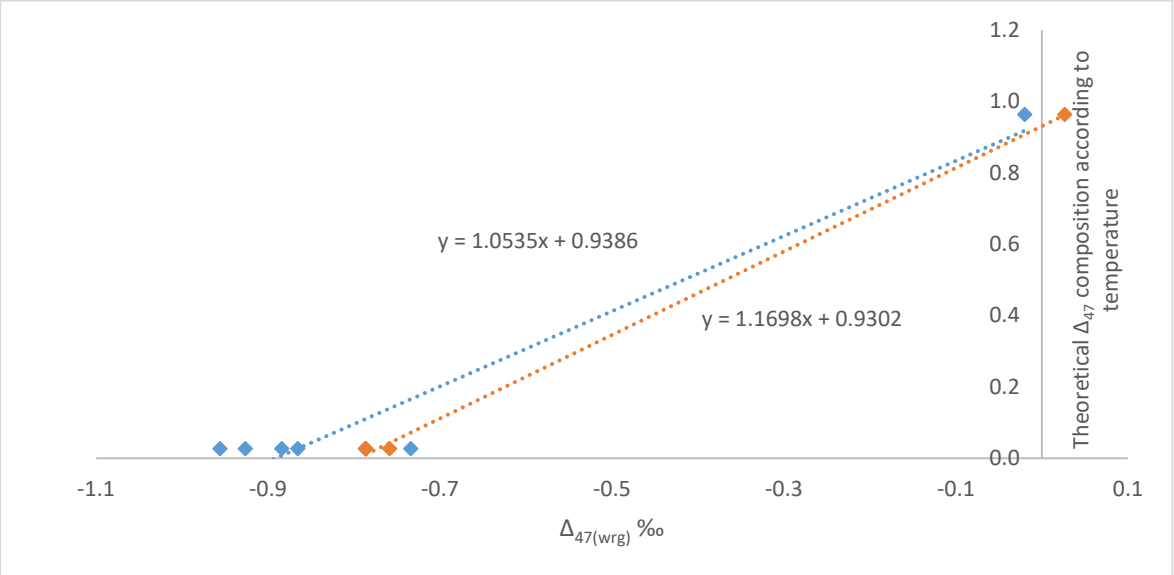

Figure 2.10 Transfer functions calculated within a three-day period from 7th December 2015 to 10th December 2015. The difference reflects how the scale compression varies before and after filament change.

There are several possible effects of changing the filament. First, the coating on the filament (and whether it is coated or not) causes a change in the temperature of emission which could cause re-equilibration of the analyte gas. It is also likely that the emission point on the filament changes over time. We tried a variety of filament types, both new and re-used, and there is no significant change either to the scale compression, or to the pattern identified with each filament change.

Improvements to the MIRA scale compression have resulted from source magnet re-magnetisation in February 2015. Values of heated gases remained much more constant (except for immediately after a filament change) and compression remains at a factor of 1.3 or less. The magnets force the lateral moving component of the electrons to move on a spiral trajectory through the source. As a filament ages, it causes wider trajectories for the electron beam as the emission point widens. As the source can only extract from a small volume, ions on the outskirts of the beam have a longer residence time and will potentially fragment and recombine. This randomises the clumped isotope signature. When a filament is changed, it emits initially from the centre, so the ions are tightly constrained. This is consistent with seeing close to no scale compression over the first few analyses, and the extraction region is roughly equal to the ionisation region. The ionisation region grows with time as the filament ages and emits from either side of the centre point, causing an increase in scale compression.

Despite this improvement, we still see scale compression, and therefore have scrambling of the sample gas within the source. A test to ensure the heated gases were carrying no contaminants from the quartz tube was done by heating a quartz tube containing no CO_2, and then completing a mass scan of the contents on MIRA. There were very few minor contaminants present at masses 53-54. These are not large enough to account for the variation we see in the heated gases. During this process however, it was noted that water vapour had been introduced to the system.

When the mass spectrometer is opened to atmosphere for maintenance, water vapour adheres to the steel surfaces inside the mass spectrometer. These are the same surfaces responsible for the generation of secondary particles that cause non-linearity. This activates the metallic surface and there is an increase in the production of secondary particles. Once the mass spectrometer is back under vacuum, it takes time for the water vapour to be completely pumped away. This could be represented by the initial lower values of heated gases (lower than -0.8 ‰), which gradually rises back to an ordinary level around -0.7 ‰. If water is present in the source, it can prevent the back reactions and reordering that cause scrambling of the gas in the source. This is due to the protons and hydroxyl radicals that would also be present in the source.

To confirm this, a BDH composition was loaded into a quartz tube and heated in the same manner as usual. However, it was analysed without going through the normal cleaning process to cryogenically remove water vapour and contaminants. The measurement on MIRA produced a much lower than normal result for a stable period (-0.86 ‰) and when a background scan was completed after the measurement, water was identified. As this lower value matches the heated gas measurements made after exposing the mass spectrometer to water vapour in the atmosphere, it appears that the presence of water could decrease scale compression on MIRA.

2.5.1.4 Contamination

By completing a mass scan when there is no gas within the mass spectrometer, it is possible to identify the quality of the vacuum within the mass spectrometer. From this we can identify intrinsic impurities present in the residual vacuum. Figure 2.11 shows the MIRA background peaks including small peak for mass 44 and for mass 47. When the 44 and 45 beams are centred at 8000 V, it is possible to see the other beam peaks shifted to the right. This is a small positive mass shift of approximately 10 V. The shift towards a higher mass shows the contaminant is lighter than the CO_2 mass 47. This suggests that the contaminant we detect could be a chlorine based molecule. We detect no heavier mass shifts, which would represent a hydrocarbon contaminant.

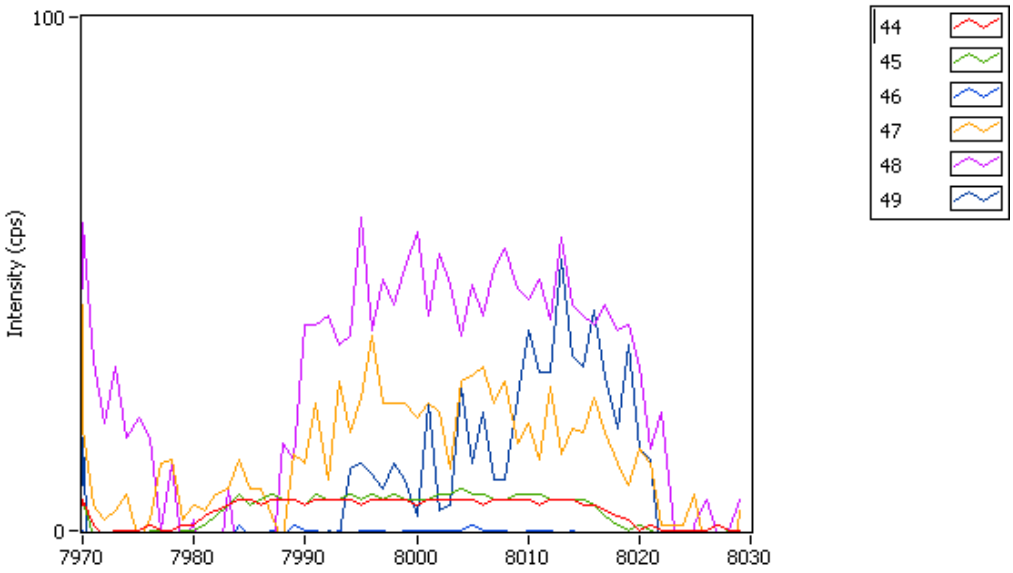

Figure 2.11 Example of a background scan on MIRA, prior to any gas entering the source. The electron current is set at 1200 µA and the source pressure is 2-3x10^{-9} mb.

We can detect contaminant peaks from mass 47 through to mass 52. A possible source of contaminant is cleaning agents used to service hardware such as the vacuum pumps, as a common cleaning agent is methyl dichloride. A key question is to what extent these contaminants impact our measurements. The contaminant peaks indicate a low abundance, approximately $1x10^{-15}$ A peaks. If the contaminant is impacting both the reference and sample gases then the effect can be ignored. However, if the contaminant only affects the sample side, there is a noticeable effect on the measurement. The mass 44 signal is approximately $4x10^{-12}$ Amps. They addition of only 0.004 ‰ to the signal would cause a 1 ‰ difference in value to the clumped isotope result. This in turn would cause an error in the calculated temperature for a sample upwards of 10 °C. Further discussion on the possible contaminants we see and how we identify them is contained in Section 3.6 of Chapter 3.

2.5.2 Instrument operating parameters

Measurements on MIRA take approximately 1.5 hours to complete. The procedure is standardised so that every analysis is treated identically and is outlined in the steps below.

1. The sample side of the mass spectrometer is evacuated to a high vacuum prior to sample loading. The internal reference bellow is opened to the external reference bellow, and the reference gas is allowed to mix and equilibrate after the previous analysis. The reference side is only fully evacuated to a high pressure before loading a new aliquot of reference gas. The gas is allowed to equilibrate between the internal and external bellows whilst the sample is loaded for approximately 30 minutes.

2. The sample is attached to the mass spectrometer and the inlet is again evacuated to a high pressure. The sample is then loaded into the sample bellow through expansion of the gas. At each stage of loading, the CO_2 is allowed to equilibrate for a minimum of five minute to ensure there is no fractionation of the gas due to Knudsen diffusion (the lighter isotopic molecules will diffuse faster than the heavier ones). Once viscous flow is achieved, the possibility of isotopic recombination is minimised and the gas can equilibrate after any initial fractionation. If a sample is particularly large, the gas volume can be cut to ensure the sample and reference gas volumes are matched.

3. After the sample is loaded, we complete a scan of the peaks to ensure they are centred. The flat tops of the scan are approximately 25 volts wide, and the beam strength is raised to $7.5x10^{-8}$ A, which is the intensity we measure at. A scan of the peak shapes, and then a scan of the ratio traces indicates how close to the centre of the peak we are measuring. Minor temperature fluctuations within the lab will change the resistance of the copper wiring coils on the magnet. A 10

V shift will mean that the signal remains on the top of the peak, but a greater shift will cause problems in the measurement. 10 V corresponds to a mass shift of approximately 1 part in 800. This correlates to a drift in the magnet of 1 part in 1600. The total coefficient of resistance of copper is 3.86 ‰ per °C. This means a magnet coil temperature change of 0.15 °C is enough to cause a voltage shift of 10 V. Within the laboratory, we have noted temperature changes between 0.5 °C to 1 °C.

4. After the peaks are checked, the system is automated. A bellows balancing algorithm ensures the pressure is such that the beam strength reaches 7.5×10^{-8} A, and between each acquisition they are re-balanced. MIRA measures four acquisitions of 20 cycles of sample and reference gas. The total integration time is 1600 seconds for sample and reference gas, and dead time after the change-over valve switches is 10 seconds.

Our instrument operation procedure has evolved over time, and this has culminated in high precision measurements. The MIRA system originally ran nine acquisitions of 20 cycles of reference and sample gas. This was later reduced to six acquisitions, and then to four as the sensitivity of the instrument was improved. The major beam current intensity was raised to 7.5×10^{-8} A from the lower signal of 4.2×10^{-8} A. This is again a reflection of the increased sensitivity of the mass spectrometer. The system was further automated in July 2013, so that between each acquisition, the sample and reference signal intensity were automatically balanced as part of the measurement routine. After the automation, we were able to run a smaller sample size with the bellows open to the inlet so that depletion rates are lower. The addition of an external reference bellow enabled us to match precisely the two gases and therefore lower depletion rates. Matching the sample and reference gas volumes ensures that depletion rates during an analysis are the same.

2.6 Data handling and reduction

The raw data output from MIRA is a text file, with counts for beams 44-49. An example of this is shown in the screenshot in Figure 2.12. As MIRA is a linear system, we take the most direct route to reduce the raw data (Figure 2.13). There are also screenshots of the excel file. As shown in Equation 2.3, we need to know the 47/44 ratio to be able to calculate Δ_{47}. Initially we derive the δ^{45} to δ^{49} values with respect to the working reference gas (wrg) of known bulk isotope composition (see above).

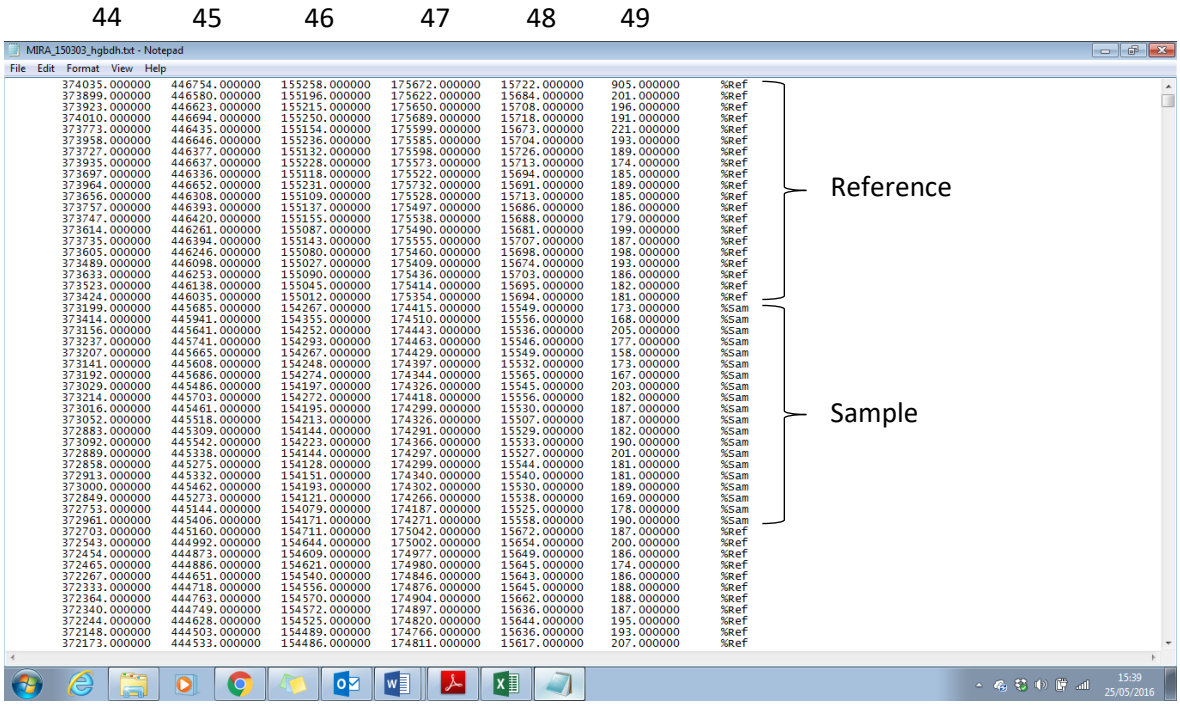

Figure 2.12 Example of raw output from MIRA. The first six columns are the raw counts for masses 44 to 49. There are alternating blocks of data according to whether the sample or reference gas was being analysed.

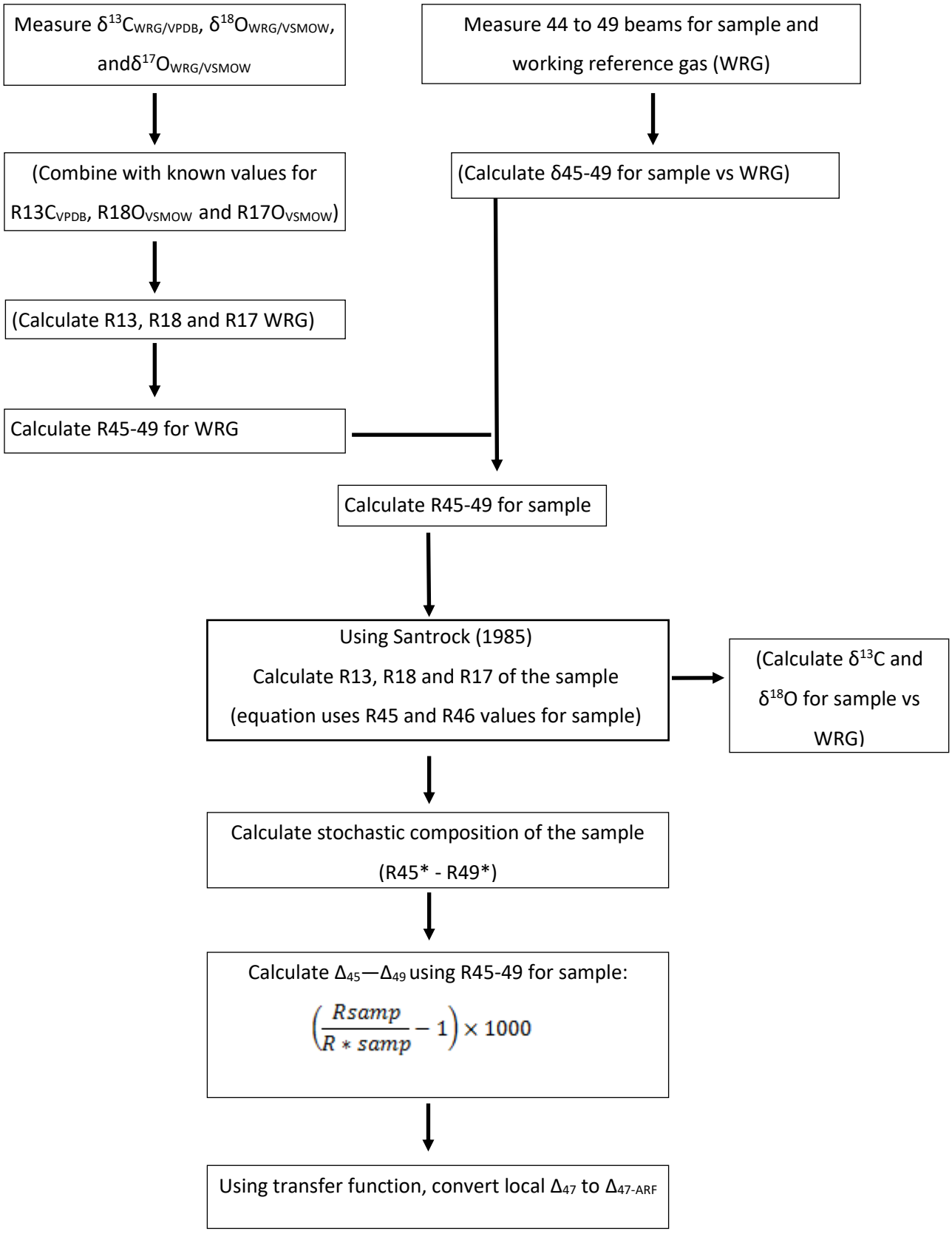

Figure 2.13 Flow diagram outlining data correction process and calculations at UEA.

The ratios R_{13}, R_{17}, and R_{18} for the reference gas are then determined by:

$$R_{13} = \left[\frac{^{13}C}{^{12}C}\right]_{wrg} = \left(\frac{\delta^{13}C}{1000} + 1\right) \times R_{13(VPDB)} \quad \text{Equation 2.21}$$

$$R_{18} = \left[\frac{^{18}O}{^{16}O}\right]_{wrg} = \left(\frac{\delta^{18}O}{1000} + 1\right) \times R_{18(VSMOW)} \quad \text{Equation 2.22}$$

$$R_{17} = \left[\frac{^{17}O}{^{16}O}\right]_{wrg} = \left(\frac{\delta^{17}O}{1000} + 1\right) \times R_{17(VSMOW)} \quad \text{Equation 2.23}$$

The reference gas ratios (e.g. $R_{13(VPDB)}$) are calibrated against known international values (Figure 2.13). Once these are calculated, they can be substituted into the equation to calculate the R_i values for the reference gas:

$$R_{47(wrg)} = 2 \times R_{13(wrg)} \times R_{18(wrg)} + 2 \times R_{18(wrg)} \times R_{17(wrg)} + R_{13(wrg)} \times \left(R_{17(wrg)}\right)^2$$

Equation 2.24

$$R_{48(wrg)} = 2 \times R_{13(wrg)} \times R_{18(wrg)} \times R_{17(wrg)} + \left(R_{18(wrg)}\right)^2 \quad \text{Equation 2.25}$$

$$R_{49(wrg)} = R_{13(wrg)} \times \left(R_{18(wrg)}\right)^2 \quad \text{Equation 2.26}$$

Once the ratio values for R_{45} to R_{49} of the working reference gas are calculated, they are substituted into the equation to calculate the ratios for the sample with respect to the working reference gas. For example,

$$R_{47(sam-wrg)} = \left(\frac{\delta^{47}sam}{1000} + 1\right) \times R_{47(wrg)} \quad \text{Equation 2.27}$$

and similar equations for R_{45} to R_{49}. The ratios R_{13}, R_{17} and R_{18} for the sample are calculated from the bulk isotopes measured in the sample (see below). Once the sample ratios are known, they can be substituted into Equation 2.28 (below) to ascertain the composition of the sample according to a stochastic distribution.

$$R^*_{47} = 2 \times R_{13(sam)} \times R_{18(sam)} + 2 \times R_{18(sam)} \times R_{17(sam)} + R_{13(sam)} \times \left(R_{17(sam)}\right)^2$$

Equation 2.28

The asterisk symbol in Equation 2.28 denotes a stochastic distribution. When both R_{47} and R_{47}* are known, their values can be substituted into Equation 2.3 and the Δ_{47} value of the sample is ascertained.

As noted in Section 2.1, there are isotopologues for mass 47-49 that contain ^{17}O. These isotopologues have a very small impact on overall Δ_{47} but must be corrected for. We apply the Santrock correction (Santrock et al. 1985) to calculate $\delta^{17}O_{VSMOW}$ based on the linear relationship between $\delta^{17}O$ and $\delta^{18}O$ (see Figure 2.13):

$$\delta^{17}O_{VSMOW} = (0.5164 \pm 0.0033) \times \delta^{18}O_{VSMOW} \quad \text{Equation 2.29}$$

After calculating the abundance ratios for both sample and reference gas from the 45 to 49 beam ratios, we again use Santrock et al (1985) to calculate the isotope ratios for ^{13}R, ^{17}R and ^{18}R of the sample (Eq. 2.30 and 2.31):

$$-3 \times R_{17}^2 + 2 \times R_{45} \times R_{17} + \left(\frac{R_{17}}{K}\right)^{\frac{1}{\alpha}} - {}^{46}R = 0 \quad \text{Equation 2.30}$$

$$-3 \times K^2 \times R_{18}^{2\alpha} + 2K \times R_{45} \times R_{18}^{\alpha} + 2 \times R_{18} - R_{46} = 0 \quad \text{Equation 2.31}$$

where α represents the fractionation factor, and K is a constant representing the relationship between ^{17}O and ^{18}O in the pool of isotopes (Figure 2.13) (Santrock et al. 1985). We use an α value of 0.5164. After these equations are solved for each sample, the R values are then substituted into Equation 2.1. We perform no PBL (pressure baseline) corrections or any corrections for non-linearity within the mass spectrometer (see Section 2.5.1.2 for a discussion of this). Once Δ_{47} has been calculated from Equation 2.1, the value is projected onto the absolute reference frame (Dennis et al. 2011) using the empirical transfer function. $\delta^{18}O$ and $\delta^{13}C$ are calculated from the measurements of R^{45} and R^{46} assuming a stochastic distribution. This means that the calculation involves circularity that should be circumvented. Mass 47 isotopologues make up approximately 40 ppm of natural CO_2, and it is suggested that $\delta^{18}O$ and $\delta^{13}C$ are independent of Δ_{47} (Eiler & Schauble 2004). This removes any requirement for a iterative calculation to circumvent the circularity (Huntington et al. 2009).

To project data on the absolute reference frame, we follow the method laid out in Dennis et al (2011). The theoretical abundances of isotopologues have been calculated using thermodynamic principles applied to spectroscopic analyses of CO_2 (Wang et al. 2004). A collection of gases with differing bulk isotope values are used but equilibrated to the same temperature. This

means the Δ_{47} values should be identical. This is ideally done at two or more temperatures (Dennis et al. 2011). A description of how we prepare our 1000 °C gases and our water equilibrated gases at UEA is outlined in Section 2.4. We then plot our heated gas values (Δ_{47} with respect to the working reference gas) against the theoretically defined value for CO_2 at this equilibration temperature taken from Wang et al. (2004). From this linear regression we can define the empirical transfer function (Dennis et al. 2011). Dennis et al. (2011) suggest that the empirical transfer function should be stable enough to maintain the same transfer function for a number of weeks, providing there have been no sudden changes to source scrambling and linearity. They suggest that a group of secondary inter-laboratory standards could be used for daily analysis of unknowns. This would identify any changes to the mass spectrometry system, although analysis of some equilibrium CO_2 should be continued alongside so that changes to the mass spectrometer can be identified (Dennis et al. 2011).

At UEA we analyse both heated and water equilibrated gases at least three times a week, and the number increases to daily measurements during any period where maintenance or improvements are occurring on either the mass spectrometer or the offline carbonate preparation system. We daily analyse one of our carbonate standards outlined in Chapter 3. This is most often UEACMST, as it is the cleanest standard and the best constrained. We find that our transfer function varies significantly immediately after a filament change, suggesting fluctuations in scale compression (Section 2.5.1.3). Otherwise, during periods of mass spectrometer stability, analysing a heated gases and equilibrated gases on average twice a week, with a daily carbonate standard is enough for us to maintain an adequate transfer function.

2.7 Stability of transfer functions

It is important to regularly check the empirical transfer function used to project data on to the absolute reference frame. Measuring the calibration gases regularly identifies any change from the norm within the mass spectrometer, and if the transfer function is incorrect, the projected Δ_{47} value will not be comparable to other data, including previously analysed data from an individual mass spectrometer. Table 2.5 shows the empirical transfer functions that were in place during my time analysing samples at UEA. The date range, transfer function, and the symbols to be used in the subsequent figures are outlined in each column. It is clear to see that there have been periods of faster and greater changes in transfer function compared to some steady periods (e.g. August 2015 to end). It is important that during periods with rapid transfer function changes, there is regular measurement of heated and water equilibrated gases to accurately constrain the transfer function.

Date Range	Transfer Function	Graph Symbol	No. of HG	No. of WEQ
121025 – 121114	1.4562 Δ_{47} +0.7887	◆	5	6
121115 - 121203	1.3659 Δ_{47}+0.7704	▲	2	5
130212 - 130322	1.093 Δ_{47}+0.7235	◆	7	5
130418 - 130716	1.485 Δ_{47}+0.8089	▲	5	5
130717 - 130813	1.4476 Δ_{47}+0.7964	×	7	4
131009 - 140409	1.4338 Δ_{47} +0.8373	■	46	39
140715 - 140929	1.294 Δ_{47} +0.9069	◆	22	10
141001 - 141017	1.2249 Δ_{47} +0.8519	▲	6	2
141020 - 150120	1.5271 Δ_{47} +0.9057	×	11	4
150126 - 150204	1.3098 Δ_{47} +0.8745	◆	7	1
150205 - 150211	1.5381 Δ_{47} +0.955	▲	4	1
150212 - 150527	1.2869 Δ_{47} +0.9351	×	26	4
150529 - 150612	1.0317 Δ_{47} +0.8864	●	11	1
150615 - 150806	1.1914 Δ_{47} +0.9095	◇	22	12
150810 - 150923	1.3591 Δ_{47} +0.9196	△	17	10
150924 - 150929	1.3058 Δ_{47} +0.8899	□	7	7
150930 - 151016	1.4386 Δ_{47} +0.9693	○	5	20

Table 2.5 Changes in transfer function through time. Dates are in YYMMDD format. There are some large variations during 2013 to early 2015, but the last three transfer functions in 2015 are stable and do not vary much in gradient or intercept. There were times when there were rapid changes in transfer function. For example, between 26th January 2015 and the 11th February, there were two different transfer functions used, with quite different gradient values (1.3098 and 1.5381).

Figure 2.14 shows a simple way to display the calibration gas data over time. The blue data points represent the water equilibrated data and the green represented the 1000 °C heated gases. This is a cumulative sum plot of the calibration gas variation from the mean over time. A period of steady gradient on Fig. 2.14 identifies periods of consistency, with no significant change to the heated gas or water equilibrated gas value. Where there is a change in the gradient, this generally corresponds to an event, such as maintenance work on MIRA or a filament change with the mass spectrometer being opened to the atmosphere. These filament changes can be seen particularly clearly in the 1000 °C heated gases in Figure 2.14, as a sudden drop in heated gas value followed by a slow plateauing curve over time, as shown in Section 2.5.1.2. The water equilibrated data stay at an almost constant gradient in Figure 2.14, with only a few sudden changes representing fluctuations in the data. Plotting the data in this manner allows us to build a picture of how the heated and equilibrated gas values change through time and their impact on transfer functions. These include all three of the gas bulk isotope compositions measured at UEA. The time scale (x-

axis) is represented by numbers as Julian dates, starting from 25th October 2012 to 27th November 2015. On some days multiple measurements were made, and these will have multiple datums.

Figure 2.15 shows the same data as a cumulative sum plot, but using the same symbols as in Table 2.4 to indicate where the changes in transfer function have occurred. Many of the filament changes and mass spectrometer maintenance line up with areas in the data showing the curving pattern and changes in gradient. Immediately after the mass spectrometer is opened to air, the transfer functions changes, and can change rapidly as the mass spectrometer returns to a high pressure of background vacuum. Plotting the data like this also enables us to look at historical data and ensure the correct transfer function is in use.

When the 1000 °C heated gas and water equilibrated gases are plotted as the measurement value over time, it is still possible to see the sudden changes in value when there is maintenance to the mass spectrometer (Fig. 2.16). A close up of one of these periods of a sudden drop followed by a plateau in the heated gas measurements is seen previously in Figure 2.6. The water equilibrated gas data fluctuates around zero, indicating it is not as affected by scale compression changes as the measurement value is close to zero.

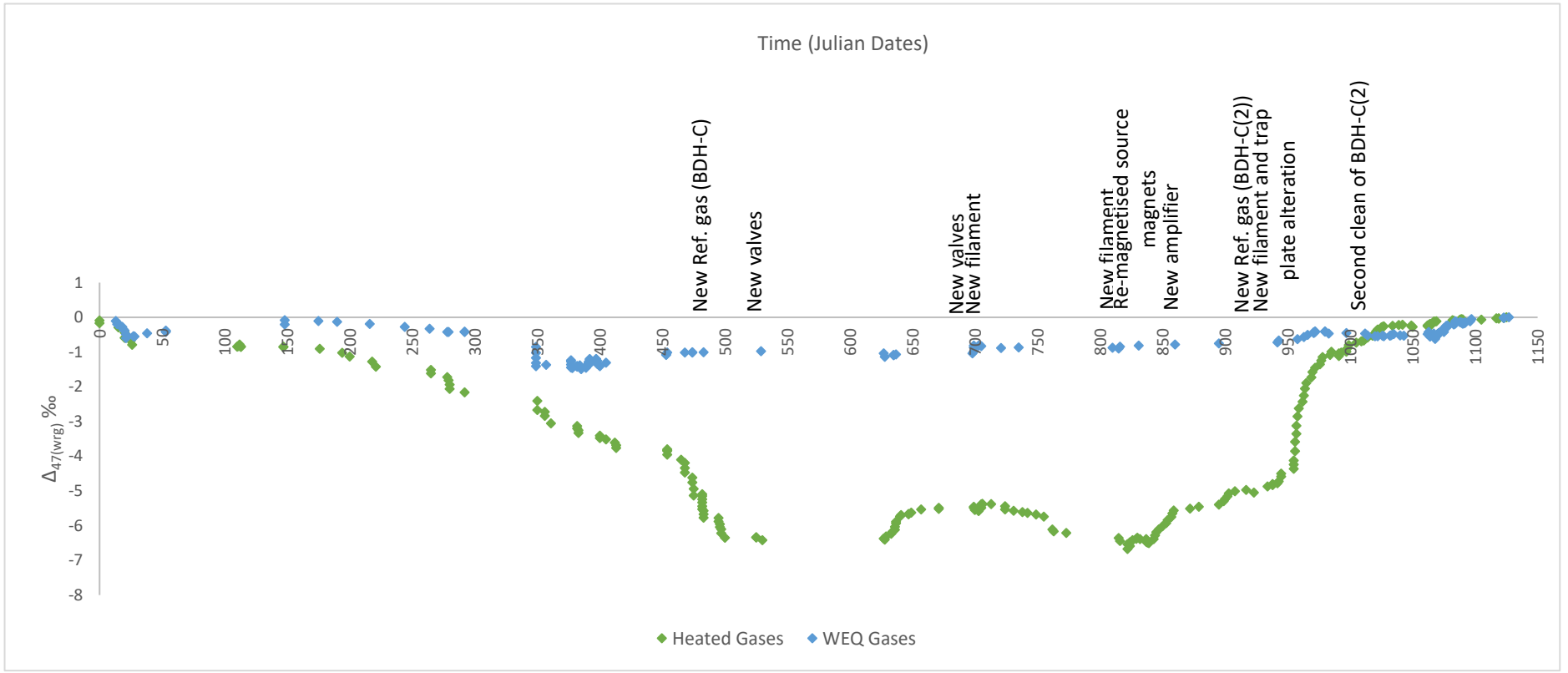

Figure 2.14 Cumulative summary plot of 1000 °C heated gases and water equilibrated gases of all three compositions. Time axis is in Julian dates. Key events are marked.

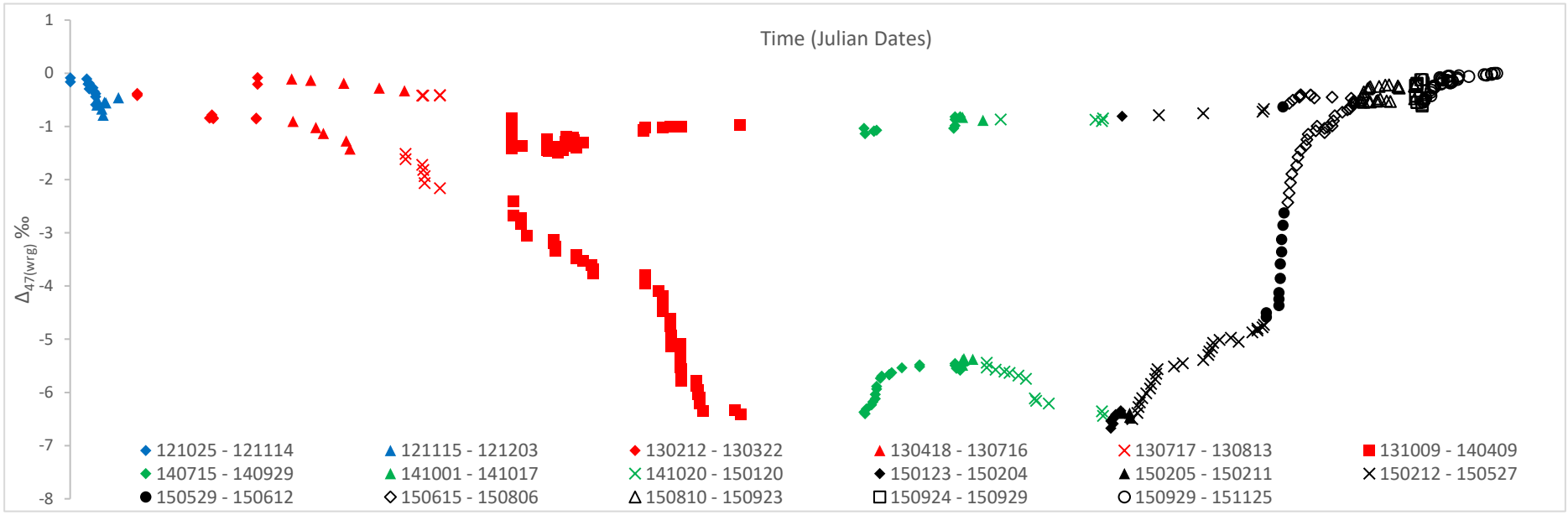

Figure 2.15 Cumulative summary plot of the variation from the mean in the heated gases and water equilibrated gases over time, including all compositions. In this graph, values are plotted with a symbol that relates directly to Table 2.5, and indicates changes in transfer function. Dates are written in YYMMDD format.

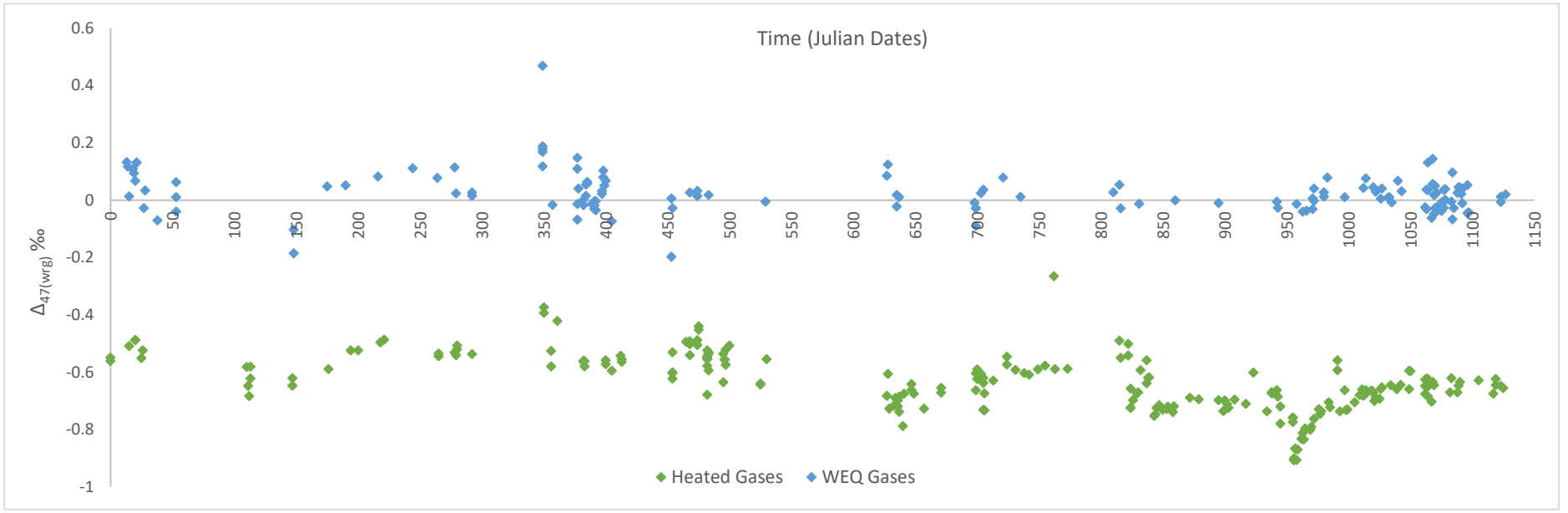

Figure 2.16 1000 °C heated gas and water equilibrated gas measurements through time.

2.8 Internal Precision

On MIRA we define precision by calculating the standard error on the δ^{47} value measured. Once each block of 20 reference and sample analyses has been averaged, we then define standard deviation. Any points outside two standard deviations are removed, and the average δ value is calculated for $\delta^{45} - \delta^{49}$. Once the standard deviation is identified, the standard error of the mean is calculated. On average, our internal precision (standard error) is 0.008 ‰ or less. This is at the shot noise limit, and is the controlling factor on how precise our measurements can be. This is very close to the 0.01 ‰ target for clumped isotope analyses, and indicates that the ion flux and count time indicated in Section 3.2.1 are adequate to achieve this high precision. A selection of results are included in Appendix I as examples of measurements made at an internal precision close to the shot-noise limit.

2.9 Conclusions

The design of MIRA means that we can successfully measure clumped isotopes of CO_2 without having to make any corrections for non-linearity. The Δ_{47} value is independent of the bulk isotope composition of the sample. This means MIRA is advantageous over the other mass spectrometers measuring clumped isotopes, as there are no complex corrections required. Whilst we do see an increased scale compression in MIRA when compared to other mass spectrometers, work on the development of MIRA is still ongoing, with the aim that we might be able to reduce this scrambling within the source. In terms of precision and sensitivity, MIRA is comparable to the other clumped isotope mass spectrometers, and is fully capable of measuring clumped isotopes to high enough precision to extract an accurate temperature value. MIRA is also shown to be a stable instrument over long periods of time.

Chapter 3 - Preparation of Carbonate Material

3.1 Introduction

The temperature signature in carbonates is recorded by the Δ_{63} (see Chapter 1 Section 1.2.3). As we cannot directly analyse this, we measure the Δ_{47} within the carbon dioxide liberated from the carbonate ion. The carbonate material is broken down by digestion with phosphoric acid to release carbon dioxide. The original bonding between the heavier isotopes in the carbonate is preserved in the product carbon dioxide (CO_2). However, the original Δ_{63} signal is modified by fractionation. The Δ_{47} signal must then be corrected for this (Guo et al. 2009). A full outline discussing the theory behind these reactions is outlines in Chapter 1. The sample gas produced requires cleaning to remove any contaminants that have the potential to cause re-equilibration of the CO_2, or to alter the mass 47 signal when analysed on a mass spectrometer. These contaminants include water vapour, chlorocarbons and hydrocarbons. Laboratories employ a series of traps to remove these contaminants, either offline or online. This chapter will outline how we prepare carbonate material at UEA, and compare our methods to those published by others.

3.2 Sample Preparation Line

We use a Pyrex glass high vacuum line with Glass Expansion (Australia) valves to produce ultra-purified CO_2. The glass line has an external diameter of 12 mm and an internal diameter of 9mm. A schematic and photograph of the prep line is shown in Figures 3.1 and 3.2. We use both a low vacuum and high vacuum pump to achieve a baseline vacuum around $6x10^{-7}$ mbar. There are two separate manifolds for low and high vacuum respectively, and three entry points each into the preparation line. This enables different sections of the line to be isolated and held under vacuum. We use a Leybold DIVAC diaphragm pump to reduce the line from atmospheric pressure, reaching a vacuum pressure of 3 mb. The pumping is then changed to a high vacuum Pfeiffer Cube pumping station where we achieve a baseline vacuum between $2x10^{-7}$ mb and $4x10^{-7}$ mb.

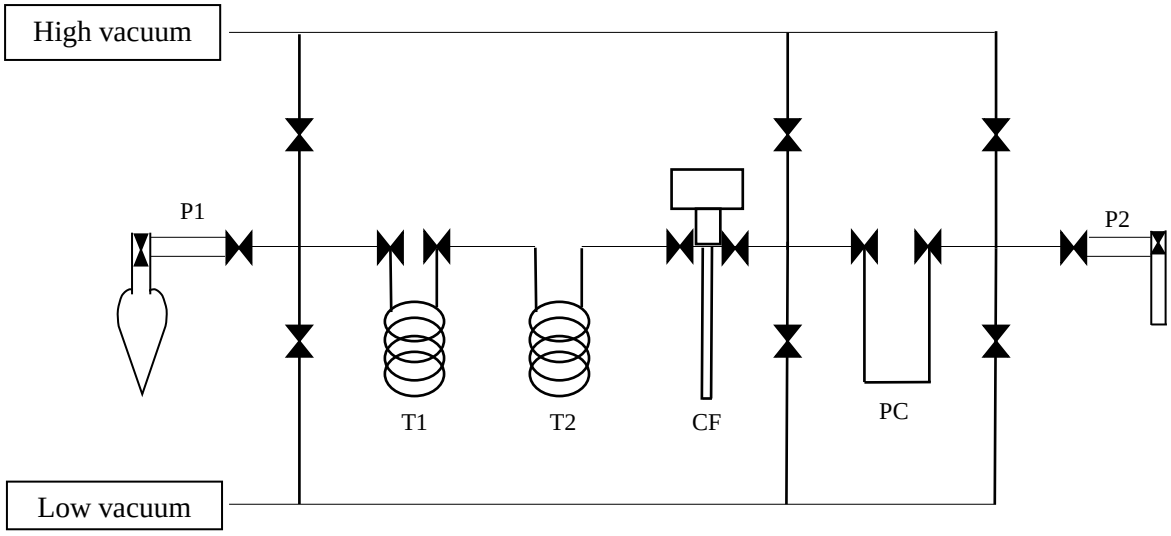

Figure 3.1 Simplified schematic of the vacuum preparation line. A double triangle indicates a valve. Letter codes are defined in text below. P – port, T – trap, CF – cold finger, PC – Poropak¬TM column.

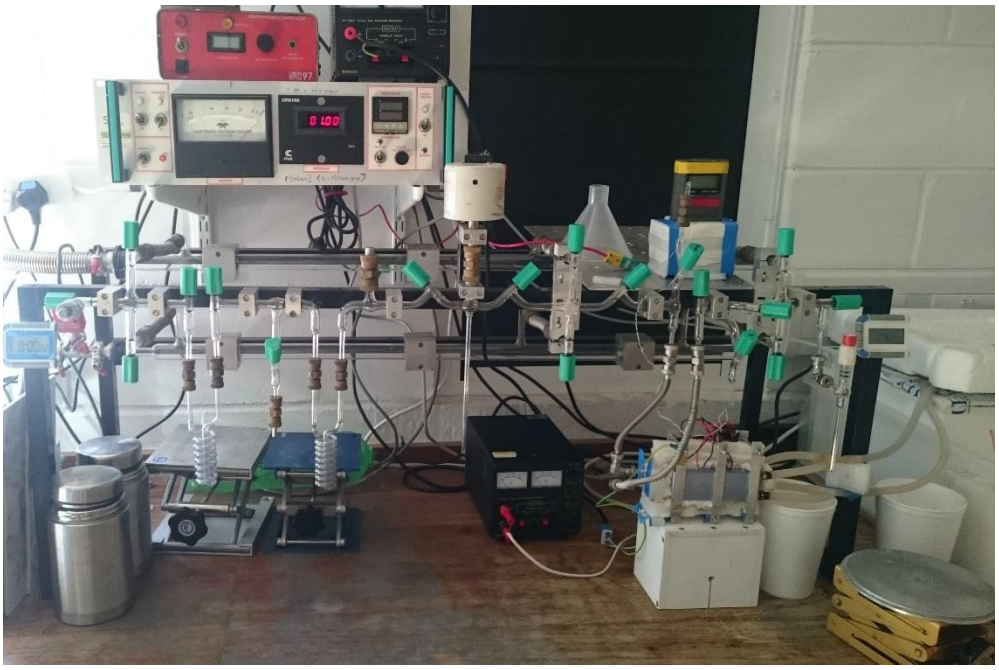

Figure 3.2 Photograph of the vacuum preparation line.

There are attachment ports at both ends of the preparation line for sample vessels. T1 and T2 are both spiral traps for freezing water vapour with valves either side to isolate each trap. Each glass trap has an external diameter of 6 mm and an internal diameter of 4 mm. The full length is approximately 0.5 m. The cold finger (CF) also has a 6 mm external diameter and 4 mm internal diameter. Attached to the cold finger is a Barocell pressure gauge. The overall volume of the cold finger, the Barocell and the sections of glass up to the valves either side is 20.3 cm^3. The CO_2 can be isolated in the cold finger for long periods of time without any leakage. The final trap is a U-shaped trap containing PoraPak™ of 50-80 mesh. This is used to remove any potential organic contaminants from the gas. This is 40 cm long with a 4 mm internal diameter. The length of PoraPak™ contained within is 21 cm, with glass wool above it and then stainless steel wool to act as a plug.

3.3 Materials/Reactants

3.3.1 Phosphoric Acid

We react our samples with phosphoric acid with a density of 1.92 g/ml. We mix and produce our dehydrated phosphoric acid in-house. Starting with 800 ml of 85 % concentration ortho-phosphoric acid, we add in small amounts of 98 % purity phosphorous pentoxide until apparent saturation. This occurs when it becomes difficult to dissolve any more phosphorous pentoxide into the acid at 70 °C (apparent saturation point). This step of the preparation takes approximately five days. During this time the acid is kept at a temperature of 70 °C during the day and is constantly stirred using a magnetic stirrer bar and hot plate. Overnight, the acid is allowed to cool to room temperature (20 °C) whilst covered in cling-film, and each morning the specific gravity is measured using a calibrated hygrometer. When the specific gravity reaches 1.92 g/ml the 1.1 L of acid that is produced is cooled to room temperature and separated into 200-220 ml aliquots and sealed in clean, dry glass Duran bottles with air tight caps. It is stored for up to 6 months prior to use.

3.3.2 Standard materials

We use a variety of standard materials, outlined below. All of our standards undergo the same reaction and CO_2 cleaning as our samples and heated gases. Table 3.1 shows the long term average values on the absolute reference frame for each standard along with their standard deviation and standard error.

Standard	Average Δ_{47} ARF	n (number of samples)	S.D.	S.E.	$\delta^{13}C$ ‰$_{VPDB}$	S.D.	S.E.	$\delta^{18}O$ ‰$_{VSMOW}$	S.D.	S.E.
UEACMST	0.383	119	0.043	0.004	1.96	0.070	0.006	39.28	0.13	0.012
UEATHC	0.564	42	0.033	0.005	2.77	0.088	0.014	26.72	0.201	0.031
UEABEL	0.631	24	0.04	0.008	2.42	0.168	0.034	41.25	0.116	0.024

Table 3.1 Average values for carbonate standards projected onto the absolute reference frame. Data from November 2012 to October 2015.

UEACMST

UEACMST is our most frequently analysed standard. It was prepared from BDH marble chips that were crushed and homogenised. The material was sieved to select particle sizes between 125 µm and 200 µm. This material has been in use in the UEA Stable Isotope Lab for approximately 27 years and its bulk isotope signal is well constrained. It has a $\delta^{13}C$ value of 1.95 ‰ $_{VPDB}$ and $\delta^{18}O$ of -2.04 ‰ $_{VPDB}$. Carrara marble is also used in other labs measuring clumped isotopes. The long term average value for UEACMST is shown in Table 3.1. On the absolute reference frame, the average Δ_{47} value from UEACMST is 0.383 ±0.043 ‰ (n=119). On the whole this is a similar standard deviation to the heated gases analysed at UEA. For example in the period between December 2015 and May 2016, the heated gases showed a standard deviation of ±0.056 ‰ (see Chapter 2).

UEATHC

This is an internal laboratory standard collected from Turkey. It is a modern hydrothermal calcite precipitated within a pipe with a constant temperature of 56 °C, located in a hydrothermal spring system in the Pumukkale region in Turkey. The calcite precipitated in a concentric precipitation pattern and includes discolouration due to oxidised iron. The material was ground into a fine powder and homogenised for clumped isotope analyses. The long term average Δ_{47} value on the absolute reference frame is 0.564 ±0.033 ‰ (n=42).

UEABEL

This is a belemnite (*Belemnitella mucronata*) collected from Weyborne Hope, on the North Norfolk coastline. It was collected from the Campanian stage of the Cretaceous period and only fragments without visible signs of alteration have been selected for measurements. The material was cleaned in diluted hydrochloric acid (HCl) in an ultrasonic bath before crushing and homogenising the sample to a fine powder. On the absolute reference frame, the average value is 0.631 ±0.04 ‰ (n=24).

ETH1

This material is part of a set gained from S. Bernasconi (ETH. Zurich) in 2013. ETH1 consists of fine powder Carrara marble heated to 600 °C for 10 hours under a pressure of 155 Mpa. This has known bulk isotope compositions but unknown clumped isotope compositions. Table 3.2 shows the results from repeated analysis on MIRA, with a comparison between the bulk isotope compositions. The average measured Δ_{47} value for ETH1 is 0.256 ±0.063 ‰ (n=17). Meckler et al. (2014) state that their measured $\Delta_{47(ARF)}$ value is 0.267 ‰. The clumped and bulk isotopic data for ETH1 in this publication is outlined in the second row of Table 3.2. The measurements made of this standard on MIRA are all slightly depleted across both bulk isotopic and clumped isotopic compositions compared to the values published in Meckler et al. (2014), but the clumped isotope value remains comparable as it is within the measurement error defined by the standard deviation. If the UEA temperature calibration (see chapter 4) is applied to the two values, there is a difference in temperature of nearly 400 °C for this same sample.

Institute	Av. Δ_{47} ARF	SD	n	SE	$\delta^{13}C$ ‰$_{VPDB}$	SD	SE	$\delta^{18}O$ ‰$_{VPDB}$	SD	SE
UEA (MIRA)	0.256	0.06	17	0.02	1.96	0.08	0.02	-2.22	0.19	0.05
ETH (MAT 253)	0.267				2.14			-2.18		

Table 3.2 ETH1 values from UEA and Zurich (Meckler et al. 2014). The published values have an unknown number of repeat analyses.

3.4 Sample Processing

3.4.1 Pre-reaction preparation

In order to analyse any standard or sample carbonate, the material needs to be in powder form. Samples of any origin are ground or drilled to a powder and homogenised using an agate mortar and pestle. No other pre-treatment was completed on any modern or fossil material in this thesis save for rinsing in distilled water, drying or crushing. Typically powdered samples between 7 mg and 10 mg are required for analysis on MIRA. Initially analyses were performed on sample sizes of 10 mg, but more recent samples have been 5-8 mg, and in some cases 2 mg have been successfully analysed. Samples were placed in either a two-legged man reaction vessel, or inside a Durham tube, within a pear shaped reaction flask. Approximately 1.5 ml of 1.92 g/cm^3 phosphoric acid was syringed into either the second chamber of the two legged man flask or in the pear-shaped reaction flask so that it surrounded the Durham tube.

3.4.2 Evacuation and Acid Reaction

Evacuation of the samples has varied in method over time to improve precision and repeatability within the results. Initially, flasks were attached to either end of the vacuum preparation line, where they were first exposed to a low vacuum. The sample flasks were gently heated with a hot air gun for a few minutes to lower the viscosity of the acid and encourage faster release of atmospheric gas bubbles from the acid. The flask was then left to pump until a vacuum of $4x10^{-6}$ bars was reached and there were no visible bubbles in the acid. To better standardise preparation between different lab users, we changed from this method to using a purpose-built manifold with five positions for simultaneous evacuation of samples (Figure 3.3). Samples are left attached to the manifold for at least five hours to pump with no heating. After evacuation, the flasks are sealed by closing the valve and are placed in a water bath held at 25 ±0.1 °C. The flasks are left for a minimum period of 30 minutes to ensure the flask, acid and sample have reached thermal equilibrium. The acid is tipped onto the sample and the reaction is allowed to proceed overnight. The reaction progress is checked after one hour to ensure the acid has completely covered the sample.

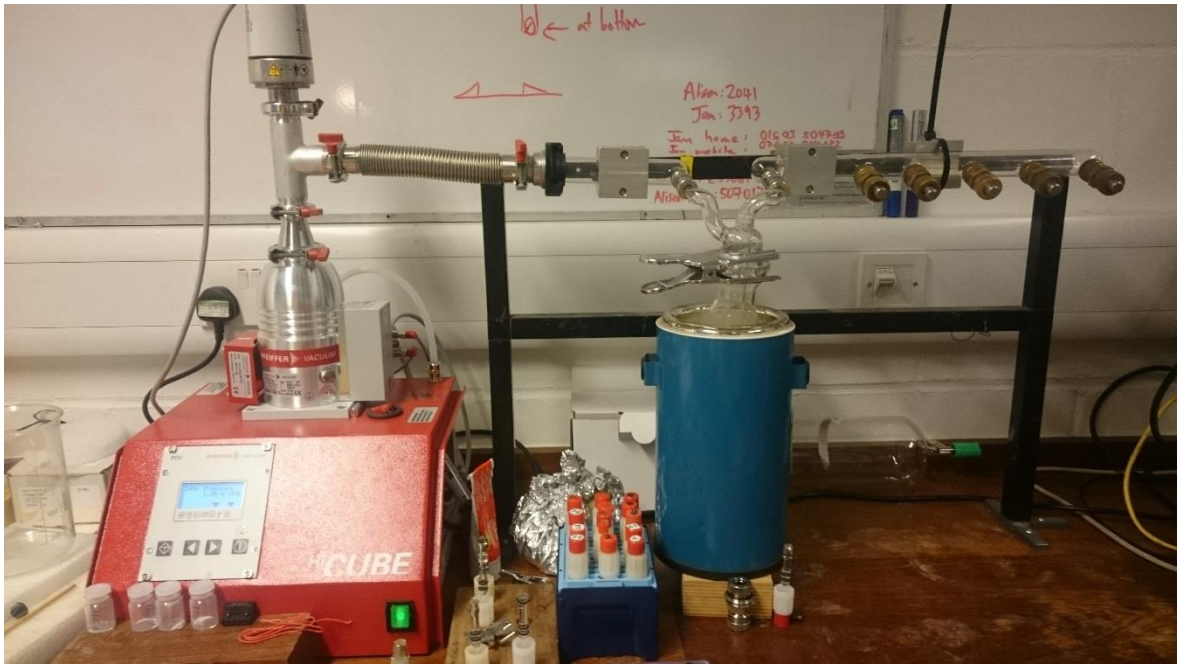

Figure 3.3 Five port evacuation manifold.

3.4.3 Gas clean-up

Once fully digested (no powder visible and no bubbles remaining in the acid) the CO_2 sample vessels are removed from the bath and attached to P1 on the manual vacuum line for cleaning (see Figure 3.1). The cleaning process takes two hours and is outlined here.

1. The vacuum line and sample connection area is evacuated to a pressure of $2x10^{-6}$ mbar or better prior to starting gas clean up. This is done using a low vacuum diaphragm pump initially, then changing to a high vacuum turbo pump to ensure a higher vacuum.
2. The sample CO_2 is transferred into the first spiral cold trap (T1) at -196 °C by immersing the trap in liquid nitrogen for 10 minutes. The liquid nitrogen level is then raised to immerse the whole trap and the condensed CO_2, and the non-condensable gases are pumped away.
3. The liquid nitrogen is then replaced by an ethanol-liquid nitrogen slush held at -115 °C. A second -115 °C mixture is placed around the second spiral trap (T2) and the cold finger is immersed in liquid nitrogen. The CO_2 is then allowed to freeze over from T1 into the cold finger (CF), via T2 with the traps chilled for 30 minutes. These are designed to remove any water vapour, as any water in T1 and T2 will remain frozen. This ensures the gases are dry. Non-condensable gases are pumped away again at the end of this stage.
4. The cold finger is then isolated and allowed to warm to room temperature. A pressure reading is taken from the Barocell gauge. This is used to calculate the yield of the sample.
5. The CO_2 then enters the final stage of clean-up. It is passed through a small U-shaped trap (PC) packed with PoraPak™ held between -20 °C and -30 °C, which removes any trace organics and hydrocarbons present within the sample. The ultrapure CO_2 is frozen into a small sample tube with a Louwers valve. This final step takes 1 hour 20 minutes. Before removal from the line the non-condensable gases are pumped away from the sample whilst the CO_2 remains under the liquid nitrogen. After this, the CO_2 is isolated by closing the valve, then the sample is attached directly to the mass spectrometer.

3.5 Yields and recovery

The pressure of each sample or standard is measured by the barocell attached to the cold finger prior to moving the gas through the PoraPak™ filled column. The volume of the cold finger has been calibrated and it is 20.3 cm^3. Using the Ideal Gas Law (Equation 3.1), it is possible to theoretically calculate the pressure of the gas produced from a certain mass of calcium carbonate:

$$pV = nRT \qquad \text{Equation 3.1}$$

where p is pressure, V is the cold finger volume, n is the number of moles of CO_2 that can theoretically be produced from the acid digestion of the calcium carbonate sample mass, R is the ideal gas constant (8.314 $kJ^{-1}mol^{-1}$) and T is temperature (degrees Kelvin). Using this expected pressure data and the actual CO_2 pressure reading when the gas is in the cold finger volume, the yield (how much of the sample has been converted to CO_2) can be calculated using Equation 3.2:

$$yield = \frac{measured\ pressure}{theoretical\ pressure} \qquad \text{Equation 3.2}$$

Figure 3.4 shows the mass of carbonate and pressure of CO_2 resulting from the acid digestion of some of the Carrara marble and Turkish calcite standards. The Carrara marble measurements generally show a higher pressure of CO_2 compared to the Turkish calcite samples. The majority of the Carrara marble data also sits just underneath the 100 % yield line, whereas the Turkish calcite plots lower than the 90 % theoretical yield line. A low yield suggests that either part of the sample has leaked away, some carbonate material has not been digested or there is less carbonate within the weighed sample to be digested than expected (a low purity sample). The Turkish calcite standard clearly shows that the yield for each separate reaction is lower than the yield retrieved from the digestion of Carrara marble. The powdered calcite is orange in colour, suggesting there could be a high iron content. If this is the case, the amount of calcite to digest in each sample is lower, and therefore there is more likely to be contamination within the sample, lowering the volume of CO_2 produced from the reaction.

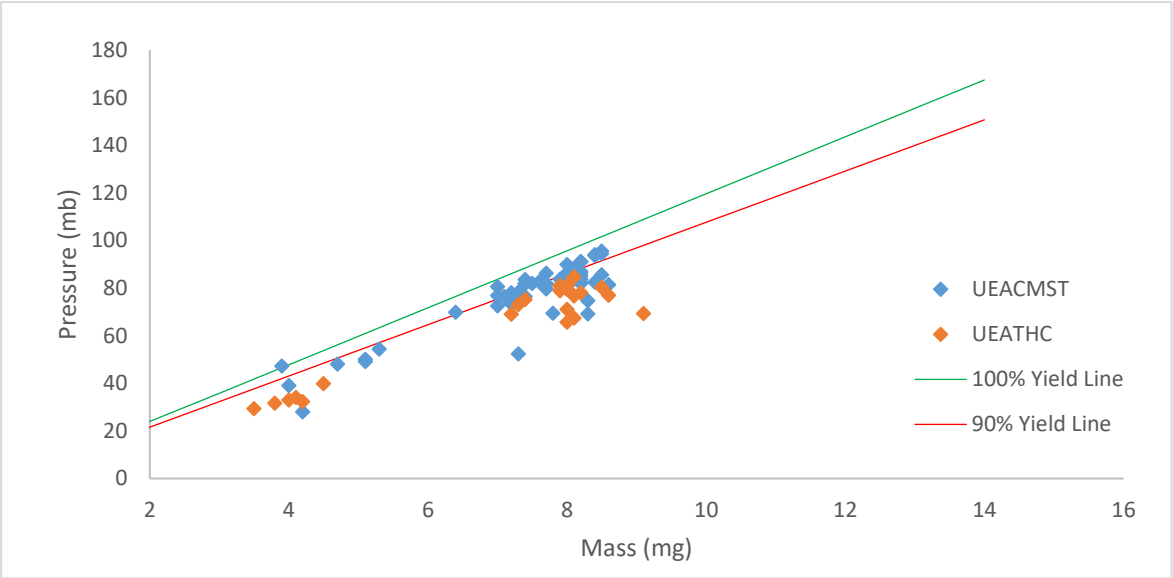

Figure 3.4 Pressures and sample masses of UEACMST and UEATHC measurements between 2014 and 2016.

Whilst we do not routinely re-measure the pressure of CO_2 after it has been passed through the PoraPak™, we are able to confirm that we have full recovery of the CO_2 after it has gone through this second stage of cleaning. This is because for selected standards or samples we have checked that the CO_2 samples have been fully recovered. They have then been re-frozen into the cold finger (via the spiral traps at room temperature) and the pressure has been measured again. Each time this has been tested, there has been full recovery of the sample. In early 2016, a test was completed to look at the adsorption of the sample gas to the PoraPak™ material. An aliquot of the mass spectrometer working reference gas was expanded into the PoraPak™ at room temperature. It was noted that some of the gas was absorbed onto the surface. The temperature was then lowered slowly in increments, whereupon it was found that approximately 50 % of the gas was absorbed onto the PoraPak™ at -30 °C. This was completely reversible once the temperature was raised back to room temperature. If the PoraPak™ was held at -20 °C for gas transferral into a tube using a pressure differential by liquid nitrogen, 100 % of the gas was recovered if sufficient time is allowed to pass to desorb the CO_2 by cryo-distillation.

3.6 Contamination

Contamination and its removal from material during the sample preparation process remains a challenge for clumped isotope measurements. There is some discussion within published work that indicates the likely contaminants. These are outlined in Chapter 2 Section 2.3.6. The key causes are non-condensable gases and contaminants that produce a signal at identical m/z to the

sample CO_2 when ionised in the mass spectrometer source. Water is also considered a key contaminant. The effect of water and its removal during the sample preparation is outlined in this chapter in Section 3.7. Non-condensable gases are removed by pumping away during the sample cleaning process. The systems we use to purify sample gases have to be adequate to remove other potential contaminants. As stated in Chapter 2, the likely contaminants that could interfere with mass 47 are hydrocarbons, halocarbons (chlorinated compounds) and sulfur compounds. These cannot be removed cryogenically and therefore the sample purification requires an extra step.

There are a variety of trap designs, and these are outlined in Section 3.8. The early studies use a packed GC column (See Section 3.8) to further clean the CO_2. This is packed with a porous benzene polymer (Ghosh et al. 2006). However, the majority of laboratories now use a similar material called PoraPak™, which is porous polymer absorbent matrix sold by scientific resource companies such as Sigma-Aldrich, filling a U-shaped trap. It is described as a copolymer of polydivinylbenzene which is extremely porous (Sigma Aldrich, Poropak™ Porous Polymer Absorbent). In the MIRA sample preparation line we use a U-shaped trap packed with 21 cm of PoraPak™. At either end of the PoraPak™ there is a glass wool plug, on top of which is stainless steel wire to add weight. Overall, the glass trap is 40 cm long with a 4 mm internal diameter. We run this trap between -20 °C and -30 °C. Lower temperatures enhance the separation of the CO_2 gas from contaminants, but require a longer transfer time (Spencer & Kim 2015) (80 minutes on the UEA preparation line). The gas flow through the PoraPak™ trap is maintained by a temperature and pressure gradient from the cold finger to the glass tube where the clean CO_2 is collected.

We use the mass 48 and mass 49 signals to assess contamination (see Chapter 2 Section 2.3.6). We have tried different configurations for the PoraPak™ trap. This was after studying Petersen et al. (2015). We temporarily changed to a shorter trap length, and experimented with the temperature it was chilled to when CO_2 was passed through it. Appendix II graphically shows the data analysed during this time period. There is a positive trend between the $\Delta_{47(wrg)}$ value, and the $\Delta_{48(wrg)}$ and $\Delta_{49(wrg)}$ values. The gradient produced by this positive relationship is similar to the gradient that can be calculated from the study of contamination in Eiler & Schauble (2004). As discussed in Chapter 2 Section 2.3.6, Eiler & Schauble (2004) deliberately added dichloromethane to air and pre-purified CO_2 samples. They found strong correlations between $\Delta_{47(wrg)}$ and $\Delta_{48(wrg)}$ values, and the signal of the mass 49 beam, described by Equations 3.3 and 3.4:

$$\Delta 47 = 0.735 \times [(mV\ mass\ 49\ in\ sample) - (mV\ mass\ 49\ in\ standard)] \quad \text{Equation 3.3}$$

$$\Delta 48 = 3.47 \times [(mV\ mass\ 49\ in\ sample) - (mV\ mass\ 49\ in\ standard)] \quad \text{Equation 3.4}$$

These relationships produce the following gradient relationships between Δ_{47}, Δ_{48}, and Δ_{49} on the local reference frame (Pers. Comms. Paul Dennis):

$$d(\Delta 48)/d(\Delta 47) = 4.72 \quad \text{Equation 3.5}$$

$$d(\Delta 49)/d(\Delta 47) = 680 \quad \text{Equation 3.6}$$

The data plotted on the two graphs in Appendix II have a line of best fit that defines the positive correlation between Δ_{47} and Δ_{48}, and Δ_{47} and Δ_{49}. This has produced a gradient of 4.2 for $d(\Delta_{48})/d(\Delta_{47})$ (Eq. 3.5) and 692 for $d(\Delta_{49})/d(\Delta_{47})$ (Eq. 3.6). These are both similar values to the original gradients suggested by Eiler & Schauble (2004) and show that plotting this relationship can indicate gross contamination from chlorine compounds. However, further work is needed to properly assess the relationship between Δ_{47} and Δ_{48}, and Δ_{47} and Δ_{49}, and whether the gradient calculated for a MAT 253 instrument can be comparable to a MIRA instrument.

Figure 3.5 contains four graphs plotting the relationships between $\Delta_{47(ARF)}$, $\Delta_{48(wrg)}$ and $\Delta_{49(wrg)}$. The Δ_{47} values are on the absolute reference frame, as this ensures there are no differences caused by using different reference gases and scale compression. Figure 3.5a and 3.5c show all of the measurements of UEACMST between November 2012 and October 2015. The x-axis of the graphs represents Δ_{47} on the absolute reference frame, and the y-axis has $\Delta_{48(wrg)}$ and $\Delta_{49(wrg)}$ values. The majority of data plots as a cloud, with some outliers.

Figures 3.5b and 3.5d show the same dataset, but with the outlying points removed. This was done by applying a filter of anything above 1 ‰ for Δ_{48} and 100 ‰ for $\Delta_{49(wrg)}$ being seen as contaminated. In both graphs, it is possible to see a slight spread in the data along a similar gradient to that calculated in Eiler & Schauble (2004). This suggests that the spread in values could be due to unsatisfactory removal of contaminants from the CO_2. However, the R^2 value is very low, suggesting the relationship is weak. Even when the error of the line is considered (calculated using the LINEST function in excel and displayed in the caption), the generated linear regressions are quite different to the those calculated in Eiler &Schauble (2004).

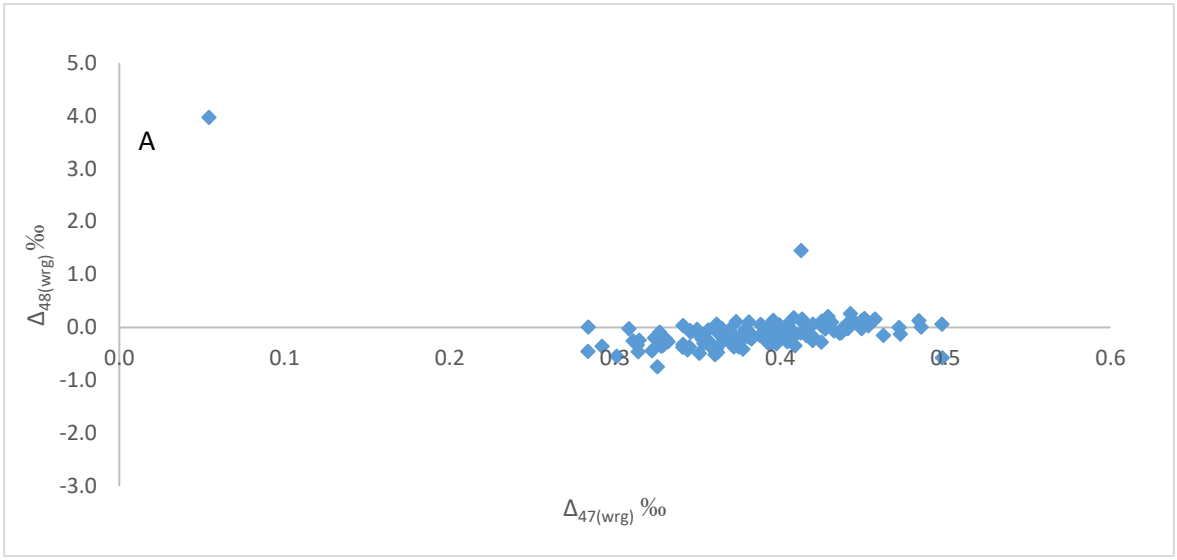
A
5.0
4.0
3.0
2.0
1.0
0.0
-1.0
-2.0
-3.0
0.0
0.1
0.2
0.3
0.4
0.5
0.6
Δ48(wrg) ‰
Δ47(wrg) ‰

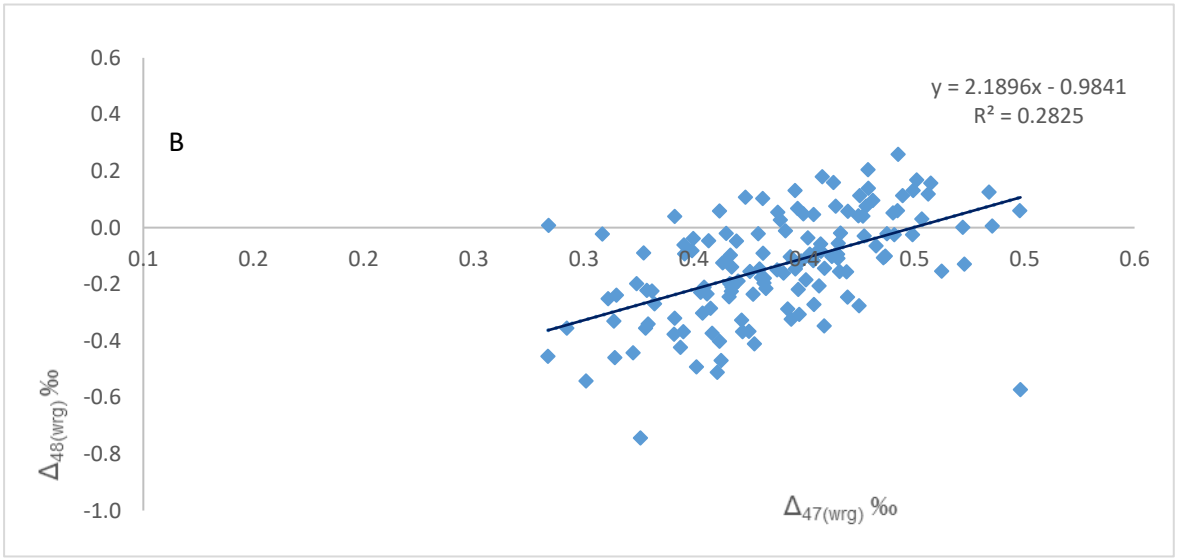
B
y = 2.1896x - 0.9841
R² = 0.2825
0.6
0.4
0.2
0.0
-0.2
-0.4
-0.6
-0.8
-1.0
0.1
0.2
0.2
0.3
0.3
0.4
0.4
0.5
0.5
0.6
Δ48(wrg) ‰
Δ47(wrg) ‰

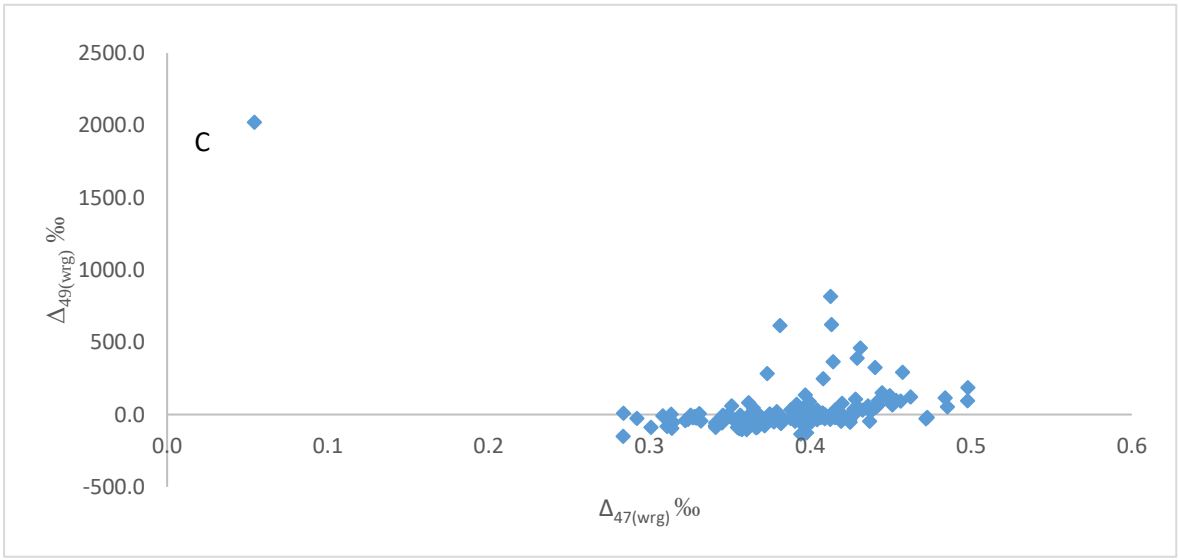
C
2500.0
2000.0
1500.0
1000.0
500.0
0.0
-500.0
0.0
0.1
0.2
0.3
0.4
0.5
0.6
Δ49(wrg) ‰
Δ47(wrg) ‰

Figure 3.5 Measurements of UEACMST between November 2012 and October 2015. Plots A and B show $\Delta_{48(wrg)}$ and $\Delta_{47(wrg)}$ with plot A showing all measured values, and plot B showing only values within the limits defining uncontaminated samples. Plots C and D show the $\Delta_{49(wrg)}$ and $\Delta_{47(wrg)}$ data in a similar manner: plot C shows all of the data and plot D shows only the uncontaminated data. For $\Delta_{48(wrg)}$ the linear regression for uncontaminated data is y = 2.1896(±0.302)x -0.9841(±0.118), and for $\Delta_{49(wrg)}$ the linear regression for uncontaminated data is y = 583.14(±95.7)x -237.93 (±36.9).

Figure 3.6 displays the UEACMST, UEATHC and UEABEL standard data, again plotting the $\Delta_{47(ARF)}$, $\Delta_{48(wrg)}$ and $\Delta_{49(wrg)}$ relationships with outlying data points removed using the same limits (anything above 1 ‰ for Δ_{48} and 100 ‰ for $\Delta_{49(wrg)}$ is seen as contaminated). A line of best fit has been added to each dataset along with the accompanying R^2 value. Again, these values are low, suggesting that whilst the gradients displayed are similar to equation 3.5 and 3.6, the covariation is weak. The errors for the linear regression for each standard are displayed in the figure caption. The errors are very poor, particularly for UEATHC and UEABEL, as there is very minimal positive relationship within these datasets, as reflected by the R^2 value.

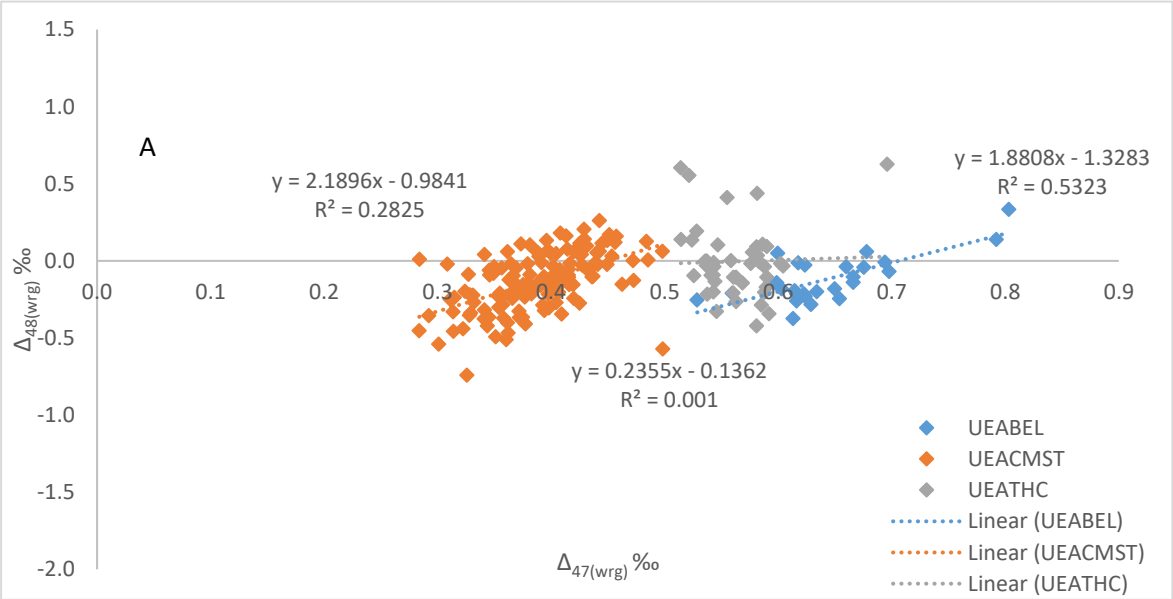

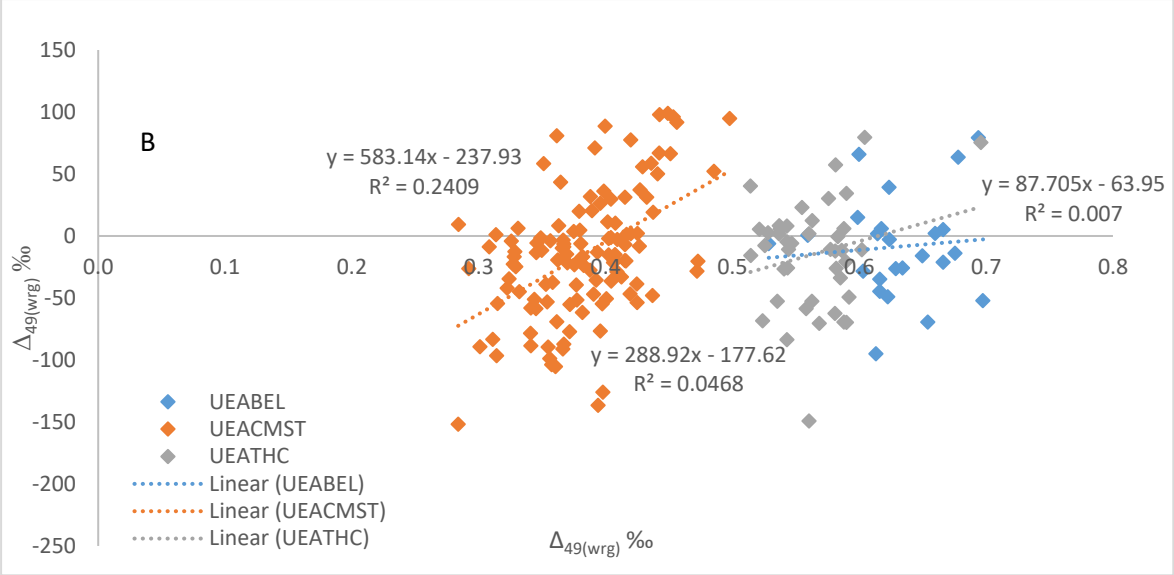

Figure 3.6 UEACMST, UEATHC and UEABEL data from between November 2012 and October 2015 displaying the relationship between Δ47(ARF), and Δ48(wrg) and Δ49(wrg). Only data with $\Delta_{48(wrg)}$ and $\Delta_{49(wrg)}$ values within acceptable limits for contamination are plotted. The linear regression and errors for UEACMST remains the same as Figure 3.5.

***UEATHC**: For $\Delta_{48(wrg)}$ the linear regression for uncontaminated data is y = 0.2355(±1.14)x -0.1362(±0.64), and for $\Delta_{49(wrg)}$ the linear regression for uncontaminated data is y = 288.92(±206.1)x -177.62 (±116.4).*

***UEABEL**: For $\Delta_{48(wrg)}$ the linear regression for uncontaminated data is y = 1.8808(±0.36)x -1.3283(±0.23), and for $\Delta_{49(wrg)}$ the linear regression for uncontaminated data is y = 87.705(±222.1)x -63.95 (±140.4).*

These contamination limits have been applied to other data sets in this thesis in the next two chapters of this thesis. The average value for UEACMST stated in Section 3.3.2 is the average value excluding contaminated values and anomalous results, and includes data from November 2012 to October 2015. Whilst there does appear to be a positive relationship between Δ_{47} and Δ_{48}, and Δ_{47} and Δ_{49}, within the data used in this thesis the covariation is weak. It is likely that much of the data may still be affected by contamination that has not been successfully removed during cleaning procedures, however further work needs to be completed to clarity how best to identify these samples.

3.7 Drying

Water vapour is also a contaminant considered to have an effect on clumped isotope analyses. Early work on bulk isotope analysis identified that even in anhydrous 100 % phosphoric acid (H_3PO_4), water is present as a product of the polymerisation of ortho-phosphoric acid and could exchange with oxygen isotopes with the CO_2 in the reaction vessel (Defliese et al. 2015). Exchange is slower when digestion occurs at 25 °C, however they noted a 0.1 ‰ shift even with 100 % H_3PO_4

suggesting that rapid preparation of CO_2 at higher temperatures is preferable (Wachter & Hayes 1985). Acid concentrations approaching 105 % H_3PO_4 are thought to absorb water produced during the reaction of carbonates, minimising the possibility of CO_2 re-equilibration. If water can re-equilibrate with the CO_2, it could change the ^{13}C-^{18}O bond abundance that we measure during clumped isotopic analysis (Wacker et al. 2013; Defliese et al. 2015).

Wacker et al. (2013) identified a trend towards a lower Δ_{47} value for a reaction at 25 °C when the sample size is increased. They suggest that the reason behind this is secondary re-equilibration between the evolved CO_2 with free water preferentially occurring in samples of smaller sizes. Defliese et al. (2015) also suggest water vapour present in the headspace of the reaction vessel can undergo re-equilibration with the sample CO_2, and at a higher temperature the water vapour pressure is higher, and the risk of re-equilibration is magnified. They suggest simultaneous reaction and freezing of the product CO_2 to minimise the risk.

All of the laboratories measuring clumped isotopes include a step to remove possible water vapour from their CO_2 samples as part of the cryogenic cleaning. Prior to passing the gas through a GC column, there needs to be cryogenic separation of any water vapour. As indicated above, we use two consecutive spiral water traps to separate water vapour from the sample CO_2. We chill the traps using two liquid nitrogen-ethanol slush mixtures in small flasks that can be placed around the traps. These are at approximately -115 °C. The sample gas is frozen under liquid nitrogen into the first spiral trap (T1) when both CO_2 and water freeze. The liquid nitrogen dewar is swapped for the warmer slush (-115 °C) on T1, and an ethanol-liquid nitrogen slush dewar is placed around the second trap T2. Once T1 has warmed to -115 °C and the second trap has cooled, the sample gas is allowed to freeze across to the cold finger due to the pressure and temperature gradient. Any water vapour is left behind in T1 (T2 is added as a precaution, but there should be no water transfer from T1 to T2).

The transfer takes 30 minutes, whereupon the pressure in the barocell returns to its baseline reading, indicating that all of the CO_2 has been frozen inside. After isolating the cold finger from the two traps, the water traps are isolated from each other, then pumped back down to vacuum individually. This allows us to see the pressure of water vapour within each trap. Ideally, the first spiral trap (T1) should contain the water from the acid digestion whereas the second water trap should not contain any water. Should the second trap contain water, it is likely that the sample gas might still contain water traces, thus this cleaning step needs to be repeated to remove any left over water vapour.

We find that this method adequately removes water vapour from our sample CO_2 gas. The temperature of the traps has to be below -80 °C, as ice will start to sublimate under vacuum at

warmer temperatures (Defliese et al. 2015). If water traces are carried into the mass spectrometer, it will affect the measurements made. Re-equilibration between water and the CO_2 has the potential to reset the Δ_{47} signal, and therefore the temperature we calculate from this. Therefore, it is vital that water is fully removed. This creates a difficult problem to solve, as it is noted that a background presence of water within the source of the mass spectrometer has the potential to reduce scrambling, and therefore scale compression (Chapter 2 Section 2.5.1.2). Further investigation into this process within MIRA is required to solve this problem.

3.8 Precision

3.8.1 Precision in standards

3.8.1.1 UEACMST

As shown in Section 3.3.2, we regularly analyse a variety of materials. This includes Carrara Marble, which is an excellent indicator of precision. Figure 3.7 shows the UEACMST measurements made between November 2012 and October 2015. These are the values converted to the absolute reference frame (Dennis et al. 2011). The symbols indicate when the transfer function changed, as discussed in Chapter 2 Section 2.7 where a key is shown. A full discussion of the common reasons why the transfer function changes and how we maintain the reference frame is outlined in Chapter 2 Sections 2.3.5 and 2.6.

Time is converted into Julian dates and is displayed on the x-axis. The Julian dates start from 23rd November 2012. The data is very constant, reflecting the constant nature of the UEACMST measurements. At day 941, there is a depletion in Δ_{47} value followed by a gradual increase. This is an example of when the filament in MIRA was changed. The UEACMST measurements are effected in a similar manner to the heated gases when the filament it changed. That is, any initial measurements over the first few days show a depleted value, before plateauing as the mass spectrometer vacuum improves. A full discussion on this is outlined in Chapter 2 Section 2.5.1.2. In Section 3.8.2 and 3.8.3 of this chapter, there will be further discussion of the precision of UEACMST.

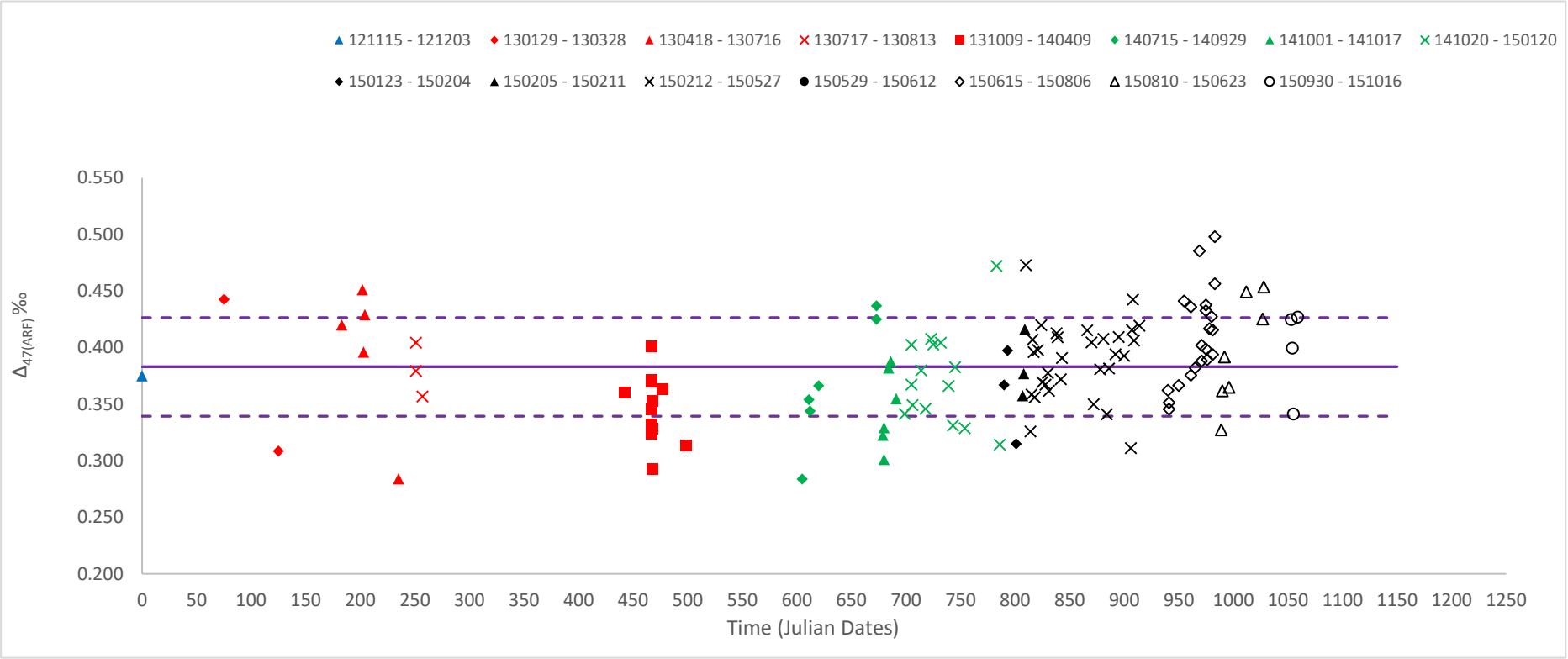

Figure 3.7 UEACMST values from November 2012 to October 2016. Datum symbols represent a date range within which a constant transfer function was used (as in Table 2.4). Dates are in YYMMDD format. Mean and standard deviation values are shown by purple lines.

Our data for Carrara marble is comparable to the values published by other laboratories measuring clumped isotopes, and also displays a similar precision. These are shown in Table 3.3. Further discussion on other published work will be in Section 3.8 of this chapter. We are able to produce data that has a high and comparable precision to these other laboratories over a long period of analysis.

Laboratory	Reference	Carrara Marble Δ_{47} Value ‰	Standard Error
UEA	--	0.383	0.004
CALTECH	Dennis et al. 2011 Tripati et al. 2015	0.392 0.394	0.007 0.006
Yale	Dennis et al. 2011	0.400	0.004
Johns Hopkins University	Dennis et al. 2011 Suarez & Passey (2014)	0.403 0.399	0.006 0.014
ETH, Zurich	Schmid & Bernasconi (2010) Meckler et al. 2014	0.363 0.397	0.005 --
UCLA	Tripati et al. 2015	0.386	0.002
Goethe University, Frankfurt	Fiebig et al. 2015	0.379	0.004
Harvard	Dennis et al. 2011 Petersen & Schrag (2015)	0.385 0.395	0.005 0.005
Imperial	Kluge & John (2015)	0.389/0.386	0.003/0.006
Tulane University (Isoprime)	Tang et al. 2014 Rosenheim et al. 2013	0.391 0.3912	0.006 0.027

Table 3.3 Carrara Marble values from a selection of other clumped isotopes laboratories.

3.8.1.2 UEATHC

The UEATHC standard has not been measured for quite as long, but still provides an ample dataset. Figure 3.8 shows the Turkish calcite measured Δ_{47} value according to the date it was measured (dates converted to Julian dates). The Δ_{47} values are again represented by different symbols according to which transfer function was in use at that time. There are fewer data points for the UEATHC standard, and they cover a narrower range of values than the UEACMST (0.514 ‰ to 0.604 ‰). This suggests there could be less variation in the Turkish calcite measurements than the UEACMST measurements.

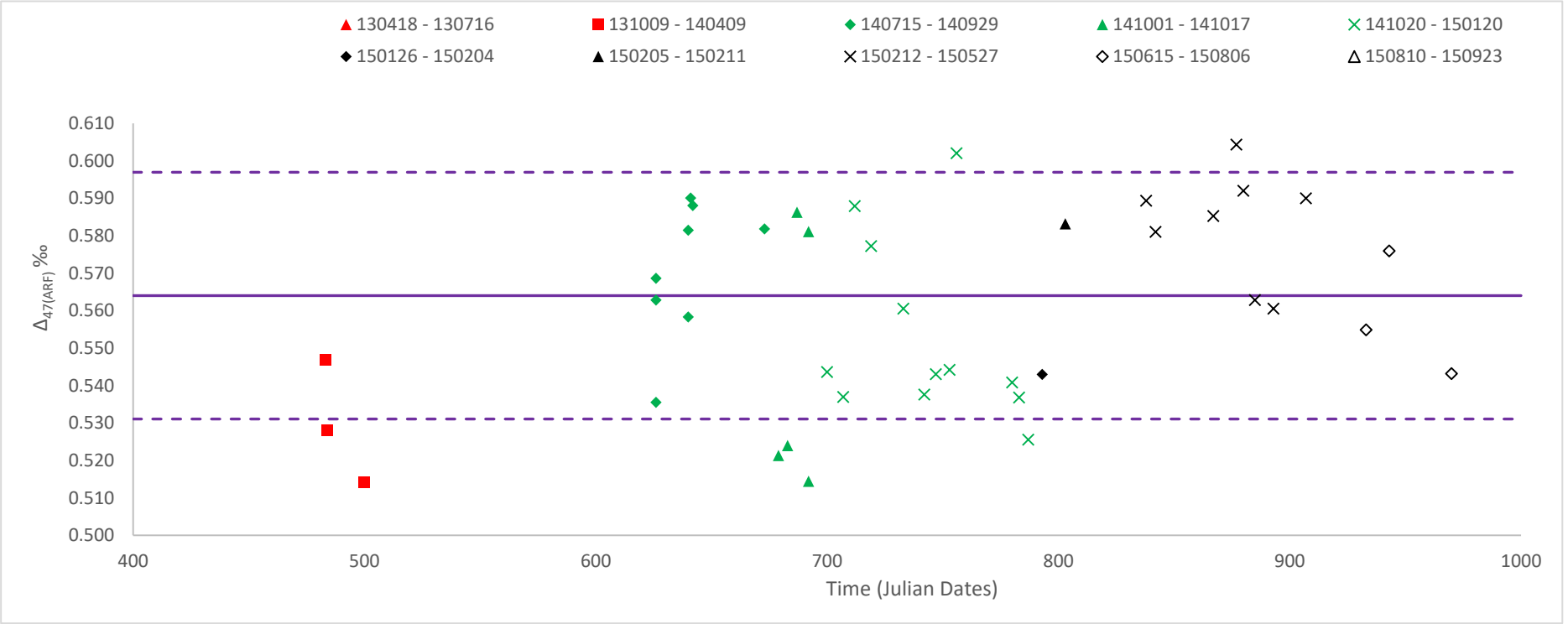

Figure 3.8 UEATHC values from October 2013 to August 2016. Datum symbols represent a date range within which a constant transfer function was used (as in Table 2.4). Dates are in YYMMDD format.

3.8.1.3 Comparison between standards

Whilst the two standards described above are quite different, it is clear to see they are both measured to a similar precision. These measurements, along with those made of UEABEL, are shown in Figure 3.9. Here they are all plotted according to the Julian dates (starting from 23rd November 2012). The Δ_{47} value is given on the absolute reference frame. Included in this figure are solid lines to indicate the average value for each standard, along with the standard deviation (1σ) brackets for the three standards (dashed lines).

The UEABEL and UEACMST standards cover the greatest range of values (and have wider standard deviation envelopes) than the UEATHC standard. It is possible that early measurements for UEACMST are affecting the standard deviation, as they show the greatest variation from the mean and were completed before MIRA and the sample preparation methods underwent modifications to improve the precision. The belemnite standard is a geological standard, and it could be the least pure standard, which potentially could cause a spread of Δ_{47} values due to potential contamination. The standard deviations and standard errors for each of the standards are outlined in Table 3.1, and appear to be comparable to the measurement precision of other laboratories.

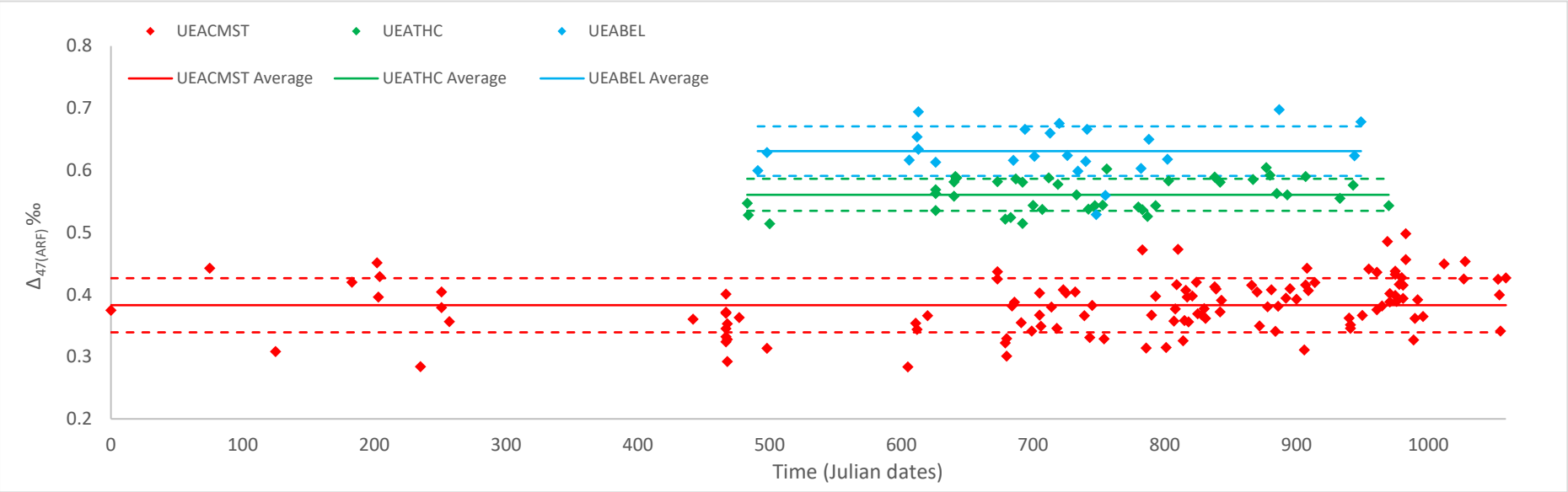

Figure 3.9 UEACMST, UEATHC and UEABEL data from November 2012 to October 2015. The line within each data set represents the mean value, and the dashed lines represent one standard deviation.

3.8.2 Short term precision

External precision is an assessment of the repeatability of analyses of the same gas sample. On MIRA, an excellent example for short term external precision is a suite of results from one gas bottle. This is "BDHequilRT", which is produced from BDH marble chips in the same manner as the BDH working reference gas (see Chapter 2 Section 2.4.3 for method of reference gas preparation). Once the gas was cleaned and dried, single aliquots of the gas have been analysed almost every day since 11th January 2016. The $\Delta_{47(wrg)}$ values for this gas for the period from 11th January 2016 to 20th May 2016 are plotted in Figure 3.10. The x-axis represents time using Julian dates. Each date since the first date of analysis is represented by a number. The full data set is contained in Appendix III. Each point represents a single analysis, with occasional multiple aliquots being measured in one day. Between the first analysis and the point marked with a black arrow, there is quite a spread in the data, with a long term trend towards a lower Δ_{47} value. We identified this as a long term, slow leaking in one of the valves of our working reference gas bottle, causing the gas to become contaminated with atmospheric air. We fitted new valves on the gas bottle at this time (marked with a black arrow).

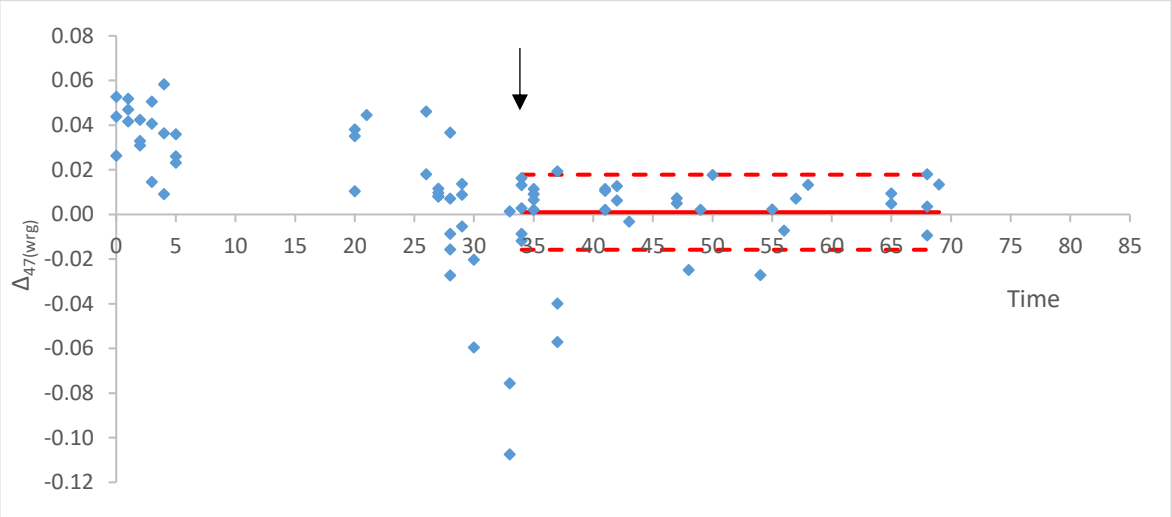

Figure 3.10 BDHequilRT data from 11th January to 20th May 2016. The red lines indicate the mean value during the stable period, with the dashed lines indicating one standard deviation envelopes. The black arrow indicates when the valves were changed, improving the precision of the data.

Once the valves had been replaced (data after the black arrow), the $\Delta_{47(wrg)}$ values became consistent, which is the area marked with the red lines. The solid red lines represent the average $\Delta_{47(wrg)}$ value (0.001 ‰), and the dashed lines are the standard deviation (1σ) (± 0.017). The majority of the measurements fall within this error envelope, with only a 0.04 ‰ range in the data. This high

precision period stretches from 16th February 2016 to 22nd March 2016, and shows how precisely MIRA can analyse sample gases (precision is at the shot-noise limit).

A second example of the high precision achievable in analyses on MIRA is shown in table 3.4. This presents 13 measurements of UEACMST measured very close together over a period of two to three weeks in October 2015. The average values for the bulk isotopic compositions along with the clumped isotopic values are shown underneath each column, along with the standard deviation and standard error (n = 13). The standard deviation and standard error for $\delta^{13}C$ values is very low, with better repeatability than the $\delta^{18}O$ measurements. A low $\delta^{18}O$ precision could be due to differences in signal intensity, or it could suggest there is some interaction with water vapour during the sample preparation. It is possible the acid is not fully dehydrated, providing a source for water vapour that the carbon dioxide could interact with. The high precision values for $\delta^{13}C$ indicates minimal fractionation of the sample during gas cleaning and loading onto the mass spectrometer. The standard error for the Δ_{47} measurements is at or close to the shot-noise limit for MIRA (depending on whether the $\Delta_{47(wrg)}$ or the $\Delta_{47(ARF)}$ value is used). The precision for $\Delta_{48(wrg)}$ is also high, with a standard error of ± 0.02. The $\Delta_{49(wrg)}$ results have not been analysed in this table. There is much variability in the values, which could suggest that some of the samples contained contaminants, reflected in four of the measurements showing Δ_{49} signals over 100 ‰. The average for $\Delta_{47(ARF)}$ is very similar to the long term average shown in Table 3.1 (see Section 3.3.2). This shows that our sample cleaning procedure and mass spectrometric measurement protocols are consistent and precise.

Date	$\delta^{13}C$ ‰$_{VPDB}$	$\delta^{18}O$ ‰$_{VSMOW}$	$\Delta_{47(wrg)}$	$\Delta_{47(ARF)}$	$\Delta_{48(wrg)}$	$\Delta_{49(wrg)}$
151013	2.03	39.43	-0.379	0.425	0.043	-38.626
151013	2.02	39.41	-0.376	0.428	0.076	105.537
151014	2.01	39.40	-0.396	0.400	0.050	88.615
151015	2.01	39.31	-0.437	0.341	0.040	-57.953
151016	2.01	39.12	-0.376	0.428	0.055	-36.381
151019	2.01	39.30	-0.377	0.427	0.041	-8.168
151020	2.02	39.28	-0.396	0.399	0.234	262.773
151021	2.02	39.30	-0.432	0.348	0.170	476.039
151022	2.01	39.22	-0.405	0.387	0.043	115.712
151023	2.01	39.29	-0.394	0.403	0.197	94.668
151027	2.03	39.18	-0.377	0.427	0.044	-61.013
151028	2.02	39.29	-0.403	0.390	0.129	14.565
Averages	2.02	39.29	-0.396	0.400	0.093	79.647
SD	0.007	0.091	0.021	0.030	0.070	
n	13	13	13	13	13	
SE	0.002	0.025	0.006	0.008	0.019	

Table 3.4 UEACMST values from the 13th October 2015 to 28th October 2015. All measurements are included, including those with high Δ49 values normally indicative of contamination (values in red). Dates are in YYMMDD format.

We have found that small changes to our sample preparation method through time has helped to improve the precision of our standards. For example, the addition of a five-port manifold for the evacuation of samples/standards prior to reaction has standardised the vacuum level and length of time for this part of the preparation procedure. It ensures that all samples are treated in the same manner. This is apparent when comparing older standard data with newer results. Table 3.5 shows the results of one such comparison. The first column shows 10 UEACMST measurements made between 2nd October 2014 and 29th October 2014. The average $\Delta_{47(wrg)}$ value, along with the standard deviation and standard error are shown at the base of the column. A second data set is shown in a similar manner. This includes UEACMST measurements from 13th October 2015 to 30th October 2015, which is almost the same data set as shown in Table 3.3. This was after the five port manifold was introduced in later summer 2015. The average, standard deviation and standard error values for this data set are shown at the base of the column of data. The standard deviation and standard error in the 2014 data set is higher than the 2015 data set. Standardising the evacuation and reaction process improved the precision of $\Delta_{47(wrg)}$ measurements of UEACMST. There have also been changes to the mass spectrometer during this period, which are likely to have improved upon measurement precision. The improvement in sample preparation methods over time does indicate that this is the limiting factor on our precision. It is demonstrated in Chapter 2 that MIRA measures at the shot-noise limit. When the sample preparation and cleaning methods are not sufficient, the

repeatability on our carbonate standards is lower (as in 2014). The BDHequilRT gas is extremely clean. Therefore, it shows an external precision close to or better than the internal precision on MIRA when measuring ultra-pure material.

	141002 to 141029		**151013 to 151030**
$\Delta_{47(wrg)}$	-0.432	**$\Delta_{47(wrg)}$**	-0.376
	-0.450		-0.396
	-0.427		-0.437
	-0.384		-0.409
	-0.379		-0.377
	-0.406		-0.396
	-0.370		-0.432
	-0.330		-0.405
	-0.353		-0.394
	-0.364		-0.377
Av.	**-0.389**		-0.386
S.D.	**0.038**		-0.437
n	**10**		-0.344
S.E.	**0.012**	**Av.**	**-0.397**
		S.D.	**0.027**
		n	**13**
		S.E.	**0.007**

Table 3.5 UEACMST values from two short time periods. The first two columns include data from 2nd October 2014 to 29th October 2014. The second two columns display data from 13th October 2015 to 30th October 2015. Mean, standard deviation and standard error values are at the base of each column of data.

3.8.3 Long term precision

Carrara marble is the carbonate material we have been analysing on MIRA for the longest period, therefore this dataset offers the best reflection of the long term precision on carbonate measurements. Figure 3.7 (section 3.8.1.1) and Figure 3.9 (section 3.8.1.3) shows the measurements of UEACMST that have been completed during my time at UEA. Any measurements that show $\Delta_{48(wrg)}$ and $\Delta_{49(wrg)}$ values outside of the limits discussed in Section 3.6 have been removed from the dataset, as these are considered to be contaminated. The x-axis in both figures represents time as Julian dates.

On some days, there have been multiple analyses of the standard and therefore some dates show a clustering of data. The first 15 to 20 measurements are clearly differing from the steady values witnessed from the rest of the data. This is likely to be due to a combination of measuring the values against the BOC reference gas, or due to inadequate sample cleaning techniques, and were measured before MIRA underwent improvements. Some of the especially depleted values

later on are likely to be caused by filament changes. There is a similar effect on the standard data as on the heated gases when the source is opened to the atmosphere. This is discussed fully in Chapter 2 Section 2.5.1.2. Otherwise, the data appears to show a better precision as time goes on. This is reflecting our improved cleaning and measuring procedures at UEA.

3.9 Comparison with published works

It is possible to compare the clumped isotope methodology at UEA with other laboratories published details. Firstly, at UEA we perform limited pre-cleaning of carbonates. Our standards, such as Carrara marble, have undergone no pre-treatment. The modern shell material (Chapter 4) and fossil material (Chapter 5) have been rinsed in de-ionised water and cleaned in a sonic bath. Other biogenic and inorganic carbonate material analysed in the laboratory has only undergone this treatment. There is some discussion in the literature of whether certain cleaning techniques affect the Δ_{47} signal. In some of the very first clumped isotope work, Ghosh et al. (2007) pre-cleaned otolith samples in hydrogen peroxide (H_2O_2) for 12 hours, prior to crushing with a pestle and mortar. Tripati et al. (2010) added an extra step to this cleaning, by sonicating in both distilled water and in methanol, after cleaning in 1 % methanol. This was applied after the foraminifera used in the Tripati et al. (2010) study were crushed. They found that when the same treatment was applied to their carbonate standards, there was no effect on their Δ_{47} values. However, Grauel et al. (2013) identified an issue with the use of hydrogen peroxide. They noted that a 10 % solution caused dissolution and overgrowths of crystal on the shells of calcite foraminifera. As this would have the potential to alter the distribution of the isotope bonds, they removed the cleaning step using hydrogen peroxide. In contrast to this, Wacker et al. (2013) found that when a selection of their bivalve samples were pre-treated with 1.5 % solutions of H_2O_2, there was no significant effect on the Δ_{47} value. However, it is important to note the difference in the strength of the solutions, along with bivalves containing a larger mass of carbonate with the potential for organic matter to remain behind in the lattice. It appears that there is still more work to be done to identify which methods of pre-cleaning are suitable for clumped isotope analysis. As there was no difference between Δ_{47} in both treated and untreated bivalves, at UEA we do not add a chemical pre-treatment step.

Reaction temperatures have also been a topic of discussion within the community. Reaction of carbonates with phosphoric acid has been the standard technique for stable isotope analysis and was originally described by (McCrea 1950). The reaction takes place at 25 °C in a closed vessel. This method was utilised in Ghosh et al. (2007) and in many clumped isotope studies since. This is also the reaction method we use at UEA. Other labs react their carbonates at 70 °C, 90 °C and 100 °C,

and apply an acid correction factor. A discussion on works using these different methods can be found in Chapter 4 (section 4.1.1.2). In theory, if the acid fractionation factor is correctly constrained and applied, a comparison can be made between samples that have been reacted at different temperatures (Henkes et al. 2013). A common acid bath is often used when materials are digested at higher temperatures. This enables the CO_2 to be immediately removed from contact with the acid and promptly cleaned and measured. This limits the amount of time that the product CO_2 has to potentially re-equilibrate with water (see Chapter 4 Section 4.4.2.2 for a discussion on this). Our data reacting at 25 °C for 12-16 hours is comparable to those using high temperature reactions. This can be seen by comparing our Carrara marble standard value ($\Delta_{47(ARF)}$ = 0.383 ‰) to the published values in listed in Table 3.3.

The next stage in the cleaning of product CO_2 is the removal of water. As outlined above, water has the potential to cause re-equilibration of the isotopes in CO_2, altering the clumped isotopic composition. In order to remove any water from the product CO_2, it is vital that there is a step of cryogenic separation. At UEA, we initially freeze the CO_2 into a trap at liquid nitrogen temperature, then warm the trap to -115 °C where the CO_2 can defrost and be drawn away whilst the water vapour remains frozen. Many of the laboratories measuring clumped isotopes use a single trap at -77.8 °C to -80 °C to remove trace water (for example: Ghosh et al. 2006; Dennis & Schrag 2010; Henkes et al. 2013). We use a colder temperature of -115 °C, similar to Grauel et al. (2013), who warm the water trap to -110 °C. Defliese et al. (2015) are also the only other lab apart from UEA to use two consecutive traps to cryogenically separate the water vapour from the CO_2. They complete this at -95 °C and indicate that ice can sublimate in a vacuum above -80 °C based on previous work (Murphy & Koop 2005) and that this difference in the removal of water could be why there are many discrepancies in clumped isotope measurements between published studies.

As discussed above, the removal of potential contaminants within the product CO_2 is vital to prevent re-equilibration or altering of the m/z = 47 signal. Whilst water and non-condensable gases can be cryogenically removed, a divinyl benzene polymer trap is also typically used to remove other contaminants (see Section 3.6). Within the published literature, there are a variety of different designs and running parameters used for this stage of CO_2 cleaning. The very early work completed by Ghosh et al. (2006) passed the sample CO_2 (entrained in a helium flow) through a 30 m long gas-chromatography (GC) capillary column packed with porous divinyl benzene polymer held at -10 °C. This was baked at 200 °C for a minimum of 30 minutes between samples. This method was also repeated in other studies such as Huntington et al. (2009), Passey et al. (2010), Yoshida et al. (2013) (and at a colder temperarture of -20 °C Henkes et al. (2013) and Wacker et al. (2013)).

Dennis & Schrag (2010) and Rosenheim et al. (2013) indicate an alternative but effective method of using the PoraPak™ Q material without the need for a carrier gas. A packed, U-shaped trap was held at -10 °C, and the pressure differential caused by the liquid nitrogen pulls the CO_2 through the trap without the need for a carrier gas. The hydrocarbons and chlorinated hydrocarbons are left behind. Eagle et al. (2013) altered the method slightly to include the addition of silver wool, which removed sulphur compounds. Grauel et al. (2013) used a straight, packed length of 1.5 cm and a lower temperature of -17 °C to clean their samples. Overall, these are the two main methods for contaminant removal within the literature, however the length of PoraPak™, temperature of the trap and time and temperature of the bake between samples is widely varied. A discussion of the variation in Δ_{47} is outlined in Petersen et al. (2015). At UEA we find that adequate removal of contaminants is achieved using a vacuum system with a PoraPak™ U-shaped trap held between -20 °C and -30 °C. The full details of the trap are outlined in Section 3.2, but we use a length of PoraPak™ considerably longer than what is described in published literature, and we take a much longer length of time to transfer the gas through the trap. The longer time period we require to transfer the sample gas ensures complete recovery and that there is no fractionation of the sample.

Overall our data can be most easily compared to other laboratories by comparison of an inter-laboratory standard, such as Carrara marble. Table 3.5 outlines some published values from each laboratory along with their standard error. The UEA long term average value is within the range of published values, and the standard error we identify is very similar to others. Between laboratories, the value for Carrara marble is very similar. It is surprising that the majority of labs produce a very similar value for this standard, and yet there is a very wide range of temperature calibrations produced when a combination of organic and inorganic material is analysed (see Chapter 4). This does suggest that the variation in some aspects of the sample preparation and cleaning procedure are not adequate enough when measuring other types of samples. For example, the variation in type of PoraPak™ trap, and the method of CO_2 transferal during this stage of cleaning could be inadequate in some laboratories, leading to contaminants altering the m/z = 47 signal. Clearly, further investigations into comparing the different sample preparation and cleaning methodologies are required to remove this variability in clumped isotope measurements.

Chapter 4 – Clumped Isotope Temperature Calibration

4.1 Introduction

In order to make use of the clumped isotope thermometer, it is vital to have a well-constrained and accurate temperature calibration. Knowledge of the temperature dependence of the equilibrium constant during formation of calcium carbonate is key to understanding the clumped isotope system. The likelihood of two heavier isotopes bonding within a carbonate structure is controlled by temperature; at lower temperatures, an increased amount of 'clumping' between these heavier isotopes occurs (Ghosh et al. 2006). A temperature calibration is based on clumped isotopic analyses of carbonate materials grown in equilibrium at known temperatures, allowing us to use clumped isotopes to constrain geological processes. The relationship between temperature and Δ_{47} is not yet completely understood and this is reflected by the large number of temperature calibrations that have so far been produced (Fig. 4.1). This chapter will briefly discuss the many discrepant calibrations, and the possible reasons for such differences. The UEA temperature calibration based on modern shell material and inorganic low and high temperature precipitates will be presented, as well as thoughts on the likely causes for the differences between temperature calibrations.

4.1.1 Previous work

To date there have been many published calibrations for clumped isotopes. They vary in the range of temperatures they cover, the types of carbonate (e.g. calcite, aragonite) and the material from which they are produced (biogenic or inorganic precipitates). There is a full list of equations and the information pertaining to them outlined in Table 4.1, and they are graphically represented in Section 4.3. There is a large variety in the slope and intercept of these lines. Considering there is only a small variation in the Δ_{47} signal within natural carbonates (varying between 0 ‰ and 1 ‰) (Eiler 2011), the range of calibrations is very large in comparison. These differences have led to much discussion in the community. There are various possible reasons for these discrepencies (discussed in this chapter) including the possibility that the different temperatures materials are reacted at, and other carbonate preparation methods, could alter the measured Δ_{47} signal.

Paper	Material	Reaction Temp °C	Range of temperatures °C	Calibration Line	Fractionation Factor
Came et al. (2014)	Modern brachiopods	25	-0.8 to 29	$\Delta_{47} = 0.0506 \times 10^6/T^2+0.1453$	
Defliese et al. (2015)	Synthetic precipitates (calcite & aragonite) Composite (precipitates & published data)	75	5 to 70 -1 to 77	$\Delta_{47} = 0.0348 \times 10^6/T^2+0.3031$ $\Delta_{47} = 0.0611 \times 10^6/T^2+0.0049$	+0.067 ‰
Eagle et al. (2013)	Modern cultured and field bivalve molluscs	90	-1 to 29	$\Delta_{47} = 0.0362 \times 10^6/T^2+0.314$	+0.08 ‰
Ghosh et al. (2006) - not on ARF	Synthetic calcite	25	1 to 50	$\Delta_{47} = 0.0592 \times 10^6/T^2-0.02$	
Ghosh et al. (2007) – not on ARF	Otoliths	25	2 to 25	$\Delta_{47} = 0.0568 \times 10^6/T^2-0.0045$	
Henkes et al. (2013)	Modern cultured and field brachiopods and molluscs	90	-1 to 29.5	$\Delta_{47} = 0.0327 \times 10^6/T^2+0.3286$	+0.092 ‰
Kele et al. (2015)	Travertines	70	6 to 95	$\Delta_{47} = 0.044 \times 10^6/T^2+0.205$	+0.064 ‰
Kluge et al. (2015)	Synthetic precipitates	90	23 to 250	$\Delta_{47} = 0.038 \times 10^6/T^2+0.259$	+0.069 ‰
Dennis et al. (2011)	Recalculation of Ghosh et al., (2006) and Dennis	25		$\Delta_{47} = 0.0636 \times 10^6/T^2-0.0047$	

	and Schrag (2010) onto ARF	90		$\Delta_{47} = 0.0362 \times 10^6/T^2+0.292$	
Dennis & Schrag (2010)	Inorganic precipitate (passive degassing)	90	7.5 to 77	$\Delta_{47} = 0.0337 \times 10^6/T^2+0.247$	+0.069 ‰
Guo et al. (2009)	Theoretical calculation	25		$\Delta_{47} = 0.0374 \times 10^6/T^2-0.2101$	
Grauel et al. (2013)	Inorganic calcites and biogenic materials including forams and otoliths. Data from other papers.	70	2 to 28	$\Delta_{47} = 0.05058 \times 10^6/T^2+0.0807$ (forams, inorganic material and estimated temperatures $\Delta_{47} = 0.0487 \times 10^6/T^2+0.1012$ (just forams and inorganic, with calculated temperatures)	
Tang et al. (2014)	Inorganic precipitation	90	5 to 40	$\Delta_{47} = 0.0387 \times 10^6/T^2+0.2532$	+0.092 ‰
Tripati et al. (2010)	Inorganic precipitation (not on ARF, includes others data) Inorganic and biogenic forams and coccoliths	25	 0.9 to 29.2	$\Delta_{47} = 0.0587 \times 10^6/T^2-0.014$ $\Delta_{47} = 0.052 \times 10^6/T^2+0.0627$	
Wacker et al. (2014)	Ostrich, bivalve, brachiopod,	90	9 to 38	$\Delta_{47} = 0.0327 \times 10^6/T^2+0.303$	+0.069 ‰

	foraminifera and cold seep carbonate				
Zaarur et al. (2013)	Ghosh et al., (2006) and new synthetic carbonates	25	1 to 65	$\Delta_{47} = 0.0526 \times 10^6/T^2+0.052$	
Petrizzo et al. (2014)	Modern bivalves	25	7 to 25	$\Delta_{47} = 0.0358 \times 10^6/T^2+0.2717$ (Background corrected data) $\Delta_{47} = 0.0323 \times 10^6/T^2+0.2918$ (Non-background corrected)	
Fernandez et al. (2014)	Synthetic pedogenic siderite	100	21 to 51	$\Delta_{47} = 0.0356 \times 10^6/T^2+0.172$	
Thiagarajan et al. (2011) all not on ARF	Solitary corals Inorganic material	25	0 to 50	$\Delta_{47} = 0.0495 \times 10^6/T^2+0.1052$ $\Delta_{47} = 0.05545 \times 10^6/T^2+0.0302$ $\Delta_{47} = 0.0597 \times 10^6/T^2+0.03112$	

Table 4.1 Published temperature calibrations from a variety of laboratories. The calibrations encompass a wide variety of materials and temperatures. For those laboratories who react at temperatures above 25 °C, where possible the acid fractionation factor used in the study is included.

4.1.1.1 Differences in scaling/correction of data

There is extensive discussion of possible reasons for discrepant calibrations presented in Henkes et al. (2013). Both they and Wacker et al. (2014) raise differences in scaling of the data and poor inter-lab calibrations as a possible reason. However, they found that the distinct temperature sensitivities of the different calibrations remain even when they are projected onto the same reference frame (e.g. the absolute reference frame suggested by Dennis et al. 2011)). Henkes et al. (2013) suggest that the differences in data correction, such as correcting for scale compression, are too small to account for the differences in temperature calibration.

4.1.1.2 Acid reaction temperatures and fractionation factor

A second possible reason that has been discussed within the published literature is whether the difference in acid fractionation factors is accurately known between high and lower temperature digestions (Henkes et al. 2013; Wacker et al. 2013; Defliese et al. 2015). The acid fractionation factor applies a constant offset between Δ_{63} (carbonate) and the Δ_{47} signal retrieved from the product CO_2 (Guo et al. 2009). It is important that the difference in acid fractionation factor is accurately known between reactions at 25 °C and 90 °C, so that data produced by digestion of carbonates at different temperatures can be compared. When raw measurements are projected onto the absolute reference frame they are calculated relative to digestion at 25 °C. Therefore, when a laboratory reacts at a different temperature, the data must be corrected to be comparable to a 25 °C reaction (Spencer & Kim 2015). Guo et al. (2009) calculated a theoretical acid fractionation factor, and the correction can also be experimentally derived in individual laboratories by reacting the same material at both 25 °C and 90 °C temperatures.

If incorrect acid fractionation factors were the reason for the discrepant calibrations, we should see the regression lines having a very similar temperature sensitivity (gradient) but with varying intercepts. Henkes et al. (2013) found that the differences in acid fractionation factor were not large enough to account for differences in temperature calibration, a conclusion supported by Defliese et al. (2015). As all of the calibration lines (Table 4.1) vary in both temperature sensitivity and intercept, it is likely that the difference in carbonate reaction temperature is not the dominant reasoning behind the variations in temperature calibrations.

4.1.1.3 Partial re-equilibration

Wacker et al. (2014) put forward the possibility that there is partial re-equilibration occurring during the sample reaction phase at either temperature. As there is oxygen exchange between any traces of water and the CO_2 produced from the reaction, it can be assumed that there

is modification of the clumped isotope signal. If the exchange reaches equilibrium, the clumped isotope value would reflect the temperature at which the sample was reacted (Wacker et al. 2014). This suggestion also ties in with work by Wacker et al. (2013) investigating the effects of sample size, and Defliese et al. (2015) investigating the effects of water re-equilibration.

Wacker et al. (2013) found that sample size had an effect on Δ_{47} values when the reaction occurs at 25 °C. Smaller samples showed a more positive and less consistent Δ_{47} value compared to larger samples. However, they saw no dependency on sample size when the carbonate material was digested at 90 °C. They also suggested that the produced CO_2 was re-equilibrating with water produced during the digestion of carbonate within the acid, and not re-equilibrating in the headspace of the reaction vessels. This occurs to a greater extent when the reaction is ongoing at 25 °C, as smaller bubbles are produced and take longer to escape from the acid, thereby causing the sample size dependency observed at 25 °C (Wacker et al. 2013).

Defliese et al. (2015) also suggest that the discrepancies between the published calibrations is likely to be procedural. They indicate that as water can react with sample CO_2 to produce carbonic acid, the clumped isotope signal can be altered during this process. They suggest that small amounts of water being present in the headspace could cause an offset during a digestion. The risk is greater at higher temperatures, and they suggest that multiple stages of cryogenic cleaning are required to fully remove water from the sample gas. They also suggest that product CO_2 should be removed immediately throughout the reaction process (Defliese et al. 2015).

Whether it is within the acid or in the headspace of the reaction vessel, re-equilibration with water is a possible source for the discrepancies between the temperature calibrations. As the reaction methods and cleaning processes vary between laboratories, this could affect the Δ_{47} values, and be the cause of discrepancy between labs.

4.1.1.4 Biological effects

In addition to differences caused by methodological artefacts, it is possible that the biogenic samples such as skeletal carbonates are undergoing processes we cannot identify. Henkes et al. (2013) suggested a series of biological processes that could affect clumped isotopes. Isotopic mixing during sampling, or possibly during growth if there are distinct reservoirs of dissolved inorganic carbon, will mean that the measured isotope value is potentially a combination of two end-members. Defliese & Lohmann (2015) further investigated the effects of mixing on clumped isotope measurements. They suggest that that mixing of bulk isotopically distinct layers within a sample (such as growth bands within a shell) or the mixing of different phases of calcite could cause the Δ_{47} temperatures to vary from the expected value. They found that mixing causes a significant

variation in Δ_{47} when a sample varies in bulk isotopic composition by 2 ‰ or larger. They suggest that whilst mixing alone cannot be significant enough to cause the discrepant calibrations, it is likely to be a contributing factor (Defliese & Lohmann 2015).

Another possible biogenic effect could be that skeletal material precipitated at lower temperatures could be more prone to recording kinetic isotope effects (Eagle et al. 2013). Eagle et al. (2013) suggest that these changes could manifest in the measured Δ_{47} values as vital effects, further suggesting that some species are more affected by this than others. At very cold temperatures, there may be a potential source of disequilibrium within the dissolved organic carbon from which the skeletal carbonate forms. When they excluded species from the very coldest locations from their temperature calibration, it did produce a slightly steeper slope. Eagle et al. (2013) also investigated whether biogenic material growing outside of the assumed time of maximum growth during summer could alter the temperature calibration. When an annual temperature was used rather than a summer temperature, there was no significant difference to the linear regression that described the relationship between bivalve skeleton and temperature.

4.1.1.5 Contaminated materials

The large number of published calibrations produced in different labs (Table 4.1) opens up the possibility that variation in sample preparation, cleaning and measurement methods could be affecting clumped isotope results. If the product CO_2 is not adequately cleaned, additions to the sample gas (contaminants) can cause interference on the mass-47 signal during measurement on the mass spectrometer, which will affect the Δ_{47} values. Discussions on contamination are not widespread within the published literature. Some discussion on possible contaminants and their effects are covered in Chapters 2 and 3, Sections 2.3.6 and 3.6. Huntington et al. (2009) suggested that elevated Δ_{48} and Δ_{49} values are indicative of contamination, which is similar to the contamination observations made at UEA. Wacker et al. (2013) found that there were minimal differences in the Δ_{48} values between samples reacted at 25 °C and 90 °C. This indicates it is unlikely that the differences in Δ_{47} values between high and low temperature reactions was due to CO_2 purity. It is also widely acknowledged that the differences in sample preparation is a likely cause for the variation in temperature calibrations (e.g. Tang et al. (2014); Defliese et al. (2015); Eagle et al. (2013)). The possible effects of contamination as a cause for the discrepant temperature calibrations will be discussed further later in this chapter.

4.1.2 Methods for precipitation of inorganic material

Several of the published temperature calibrations include both low and high temperature inorganic material. The fractionation between water and oxygen isotopes has been investigated for many years, and is used as a method to calculate the calcite precipitation temperature. The fractionation factor between calcite and water is controlled by a number of factors, such as temperature, pH and precipitation rate. Being able to precipitate calcium carbonate in controlled conditions and measure the fractionation factor (α) is therefore ideal. There has been some investigation into whether the clumped isotopic signal is in equilibrium during calcite precipitation, and what effect the above mentioned factors have on the Δ_{47} value. This section will focus on lower temperature precipitation at a similar temperature to those produced at UEA.

There are various possible methods to precipitate inorganic calcium carbonate within a controlled laboratory environment but there still is some discussion about the conditions under which calcite will precipitate in equilibrium. Kim & O'Neil (1997) produced calcium carbonate by producing a bicarbonate solution with CO_2 bubbled through it first, using equal concentrations of XCl_2 and $NaHCO_3$, where *X* represents a choice between different chlorides (e.g. $CaCl_2$, $MgCl_2$) to produce different carbonates as required. This solution was afterwards bubbled with nitrogen gas to remove the carbon dioxide. The solution became saturated and precipitated carbonate, taking between one and five days to produce enough mass for isotopic analysis (Kim & O'Neil 1997). Ghosh et al. (2006) used a variant of this method when they assessed the relationship between Δ_{47} and precipitation temperature. CO_2 was bubbled through a solution with $CaCO_3$, then forced out to stimulate precipitation. Zaarur et al. (2013) re-assessed this relationship, and also used this method to precipitate inorganic calcium carbonate, taking between four days and a few weeks to produce an adequate amount of material for clumped isotope analysis.

Dennis & Schrag (2010) used a passive degassing method to precipitate calcium carbonate. They created separate solutions of $NaHCO_3$ and $CaCl_2$ before slowly adding one solution to the other. This final solution was exposed to the atmosphere allowing it to passively degas. The precipitated material was collected between one to four days after the solutions were mixed. When this material was analysed to demonstrate the relationship between Δ_{47} and precipitation temperature, it produced a much shallower regression slope than that of Ghosh et al. (2006), which relied on more active CO_2 degassing.

Dietzel et al. (2009) state that inorganic calcite spontaneously precipitated over a very short period is less likely to be in isotopic equilibrium, although they also found that even calcite precipitated over a longer amount of time may show kinetic effects on oxygen isotope fractionation. They review a large body of experimental and theoretical work that suggests that if

calcite is precipitated slowly enough at low temperatures, it forms close to, or at, oxygen isotopic equilibrium. This is supported by Coplen (2007), who studied calcite precipitated naturally in a cave system, although they indicate that equilibrium oxygen isotope fractionation factors may be underestimated. They showed that this cave calcite was either very close to, or in thermodynamic oxygen isotope equilibrium. The slow diffusion mechanism outlined by Dietzel & Usdowski (1996) was used by Tang et al. (2014) to investigate clumped isotope signals recorded during inorganic calcite precipitation to produce their own temperature calibration. The success of this slow diffusion method for clumped isotopes encouraged us to use this method of calcite precipitation in the UEA lab.

4.1.2.1 Possible effects on temperature calibrations

As many of the clumped isotope temperature calibrations include inorganic calcium carbonate precipitated in laboratories under controlled conditions, it is important to understand the possible effects on clumped isotopes. Tang et al. (2014) investigated the effect of precipitation rate, pH and ionic strength on the clumped isotope values measured from inorganic calcite precipitated under controlled conditions. They found that clumped isotopes are generally less sensitive to these parameters than oxygen isotopes are. This was especially clear in studying the changes in isotopes caused by a range in pH. Oxygen isotopes were altered by a wide range of pH values, whereas clumped isotopes were only affected when the pH rises above 9.0. Changes in pH can cause changes in the dissolved inorganic carbon (DIC), which can mean that some DIC may not be in equilibrium with the fluid. This is similar to a possibility identified by Henkes et al. (2013) that variation in DIC species could have an effect on biological carbonate too, although it seems that clumped isotopes more readily reach equilibrium than bulk oxygen isotopes (Tang et al. 2014).
Tang et al. (2014) identified a temperature calibration using their synthetic material, listed in Table 4.1.

There has been some further investigation into the inorganic precipitation of carbonate and how the precipitation conditions may affect the clumped isotope signature. Tripati et al. (2015) precipitated inorganic calcite using an active degassing method alongside analysis of modern coral material to assess the influence of variables such as solution chemistry on both clumped isotope and oxygen isotope values. They found that if a calcite mineral grows slowly enough, over a time period such as the calcite from Devil's Hole cave (up to 0.8 μm a^{-1}, (Coplen 2007)), Δ_{47} values will be independent of the growth rate and the solution chemistry, even if the $\delta^{18}O$ of the calcite exhibits disequilibrium. This is providing the crystal has reached equilibrium within the mineral lattice. If

there is rapid growth of the calcite crystal (over days or weeks), the chemistry of the solution will affect the Δ_{47} signal. This was identified from their analysis of controlled growth of coral material, which showed a range of Δ_{47} values despite identical growth temperatures. They suggest that under rapid growth, changes to the solution, such as its pH value, will cause changes in the Δ_{47} value. They also identify a temperature calibration (shown in Table 4.1) that is similar to the Ghosh et al. (2006) temperature calibration, which is steeper than the synthetic temperature calibration produced by Tang et al. (2014).

Tang et al. (2014) identified that different speeds of inorganic carbonate precipitation could produce DIC species that are not in equilibrium with the fluid, and this conclusion is supported by Tripati et al. (2015). Tripati et al. (2015) suggest that the effect on Δ_{47} could be more extensive. However, it is clear that the Δ_{47} isotopic value can be in equilibrium simultaneously to the oxygen isotope values showing the effects of precipitation in disequilibrium. Tang et al. (2014) conclude that the discrepancies between the many temperature calibrations are more likely to be due to varying analytical methods rather than disequilibrium issues during inorganic precipitation. It appears that further detailed research is required to draw a clear conclusion as to the extent variable conditions of precipitation have on the Δ_{47} signal.

4.2 Experimental

4.2.1 Skeletal (shell material)

Modern brachiopod shells analysed in this study were from two sets of shells donated by Juraj Farkas and Elizabeth Harper. The Farkas shell set includes a variety of species and covers a temperature range from 5.57 °C to 21.55 °C. There are three species present in the Harper shell set, two of which cover a similar range in temperature (from 13.45 °C to 14.26 °C), whilst the third shell is from a cold Antarctic location (from 0.3 °C to 1.7 °C). Table 4.2 shows the shell species, collection location and temperature range for each shell, and Figure 4.1 displays a world map with the shell locations marked.

Sample Number	Shell Species	Co-ordinates/Location Name	Collection Temperature °C	Collection Depth (m)
	Liothyrella uva.	67°34 S 68°08 W, Rothera Point, Adelaide Island	0.3-1.7	15-25
	Liothyrella neozelanica	45°25 S 167°07 E, Doubtful Sound, South Island	13.5-14.3	4-18
	Terebratella sanguinea	45°25 S 167°07 E, Doubtful Sound, South Island	13.5-14.3	4-18
1	*Liothyrella sp.*	44°30'24 S 175°56'27.63 E, New Zealand	5	700
2	*Macandrenia cranium*	70°56.002N 22°12.326 E	7	193
3	*Macandrenia cranium*	70°55.138N 22°11.259 E	7	201
4	*Terebratulina retusa*	67°31.9N 9°30.3E	7	318
5	*Terebratulina retusa*	64°05.916N 8°05.494E	7.7	287
6	*Macandrenia cranium*	59°05.616N 10°47.952E	8	110
7	*Terebratulina unguicula*	San Juan Island, Friday Harbour	8.6	83
8	*Terebratalia transversa*	San Juan Island, Friday Harbour	8.8	64
9	*Terebratalia transversa*	San Juan Island, Friday Harbour	8.8	36
10	*Terebratalia transversa*	San Juan Island, Friday Harbour	8.8	73
11	*Terebratalia transversa*	San Juan Island, Friday Harbour	8.8	73
12	*Terebratalia transversa*	San Juan Island, Friday Harbour	8.8	
13	*Terebratalia transversa*	San Juan Island, Friday Harbour	8.8	
14	*Hemithiris psittacea*	San Juan Island, Friday Harbour	8.8	19
15	*Macandrenia cranium*	56°29.98N 17°18.63W	8.8	683
16	*Terebratulina retusa*	56°29.84N 17°18.30W	8.8	668
17	*Dallina septigera*	51°27.16N 11°43.61W	9.6	905

18	*Terebratalia transversa*	48°5N 123°W	10	
19	*Terebratalia transversa*	47°N 122°W, Pudget sound, seattle	10.5	
20	*Laqueus erythreus*	California	10.5	90
21	*Grypheus vitreus*	42°N 6°W	13.3	400
22	*Calloria inconspicua*	43°S 180°W, Doubtful Sound, New Zealand	13.7	20
23	*Terebratella sanguinea*	43°S 180°W, Doubtful Sound, New Zealand	13.7	20
24	*Notosaria nigricans*	43°S 180°W, Doubtful Sound, New Zealand	13.7	20
25	*Liothyrella neozelanica*	43°S 180°W, Doubtful Sound, New Zealand	13.7	20
26	*Terebratulina unguicula*	43°S 180°W, Doubtful Sound, New Zealand	13.7	20
27	*Calloria inconspicua*	43°S 180°W, Doubtful Sound, New Zealand	14	0.5
28	*Cryptopora curiosa*	Red Sea	20.5	313
29	*Platidia anomioides*	Red Sea	20.5	567
30	*Argyrotheca sp.*	Red Sea	20.5	373
31	*Megerlia echinata*	Red Sea	20.5	90
32	*Pictothyris (picta?)*	35.5°N 139.5°E, Yokohama, Japan	21.5	20

Table 4.2 Collection data for both sets of shells. Those with names were donated by Elizabeth Harper, and those with numbers were donated by Juraj Farkas. The shells are likely to have incorporated the growth temperature as a summer growth mean rather than the specific temperature listed for the Farkas shells. Unfortunately, there is limited depth and temperature data reported for this shell suite. The Harper shell suite defines a temperature range for each shell, which is reflected as temperature error added to the analyses later in this chapter.

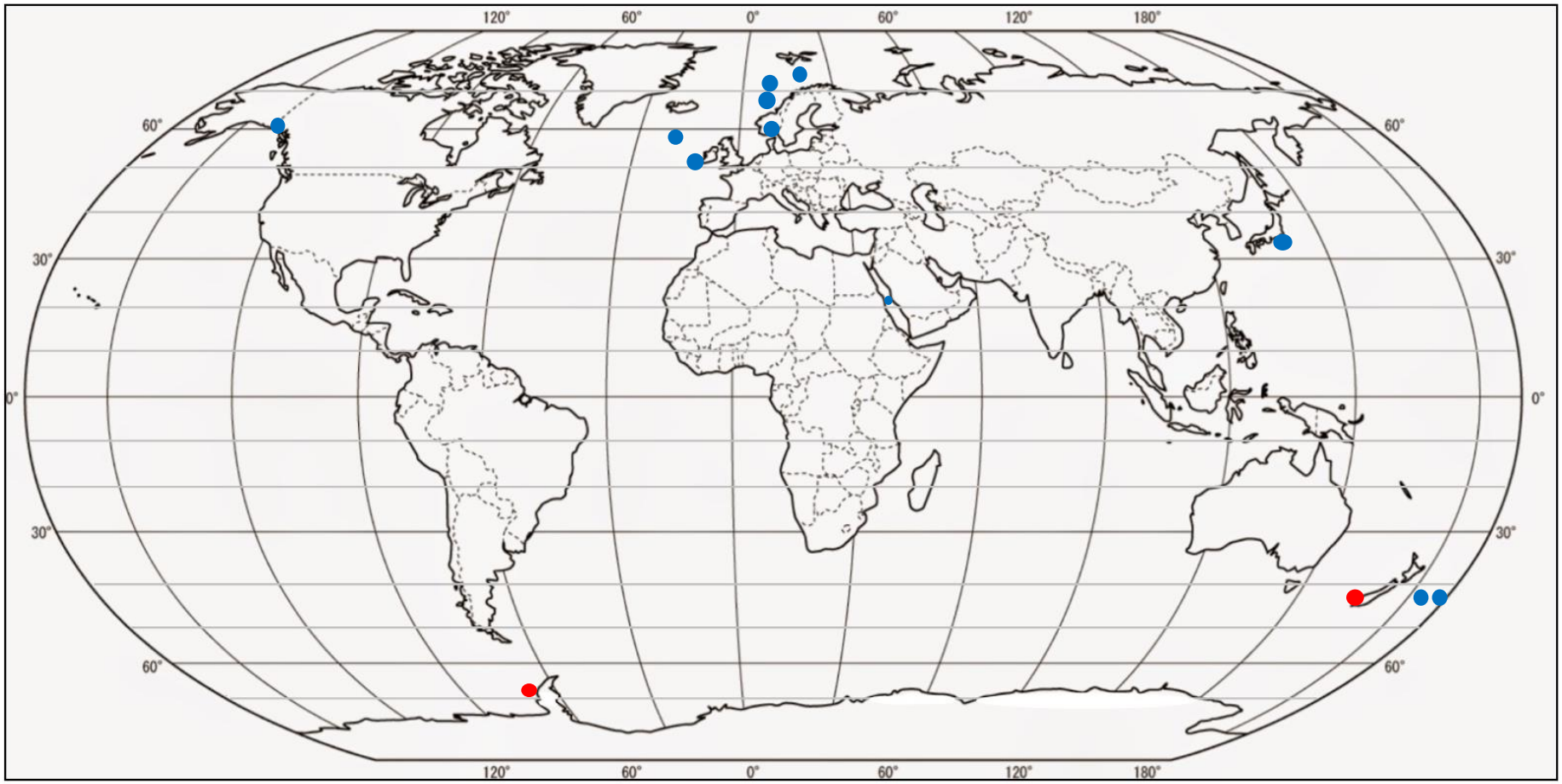

Figure 4.1 World map displaying locations from where shells were collected. The blue dots represent the Juraj Farkas shells, and the red dots represent the Elizabeth Harper shells.

4.2.2 Shell preparation and analysis

The two sets of shells have not been pre-treated chemically. They were washed in de-ionised water and any organic material was scraped away using a scalpel. The Farkas shells were broken into fragments prior to their arrival at UEA, with the largest around 75 mg in weight prior to crushing. For each of the Harper shells, one valve out of the two were used, which provided ample material for analyses. Due to the large volume of material, a single *Liothyrella neozelanica* valve was cut in half, and one piece was used for analyses. Whilst scraping the shell surface removes any surface organic material, it does leave the possibility that inter-crystalline organic material remains.

All of the shells were ground and homogenised using an agate pestle and mortar, then transferred into small sample tubes. There was no distinguishing made between primary, secondary and tertiary layers of calcite. Because the material from Juraj Farkas consisted only of partial shells, there was less material available for analyses. Sample aliquots between 7-10 mg were used as detailed in Chapter 3 Section 3.4. Briefly, the powdered sub-samples are reacted offline with approximately 1.5 ml of 1.9 g/cm^3 phosphoric acid at a temperature of 25 °C ±0.1 °C overnight (a minimum of 16 hours). The CO_2 was then cleaned on the manual vacuum line, where water and other possible contaminants are cryogenically removed. The clean CO_2 samples stored in Pyrex tubes and isolated by a LH valve are then transferred to the MIRA mass spectrometer and analysed on the same day. This reduces the possibility of clumped isotopic signal resetting due to re-equilibration or contamination due to possible leaking gas vessel. The raw data was processed as outlined in Chapter 2 Section 2.6 and all clumped isotope results are reported on the absolute reference frame (ARF) unless otherwise stated.

4.2.3 Precipitation of inorganic carbonate at controlled temperatures

Inorganic calcium carbonate was precipitated using the slow CO_2 diffusion method adapted from Tang et al. (2008) Dietzel et al. (2009) and Tang et al. (2014). The schematic and photographs in Figure 4.2 outlines the method set-up. A 500 ml polyethylene bottle with a wall thickness of approximately 1-2 mm containing a solution of 0.83 M $NaHCO_3$ was placed within an external solution held within a large glass desiccator. This external solution contains 0.01 M $CaCl_2$ and 0.005 M NH_4Cl to act as a buffer. The outer solution was stripped of atmospheric carbon dioxide by bubbling nitrogen gas through it for approximately 2 hours. The inner solution has a high partial pressure of CO_2 and so CO_2 gas will diffuse slowly through the polyethylene membrane (the bottle wall) into the outer solution. Here it reacts with calcium ions to precipitate calcium carbonate. The desiccator was kept on a stirrer plate for the entire length of the experiment to ensure a well-mixed solution. Two successful experiments produced two batches of calcium carbonate that were used in the temperature calibration.

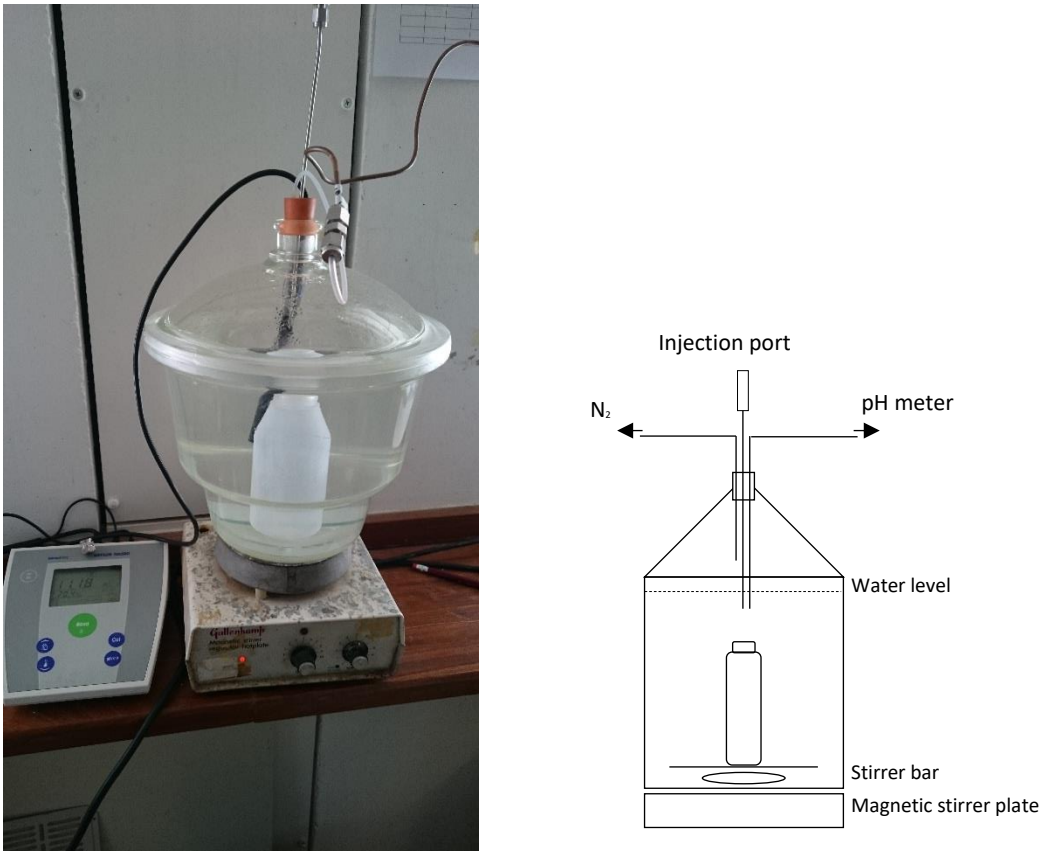

Figure 4.2 Photo and schematic of low temperature precipitation equipment.

The two experiments lasted five months (ending in December 2014) for one and three and a half months (ending June 2015) for the other. The first was kept at an average of 21.5 °C and the other at 20.5 °C. The average pH of the first experiment was 8.13 and the second was 8.69. Once enough material had precipitated, the outer solution was vacuum filtered through a cellulose acetate filter. The desiccator was then rinsed immediately with deionised water and left to air dry. Once the desiccator was dry, it's internal wall was scraped with a silicon spatula to remove the very fine calcium carbonate precipitate and the powder was stored in a small clean vessel.

4.3 Results

4.3.1 Identification of contamination

Using the $\Delta_{48(wrg)}$ and $\Delta_{49(wrg)}$ values for the measured samples, it is possible to identify and discard analyses which show contamination. A description of contamination effects is outlined in Chapters 2 and 3, Sections 2.3.6 and 3.6. Any measurements with >1 ‰ $\Delta_{48(wrg)}$ and >100 ‰ $\Delta_{49(wrg)}$ were viewed as contaminated and removed from the dataset. High $\Delta_{48(wrg)}$ and $\Delta_{49(wrg)}$ values are associated with contamination, which is likely due to insufficient cleaning procedures. For example, shell 22 was analysed three times, with three separate reactions. The resulting $\Delta_{47(ARF)}$ values are quite different, showing 0.586 ‰ for the first analysis, 0.971 ‰ for the second and 0.583 ‰ for third. The anomalous middle value also shows an elevated $\Delta_{49(wrg)}$ value (the respective $\Delta_{49(wrg)}$ values for each measurement are -47.235 ‰, 302.247 ‰ and -38.038 ‰). Thus the second measurement has both an elevated $\Delta_{47(wrg)}$ and $\Delta_{49(wrg)}$ signal. This occurrence is observed in the majority of the shell analyses where there is poor reproducibility between individual analyses.

The highest $\Delta_{48(wrg)}$ and $\Delta_{49(wrg)}$ values are within the Farkas shell suite, showing values of Δ_{48} up to 3.168 ‰, and Δ_{49WRG} values up to 1172.616 ‰. The highest $\Delta_{48(wrg)}$ value for the Harper shells is 0.897 ‰, and the highest for $\Delta_{49(wrg)}$ is 196.983 ‰. Of the 94 measurements made on the two shell datasets, removal of data showing high $\Delta_{48(wrg)}$ and $\Delta_{49(wrg)}$ values left 70 analyses, which were used to calculate averages for each shell specimen (see Table 4.3).

The same exclusion procedure was used to identify and remove the data corresponding to measurements with elevated $\Delta_{48(wrg)}$ and $\Delta_{49(wrg)}$ values for analyses using aliquots of the inorganic material precipitated under controlled temperatures. Only one analysis was removed from the controlled temperature precipitates, suggesting that the inorganic material is much cleaner than the shell materials. This could perhaps be due to intercrystalline organics that were not removed prior to analysis. All of the data displayed in the following results section is the filtered data. A further discussion on contaminated data appears in Section 4.4.2.3.

4.3.2 Farkas shell suite

A total of 26 shells from the suite of 32 donated by Juraj Farkas were analysed on MIRA. The first analyses were completed between November 2012 and June 2013, and the final measurements were completed during January and February of 2014. Only 26 shells from the set were measured because some shell fragments were not big enough for clumped isotope analysis. During the period of measuring these shells, 10 mg of carbonate material was required for each analysis. Some of the shells had enough material for repeat analyses (see Table 4.2) and for these a mean value is shown, along with its standard deviation and standard error.

Shell Name/Number	Collection/Growth T °C	Single/Av. Δ_{47} ARF ‰	SD of Δ_{47} ARF	SE of Δ_{47} ARF	Single/Av. $\delta^{13}C$ $‰_{VPDB}$	Single/Av. $\delta^{18}O$ $‰_{VSMOW}$ Calc @ 25°	n
1	5.57	0.703			1.63	33.83	1
2	7.18	0.769			2.04	33.45	1
3	7.18	0.767	0.009	0.006	2.46	33.76	2
6	8.08	0.768			1.74	33.08	1
9	8.8	0.758			-2.92	29.31	1
11	8.8	0.679	0.071	0.050	-2.04	29.02	2
12	8.8	0.607			-1.97	29.06	1
13	8.8	0.562			-0.98	30.74	1
14	8.8	0.586			-2.75	29.25	1
15	8.87	0.672	0.114	0.066	1.35	33.13	3
16	8.87	0.573			1.66	34.08	1
18	10	0.610	0.023	0.017	0.42	31.39	2
21	13.3	0.566			2.56	33.85	1
22	13.65	0.585	0.002	0.002	0.21	31.22	2
23	13.65	0.621	0.042	0.024	1.12	31.87	3
24	13.65	0.720			1.09	31.58	1
25	13.65	0.676	0.136	0.079	1.98	31.32	3
26	13.65	0.656	0.046	0.033	-0.08	31.18	2
31	20.5	0.674			2.13	30.67	1
32	21.55	0.668			0.97	30.94	1
Liothyrella uva.	1	0.766	0.045	0.015	1.04	34.08	9
Terebratella sanguinea	14	0.721	0.050	0.013	-0.26	30.40	15
Liothyrella neozelanica	14	0.694	0.057	0.015	1.87	31.64	15
Precipitate Dec 2014	21.5	0.695	0.034	0.010	-19.70	22.33	11
Precipitate June 2015	20.5	0.738	0.022	0.011	-19.74	21.51	4

Table 4.3 The mean clumped isotope (Δ_{47}) and bulk isotopic values (δ18OVSMOW and δ13CVPDB) for both shell suites and the two batches of inorganic precipitate. The Farkas shells are identified by their shell numbers and the Harper suite by their names. The species and growth temperature are also shown in Table 4.3.

Even with the removal of those measurements that display elevated $\Delta_{48(wrg)}$ and $\Delta_{49(wrg)}$ values suggestive of contamination, there is still a large spread in the $\Delta_{47(ARF)}$ values with some anomalous results. For example, the most enriched $\Delta_{47(ARF)}$ measurement (0.776 ‰) and the lowest $\Delta_{47(ARF)}$ (0.521 ‰) are both measurements of shell 25, for which the collection temperature was 13.65 °C. None of these measurements is associated with elevated $\Delta_{48(wrg)}$ and $\Delta_{49(wrg)}$ values, and the bulk isotopic values are very consistent within the triplicate analysis of this shell. This suggests that there are other possible sources of error, which will be discussed later.

4.3.3 Harper shell suite

The Harper suite of shells, composed of 4 shells, was analysed at a much later date than the Juraj Farkas shells, during 2015. The method for sample gas cleaning and analysis on the mass spectrometer was, at this time, much improved compared to early 2013, when the Farkas shells were analysed (see Chapter 3). Three of the shells, with the most detailed temperature records, were chosen for development of the temperature calibration and results are shown in Table 4.2. The three shell species used from this suite grew in a range of temperatures (see Section 4.2.1 for a full outline), thus the growth temperature was calculated as the mid-point temperature for the range described. Therefore, for the *Liothyrella uva.* shell a value of 1 °C was used, and for the *Terebratella sanguinea* and *Liothyrella neozelanica* a value of 14 °C was used for the average collection temperature. Each of the three shells was analysed multiple times for clumped isotopes, producing mean values of 0.776 ‰ ±0.015 for *Liothyrella uva.,* 0.721 ‰ ±0.013 for *Terebratella sanguinea* and 0.694 ‰ ±0.015 for *Liothyrella neozelanica* (Table 4.3). There is still quite a range in Δ_{47} value within each set of replicates. For example, the *Liothyrella neozelanica* sample has the greatest Δ_{47} range, from 0.608‰ to 0.829‰. This produces a difference of 0.221‰.

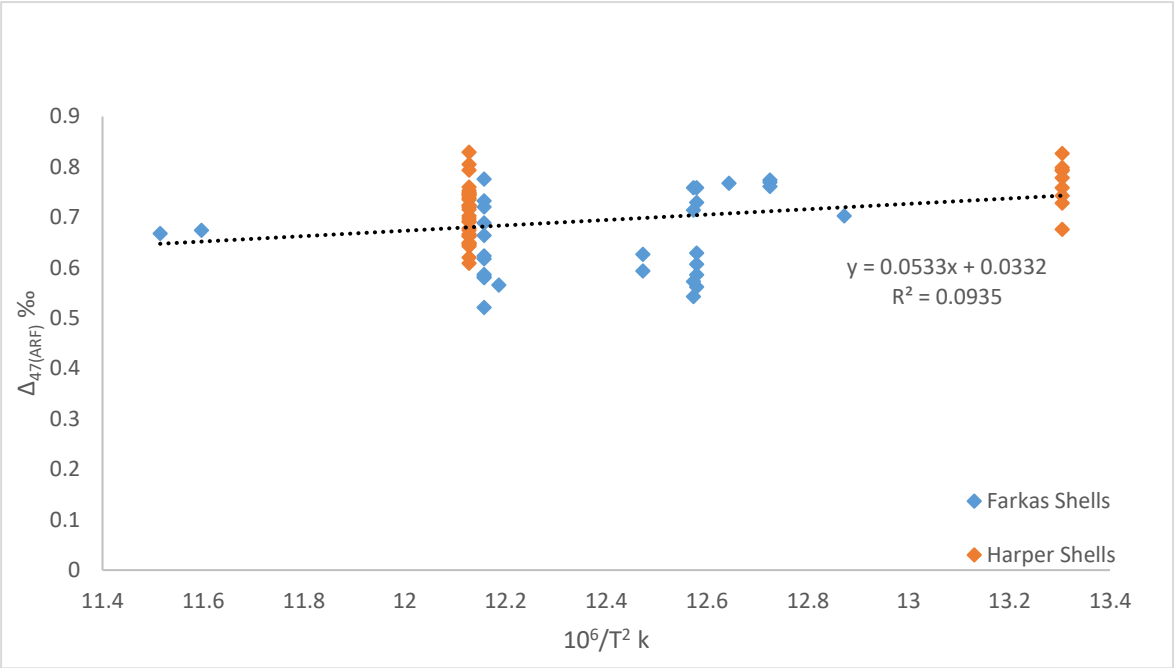

Figure 4.3 Linear regression for the Farkas and Harper shell suites. The relationship between temperature and Δ_{47} is y = 0.0533(±0.02)x +0.0332(±0.23).

Figure 4.3 shows the regression line produced when both sets of shell material are plotted in terms of the $\Delta_{47(ARF)}$ value in relation to growth or collection temperature. Here temperature is plotted as $10^6/T^2$ (T in Kelvin). The linear regression was plotted using the best fit line described by Equation 4.1:

$$\Delta_{47(ARF)} = \frac{5.33\times10^4}{T^2} + 0.0332 \qquad \text{Equation 4.1}$$

4.3.4 Calcium carbonate from inorganic precipitation experiments

I completed two slow diffusion-method inorganic calcite precipitation experiments at room temperatures and successfully collected the calcium carbonate. The full method for precipitation is outlined in Section 4.2.3. The two successful experiments gave enough material to make multiple analyses. The average results, standard deviation and standard error are shown in Table 4.3. For the experiment completed at 21.5 °C, the average value is 0.695 ‰ ±0.01, and for the 20.5 °C experiment the average $\Delta_{47(ARF)}$ value is 0.738 ‰ ±0.011. The range in the data for each precipitation experiment is much lower than that displayed in the Harper shell suite. The experiment at 21.5 °C produced a range of $\Delta_{47(ARF)}$ values between 0.636 ‰ and 0.764 ‰, which is a difference of 0.128

‰. The 20.5 °C experiment gives an even lower range value of 0.047 ‰. This suggests the powder is homogenous.

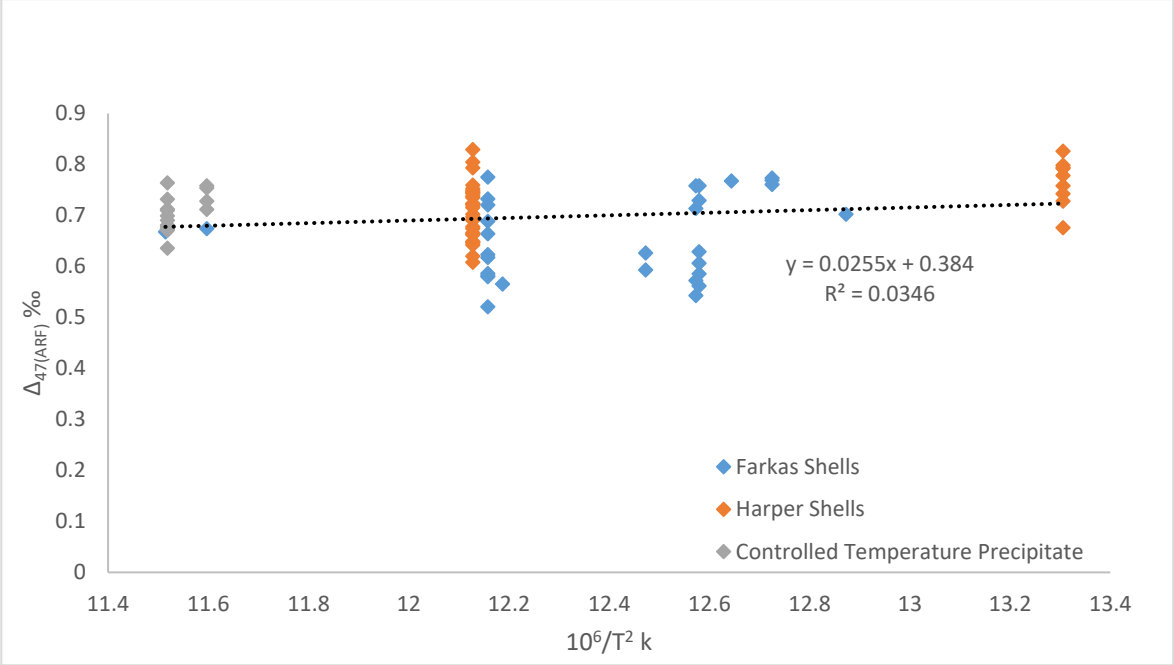

Figure 4. 4 Linear regression for the Farkas and Harper shell suites. The relationship between temperature and Δ_{47} is y = 0.0533(±0.02)x +0.0332(±0.23).

Only one analysis showing elevated $\Delta_{49(wrg)}$ was removed from the controlled temperature precipitation data. The $\Delta_{48(wrg)}$ value was within the accepted limits for an uncontaminated sample, but the $\Delta_{49(wrg)}$ was above 100 ‰. Data for the two shell suites and the controlled temperature precipitation $\Delta_{47(ARF)}$ values are plotted in Figure 4.4 against the growth, collection, or precipitation temperature ($10^6/T^2$, T in Kelvin). The linear regression fitted to this set of data produces a line described by Equation 4.2:

$$\Delta_{47(ARF)} = \frac{2.55\times10^4}{T^2} + 0.384 \qquad \text{Equation 4.2}$$

Compared to Equation 4.1, the slope of the regression line has changed with the addition of the controlled temperature precipitate, as more data is added to the higher temperature end of the line. Finally, Figure 4.5 shows the variability in Δ_{47} measurements compared to $\delta^{18}O_{VSMOW}$ measurements on MIRA for the shells and controlled temperature precipitates. There is a clear relationship between the growth temperature of the calcite and the $\delta^{18}O_{VSMOW}$ (blue data points) (R^2 = 0.62), therefore we would expect to see a variation in Δ_{47} values with growth temperature.

The laboratory precipitates have a far better precision for the repeat analyses than the organic shell material. Δ_{47} values (red data points) have a less clear relationship with growth temperature in comparison, with a lower precision. The wide spread in Δ_{47} values within the organic shell material makes the temperature variability unclear. The UEA temperature calibration therefore uses a combination of biogenic and inorganic calcite to better constrain the temperature relationship. This is similar to other temperature calibrations, such as Grauel et al. (2013) and Tripati et al. (2010) who have used combinations of organic and synthetic calcite.

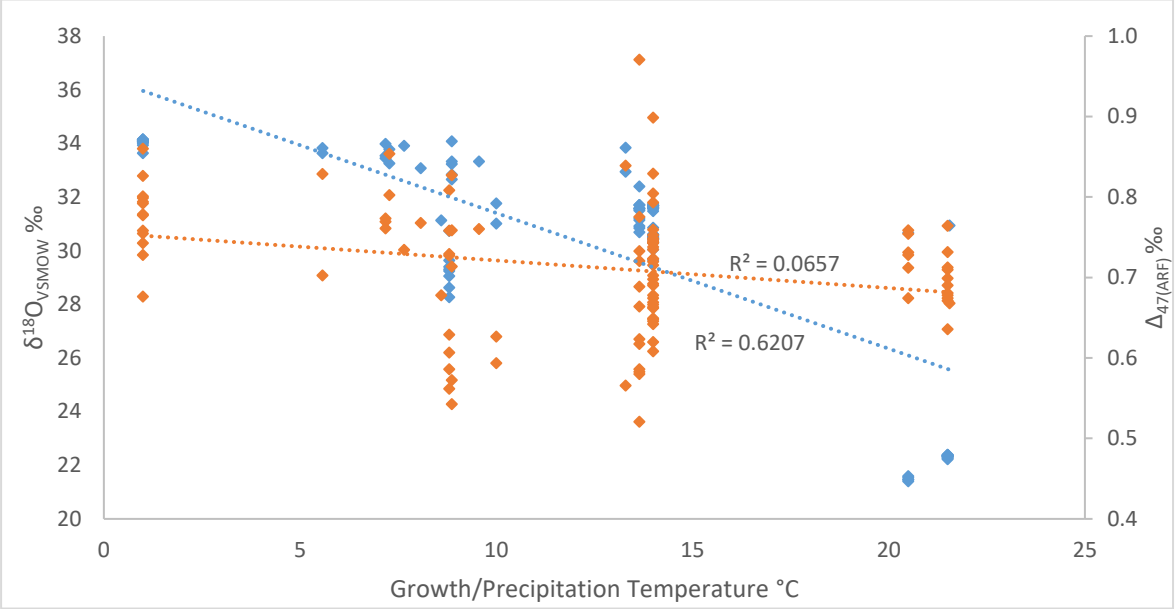

Figure 4.5 The two shell suites and low temperature precipitate displaying variability between oxygen isotopes, clumped isotopes and the growth temperature.

4.3.5 Temperature calibration

The three sets of data outlined above are all 25 °C or lower temperature inorganic and biogenic carbonate materials. At UEA we regularly analyse a higher temperature inorganic calcium carbonate standard, used as an internal standard. This is the Turkish hydrothermal calcite (THC), which is described in Chapter 3, Section 3.3.2. This material was precipitated at a constant temperature of 56°C, and has an average Δ_{47} value of 0.564 ‰ ±0.005. I have added the data for this material to the three datasets described above and the relationship between Δ_{47} and temperature ($10^6/T^2$, T in Kelvin) is shown in Figure 4.6. Equation 4.3 describes the linear regression for this larger dataset:

$$\Delta_{47(ARF)} = \frac{4.26\times10^4}{T^2} + 0.1737 \qquad \text{Equation 4.3}$$

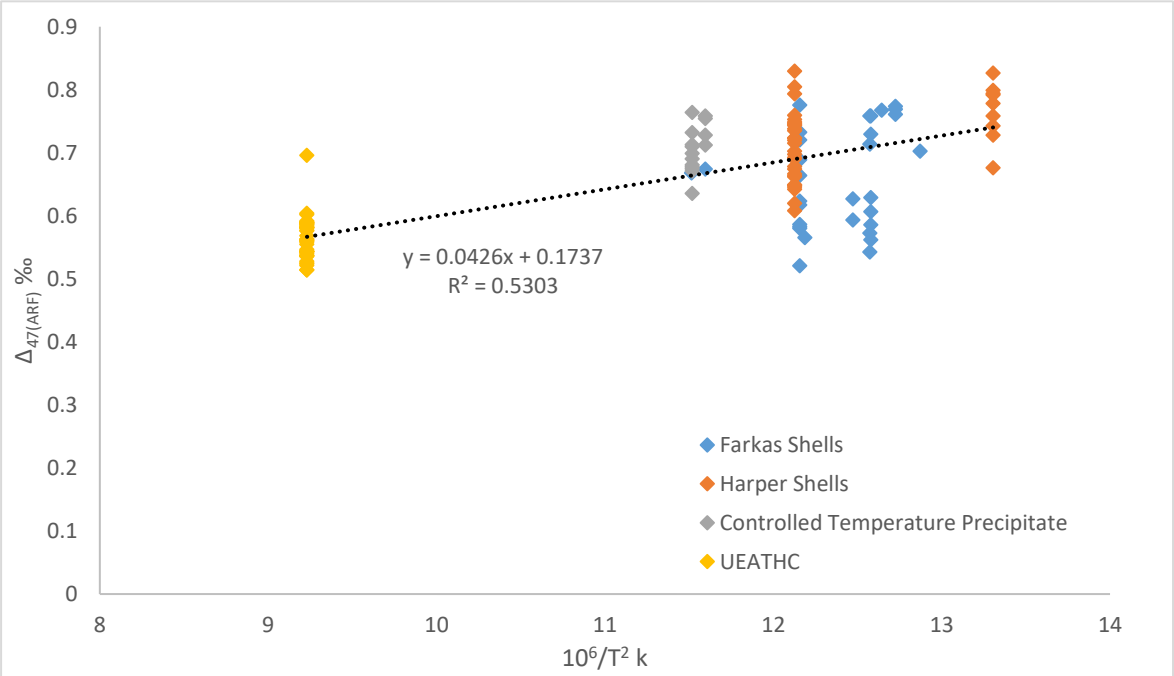

Figure 4.6 Shell data, temperature controlled precipitates and 56 °C Turkish calcite plotted to show the relationship between temperature and $\Delta_{47(ARF)}$. The linear regression is y = 0.0426(±0.004)x +0.1737(±0.041).

To minimise the effects of outlying data the data from Figure 4.6 is re-plotted using averages for each of the lower temperature samples; these are presented in Table 4.4. This dataset was calculated by averaging the data for each shell species at the given growth temperature. This produces 22 data points. The standard deviation and standard error are also shown in Table 4.4 where multiple analyses have been done on a sample. The linear regression of this averaged dataset when plotted to show the relationship between temperature and Δ_{47} is displayed in Figure 4.7.

$$\Delta_{47(ARF)} = \frac{3.5\times10^4}{T^2} + 0.2416 \qquad \text{Equation 4.4}$$

Sample Name/Number	Coll. T °C	Average Δ_{47} at T per species	SD	SE	n
1	5	0.703			1
2 and 3	7	0.768	0.006	0.004	3
6	8	0.768			1
9 to 13	8.8	0.657	0.083	0.037	5
14	8.8	0.586			1
15	8.8	0.672	0.114	0.066	3
16	8.8	0.573			1
18	10	0.610	0.023	0.017	2
21	13.3	0.566			1
22	13.7	0.585	0.002	0.002	2
23	13.7	0.621	0.042	0.024	3
24	13.7	0.720			1
25	13.7	0.676	0.136	0.079	3
26	13.7	0.656	0.046	0.033	2
31	20.5	0.674			1
32	21.55	0.668			1
Liothyrella uva.	1	0.766	0.045	0.015	9
Terebratella sanguinea	14	0.721	0.050	0.013	15
Liothyrella neozelanica	14	0.694	0.057	0.015	15
Precipitation December 2014	21.5	0.695	0.034	0.010	11
Precipitation June 2015	20.5	0.738	0.022	0.011	4
UEATHC	56	0.564	0.031	0.005	42

Table 4. 4 Shell data averaged according to each species at each temperature. Precipitation data and UEATHC mean values also included.

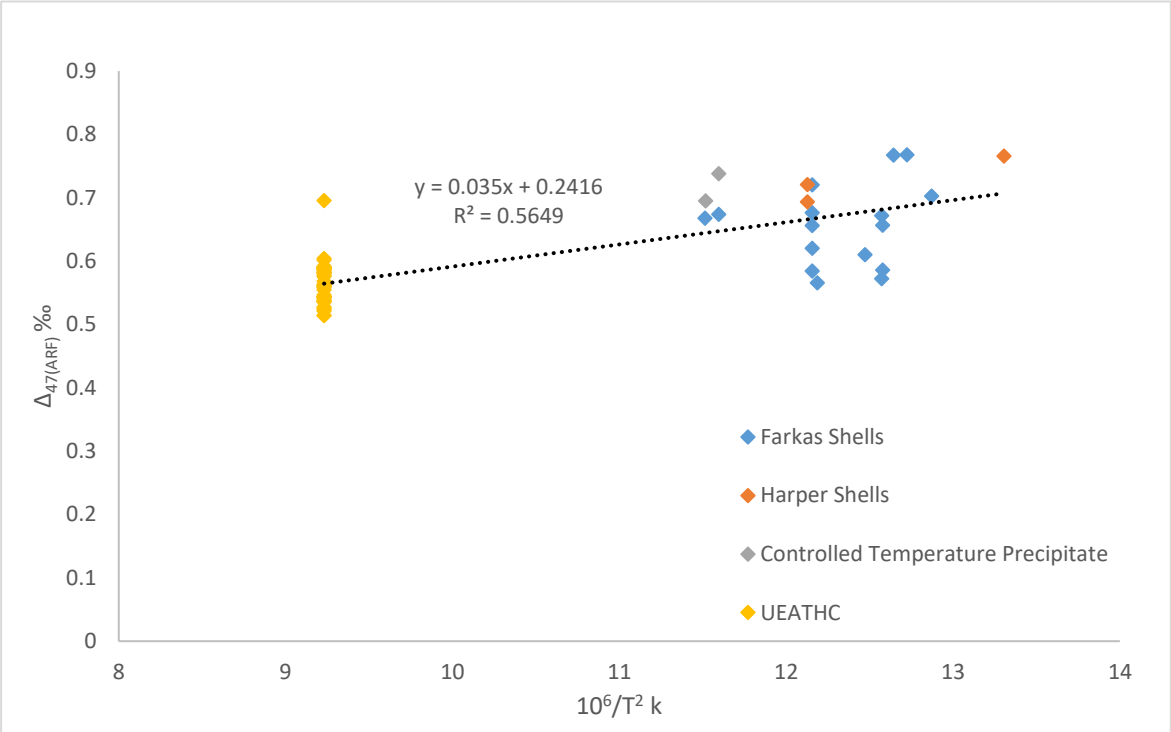

Figure 4.7 Relationship between temperature and Δ_{47} for the shells, controlled temperature precipitates and the Turkish calcite (data in Table 4.4). Linear regression errors are y = 0.035(±0.004)x +0.2416(±0.041).

4.3.6 Discussion of errors

The final linear regression (Equation 4.4) is calculated using the averaged values of the data for replicate analyses of the same species at the same temperature. The linear regression was calculated with the assumption that all of the error is on the y-axis. This is not strictly correct, because there is to a small error on the x-axis also. The temperature recorded for each shell is likely to be an average, a dominantly summer growth temperature average or a temperature taken at the time of collection that does not reflect the temperature regimes experienced by the organism during its lifetime. However, the assumption that the temperature we used is representative of the precipitation/deposition temperature is justifiable because the error on the x-axis ($10^6/T^2$) is small compared to the error on the y-axis. Figure 4.8 shows error envelopes representing 1σ and 2σ. The upper and lower limits of the error envelope are curved, which reflects the increased amount of data occurring at the point where the limits are narrowest. Further away from this area the confidence limits increase, becoming further apart.

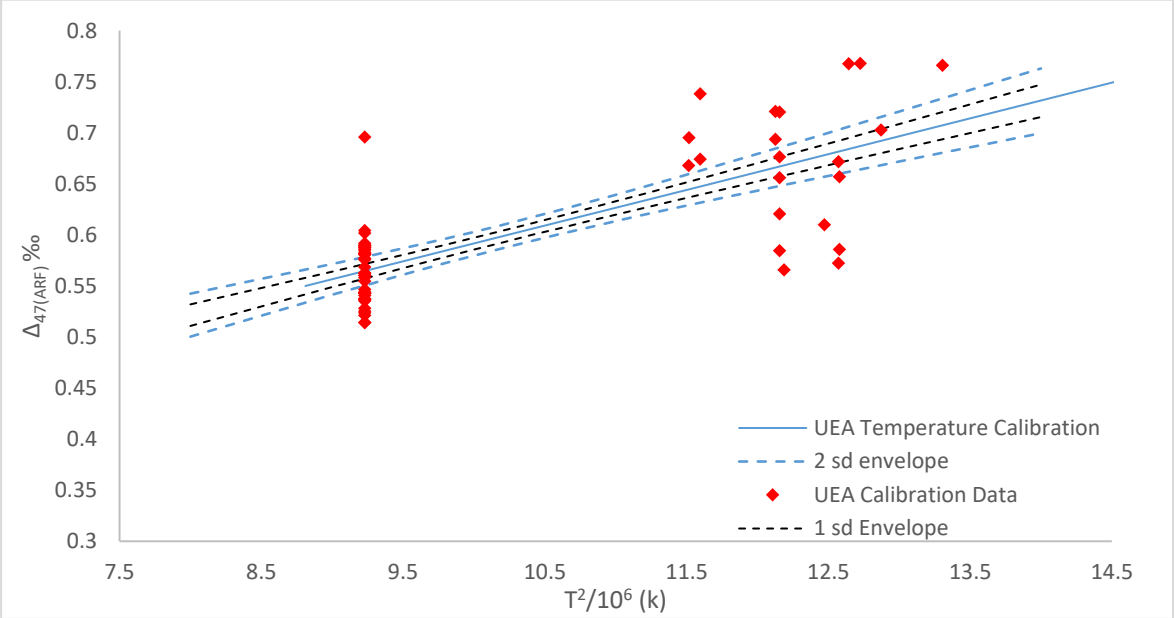

Figure 4. 8 UEA temperature calibration plus the data used to calculate it are displayed with the 68 % and 95 % confidence intervals.

Any data that falls outside of the y-axis confidence envelope is caused by random error in the measurements. Plotting the mean of these analyses minimises the effect of any anomalous results. There is still a considerable amount of the shell data lying outside of the envelopes, suggesting a poor precision and further analyses required to understand the relationship between temperature and clumped isotope value in these shells. Figure 4.9 shows the final regression line,

described by Equation 4.4, along with data used to calculate the temperature calibration. Where there is a mean value plotted (calculated from multiple analyses), the standard deviation of the mean (standard error) has been added in the form of error bars on the y-axis. Where there has been only one analysis, the mean standard deviation of the shell analyses has been added as a source for likely error bars (±0.057). Where known, the growth temperature error has also been added to the data points as error bars for the x-axis. These are only known for the inorganic precipitates and the Harper shell suite.

It is possible that systemic errors due to instrumental and sample preparation artefacts are affecting the data. I have tried to remove this by first eliminating contaminated samples using set boundaries for $\Delta_{48(wrg)}$ and $\Delta_{49(wrg)}$. A discussion of how contamination is present or can be added to a sample during its preparation is discussed in Chapter 3 (Section 3.6). The two different sets of shells used to determine the temperature calibration were analysed over two separate periods of time. The Farkas shell suite does appear to have more anomalous values, and more data points were removed from this shell set due to contamination than the Harper set. This could be due to the methods and analytical protocols on MIRA, which were not as developed or reliable at removing contamination as some of the more recent work.

The large variations in the Δ_{47} values seen in the Farkas shell suite could also be due to the material analysed. These shells were only fragments of the whole specimens and it is possible that the fragments that were ground up were not representative of the whole shell because the shell itself was heterogeneous.

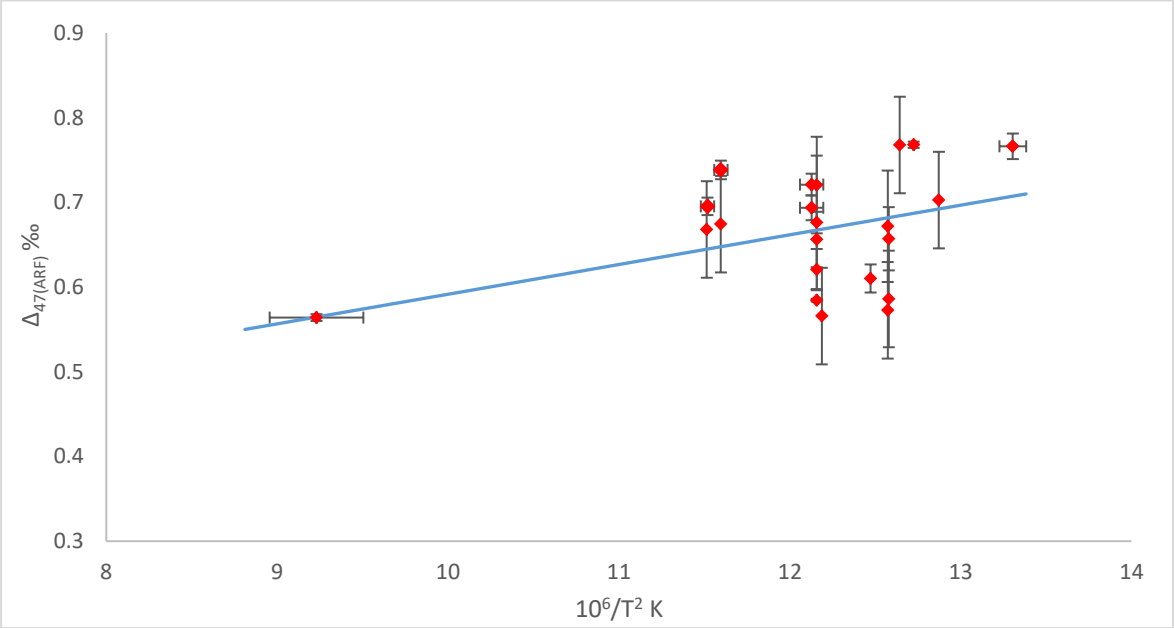

Figure 4.9 The UEA temperature calibration plotted as a blue line. The data used to calculate the linear regression is plotted in red. Errors on the y-axis reflect the measurement precision for the samples, with the average standard deviation for the shell suites shown for those shells with only one analysis. Where known, the growth or precipitation temperature error is shown on each data point (x-axis error bars).

4.4 Discussion

4.4.1 Comparison with other clumped isotope temperature calibrations

The temperature calibration developed for the UEA MIRA mass spectrometer is comparable to most other published calibrations (see Section 4.1). It agrees particularly with the theoretical temperature relationship described by Guo et al. (2009), when carbonate material is digested at 25 °C. This linear regression is derived from the polynomial Equation 18 of Guo et al. (2009), relating the temperature sensitivity and the Δ_{47} value. The theoretical calibration line is described by Equation 4.5:

$$\Delta_{47(ARF)} = \frac{3.74 \times 10^4}{T^2} + 0.2101 \qquad \text{Equation 4.5}$$

Figure 4.10 shows the UEA temperature calibration in blue, with the 95 % confidence envelope. In solid purple, the Guo et al. (2009) theoretical temperature calibration plots almost identically to the UEA temperature calibration (Equation 4.4). The temperature sensitivity of the Guo et al. (2009) calibration is within the confidence limit of the UEA calibration and its gradient and intercept are almost identical. The addition of the higher temperature material (56 °C UEATHC) pin the higher temperature end of the calibration and show that a single line can define the relationship between temperature and Δ_{47} across a range of samples and materials. As we react our samples at 25 °C, it is encouraging that the UEA calibration is identical within measurement error to the theoretical line.

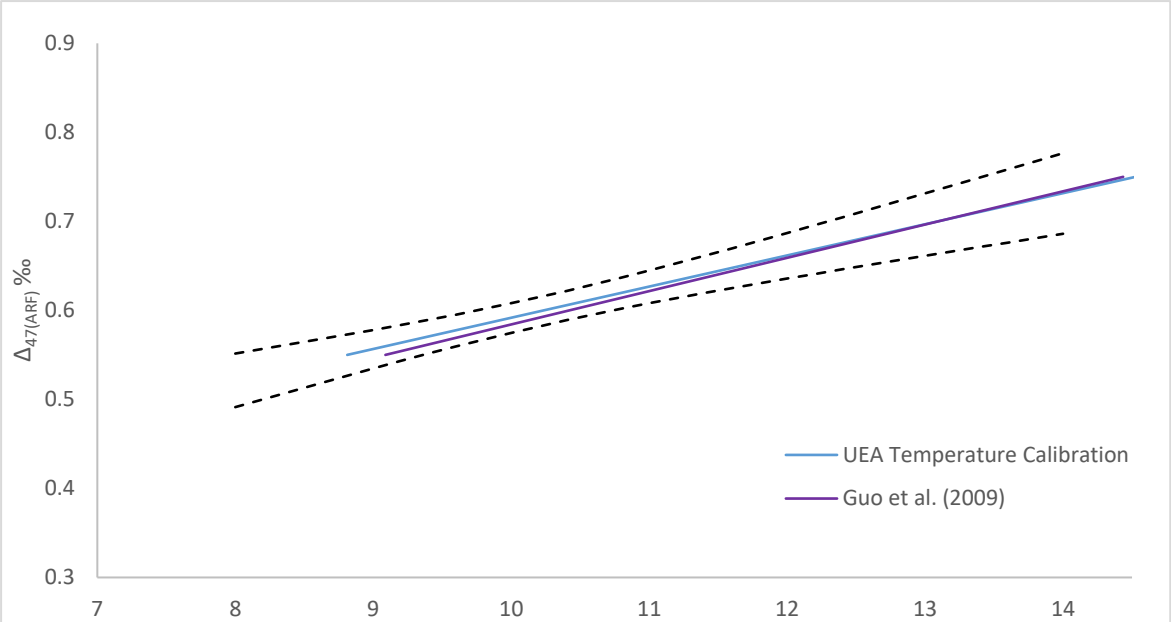

Figure 4.10 The UEA temperature calibration in blue, compared to the near identical Guo et al. (2009) regression line (purple).

The fact that the intercept determined by the Guo et al. (2009) theoretical calibration lies within our 1σ confidence envelope makes the UEA temperature calibration unique. To our knowledge, it is the only calibration line that appears to do so. The temperature calibrations published by Petrizzo et al. (2014) and Wacker et al. (2014) are regression lines with similar temperature sensitivities and intercepts to our UEA calibration (within measurement error). These linear regressions are plotted along with the UEA calibration in Figure 4.11. These two published calibration lines lie just outside the confidence intervals with a very similar slope to the UEA line. The shell only linear regression is also shown in Figure 4.11. As the two published calibrations primarily use shell and foram material, the shell-only temperature calibration is directly comparable. The errors on the UEA shell line are large, but the gradients are comparable with the published calibrations. The intercept is very different however (0.0332±0.23 compared to 0.3030±0.0308 for Wacker et al. (2014) and 0.2717±0.0734 for Petrizzo et al. (2014)). The analysis of organic material on MIRA has produced quite different results compared to the other laboratories, and the so the addition of the inorganic calcite to the temperature calibration is important at this stage. Further measurements of organic modern material, such as forams or bivalves will hopefully improve the precision of the lower temperature section of the temperature calibration.

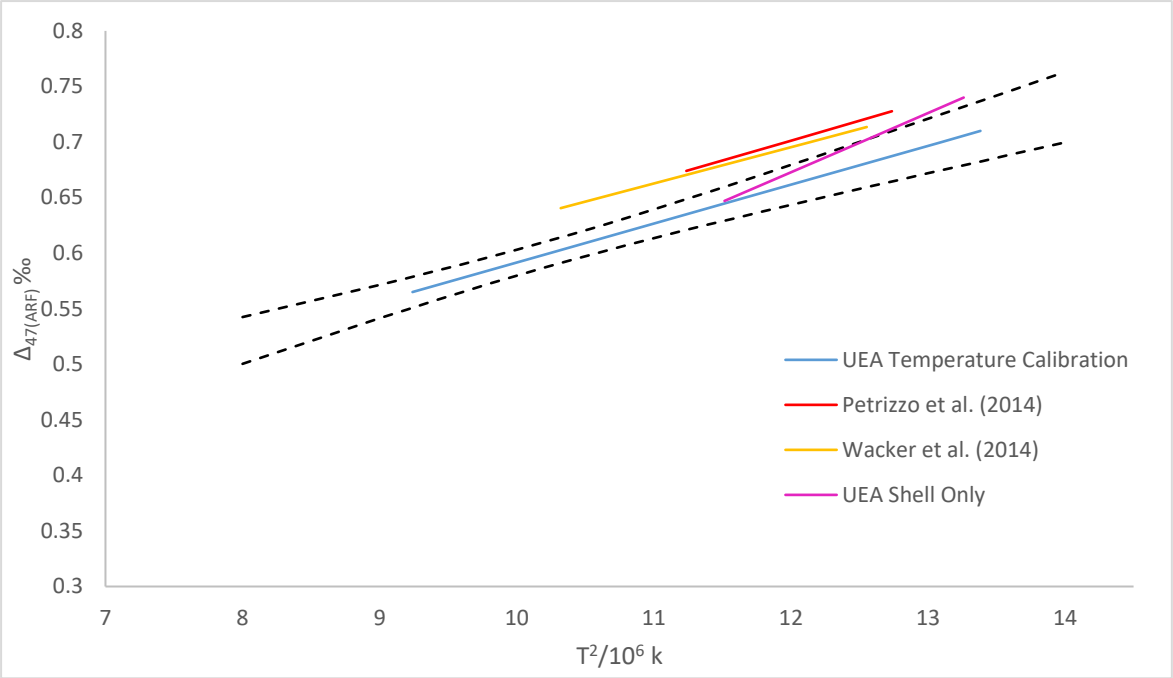

Figure 4.11 The UEA temperature calibration (blue) with the Petrizzo et al. (2014) and Wacker et al. (2014) calibrations plotting just outside the confidence envelopes. Measurement error for Petrizzo et al. (2014) is Δ_{47} = 0.0358(±0.006) x $10^2/T^2$ +0.2717(±0.0734), and for Wacker et al. (2014) is Δ_{47} = 0.0327(±0.0026) x $10^6/T^2$ +0.303(±0.0308).

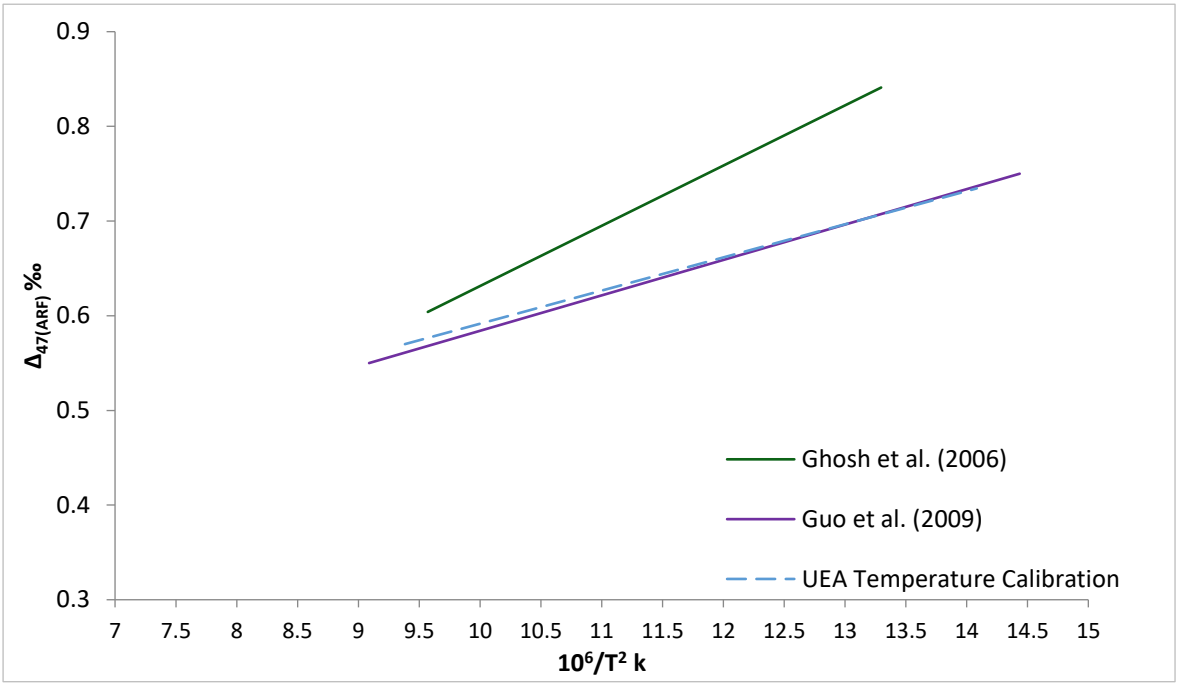

Figure 4.12 Comparison between the UEA temperature calibration, the experimental Ghosh et al. (2006) calibration and the theoretical linear regression of Guo et al. (2009).

The first experimentally determined temperature calibration line by Ghosh et al. (2006) has a much higher temperature sensitivity (gradient) than the UEA and theoretical calibration line (Guo et al. 2009). For comparison, the UEA, theoretical and Ghosh et al. (2006) temperature equations are shown altogether in Figure 4.12. The discrepancy between the steeper and shallower lines is surprising as the Ghosh et al. (2006) line was based on a combination of inorganic and biogenic material with samples reacted at 25 °C, a similar method to UEA. However, they completed the calibration using coral material, which has been subject to much debate, as some recent work suggests that some corals do not precipitate aragonite in equilibrium conditions (Ghosh et al. 2006; Eiler 2011). This could be a reason for the differences between the calibrations.

All of the published clumped isotope temperature calibrations are shown in Figures 4.13 and 4.14. Because of the numerous published calibrations, they have been split into two groups. Figure 4.13 shows those that were based on material which was reacted at 25 °C, and Figure 4.14 shows those based on reactions conducted at 70 °C or above. The UEA temperature calibration and the theoretical 25 °C calibration (Guo et al. 2009) are also plotted on both graphs for reference. The linear regression equations and the material type for each of the plotted calibrations are listed in Table 4.1. Both graphs show a variety of different gradients, with some steeper and shallower ones present in both groups.

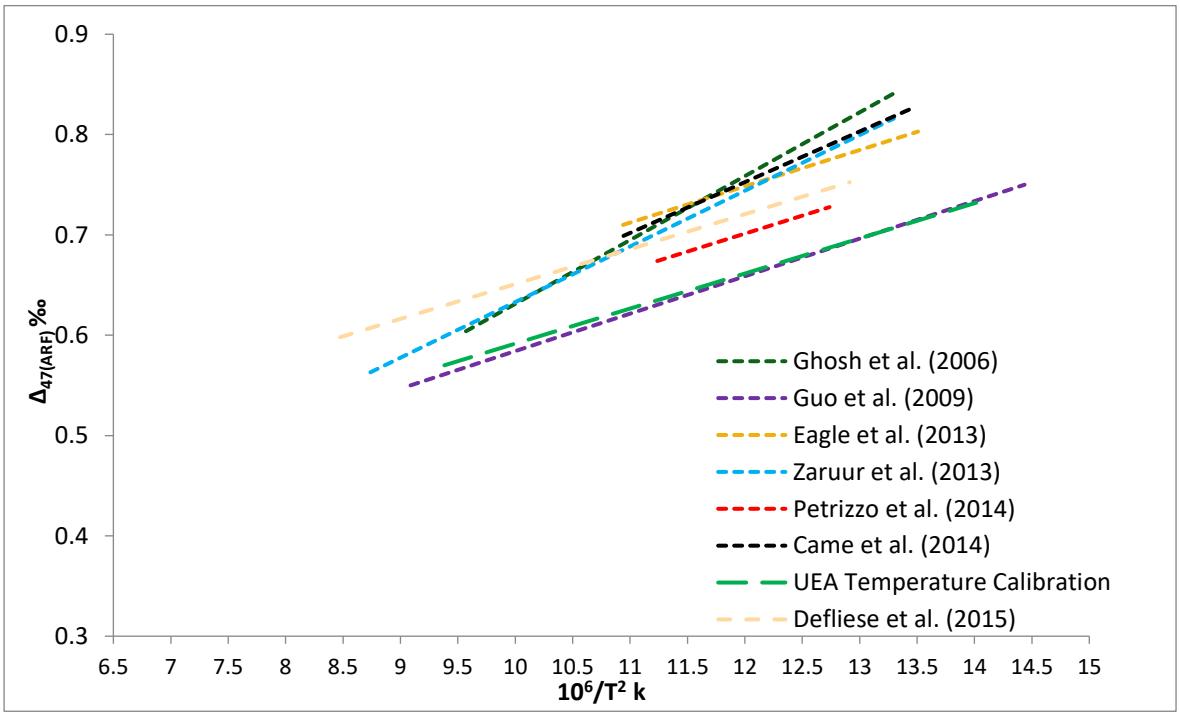

Figure 4.13 Published clumped isotope temperature calibrations for carbonate material reacted at 25 °C.

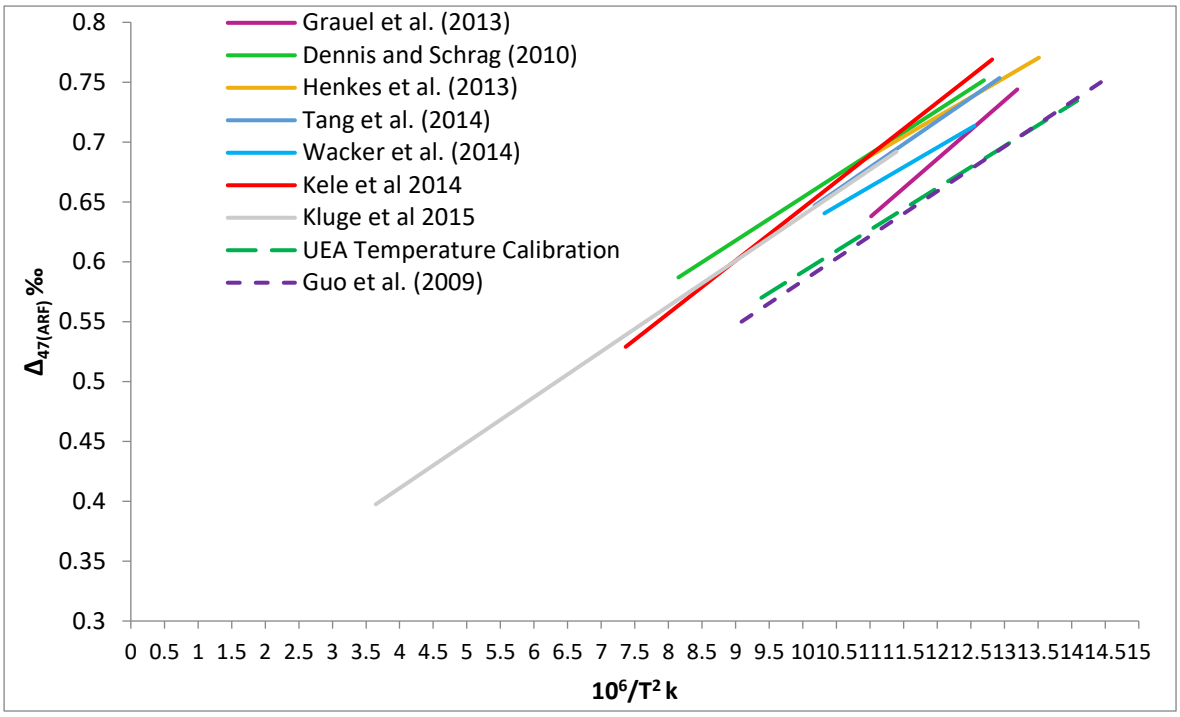

Figure 4.14 Published clumped isotope temperature calibrations for carbonate material reacted at 70 °C or above.

As mentioned above, the UEA calibration is most similar to the calibrations published by Petrizzo et al. (2014) and Wacker et al. (2014). These show gradients of a similar value to the UEA calibration, but are offset towards higher Δ_{47} values which raises the intercept. It is interesting to note that these two calibrations were produced by sample reactions at different temperatures. Wacker et al. (2014) react their samples at 90°C and the calibration is based on a combination of biogenic material (ostrich egg shell, brachiopod and bivalve shells and foraminifera) and inorganic (cold seep) material. Petrizzo et al. (2014) reacted samples at 25°C and used only bivalve shells. This does suggest that reaction temperature may not be the dominant cause of varying calibrations. The fact that these two calibrations are the most similar to the UEA calibration, and similar to each other, suggests that calibrations made only of biogenic material can be comparable to calibrations made of both biogenic and inorganic.

The other temperature calibrations all vary in gradient compared to the UEA calibration and the Guo et al. (2009) theoretical line. Defliese et al. (2015), Eagle et al. (2013), Henkes et al. (2013), Wacker et al. (2014) and Petrizzo et al. (2014) all have gradients that are shallower than the UEA temperature calibration (within measurement error) but are offset to higher Δ_{47} values. This appears to be the case regardless of reaction temperature. The other published calibration lines plotted in Figures 4.13 and 4.14 all have steeper gradients, as well as being offset to higher Δ_{47} values.

4.4.2 Identifying the source of discrepant calibrations

As outlined in section 1.1, the reasons behind the varying temperature calibrations is currently under debate. A discussion of possible causes is given below.

4.4.2.1 Differences in scaling and correction of data

As outlined in Section 4.1.1.1, the current community view is that differences between calibrations are too large to be caused by corrections or projection onto the absolute reference frame. Once projected onto the absolute reference frame (Dennis et al. 2011) there are still clear differences between all published calibrations. A key difference between the temperature calibration on MIRA and those produced on other mass spectrometers is that we do not need to correct for measurement artefacts such as non-linearity, which may be why its calibration is so similar to the theoretical 25 °C calibration line and lower in temperature sensitivity than many of the calibration lines (Chapter 2 Section 2.5.1.2). The majority of other laboratories use the Thermo Finnegan MAT 253 mass spectrometer, which produces data that requires additional corrections. There are a variety of methods employed to correct for non-linearity, which have the potential to cause variations between instruments. Whilst this is not the key reason for varying temperature calibrations, it has the potential to be contributing to the problem.

4.4.2.2 Partial re-equilibration

Water is a serious problem to clumped isotope measurements. It is created as a by-product of the ortho-phosphoric digestion of the sample calcium carbonate. Section 4.1.1.3 of this chapter outlines some of the possible ways water is able to re-equilibrate with the product carbon dioxide. Water is present within the system at a high vapour pressure, making it more likely to equilibrate with the CO_2. Defliese et al. (2015) also note that vapour pressure increases when the acid is under a higher temperature (90 °C) when compared to the pressure at 25 °C. If re-equilibration does occur, it would change the slope of the linear regression. The high temperature end would be most affected as it is furthest from the room temperature equilibration with the water. There would be a rotation of the line around a low temperature point, with a reduction of the gradient. This is why it is essential to fully remove water during the sample gas cleaning procedure.

All of the published temperature calibrations show variation in gradients. However, only a few show a shallower gradient than the theoretical 25 °C digestion temperature calibration line of Guo et al. (2009). Therefore, it is likely there are other factors causing the calibration lines to rotate to a steeper gradient. This reduction in gradient does not appear to affect the UEA temperature calibration.

4.4.2.3 Contaminated materials

As stated in Section 4.1.1.5, there is limited discussion regarding the effects of contamination on clumped isotopic measurements. Huntington et al. (2009) state that Δ_{48} and Δ_{49} can be monitored as indicators of contamination. We have also used both mass-48 and 49 signals to identify contaminated samples in our data set. For a full outline on contamination effects see Chapters 2 and 3, Sections 2.3.6 and 3.6.

Figure 4.15 shows the effects of removal of contaminated samples on the linear regression defined at UEA. The graph shows three different linear regressions applied using the Microsoft Excel function. The three datasets corresponding to each linear regression are also plotted on the graph. This dataset uses all of the measurements, including those with $\Delta_{48(wrg)}$ and $\Delta_{49(wrg)}$ values considered to be contaminated. Equation 4.6 describes this regression:

$$\Delta_{47(ARF)} = \frac{4.29\times10^4}{T^2} + 0.1862 \qquad \text{Equation 4.6}$$

When limits are placed on $\Delta_{49(wrg)}$ values to define contaminated samples, there is a rotation in the linear regression. An initial $\Delta_{49(wrg)}$ limit of 200 ‰ was applied to the data as the upper limit for non-contaminated measurements. This dataset is plotted in green, showing some of the higher Δ_{47} values were removed as a consequence. The linear regression describing the relationship between temperature and Δ_{47} is represented by Equation 4.7 below. This regression varies only slightly from the initial one using all measurements.

$$\Delta_{47(ARF)} = \frac{4.28\times10^4}{T^2} + 0.1814 \qquad \text{Equation 4.7}$$

Finally, a value of 100 ‰ for $\Delta_{49(wrg)}$ was used as a limit to define a contamination limit. If a sample showed a value of less than 100 ‰ it was retained in the dataset. This data is potted in red on Figure 4.15, and its respective linear regression is also plotted as a red line. The equation describing this regression is represented by Equation 4.8:

$$\Delta_{47(ARF)} = \frac{3.13\times10^4}{T^2} + 0.3127 \qquad \text{Equation 4.8}$$

The line representing Equation 4.8 on the plot shows a larger rotation towards a shallower gradient. Many of the values showing a high $\Delta_{47(ARF)}$ have been removed from the dataset. These

high $\Delta_{47(ARF)}$ values are caused by contamination remaining in the sample after the cleaning process, and altering the mass-47 signal within the mass spectrometer during analysis. This is a likely possible reason for why many calibration lines have a much steeper gradient than the temperature calibration at UEA.

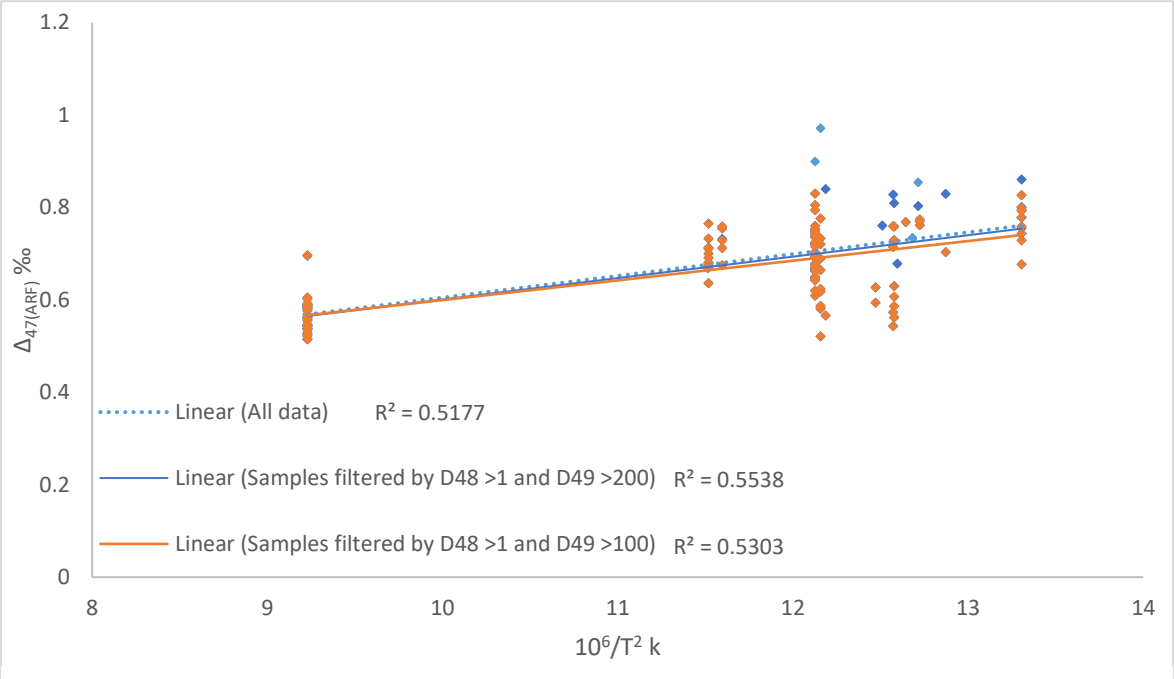

Figure 4.15 All data; both shell datasets, the controlled temperature precipitate and the 56 °C Turkish calcite, and linear regression for this data is the solid blue line. The dashed blue line indicates the linear regression between temperature and Δ47 when the most outlying data points were removed ($\Delta_{49(wrg)}$ >200 ‰). This equation is very similar to the regression describing all data. The orange line represents the linear regression when there is more stringent removal of contaminated data points and describes the red data points.

Contamination appears to have a greater effect than has been previously identified. Few publications state information about their Δ_{48} and Δ_{49} values, criteria used to identify contaminated material, or criteria for rejection of values. Huntington et al. (2009) suggest that samples having a value greater than 2 ‰ on Δ_{48} is representative of contamination. When compared with my data, this limit does not appear to be stringent enough (in the UEA data, samples with a $\Delta_{48(wrg)}$ greater than 1 ‰ were removed). Contamination of samples is likely to be caused by inadequate sample preparation and cleaning (see Chapter 3, section 3.6 for a full discussion). Interestingly, for pure inorganic samples such as Carrara marble, most labs produce values that are very similar (see Chapter 3 Section 3.8.1.1 for a table summarising these values). The calibration published by Ghosh et al. (2006) was entirely made up of synthetic calcite (likely to have the least contamination), and yet this is the steepest temperature calibration. This could suggest that contamination is not the entire cause of variation between calibrations, although none of the samples were measured more

than once (Zaarur et al., 2013). However, for the majority of the temperature calibrations some biogenic material was used, which will contain organic contaminants. It is the analysis of these samples that shows results that vary significantly between the labs. This is likely to be a cause of the variation between temperature calibrations.

4.4.3.2 *Is the controlled temperature precipitation in equilibrium?*

The averaged fluid compositions for the two controlled temperature precipitation experiments have been calculated using Equation 4.9:

$$1000 ln\alpha(calcite\text{-}water) = 18.03(10^3 T^{-1}) - 32.42 \quad \text{Equation 4.9}$$

This equation was derived by Kim and O'Neil (1997) and describes the oxygen fractionation between water and calcite at low temperatures. The $\delta^{18}O_{fluid}$ was calculated twice, once from the precipitation temperature measured in the lab and once from the temperature retrieved from the Δ_{47} value. These values are shown in Table 4.5. The values calculated from the known controlled temperature around 20 °C are similar, whereas the fluid value calculated from the Δ_{47} derived temperature are very different for the two experiments. This difference seems unrealistic and could be a product of anomalous Δ_{47} values. For example, a change in Δ_{47} of 0.05 ‰ can change the Δ_{47} derived fluid oxygen isotope value by nearly 3 ‰. The mean Δ_{47} for each precipitate is 0.695 ‰ and 0.738 ‰, with a standard error of the mean for each of ± 0.01 ‰. These two Δ_{47} values are within 0.043 ‰ of each other, therefore we would expect to see a variation of no more than 3 ‰ for the fluid oxygen isotope values derived from the clumped isotope temperatures. The variation in these clumped isotope fluid values seen in Table 4.6 is 3.63 ‰, which is larger than expected variation. This suggests that anomalous Δ_{47} values are not completely responsible for the variation in fluid isotopes.

Precipitation Experiment	**Temperature °C**	**$\delta^{18}O_{fluid}$ expected**	**$\delta^{18}O_{fluid}$ from Δ_{47} Temperature**	**Measured $\delta^{18}O_{fluid}$**
December 2014	21.5	-6.66	-10.21	Not Measured
June 2015	20.5	-7.67	-13.84	-7.17

Table 4.5 Calculated fluid isotopes for the controlled temperature precipitates. For June 2015 precipitate, the oxygen isotope composition of the fluid was also measured.

A selection of samples of the fluid from which the second inorganic precipitate (June 2015) was produced were directly analysed to determine their $\delta^{18}O_{fluid}$ value. This was completed on a Picarro CDRS analyser. The average value for the direct measurement of $^{18}O_{fluid}$ vs VSMOW was -7.17 ‰, which is very close to the Norwich tap water value, -7.2 ‰. This measured value is also very close to the value calculated using the measured room temperature combined with the measured $\delta^{18}O_{calcie}$ for this precipitate ($\delta^{18}O_{fluid}$ = -7.67 ‰). This suggests that the precipitation was completed in equilibrium.

Using the measured fluid isotope value for the June 2015 precipitate (-7.17 ‰) combined with the measured $\delta^{18}O_{calcite}$ it is possible to calculate the value for alpha (α) using Equation 4.9. The value calculated for *1000ln*α is 28.47. When this value is plotted on the same graph as the Kim & O'Neil (1997) equilibrium calibration, it plots below the line (Fig. 4.16). Kim & O'Neil (1997) produced calcium carbonate at a greater rate, by bubbling nitrogen gas through a supersaturated bicarbonate solution and took only 1-5 days to produce carbonate material. The calcite equilibrium line in Figure 4.16 was therefore produced by precipitating calcite in very different conditions, yet the *1000ln*α value calculated from the experiments in this study is very similar to the expected value.

The *1000ln*α value identified by Coplen (2007) is also displayed in Figure 4.16. This was derived from measuring the calcite from the Devils Hole cave in Nevada. They also measured the groundwater $\delta^{18}O$ value, which when combined with the calcite oxygen isotope value shows a *1000ln*α value of 28.09. They extrapolated a temperature calibration line from this point, which is displayed on the graph. This alpha value and calibration line is significantly different from the Kim and O'Neil (1997) line, and the analysis of the fluid oxygen isotopic value of the June precipitation plots away from the line. This would suggest that the precipitation is not in equilibrium. The Coplen (2007) study analysed material from within a natural system, whereas the Kim and O'Neil (1997) study used inorganic precipitates. The difference between the two calibrations could suggest that one of the systems is not in equilibrium.

It has already been discussed that the clumped isotopic value measured from inorganic precipitation can be in equilibrium with the fluid whilst the oxygen isotopes are not, raising the question that perhaps not all inorganic laboratory precipitated calcites are in equilibrium with their fluid, whilst natural systems may well be. The calcite from the Devils Hole cave was found to have a Δ_{47} derived temperature of 30.6 °C when measured by Kluge et al. (2014). They found that this formation temperature was consistent with their measured modern groundwater temperature of 32.8-34.3 °C. The similarity between the Δ_{47} derived temperature and the measured temperature suggests that the calcite was precipitated in equilibrium with the formation fluid, therefore

supporting the study by Coplen (2007), which concluded that laboratory precipitates may not be in equilibrium. Both studies suggest that the fractionation factor between calcite and water may need to be re-evaluated, as they are based on laboratory precipitates shown to be in disequilibrium. The alpha value calculated in this study is more similar to the laboratory precipitates of Kim & O'Neil (1997) than the natural system of Coplen (2007). Therefore, it is likely that this material has not precipitated in oxygen isotope equilibrium.

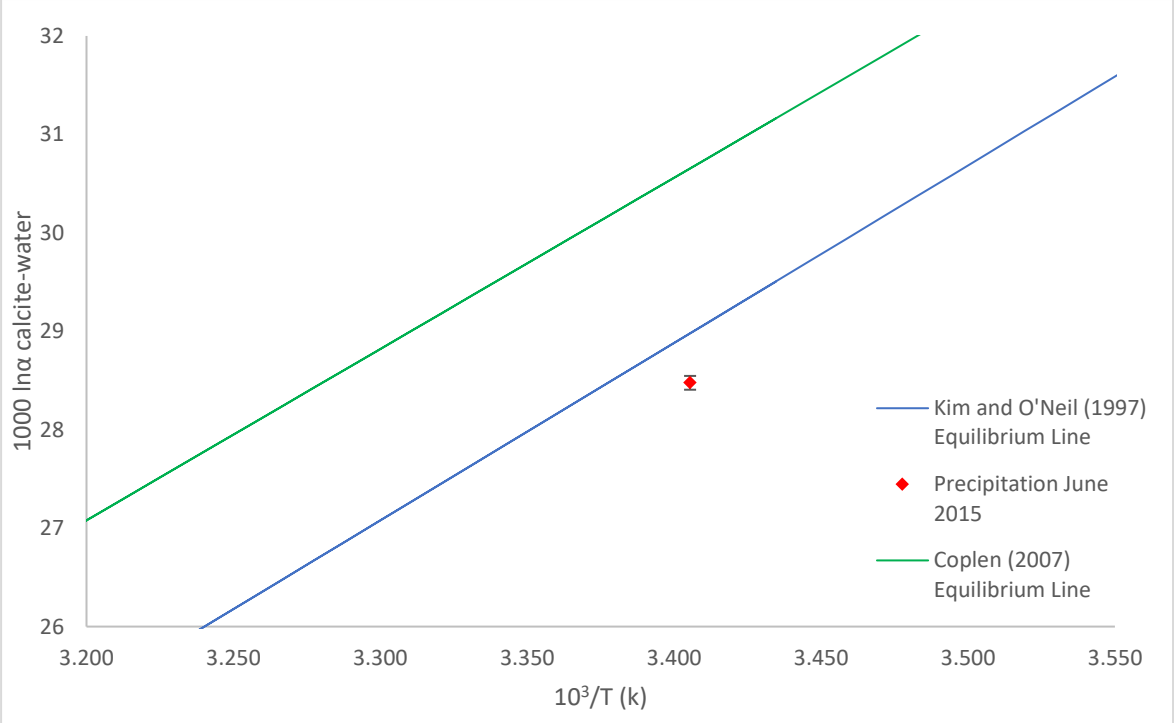

Figure 4.16 The 1000lnα value calculated for the June 2015 precipitate is shown as a red datum on the graph. The blue line represents the Kim and O'Neil (1997) equilibrium calibration line for calcite and water. The green line is the extrapolated line defined by Coplen (2007) based on the 1000lnα *calculated from the calcite Devils Hole Cave, Nevada.*

As discussed in Section 4.1.2.1, it is possible that the clumped isotopic value can be in equilibrium with the fluid whilst the oxygen isotopes show disequilibrium. This is true for very slow precipitation (such as natural cave calcite). When rapid precipitation occurs it is highly likely that both the clumped isotopes and oxygen isotopes will be in disequilibrium with the fluid (Tripati et al. 2015). For laboratory precipitated calcites precipitated more rapidly than natural calcite, this means that the pH at which calcite has precipitated could affect the isotopic composition. Tang et al. (2014) found that clumped isotopes are less likely to be affected by pH if the range of pH is kept low, ideally less than pH 9. The two controlled temperature precipitation experiments were kept to low pH values. The December 2014 experiment had an average pH of 8.13, and the June 2015 experiment had an average pH of 8.69. These pH measurements were made at least once every other day using an in situ pH meter. Maintaining a pH value below 9 but within a narrow range

ensures that the clumped isotope value of the calcite is likely in equilibrium with the fluid from which it precipitated. However, in light of how far away the fractionation factor of the temperature controlled laboratory precipitate is from the natural calcite at Devils Hole, it would seem that the oxygen isotopes are not in equilibrium. It is still uncertain as to whether the clumped isotopes are in equilibrium or not, as they have shown to be independent of changes in solution chemistry if they are precipitated slowly enough and at pH values under 9.0.

4.5 Conclusion

From the number of published temperature calibrations, and the fact that a clear reason for differences between them is still uncertain, the clumped isotope community is currently in the position of needing a local temperature calibration for each lab, rather than one single linear regression. For example, a clumped isotope value of 0.6 ‰ would identify a temperature range of 28 °C to 69 °C when a selection of the different calibrations is used. For geological material, there is no reason why each individual calibration cannot produce reasonable temperatures within its local laboratory.

The UEA temperature calibration presented in this chapter is produced from analysis of shell material and inorganic high and low temperature precipitates grown at known temperatures. The calibration is similar to the theoretical, 25 °C digestion linear regression calculated by Guo et al. (2009). It also shows that one single equation can describe the relationship between temperature and clumped isotope composition, for temperatures between 0 °C and 56 °C.

In Section 4.4, there is a discussion about what could be the cause for the discrepancies between the different temperature calibrations. If the differences were caused by different reaction temperatures and inadequate understanding of different fractionation factors, we should see similar gradients with vertical intercept differences. This is not the case, as we see a variety of gradients and intercepts. If the dominant cause was re-equilibration particularly occurring at higher reaction temperatures due to high water vapour pressures, we should see the different temperature calibrations rotating around the higher temperature end and increasing the gradients. Again, we see a variety of gradient changes, both shallower and steeper gradients, whilst the majority of labs get similar values for high temperature calcites such as Carrara Marble (see Chapter 3 section 3.8.1.1 and Table 3.3). The projection of clumped isotope data onto the absolute reference frame removes the possibility of mass spectrometer analytical artefacts producing these discrepancies. This includes correcting for non-linearity and scale compression issues that many instruments suffer from.

The remaining likely possibility for the discrepant calibrations is inadequate cleaning of sample CO_2 during the preparation process. This would allow contaminants within the system to interfere with the mass-47 signal during measurement and therefore alter the Δ_{47} value. The offline preparation system at UEA is outlined in Chapter 3, and can produce ultra-pure CO_2. This is a likely reason for the UEA temperature calibration being so close to the theoretically predicted calibration. The fact that many laboratories retrieve the same value for standards such as Carrara Marble could be because this is a carbonate that is already essentially free from contaminants. Biogenic material is much more likely to have contaminants, meaning that the variation of values between laboratories is due to the variation in ability to completely remove these contaminants. Future work requires investigation into the effects of different types of contaminants, and ideally improvements in CO_2 purification systems to ensure they are successfully removed.

Chapter 5 - Anticosti Island study

5.1 Introduction

The rationale behind this study was the application of the clumped isotope technique to try and resolve palaeoenvironmental temperatures and wider conditions from fossils and limestone that formed during glacial to interglacial changes. The end-Ordovician Hirnantian glaciation was identified for this (Fig. 5.1). This global glaciation is still not fully understood in terms of the conditions at the Earth's surface during the glaciation or the extent and sequencing of the glacial cycles. Outcrops that record this event are widespread, including Dobb's Linn (Scotland) (Underwood et al. 1997), Anticosti Island (Canada) (Desrochers et al. 2010), the East Baltic region (including locations in Estonia and Latvia) (e.g. Brenchley et al. 2003) and the Anti-Atlas of Morocco (Loi et al. 2010) are perhaps the best studied. These sites cover both high and low palaeolatitudes and are correlated using chemostratigraphy, particularly a global carbon isotope excursion (Ghienne et al., 2014), and in some cases biostratigraphy; there are however, challenges remaining in order to correlate between near-field and far-field sites.

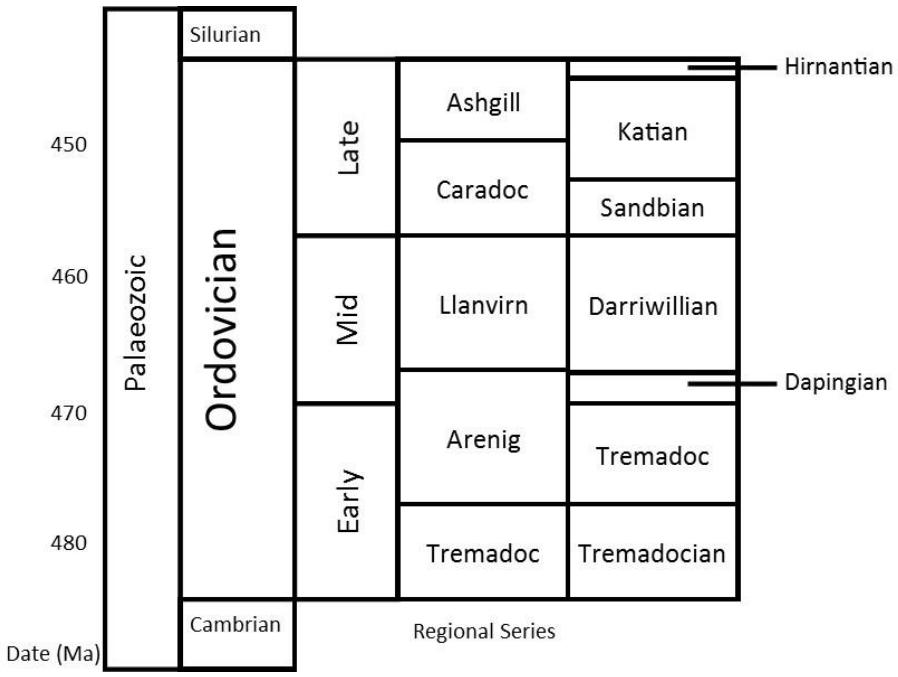

Figure 5.1 Stratigraphic column outlining the different stratigraphic nomenclature, comparing the UK stratigraphy (regional series) with global stages. Re-drawn from BGS online support material.

The global carbon isotope excursion is recorded in marine carbonate sediments and skeletons, caused by major changes in the carbon cycle during the onset of the glaciation (Brenchley

et al. 2003). The excursion presents as a positive shift in the $\delta^{13}C$, and is often accompanied by a simultaneous positive excursion in $\delta^{18}O$. There has been debate as to how extensive the global ice volume was during the end-Ordovician glaciation, with some workers identifying a similarity between the Hirnantian glaciation, and the extent and style of the end-Cenozoic glaciation extent and style (Finnegan et al. 2011; Ghienne et al. 2014). It has been speculated that the ice sheet volume is comparable or greater to that of the Last Glacial Maximum (LGM) (Finnegan et al. 2011). The maximum volume of the Laurentide ice sheet during the Last Glacial Maximum was around $37x10^6$ km^3 (Licciardi et al. 1998). If the hypotheses proposed by Le Heron & Dowdeswell (2009) are used, it is likely that the Hirnantian ice reached a latitude of 60 °S (Sheehan 2001). Le Heron & Dowdeswell (2009) calculated the size of the ice sheet over Northern Gondwana and if the hypothesis of three smaller ice sheets is used, the total ice volume is $27.45x10^6$ km^3, smaller than the ice coverage during the LGM. If just one large ice-sheet was present, the calculated ice volume is $257.4x10^6$ km^3 and would yield a much greater extent of ice than during the LGM. There is thus a possibility that the end-Ordovician glacial ice volume was comparable to the ice volume of the LGM, meaning that the lower latitudinal seawater temperature changes could be comparable. Clumped isotopes have the potential to identify a temperature signal, and, when combined with carbonate $\delta^{18}O$, help to decouple temperature changes from ice volume changes.

This chapter focuses on end-Ordovician sedimentary rocks on Anticosti Island located in the Gulf of Saint Lawrence (Fig. 5.2). The rocks here are interbedded limestone and shales with abundant fossil material. The sedimentary sequence spans from approximately 455 Ma to 428 Ma, including the Hirnantian globally significant glacial episode (for example, Desrochers et al. (2010)). These end-Ordovician sediments were deposited in shallow tropical seawater at an inferred palaeolatitude of 10-15 °S along the eastern margin of Laurentia (Achab et al. 2011 and references therein). The Anticosti limestone and fossils thus have the potential to record low latitude temperature and seawater isotopic composition variations caused by ice volume changes during glacial episodes. The sequence is well suited to test the viability of the clumped isotope technique on geological sequences. Previous clumped isotope studies presented data that identifies excursions in $\delta^{18}O_{carb}$, $\delta^{18}O_{fluid}$ and in the Δ_{47} derived temperature (Finnegan et al. 2011) from which they calculated warm tropical ocean temperatures except for a cooling event during the final glacial event of the Hirnantian.

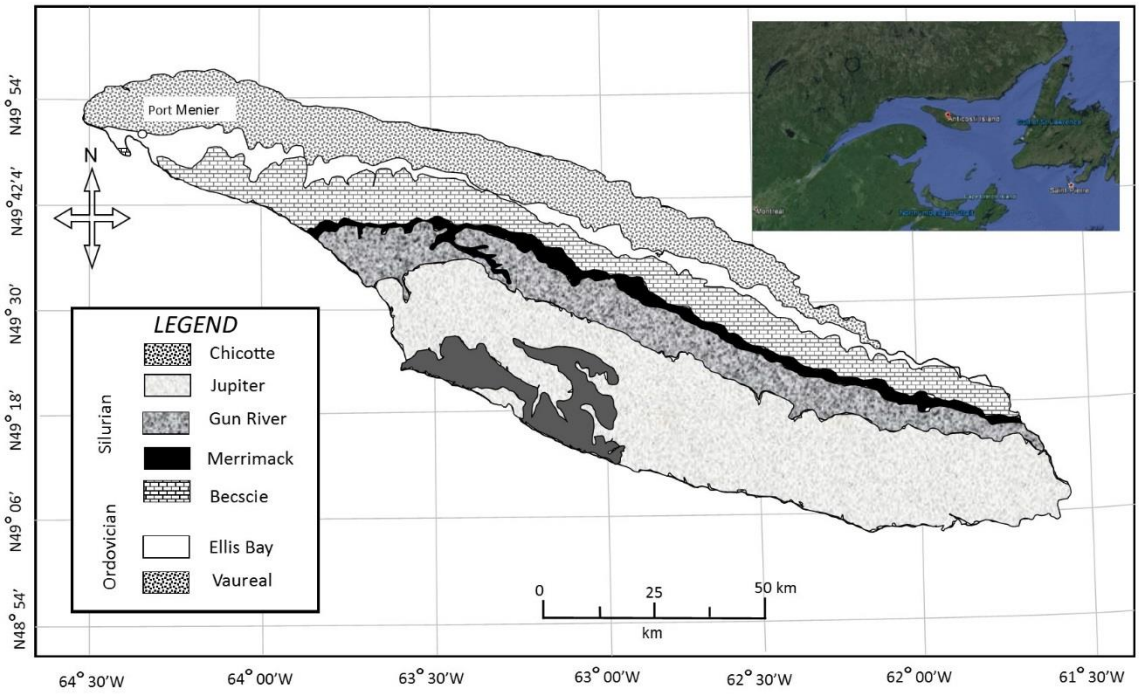

Figure 5.2 Schematic of Anticosti Island and its geological sequence. Inset map indicates location within the Gulf of St. Lawrence. Geological map based on Desrochers and Gauthier (2009) (Carte géologique de l'ile d'Anticosti), inset from GoogleEarth.

5.1.1 Geological Setting

The Anticosti Island sedimentary sequence represents the onshore part of the Anticosti Basin (Achab et al. 2011), and forms the eastern section of the St. Lawrence Platform (Chi et al. 2010; Bordet et al. 2010; Achab et al. 2011; Desrochers et al. 2012), moving to between 15° and 20° south during the Early Silurian (Desrochers 2006). The St. Lawrence Platform developed along the Laurentian continental margin, and the Anticosti Basin contains two broad sedimentary packages. These include a Cambrian to Lower Ordovician passive margin succession, and a Middle Ordovician to Lower Devonian foreland basin succession (Desrochers et al. 2012). Foreland basin development was simultaneous with the onset of Taconian accretion, finishing as a successor basin after the Taconian thrusts were emplaced southward during the final stages of the Taconian orogeny (closure of the Iapetus Ocean). However the succession on Anticosti is little affected by the stresses of the Taconian Orogeny (Achab et al. 2011; Desrochers et al. 2012 and references therein) and only records minor stresses of the Acadian Orogeny (Bordet et al. 2010; Desrochers et al. 2012). To the north, the oldest basin sediments (the Lower Ordovician Romaine Formation) lies directly on the

Pre-Cambrian basement (Chi et al. 2010). To the southwest and southeast the basin meets thrusted material of the Appalachian Orogeny (Desrochers et al. 2012).

The eastern section of the Anticosti basin lies underwater off the coast of Newfoundland, but is thought to preserve Lower Cambrian to Devonian sediments (Desrochers et al. 2012). The western section of the basin is also mostly underwater, but the subaerial section forms Anticosti Island, along with the Mingan Islands and their adjacent mainland. Here strata from Lower Ordovician to Upper Silurian is preserved (Fig. 5.2) and it is possible sedimentation continued into the Middle Devonian (Bordet et al. 2010).

The Anticosti Island strata comprise shallow water, storm-dominated carbonate ramp deposits outcropping along a 200km section dipping slightly to the southwest. (Achab et al. 2011; Desrochers et al. 2010). All samples in this study come from the north-western edge of the island (Anse aux Fraises to Pointe Laframboise), which comprises tropical storm-dominated offshore carbonate facies (Desrochers et al. 2010). Back-stripping models (Long 2007) suggest peak subsidence rates occurred during deposition of the Katian Vauréal Formation (17.9 cm/ka), which then slowed to less than 1 cm/ka during deposition of the Hirnantian Ellis Bay Formation. Subsidence remained low, dropping to 0.2 cm/ka during the deposition of the Silurian Chicotte Formation. However, there is a disconformity due to rapid sea level fall above the base of Chicotte Formation that makes this estimate less certain. Subsidence was caused by sediment loading, tectonic loading from thrust sheet emplacement and thermal subsidence (Long 2007). This long subsidence history allowed for more or less continuous deposition (Ghienne et al. 2014; Long 2007).

Anticosti Basin strata shows little evidence of serious tectonic deformation (Chi et al. 2010 and references therein). Seismic surveys reveal some faulting, but only within the lower Ordovician section, while fracture sets are present in the Lower Silurian rocks (Bordet et al. 2010; Pinet et al. 2012; Chi et al. 2010 and references therein). These features are probably caused by the Appalachian Orogeny, or by younger structural events (Bordet et al. 2010). Exploratory wells show the Anticosti section was at least 3.85 km thick (Pinet et al. 2012) although there is some debate as to how thick the succession may have been before erosion (discussed in Section 5.1.7).

5.1.2 Anticosti stratigraphy

Work on the Ordovician of Anticosti Island has been ongoing since the Geological Survey of Canada first mapped the island (Richardson (1857), Billings (1857)). The first formal lithostratigraphic names were proposed by Schuchert and Twenhofel (1910), based on coastal exposures. Further stratigraphic refinement and mapping of the island interior followed (Twenhofel, 1921 and 1928) including formal recognition of the Ellis Bay formation and its 10

informal members. Twenhofel also defined an Ordovician-Silurian boundary at the then contact between the Ellis Bay and Becscie Formations (Achab et al. 2011). This lithostratigraphy was the basis for Bolton (1961, 1970,1972) and Copeland (1970, 1973, 1974) to further refine correlation with biostratigraphy (Sami & Desrochers 1992). Bolton's work divided the Ellis Bay Formation into fewer members, but maintained the position of the Ordovician-Silurian boundary (Achab et al. 2011).

Placement of the Ordovician-Silurian boundary has been in contention for many years, and correlating between the eastern and western ends of the island has also proven difficult. Work by Petryk (1979, 1981) re-defined the boundary between the Ellis Bay and Becscie Formations, recognising a distinctive oncolite bed and coral bioherm complex as a single member called the Laframboise Member by Long and Copper (1987). They correlated their eastern Island formations with the work of Bolton and Petryk from the western end (Achab et al. 2011). Changes in brachiopod communities at the eastern end of the island helped identify sea level fluctuations (Johnson et al., 1981) and further biostratigraphic work has aided both internal and global correlations (Sami & Desrochers 1992).

Copper (2001) used graptolite faunas to help position the Anticosti succession in its global stratigraphic context, and to identify the timings of mass extinctions. The Ellis Bay Formation was shown to be Hirnantian due to clear, post-Richmondian fauna and the disappearance of Hirnantian fauna was used by Copper (2001) to define the stratigraphic position of the Ordovician/Silurian boundary. Ordovician corals and brachiopods are missing from the Becscie Formation, confirming its Silurian age (Copper 2001). Graptolite biostratigraphy requires further refinement whilst brachiopod biostratigraphy has produced opposing views as to whether the Hirnantian is represented by the whole Ellis Bay Formation or just its upper part. A new stratigraphic framework using chitinozoans supports the former view (Achab et al. 2011; Achab et al. 2013).

Bulk isotopic analysis of the Anticosti Ordovician/Silurian sequence (Orth et al. 1986; Darrel G.F. Long 1993; Qing & Veizer 1994; Young et al. 2010a; Desrochers et al. 2010; Jones et al. 2011, Delabroye et al. 2011 and Mauviel & Desrochers 2016) have revealed a 4 ‰ positive $\delta^{13}C$ excursion in the Hirnantian-age Laframboise Member. Some also record an oxygen isotope excursion at the same point (Azmy et al. 1998b; Darrel G.F. Long 1993; Brenchley et al. 2003; Jones et al. 2011) but there is less published work on this, and it is not well recorded at the eastern end of the Island, likely due to the compression of the cycles here (Darrel G F Long 1993). These results in conjunction with the biostratigraphy mean that Anticosti can be related to global Ordovician and Silurian strata. In particular, the position of the Hirnantian carbon isotope excursion and its return to background

levels combined with the presence of *Ancyrochitina ellisbayensis* suggests the Ordovician/Silurian boundary occurs a few metres into the basal Becscie Formation (Figure 5.3) (Achab et al. 2011).

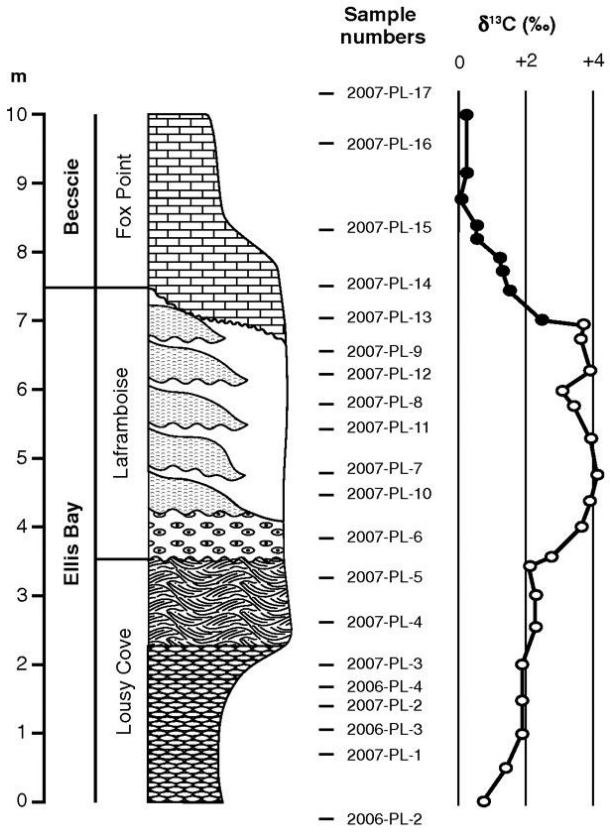

Figure 5.3 Example of isotopic record from chitinozoans sampled from Pointe Laframboise displaying $\delta^{13}C$ excursion (Achab et al., 2011).

On Anticosti there is a notable smaller carbon isotope peak recorded at the transition between the Katian and Hinantian as well as other enrichments appearing in multiple stratigraphic positions within the succession (Ghienne et al. 2014). This could correlate to the previous suggestion the end-Ordovician glaciation occurred as a sequence of glacial cycles rather than a single short glacial event. This is in contrast to the general suggestion that only one excursion occurred restricted to a single glacial event. However, Ghienne et al. (2014) also noted that there are hiatuses within the Anticosti stratigraphy and that correlating the different global Ordovician/Silurian strata using the carbon isotope excursion is not as straightforward as previously thought.

5.1.3 Cyclicity recorded in Anticosti sediments

The Anticosti sedimentary sequence has long been recognised as cyclic (for example, Long (1993). Sequence stratigraphic interpretations suggest the late Ordovician section records changes in sea level (Desrochers et al. 2010; Ghienne et al. 2014). Copper (2001) noted that the changing presence between coral reefs and single coral specimens throughout the sequence reflected the changing environmental conditions on the shelf. Long (2007) studied tempestite frequencies recorded in the Anticosti strata, finding them well matched to inferred sea level changes.

The Upper Ordovician Anticosti sequence is interpreted as a series of transgressive-regressive cycles (Copper 2001; Desrochers et al. 2010). These cycles represent a multi-order climate signal (Ghienne et al. 2014), and are thought to represent sea level changes during the glacial and inter-glacial periods of the Hirnantian (Copper 2001). Combining the tempestite work with lithological studies (Long 2007; Sami & Desrochers 1992) indicates relative sea level change cycles of >1m.y., approximately 400,000 years and 100,000 years or less respectively (Desrochers et al. 2010).

For this study, the sequence was divided into transgressive system tracts and regressive system tracts, using the classification outlined in Desrochers et al. (2010) and (Ghienne et al. 2014). Transgressive system tracts are bounded by a maximum flooding surface above and the sequence boundary below, with regressive system tracts defined by the maximum flooding surface below and the sequence boundary above (Desrochers et al. 2010). There are at least three larger cycles in the studied sequence, each lasting approximately 1.2 Ma. These cycles represent discrete periods of glaciation, separated by de-glacial periods. Four sea level peaks can be identified if the 400,000-year orbital-period is controlling cyclicity during the Hirnantian Stage, and the first four transgressive-regressive sequences in the Ellis Bay formation represent these. The fifth transgressive-regressive cycle is represented by the Laframboise Member and defines a brief interglacial period. The base of the Becscie Formation shows transgressive strata representing the last section of the Hirnantian stage when rapid deglaciation was occurring (Desrochers et al. 2010).

Figure 5.4 An aerial shot taken by Paul Dennis over the platform on the Western side of Anticosti. Where the maximum flooding surface occurs for each 1.2 Myr cycle, it is possible to see the shale bed being preferentially eroded, causing a substantial cut in (black arrow). It is possible to see higher frequency cycles also showing an indent into the platform (red arrows).

Each 1.2 Ma package contains between two and five of the higher frequency transgressive-regressive (T-R) cycles (André Desrochers, pers. comm.). We sampled from the second and third of the 1.2 Ma packages, which covers the end Hirnantian and the Ordovician/Silurian boundary. These clearly contain higher frequency cycles. There is a gradual reduction in accommodation space (Long 2007) as the sequence progresses, which reflects the pulsed nature of the glaciations. During the higher frequency cycles the maximum flooding zone is represented by a shale bed, followed by a transgressive sediment package. Figure 5.4 shows an aerial view of how the maximum flooding zone deposits differ from the rest of the package. It is possible for the sea level changes to be offset from the facies changes because of the layering of higher and lower frequency cycles on Anticosti. Therefore, it is possible to have a lowstand (lowest sea level points) of a high frequency cycle as part of a maximum flooding zone in a large, 1.2 Ma sequence (André Desrochers, pers. comm.)

5.1.4 Detailed stratigraphy and sampling

Sampling for this work concentrated on the western section through offshore storm-dominated carbonate facies (Desrochers et al. 2010). The sampled transect is shown as a sedimentary log in Figure 5.5 and as photographs in Section 5.2. Representative field photographs of each stratigraphic horizon are also shown in Figures 5.6 -5.8.

Figure 5.5 Stratigraphic log of the sampled section. The key to symbols is on the previous page. Arrows indicate locations from which samples were taken, with the accompanying text outlining the material types. A3 size diagram shown in Appendix VI

5.1.4.1 Lousy Cove Member (part of Ellis Bay Formation)

The Lousy Cove Member contains the latter half of the second glacial cycle, and the start of the third cycle (Ghienne et al. 2014). Samples were taken from the upper 12 m from the member at the western end of the island (see Fig. 5.6 for photographs) in order to try and identify the ambient bulk isotope signature prior to the carbon isotope excursion. The lower 3 m of the sampled section are dominated by nodular calcareous shales, interbedded with limestone. The limestone beds are fine grained wackestones with some thin-shelled brachiopods. Above this the member becomes limestone-rich but is mostly devoid of fossils. The beds gradually coarsen upwards to a sharp contact after which the limestone becomes a massive bioclastic limestone with some bioturbation. The sharp boundary at 9 m marks the maximum flooding surface of the second T-R cycle of Ghienne et al. (2014). The Lousy Cove member remains as a massive limestone with beds approximately 50 cm thick, with fossils (rugose corals and brachiopods) restricted to narrow seams and laminations, before the erosional contact with the Laframboise Member. Some Individual beds contain hummocky cross stratification and coarsen upwards.

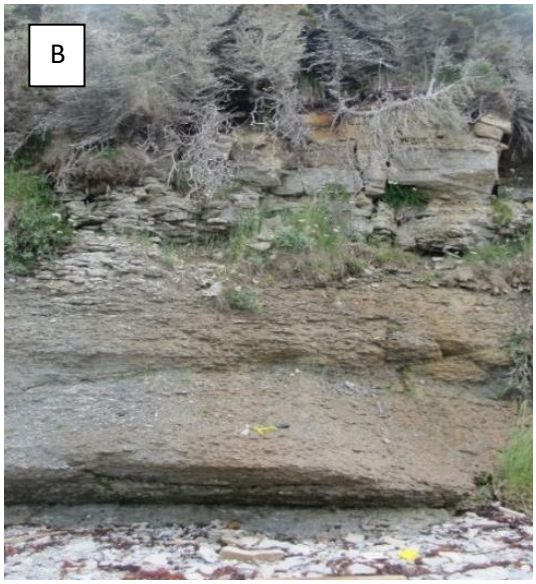

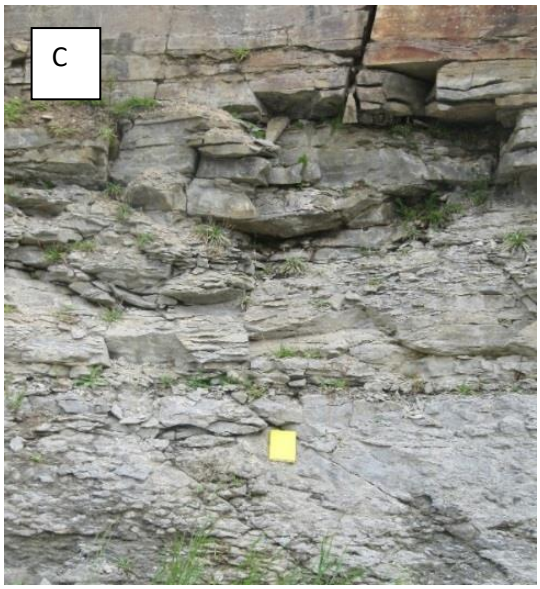

Figure 5.6 Photographs of the Lousy Cove Member. 5.5a shows nodular calcareous shales interbedded with limestone. 5.5b shows contact between lower shaley 3 m and the limestone beds above. 5.5c indicates the change into the massive limestone.

5.1.4.2 Laframboise Member (part of Ellis Bay Formation)

The Laframboise member is approximately 2 m thick, controlled locally by the upper topography of bioherms. This member is very distinctive and is bound by erosional surfaces (Desrochers et al. 2010) with a basal oncolite bed, containing intraclasts and fossil fragments. Individual oncoids are up to pebble-sized but fines upwards through the bed (Desrochers et al. 2010). Above the oncolite bed a sequence of microbial/coral bioherms are interspersed with thinly-bedded muddy limestone and shales. The bioherms were constructed by a combination of microbial calcites, rugose and tabulate corals and also bryozoans. The limestone and shale 'interbeds' can be

traced laterally through the formation, making it easier to sample accurately at high resolution. Figure 5.7 shows the contact between the Laframboise Member and the Becscie Formation.

As deposition changes between limestone and shale overlying (controlled by sea level fluctuations) the bioherms expand and contract laterally. The bioherms developed at the same rate as accommodation space developed. A small change in the water depth causes shale beds to be deposited instead of organic material, suggesting these are 'catch-up' reefs (André Desrochers, pers comms). These high frequency changes in the sediment deposition and bioherm building suggests it may be possible to extract very high frequency isotope changes during this interglacial period.

There are no brachiopods visible in the Member, although it may be possible to see some material in the upper surface of each bed (collecting from the platform section of Anticosti would determine this) (André Desrochers, personal communication). Across the other side of this peninsular, very little of the Laframboise member is visible in the cliffs, but it is possible to walk on the platform and see the circular depressions caused by the reefs. This upper section of the Laframboise Member is capped by an erosional surface, but the overlying Becscie strata drapes over the Laframboise, cutting into it up to a 0.5 m depth.

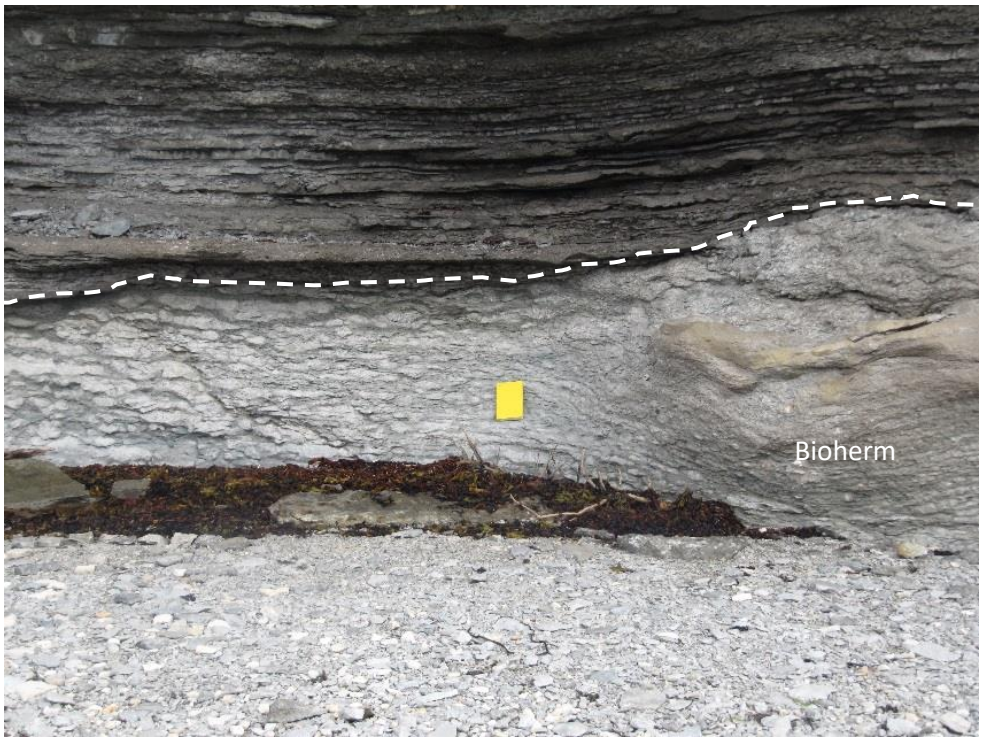

Figure 5.7 The Laframboise member with a bioherm to the right of the photograph. The Fox Point Member of the Becscie Formation can be seen in a sharp contact, overlying and also draping over the bioherms (white dashed line marks boundary).

5.1.4.3 Fox Point Member (part of Becscie Formation)

The Becscie formation has a sharp contact with the Laframboise Member and sits directly over the bioherms/reefs. Draping occurs over the inter-reef sections of the Laframboise Member. The Ordovician-Silurian boundary lies approximately 3 m into the Becscie Formation, where the carbon isotope signal returns to background (André Desrochers, personal communication, Achab et al. 2011). The basal Fox Point Member (Desrochers et al. 2010), is the only part sampled in this study. It consists of fine grained laminated limestones interbedded with carbonate mudstones. Fossil presence (mainly brachiopods and crinoids) decreases upward in the sampled section, accompanied by some bioturbation. Figure 5.8 shows the interbedding within the Fox Point Member.

Figure 5.8 The Fox Point Member of the Becscie Formation has thin interbeds of limestone and shales, and displays higher frequency cycles within its packages of sediment.

5.1.5 Burial History

As this study is attempting to measure environmental palaeotemperatures, it is important to understand the thermal history of the sediments. This is important as sustained burial at

temperatures greater than 130 °C is likely to reset the clumped isotope temperature to the diagentic burial temperatures (Henkes et al. 2014). The burial history of Anticosti Island is based on several lines of evidence and summarised in Figure 5.9.

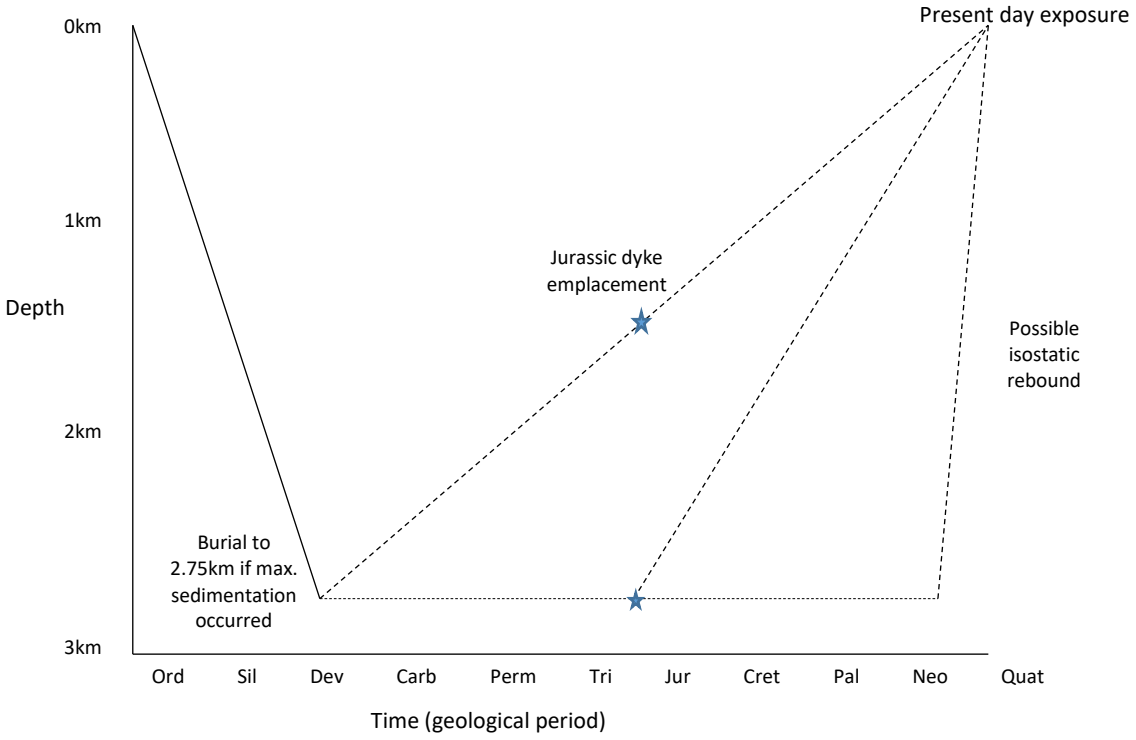

Figure 5.9 A graphical outline of the burial history for Anticosti Island, from the perspective of the outcrops sampled. Dashed lines represent possible scenarios for uplift of the sequence. The star marks the time of the dyke emplacement.

The Anticosti Basin is part of the St. Lawrence platform, and is approximately 70 km north of the Taconian deformation front (Bordet et al. 2010). The late Ordovician succession does not record any of the compression caused by the Appalachian orogeny (Desrochers et al. 2010). As might be expected, the nature of the basin varies through time as the Iapetus suture changed (Long 2007). After developing from a passive basin margin in the early Ordovician, the Anticosti Basin became a foreland basin. Accretion began on the Laurentian margin (Desrochers et al. 2010) as the Appalachian tectonic wedge moved across the autochthonous material of the St Lawrence Platform (Pinet et al. 2014). During the Late Ordovician the Taconian thrust sheets underwent final emplacement and the Anticosti basin became a successor basin (Desrochers et al. 2010).

The youngest sediments found on Anticosti are late Telychian (from the Llandovery of the Silurian period) (Long 2007). The post Llandovery depositional history is uncertain, but it is thought that between 2.3 and 3.5 km of sediment were deposited above the Anticosti Group (428 Ma) and have been subsequently eroded (Chi et al. 2010; Pinet et al. 2012 and references therein). In the

offshore section of the basin, high-resolution seismic data shows there is approximately 1.14 km of younger material deposited above the equivalent strata exposed onshore that post-dates the Silurian Chicotte Formation (the youngest formation recorded on Anticosti). Anticosti Island itself has a maximum sedimentary thickness (not all exposed) of 3.85 km based on the drilling of exploratory wells (Pinet et al. 2012). All formations thicken toward the south and east of Anticosti; there is a thickness of approximately 915 m in the north, and greater than 3660 m in the south. The platform can also be traced offshore under the Gulf of St Lawrence to approximately 12 km southwest of the island (Bordet et al. 2010). The estimated 1.14 km strata extra offshore is only half of the possible thickness assumed to have been eroded from the southern section of Anticosti Island (Pinet et al. 2012).

Thermal maturation data from Anticosti Island on organic matter in the Upper Ordovician Macasty Formation shales (stratigraphically below the Vauréal Formation) contain a minimum of 3.5 % total organic carbon (Bertrand & Heroux, 1987) indicated burial depth to at least the oil and gas windows (Chi et al. 2010; Bertrand et al. 1987). However numerical modelling by Chi et al. (2010) indicated that burial of the Vaureal and Ellis Bay formations was 1 – 2 km deep at the NNE end of the Island. This would indicate that whilst the offshore section of the Anticosti Basin was buried below 3.6 km, the sampled section was buried to a maximum of between 1 and 2 km. This is supported by Conodont Alteration Index (CAI) data from McCracken & Barnes (1981) who found that conodonts in the Ellis Bay Formation had CAI values of 1.5 or less, indicating burial temperatures 90 °C or less.

The scenario outlined in Figure 5.8 is a possible sequence of events. According to Chi et al. (2010) the maximum burial for the Macasty Formation (Upper Ordovician) was at 386 Ma, during the Mid Devonian. Using their suggestion, based on works by Bordet (1987, 1990) that a minimum of 2.3 km of sediment was deposited above the Anticosti Group to the south and has since been eroded, Figure 5.8 shows the approximate time of maximum burial and the approximate burial depth for the sampled interval (Ellis Bay Formation/Becscie formation boundary). I have used a maximum burial value of 2.75 km, although it is possible the thickness of the Silurian to Devonian sediments were lower in the north. It is also known that dykes found on Anticosti were emplaced in the Jurassic, associated with the opening of the Atlantic Ocean (Bordet et al. 2010). These cut the Palaeozoic strata (Long 2007) and must have been emplaced when the strata were still buried. This means there are three possible models for the uplift and exposure of the Ordovician rocks. They may have been slowly uplifted after the point of maximum burial, or uplifted after the Jurassic dyke emplacement. Overall, this suggests that the strata was potentially held at 90 °C from between the mid-Devonian to the Jurassic, a time length of 160 Ma or longer.

5.2 Methods

5.2.1 Methods – Collection of material

Sampling was completed around the headland at Point Laframboise (Figure 5.9) between 49°48’32 N, 64°25’26 W and 49°47’58 N, 64°24’55W. This section of the coastline displays a cliff, in which the shelf succession representing the Late Ordovician and Early Silurian is clearly displayed. There is a thin strip of modern beach which separates this cliff from the platform (see Section 5.1.4 for views of the cliff face). The bedding dips between 2-4 ° towards the south, producing a continuous outcrop younging to the southeast. This meant we were able to walk along a complete section of outcrop from the end Ordovician into the Early Silurian. The sampled sequence included material from the Lousy Cove and Laframboise members and the Fox Point Member of the Becscie Formation, spanning deposits formed both before and after the Hirnantian glaciation event (see also the stratigraphic column in Figure 5.5).

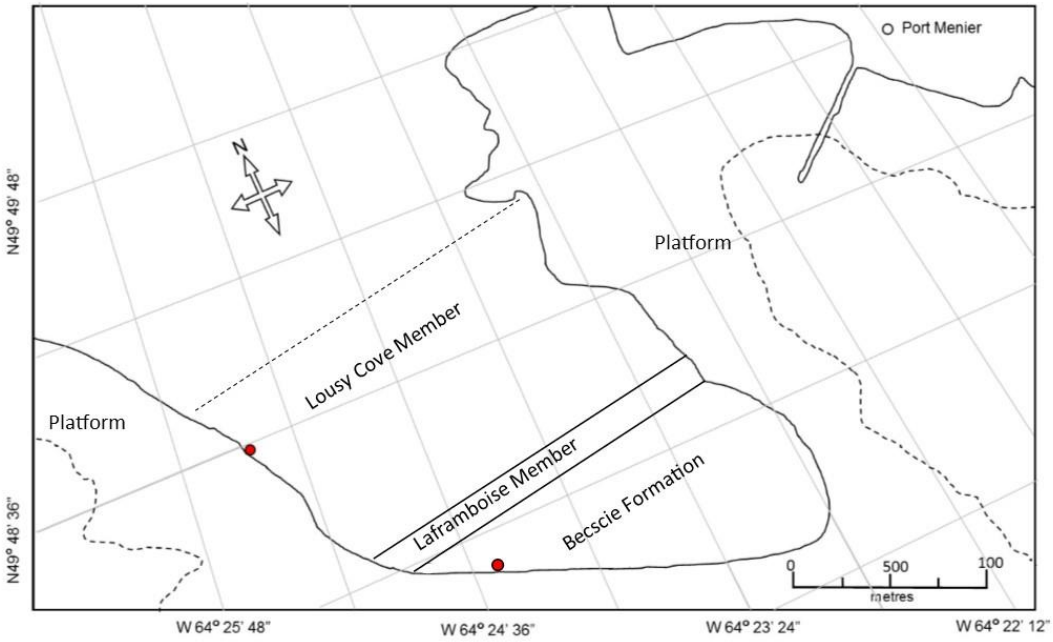

Figure 5.10 Simple map of the Laframboise Peninsular from which the samples were taken. Sampling occurred between the two red points. The platform around this section of the island is outlined with a dotted line.

Samples were collected at 1 m vertical spacing through the section. This was achieved by identifying specific bedding planes and tracing them laterally along section, providing a series of fixed points to measure between. These were identified after an initial walk of the sequence. One of the bed markers can be seen in Figure 5.8 next to the metre stick. As a number of single beds were possible to trace for several metres horizontally, these provided a point of reference for each metre vertically. Sampling frequency increased in the Laframboise member to every two to three centimetres to ensure capture of the carbon isotope excursion (See Section 5.1.2) along with any higher resolution palaeoenvironmental changes. All of the sample intervals are identified on the stratigraphic log in Figure 5.5. Samples were collected using a hammer and chisel, and a range of material was collected including micritic, skeletal fossils, and whole rock material. All of the samples were taken from within the second and third major sequences recorded on Anticosti.

5.2.2 Methods – analysis of material

5.2.2.1 Clumped isotope analysis

The analytical protocol for measuring clumped isotopes in carbonate samples on MIRA are given in Methodology Chapters 2 and 3. Samples were generally rock chunks containing fossils (brachiopods, rugose corals, tabulate coral sections and trilobites), crystalline cement material or were fine-grained micritic samples with no visible fossil material. Once the sample material was chosen from the collected section, each chunk was cleaned and sonicated in distilled water. A Dremel hand drill was then used to powder the material to isolate it from the whole rock. For thin-shelled brachiopod samples, often a selection of shells within each rock chunk were used to obtain a composite sample powder. On the whole, each species was kept separate where species were identifiable. For a list of some of the species present see Figure 5.11. Trilobite segments were treated in a similar manner. Any material extracted from rugose corals was not mixed between corals – generally there was enough material for clumped isotope analysis without the need for combining samples. In some cases, there was a definite texture change in calcite between the inner and outer sections of the coral. The inner sections of the coral often appeared lighter in colour and were softer when drilled. The outer layer was darker and harder, which could suggest some micritic material within the sample. In some instances, these inner and outer layers were separately sampled also. Micrite samples and crystalline areas were drilled in localised areas of each sample in an attempt to reduce heterogeneity. The powder was transferred to a small sample vial, and these were shaken to mix the powder, again reducing the chance of heterogeneity within the sample.

All samples were reacted offline at 25 °C and underwent CO_2 clean-up on the glass vacuum line. Room temperature equilibrated gases and 1000 °C heated gases were measured alongside the samples to establish a transfer function between the local and absolute reference frames (Dennis et al. 2011). In addition, this allowed monitoring of changes in calibration that are associated with drift in the working reference gas composition and scale compression of the mass spectrometer. Carbonate standards were also measured alongside the samples. Standards used were UEACMST, UEATHC, UEABEL, and ETH1, and these allowed us to estimate the long term accuracy and precision of the measurements. The full details of sample preparation and analysis are outlined in Chapters 2 and 3.

5.2.2.2 Bulk isotope analysis

Bulk isotope analyses are considered to be the $\delta^{18}O$ and $\delta^{13}C$ values recorded in the collected material. The measurements were carried out on the Europa SIRA series II dual-inlet IRMS at UEA. This instrument is a VG SIRA fitted with a Europa Instruments pinta-bloc micro dual-inlet and is interfaced with a common acid bath sample preparation system. Batches of 47 samples weighing between 60-80 µg, including 8 UEACMST standards were loaded and digested in the common acid bath held at 90 °C with 102 % phosphoric acid. The bulk isotope values given by the two mass spectrometers are identical within measurement error. The aliquots for bulk isotope analysis were taken from powders that were originally drilled for clumped isotope analysis.

5.2.2.3 Trace element analysis

Trace element analysis was completed using the New Wave Plasma UP-213 nm laser system coupled to a Thermo-Electron X Series ICP-MS. Small blocks approximately 5 mm thick were cut from a selection of five samples. Different material types were analysed – skeletal material including brachiopods and corals, along with micrite and crystalline cement sections. Helium was used as a carrier gas and each sample was calibrated using the glass standards NIST-610 and NIST-612. The data was processed using a calibration built on the known NIST-610 and NIST-612 glasses, along with normalising the data to 40 % calcium content as an internal standardisation technique. Sampling was completed using discrete laser spots on areas of interest. Some pre-ablation was tested on micritic material, but other areas were not pre-ablated. A 200 µm diameter spot size was used, with laser output at 55 % and a repetition rate of 5 Hz. The dwell time on each point was 40 seconds. Some material was also analysed in solution using atomic emission spectroscopy. Material was digested in acetic acid, with the supernatant analysed in a Varian Vista Pro Axial ICP-AES.

5.2.2.4 Optical analysis

Thin sections are 30 µm thick held in epoxy resin and polished to 1 µm. The microscope used to study and photograph the thin sections was a Leica petrographic model DM2500M with attached digital camera. The cathodoluminesence photographs were taken using an Optical Cathodoluminesence System Model 8200 Mk 5-1 by Cambridge Image Technology Ltd using a Nikon Labophot-2 microscope.

5.3 Results

5.3.1 Petrography: preservation and diagenesis

It was important to establish the quality of skeletal fossil preservation before geochemical sampling to ensure that the derived data could be understood in its correct context. This was achieved using thin sections and acetate peels made from a selection of samples chosen to include a representative range of limestone and fossils within the sampled sequence. A full description of key thin section attributes (mineralogy, skeletal composition, textures/diagenetic fabrics) are given in Table 5.1. Thin sections and peels were stained with alizarin red S and potassium ferricyanide (Dickson, 1965) to identify ferroan and non-ferroan calcites and dolomite. The thin sections were also studied under cathodoluminesence (CL) prior to staining to help reveal and better distinguish original and diagenetic fabrics (Miller 1988).

Transect position	Rock Classification	Matrix features	Fabrics/Textures	Fossils	Fossil Mineralogy	Cement textures	Diagenetic Features	CL Features
0 m Lousy Cove Member	Bioclastic packstone – grain supported limestone	Very fine (micritic), dark mud with sparry calcite. Almost too fine to make out individual calcite crystals.	Coarse grained fossils (2-3 mm) with fine matrix.	Large brachiopod shell fragments, crinoid osicles, rugose corals, trilobite spines. Few fossils are actually touching.	Brachiopod calcite is fibrous. Rugose corals are large-size sparry crystalline infills.	Drusy calcite in infills	Drusy spar infilling corals, also appearing in gastropod moulds. Some brachiopods have dark rims – could be pyrite or solution seams.	Brachiopod shells are dark, sparry calcite infills are light orange, trilobites are between. Some rims of brachiopods are brighter orange.
0.6 m Lousy Cove Member	Bioclastic wackestone	Stronger mud component with some patches of spar.	Fossils (up to 500 µm) with very fine grained matrix.	Corals, crinoid osicles. Fossils appear packed in patches.	Crinoids show possible dissolution textures.	Sparry calcite veins	Large fractures/veins filled with secondary calcite but doesn't feed into fossils – different CL textures.	Crinoid ossicles blend into matrix orange luminescence.
1.3 m Lousy Cove Member	Bioclastic packstone	Matrix of mud and sparry calcite	Fossils, including rugose corals up to 500 µm	Crinoid osicles, grastropods, rugose corals, trilobites and brachsiopod fragments	Rugose coral colony shows some with darker walls. Not many fossil grains are touching.	Appears light brown here	Possibility of grains jammed together.	Some bright coloured flecks visible in coral infills.
5.7 m Lousy Cove Member	Bioclastic wackestone	Sections of micrite finer, coarser patches possibly contain more spar,	Finer grained fossil fragments here, up to 1-2 mm.	Fossil material is very fine and fragmented, and is not evenly distributed across the slide.	Echinoid and brachiopod fragments	Limited large sparry cements	Sparry cement veinlets.	Some patches of matrix have lower luminescence than others.

		spar is less than 50 µm in size		Fine brachiopod shell fragments.				
10.7 m Lousy Cove Member	Carbonate mudstone	Extremely fine micritic matrix with very fine sparry calcite (approx. 20 µm).	Some possible flattening of sparry calcite grains and orientation in one direction.	Small gastropod, brachiopod and trilobite fragments	Possible brachiopod fragment, very limited fossil material.	Very fine cement within matrix	Limited sparry calcite infills.	Luminescent matrix, darker than coral material
12 m Lousy Cove Member	Packestone	Micritic matrix with varying size of sparry calcite.	Large fossil fragments present up to 5 mm.	Brachiopod shell, trilobite and crinoid fragments held within coarse secondary calcite.	Grain boundaries between fossils not touching.	Coarse vein sparry infills present.	Syntaxial overgrowth in crinoid osicles/echinoderm material.	Brachiopods are dark, micritic matrix luminesces
12.3 m Laframboise Member	Bioclastic wackestone	Micritic matrix with some more sparry calcite patches.	Some fossil fragments present, spar is present in the matrix and is coarser than previously seen (still very fine).	Brachiopod shell fragments, fossil fragments are very fine. Some coral present, trilobite segments also featured.	Pyrite present. Some void-filling sparry calcite	One large grain that has been replaced with finer sparry calcite. Calcite appears to be dirty in some areas of this infill and there is a suggestion of laminae. This could have been a stromatolite	Microspar present as crystals appear dirty.	Dolomite rhombs, up to 0.5 mm present. Flecks of blue suggest detrital feldspars. Small brachiopod and trilobite fragments do not luminesce, matrix is orange colour.

						or microbial feature.		
13 m Laframboise Member (IR)	Bioclastic wackestone	Micrite has larger sparry grains in this sample.	Some large brachiopod fragments, otherwise fossil material is very broken.	Uneven distribution of fossils including crinoid osicles, brachiopod and trilobite material. Some microbial encrusting present.	Brachiopod fragments show original calcite textures.	Vein infills and large patches of sparry calcite.	Some sparry calcite patches and veinlets	Feldspar fragments present, very small. Dull orange micritic matrix, brachiopod and trilobite show no luminescence.
13.83 m Laframboise Member (IR)	Bioclastic wackestone	Very fine micritic matrix with some sparry patches present.	Limited fossil material, some possible fragments but very small (<1 mm)	Microbial tubes, coral fragments. Other fossils fragments are too fine to identify.	Very fine possible sparry calcite visible between layering of microbial material.	Coral infills are sparry where visible	Veinlets filled with sparry calcite, some void spaces filled also, smaller than previous slides.	Dull orange matrix, coral fragments brighter.
13.98 m Laframboise Member (IR)	Bioclastic wackestone	Micritc matrix with sparry calcite.	Very fine fossil fragments approx. 500 µm in size.	Microbial encrusted tubes infilled with calcite, shell material and coral fragments but very fine. Not very closely packed	Dark and light banding in microbial tubes are bands of early cemented sparry calcite into gaps between microbial layers. Some serpulids or gastropod present. Dirty brown colouring could be recrystallized micrite or silt.	Dog tooth terminations and drusy textures infilling voids. Central infill high birefringence, outer is low.	Veinlets, possible spar infill with shelter of shells	Veinlets are brighter orange CL response, shell material is dark
15.5 m Becscie Formation	Carbonate mudstone	Extemely fine muddy matrix with very fine spar that is	No clear fossil fragments	---	---	---	Some patches of sparry calcite present, quite fine.	Dull orange micrite

		not easily visible.						
16.9 m Becscie Formation	Bioclastic packstone	Micritic and sparry calcite matrix.	Fossil fragments, up to 2-3 mm in some cases, some very fine.	Finer fossil detritus, some brachiopod shell material, triloboites, crinoid osicles and rugose corals. Crinoid osicles show splitting with sparry calcite present.	Pyrite present. There is a lot of fossil material present, similar appearance to other fossiliferous samples.	Sparry calcite has infilled corals.	Some syntaxial overgrowth here. Possible dark solution seams. Possible pressure solution amongst closer packed grains.	Darker fossil fragment response, matrix is dull orange. Sparry calcite round crinoid osicles lumineseces.
19.7 m Becscie Formation	Carbonate mudstone	Fine muddy matrix with sparry calcite grains.	Some possible flattening of sparry calcite grains and orientation in one direction.	Very limited skeletal material	Some possible quartz flecks present, spar in micrite is extremely fine	---	Can see blurred boundaried in sparry calcite in matrix at high magnification which suggests interlocking grain growth.	Dull orange micrite

Table 5.1 Summary of key features identified in thin sections. Analyses were completed using optical light microscopy and CL analysis.

Brachiopod shells are quite common throughout the sampled sequence (Fig. 5.11) and are often used as target material for Palaeozoic skeletal geochemical proxies of ocean conditions (for example, Veizer et al. (1986)). Only partial identification of the shells has been possible, as many are fragmented. The genus or family names of shells present in the sampled sequence are *Plaesiomys, Mendacella, Strophomenide, Hebertella* and *Sowerbyella* (Pers. Comm. Jisuo Jin and André Desrochers 2014). Photographs of these species are shown in Figure 5.11. Unfortunately, these brachiopods are mostly thin-shelled (1-2 mm thick), making micro-drilling for sampling a challenge. One effective sampling strategy was to lightly mill across an exposed shell surface, avoiding the micritic matrix. Even using this approach a few individual shells had to be grouped together to gather enough material for clumped isotope analysis. This could have led to mixing of genera/species sampled, but was unavoidable.

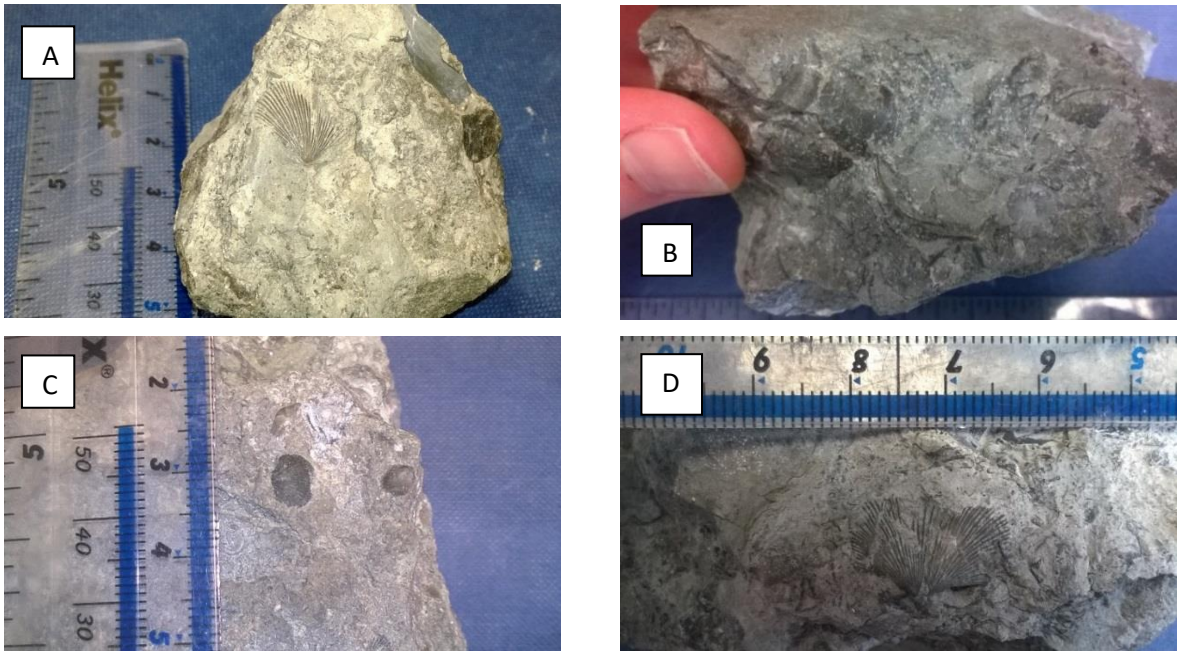

Figure 5.11 Brachiopod and brachiopod fragments sampled in this study. Genera are likely to be A – Hebertella, B - Strophomenide (Eostrophonella), C- Mendacella, D - Hebertella.

Tabulate and rugose corals (Laframboise Member) were clearly visible in the field and in hand specimen (Fig. 5.12) but it was noted that in all cases most inter-septal spaces were infilled by a carbonate cement (Fig. 5.12a). Due to the sample mass required for clumped isotope analysis, sampling of coral septal-walls was not possible and it was assumed that samples from within the coral colonies were therefore dominated by cement and not original skeletal material. Some rugose coral specimens show a gradation of septal preservation decreasing toward a more cement

dominated portion (Fig. 5.12c). The outer wall of the corals often appears darker than internal septal walls in thin section, but there is little evidence the walls are better preserved. Figure 5.24b (Section 5.4.2.1) shows the coral walls to be drusy spar, suggesting recrystallization of the wall.

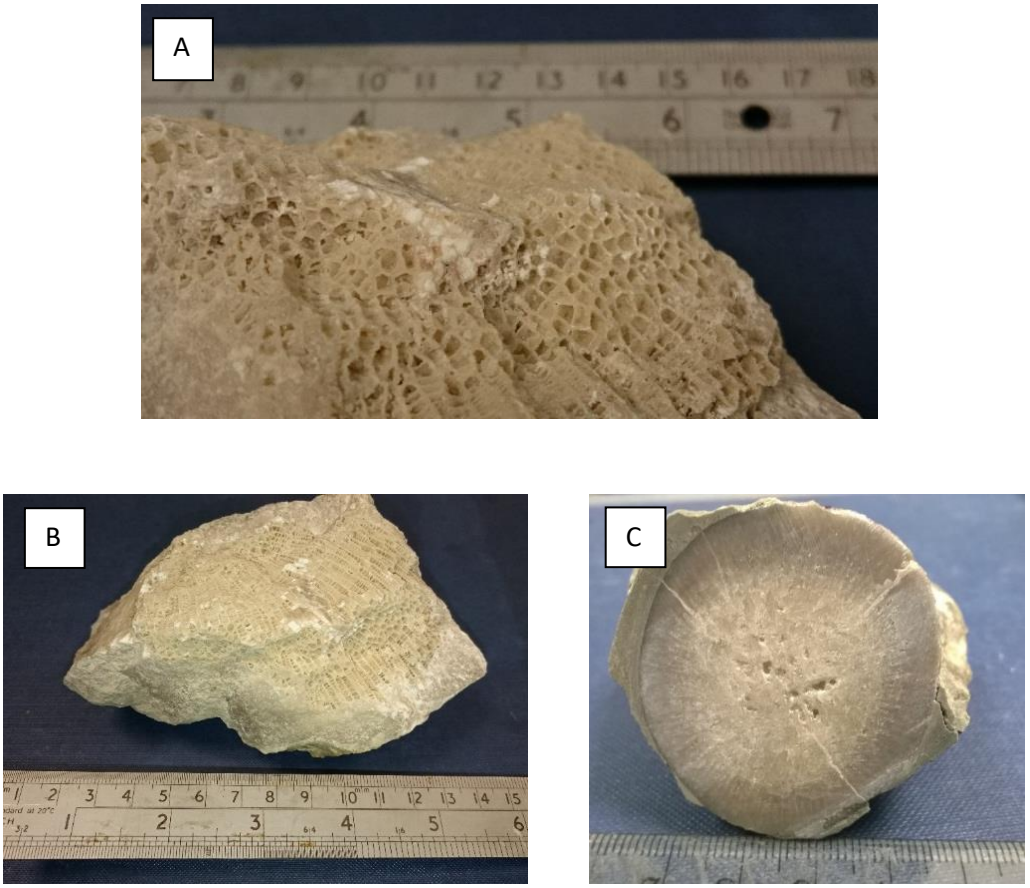

Figure 5.12 A and B show a typical tabulate coral. C is a solitary rugose coral, with some drill markings.

Vein cement is present throughout much of the sampled section (Figure 5.13) allowing discrete sampling of diagenetic cements. Individual vein calcite crystals are at least 2 - 3 mm along the long-axis, as the body of the crystal grows away from the rock surface. There is some minor colour variation within the cements.

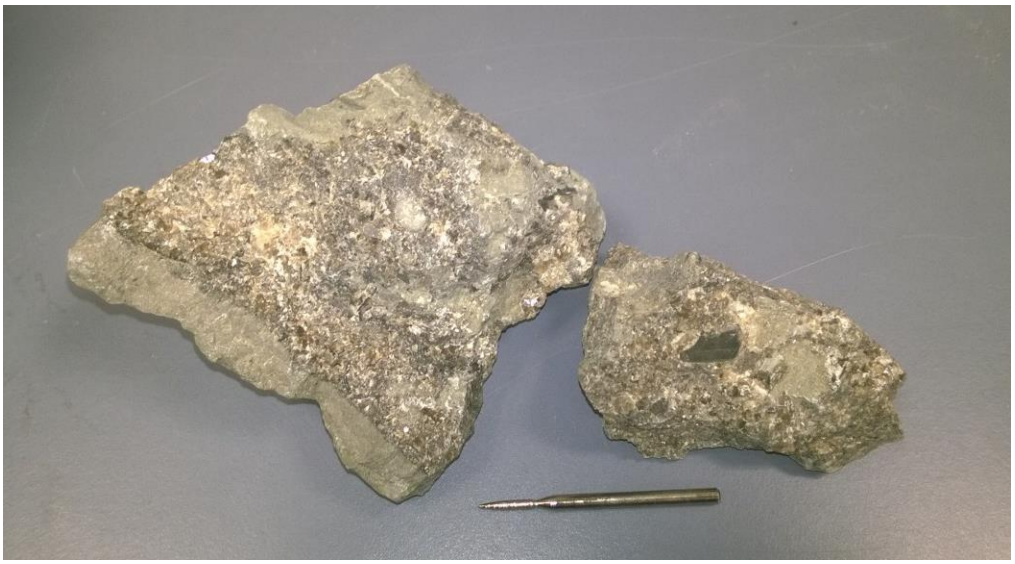

Figure 5.13 Varying colours of void cement visible in the left sample. There are also some broken trilobite fragments and possibly a coral fragment within the spar. Drill bit is 3 cm in length.

5.3.2 Oxygen and carbon bulk Isotopes

Using results obtained from both the MIRA and Europa instruments, there are 87 measurements of bulk isotope compositions from the sampled section. These are reported with respect to VPDB and are listed in Table 5.2. These were collected along the stretch of outcrop, covering a vertical distance through the sequence of 21.5 m (see Figure 5.5 for description of sample locations and stratigraphy). This sample set includes material from the upper Lousy Cove and the Laframboise members of the Ellis Bay Formation and the lower Becscie Formation. The material type, position and $\delta^{13}C$ and $\delta^{18}O$ values are reported in Table 5.2. The samples are categorised in both the table and graphs according to the material type. This includes brachiopods, rugose and tabulate corals, trilobite spines or plates, micrite (fine grained mud-rich matrix) and cements (post-depositional diagenetic precipitates within veinlets or voids) or cemented whole rock samples.

Sample Type	Member/Formation	Position in Transect (m)	Av. $\delta^{13}C$ ‰$_{VPDB}$	SD $\delta^{13}C$ ‰$_{VPDB}$	SE $\delta^{13}C$ ‰$_{VPDB}$	Av. $\delta^{18}O$ ‰$_{VPDB}$	SD $\delta^{18}O$ ‰$_{VPDB}$	SE $\delta^{18}O$ ‰$_{VPDB}$	Number of repeats (n)
Tabulate Coral	Laframboise Memb.	14.1	2.23	0.025	0.012	-3.77	0.056	0.028	4
Tabulate Coral	Laframboise Memb.	13.5	2.09	0.451	0.202	-4.65	0.372	0.167	5
Rugose Coral Outer	Laframboise Memb.	14	3.07	0.119	0.059	-3.53	0.174	0.087	4
Rugose Coral Outer	Laframboise Memb.	14.1	3.04	0.034	0.017	-3.34	0.089	0.045	4
Rugose Coral	Laframboise Memb.	13.9	3.85	0.079	0.045	-2.71	0.182	0.105	3
Rugose Coral	Laframboise Memb.	13.6	3.70	0.298	0.172	-2.83	0.245	0.141	3
Rugose Coral	Laframboise Memb.	13.8	2.59		0.010	-5.34		0.043	1
Rugose Coral	Lousy Cove Memb.	11.9	2.94		0.010	-2.69		0.050	1
Rugose Coral	Laframboise Memb.	14.1	2.76		0.010	-4.30		0.050	1
Rugose Coral Outer	Laframboise Memb.	13.9	3.25	0.128	0.074	-3.45	0.172	0.099	3
Rugose Coral Middle	Laframboise Memb.	13.9	2.81	0.082	0.047	-4.81	0.061	0.035	3
Rugose Coral Inner	Laframboise Memb.	13.9	2.31	0.196	0.113	-4.75	0.361	0.208	3
White Crystalline	Lousy Cove Memb.	1.3	0.65	0.016	0.010	-5.11	0.107	0.062	3
Dark Crystalline	Lousy Cove Memb.	11.9	2.26	0.438	0.196	-4.14	0.509	0.228	5
Dark Crystalline	Lousy Cove Memb.	1.3	0.25	0.289	0.204	-4.07	0.072	0.051	2
Whole Rock Sample	Laframboise Memb.	14.6	1.61	0.018	0.013	-3.77	0.035	0.024	2
Crystalline Grainstone	Becscie Fm.	14.8	1.81	0.068	0.040	-4.66	0.087	0.050	3
Crystalline Grainstone	Becscie Fm.	16	0.73		0.010	-3.28		0.050	1
Crystallline	Becscie Fm.	15.5	0.76		0.010	-3.11		0.050	1
Tabulate Infill	Laframboise Memb.	13.5	2.09	0.115	0.082	-4.26	0.256	0.181	2
Brachiopod	Becscie Fm.	15	1.24	0.178	0.079	-3.62	0.160	0.072	5
Brachiopod	Lousy Cove Memb.	0	0.10	0.130	0.065	-3.66	0.278	0.139	4
Brachiopod	Becscie Fm.	16.65	0.67	0.072	0.036	-3.61	0.105	0.053	4
Brachiopod	Lousy Cove Memb.	2	-0.18	0.348	0.201	-3.71	0.369	0.213	3
Brachiopod	Lousy Cove Memb.	7.2	0.27	0.063	0.036	-3.63	0.076	0.044	3

Brachiopod	Lousy Cove Memb.	4.8	0.10	0.171	0.086	-3.53	0.317	0.159	4
Inter-reef Brachiopods	Laframboise Memb.	12.51	3.79	0.281	0.141	-2.28	0.293	0.147	4
Brachiopod	Lousy Cove Memb.	4.5	0.25	0.051	0.029	-3.32	0.129	0.075	3
Brachiopod	Lousy Cove Memb.	8.2	0.48	0.021	0.012	-3.51	0.090	0.052	3
Brachiopod	Becscie Fm.	16.9	0.30		0.010	-3.10		0.050	1
Trilobite	Becscie Fm.	14.6	0.25	0.034	0.019	-3.64	0.022	0.013	3
Trilobite	Lousy Cove Memb.	1.3	0.30	0.173	0.087	-4.30	0.151	0.075	4
Trilobite	Lousy Cove Memb.	2	0.21	0.241	0.139	-3.82	0.328	0.189	3
Trilobite	Becscie Fm.	15	0.95		0.010	-3.91		0.050	1
Trilobite Plate	Lousy Cove Memb.	8.2	0.45		0.010	-2.87		0.050	1
Trilobite	Becscie Fm.	16.9	0.52		0.010	-4.15		0.050	1
Inter-reef Micrite	Laframboise Memb.	13	3.94	0.130	0.065	-2.55	0.027	0.013	4
Inter-reef Micrite	Laframboise Memb.	13.9	2.95	0.085	0.043	-3.01	0.165	0.082	4
Micrite	Becscie Fm.	21.5	-0.08	0.130	0.058	-3.92	0.064	0.029	5
Micrite	Lousy Cove Memb.	5.7	0.56	0.113	0.056	-3.61	0.098	0.049	4
Micrite	Lousy Cove Memb.	11.7	1.87	0.254	0.127	-4.21	0.417	0.209	4
Micrite	Lousy Cove Memb.	3	0.48	0.010	0.007	-3.48	0.066	0.047	2
Micrite	Lousy Cove Memb.	8.7	1.34		0.010	-3.33		0.050	1
Micrite	Lousy Cove Memb.	9.1	1.59		0.010	-3.43		0.050	1
Micrite	Lousy Cove Memb.	10.7	1.98		0.010	-3.13		0.050	1
Micrite	Lousy Cove Memb.	11.1	2.32		0.010	-3.30		0.050	1
Micrite	Laframboise Memb.	12.3	2.91		0.010	-2.94		0.050	1
Micrite	Laframboise Memb.	13.71	3.15		0.010	-3.50		0.050	1
Micrite	Laframboise Memb.	13.83	3.19		0.010	-3.12		0.050	1
Micrite	Laframboise Memb.	13.98	3.13		0.010	-3.13		0.050	1
Micrite	Becscie Fm.	17	0.27		0.010	-3.88		0.050	1
Micrite	Becscie Fm.	17.4	0.80		0.010	-3.51		0.050	1

Micrite	Becscie Fm.	18.4	-0.01		0.010	-4.61		0.050	1
Micrite	Becscie Fm.	19.5	0.65		0.010	-3.53		0.050	1
Micrite	Becscie Fm.	19.7	0.34		0.010	-3.53		0.050	1
Micrite	Becscie Fm.	20.5	0.41		0.010	-3.74		0.050	1
Micrite	Lousy Cove Memb.	0.6	-0.35		0.010	-4.19		0.050	1
Micrite	Lousy Cove Memb.	7.2	0.65		0.010	-2.93		0.050	1
Micrite	Lousy Cove Memb.	8.2	0.56	0.120	0.085	-3.56	0.225	0.159	2
Micrite	Lousy Cove Memb.	11.3	2.06		0.010	-3.99		0.050	1
Micrite	Lousy Cove Memb.	11.5	1.96		0.010	-4.27		0.050	1
Micrite	Lousy Cove Memb.	11.9	1.67		0.010	-3.84		0.050	1
Micrite	Lousy Cove Memb.	12	2.00		0.010	-3.80		0.050	1
Inter-reef Micrite	Laframboise Memb.	12.2	3.41		0.010	-3.09		0.050	1
Inter-reef Micrite	Laframboise Memb.	12.45	3.79		0.010	-2.57		0.050	1
Inter-reef Micrite	Laframboise Memb.	12.51	3.91		0.010	-2.64		0.050	1
Inter-reef Micrite	Laframboise Memb.	12.65	3.61		0.010	-2.50		0.050	1
Inter-reef Micrite	Laframboise Memb.	12.81	4.15		0.010	-2.58		0.050	1
Inter-reef Micrite	Laframboise Memb.	13.32	4.06		0.010	-2.66		0.050	1
Inter-reef Micrite	Laframboise Memb.	13.42	3.07		0.010	-3.78		0.050	1
Inter-reef Micrite	Laframboise Memb.	13.61	3.13		0.010	-3.69		0.050	1
Inter-reef Mudstone Micrite	Laframboise Memb.	13.7	1.53		0.010	-3.83		0.050	1
Inter-reef Micrite	Laframboise Memb.	14.15	2.94		0.010	-2.98		0.050	1
Inter-reef Micrite	Laframboise Memb.	14.3	3.05		0.010	-3.52		0.050	1
Inter-reef Mudstone Micrite	Laframboise Memb.	14.5	1.82		0.010	-3.40		0.050	1
Micrite	Becscie Fm.	15.8	0.96		0.010	-3.37		0.050	1
Micrite	Becscie Fm.	16.25	0.93		0.010	-3.65		0.050	1
Micrite	Becscie Fm.	16.5	0.79		0.010	-3.46		0.050	1
Micrite	Becscie Fm.	16.65	0.49		0.010	-3.69		0.050	1

Micrite	Becscie Fm.	16.9	0.50		0.010	-4.04		0.050	1
Whole Rock	Becscie Fm.	14.6	1.70		0.010	-3.74		0.050	1
Micrite	Lousy Cove Memb.	0	0.44	0.038	0.027	-3.67	0.125	0.088	2
Micrite	Lousy Cove Memb.	1.3	0.40	0.007	0.005	-3.90	0.033	0.023	2
Micrite	Lousy Cove Memb.	2	0.52	0.042	0.030	-3.95	0.101	0.072	2
Whole Rock	Lousy Cove Memb.	4.5	0.33	0.348	0.246	-4.16	0.321	0.227	2
Whole Rock	Lousy Cove Memb.	4.8	0.38	0.010	0.007	-3.99	0.064	0.045	2
Micrite	Lousy Cove Memb.	0.6	-0.25	-0.25	0.010	-3.93	-3.93	0.050	1

Table 5.2 Carbon and oxygen isotope results including values from both MIRA and the Europa mass spectrometers. Where only one sample has been analysed, there is no standard deviation listed. In the standard error column there is a value which is the average standard deviation measured on UEACMST on either the MIRA or the Europa, depending on which instrument was used for the measurement.

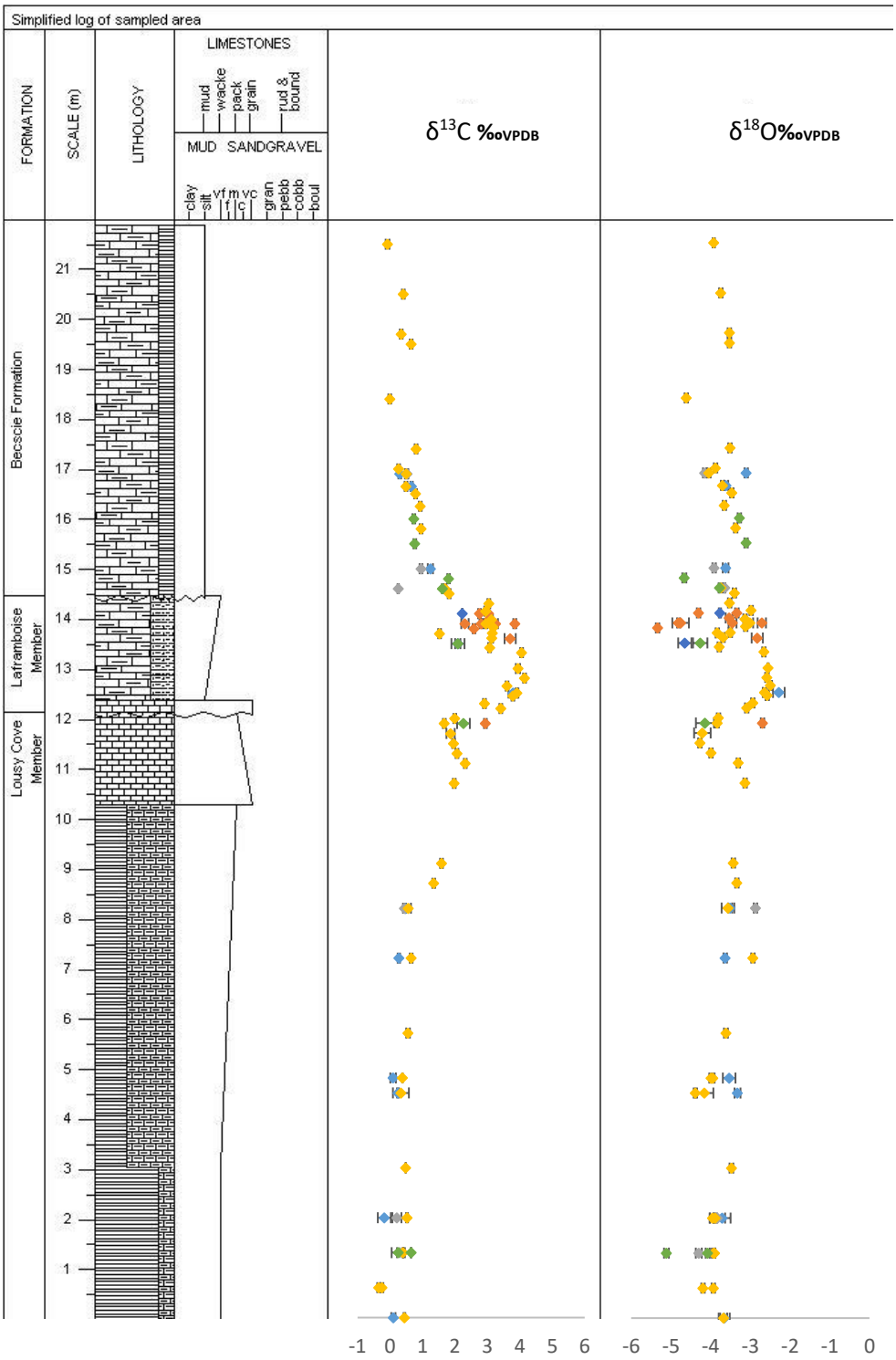

Figure 5.14 Carbon and oxygen isotope results plotted according to their stratigraphic location. Includes rugose corals (orange), micrite (yellow), brachiopods (dark blue), trilobite segments (grey), tabulate corals (light blue) and cement (green).

In Figure 5.14 $\delta^{13}C$ and $\delta^{18}O$ values for all of the samples are plotted relative to their stratigraphic position. These are an averaged value according to the material type at each point sampled. The stratigraphic position is identified in metres above the start point late in the Lousy Cove member. The samples are colour coded according to the material type. The stratigraphic section is aligned to the left of the plots.

The $\delta^{13}C$ values (first column) range from -0.35 ±0.04 ‰ to 4.14 ±0.04 ‰. The dominant feature of the profile is a positive peak with an amplitude of almost 4 ‰, occurring within the Laframboise Member and extending into the first metre of the Becscie Formation. This excursion is independent of sample type; different sample types from the same stratigraphic horizons have similar $\delta^{13}C$ values. The similarity in $\delta^{13}C$ irrespective of sample type is a feature of the whole of the sampled section.

Between 0 m and 8.2 m, the samples show low $\delta^{13}C$ values ranging from -0.35 ±0.04 ‰ to 0.56 ±0.06 ‰. The values also appear to show a slight increase moving vertically up the section to comparatively more enriched values. The $\delta^{13}C$ value drops sharply between 13.5 m and 14 m, before returning more gradually to background values at 17 m. Averaging the data allows us to see the shape of the excursion more easily, removing some of the spread in the data.

The second column in Figure 5.14 shows the $\delta^{18}O$ values. The record matches very closely to the shape of the $\delta^{13}C$ values, with a depletion at the end of the Lousy Cove Member, followed by an enrichment forming a peak early in the Laframboise Member, before returning to background values early in the Becscie Formation. The amplitude of this peak is 2.52 ‰. There is a trough early in the sequence between 0 m and 2 m, which appears to be irrespective of a sample material. The values here range from -3.88 ±0.04 ‰ to -5.11 ±0.06 ‰. The $\delta^{18}O$ value then remains constant between 4.5 m and 10.7 m, ranging from -3.13 ‰ to -4.4 ‰.

At 11.1 m, the $\delta^{18}O$ values then show a small depletion, before rising to form a peak at 12.5 m. The most enriched value is represented by a brachiopod sample at -2.28 ±0.15 ‰. The peak persists until approx. 14 m, and then the oxygen isotope values start to go down. There is some spread in the data here, but the values return to background between -4.61 ±0.04 ‰ and -3.10 ±0.04 ‰ at 15.5 m.

Looking at both the carbon and oxygen isotope data, it seems that most spread in data is within the rugose corals. This is especially obvious in the oxygen data between 13.8 m and 14.1 m. The micrite dataset is the largest, with material being sampled at almost every point in the sequence. The micrite values for the carbon and oxygen isotopes follow very similar patterns, and can be easily followed to outline the patterns in the dataset.

In Figure 5.15, the $\delta^{13}C$ and $\delta^{18}O$ are plotted against one another. The data is colour-coded according to sample material. The data lies in four distinct areas, as outlined by the circles. The lowermost circle is the data from before and after the two major positive excursions in carbon and oxygen (excursion lies between 12.2 m and 15.5 m). This is characterised by a slight positive correlation. Above this is a grouping of data which covers the section interval between 7.2 m and 11.1 m. Here, the carbon isotopes show a gentle increasing enrichment toward the peak, whereas the oxygen isotope data remains constant. This is reflected by a slight vertical trend visible despite the slight spread of the data in this area.

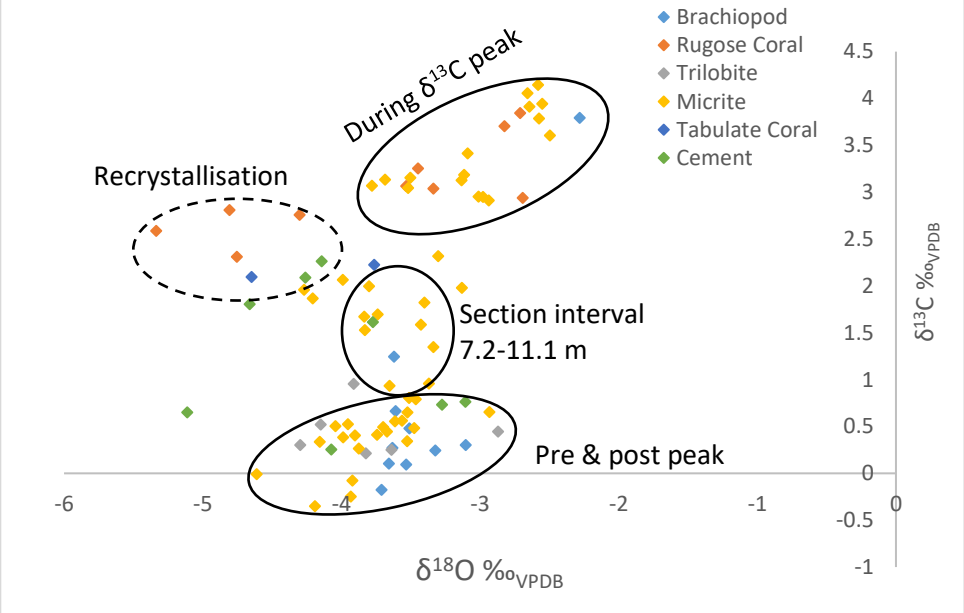

Figure 5.15 Carbon and oxygen isotope analyses plotted against one another. The analyses group in four areas, labelled on the cross plot.

The bulk isotope data in the section recording the positive isotope excursions is very well matched, and this produces a second area on Figure 5.15 with a positive relationship. This is within the circled labelled "During $\delta^{13}C$ peak". Once carbon and oxygen isotope levels return to background levels after the excursion, the data is all grouped with the "Pre and post peak" circle. The final data points appear to group to the left of the graph, and could represent cements and recrystallised samples. This field contains no micrite or brachiopod data, but does include rugose corals, cement material and a tabulate coral sample.

5.3.3 Clumped Isotopes

5.3.3.1 Data Quality - Contamination

There is a potential for the samples collected from Anticosti to not entirely be calcium carbonate. During the reaction phase of clumped isotope analysis, the acid remaining after some samples reacted was cloudy, and occasionally contained particulate matter that had not reacted with the phosphoric acid. Appendix IV shows the results of a digestion analysis of the calcium carbonate content in a fossiliferous whole rock sample and a micritic sample to understand how much of the sample material is calcite. The weights of the remaining residue suggest between 6 % and 7 % of the samples tested contain materials that are not calcium carbonate (did not digest in acetic acid).

It is possible to identify contaminated samples using $\Delta_{48(WRG)}$ and $\Delta_{49(WRG)}$ values. In Chapter 3, section 3.6 there are $\Delta_{48(WRG)}$ and $\Delta_{49(WRG)}$ boundary limits defined for clumped isotope measurements within which samples can be considered uncontaminated. For $\Delta_{48(WRG)}$, any value over 1 ‰ is likely to be contaminated, and for $\Delta_{49(WRG)}$ any result greater than 100 ‰ is likely to be contaminated. For the material used in this chapter, the possible sources of contamination include those discussed in Chapter 3 (such as non-condensable gas and water vapour) but also include potential contaminants from within the fossil material itself. This includes surface debris, such as soil and particular matter, which would hopefully be removed during the rinsing and sonicating process prior to drilling. It may also include materials in the makeup of the carbonate itself. These can be potentially identified by trace element analysis identifying those samples which could have undergone diagenetic alteration (see Section 5.3.4), but could also include clay materials and minor iron and manganese oxides which could be naturally included in or on the carbonate lattice.

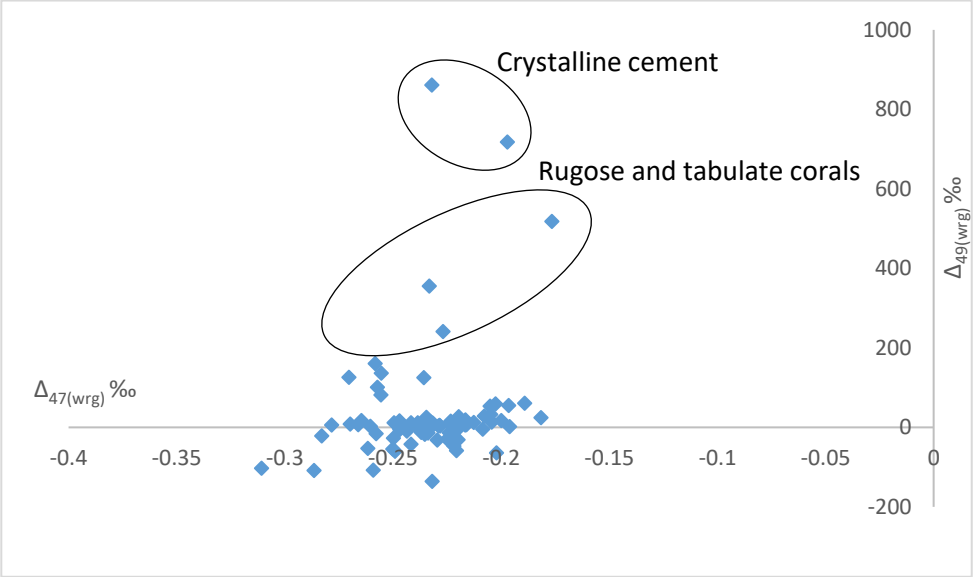

Figure 5.16 The materials showing the highest $\Delta_{49(wrg)}$ values are cement calcites.

Figure 5.16 shows the relationship between $\Delta_{47(WRG)}$ and $\Delta_{49(WRG)}$. Here it is clear there are some outliers with extremely high Δ_{49} values, up to 861.262 ‰. Those samples that were identified as having anomalously high Δ_{49} results were only samples that were clearly cement or void filling calcites, or were the secondary calcite that had precipitated within the rugose and tabulate coral structures. The data showing these potentially contaminated values has been removed in line with the boundary limits set in Chapter 3.

5.3.3.2 Clumped isotope Results

The clumped isotope composition for 28 samples from the same 22 m vertical sequence as the bulk isotopes have been measured. They are reported on the absolute reference frame (Dennis et al. 2011) and are listed in Table 5.3 (see Figure 5.4 for a description of sample locations and stratigraphy). Figure 5.17 shows the average clumped isotope values in their stratigraphic context. This data set includes values from the Lousy Cove and Laframboise Members of the Ellis Bay Formation, and the Fox Point Member of the Becscie Formation. The sampling strategy for clumped isotopes was biased to focus on the interval that represents the Hirnantian glaciation. The samples have again been categorised according to the material type – brachiopods, rugose and tabulate corals, trilobite thoracic segments, micrite (fine-grained mud-rich matrix) and cements (diagenetic precipitate post-deposition within veinlets or voids) or cemented whole rock samples.

Sample Type	Member/Formation	Position in transect (m)	Av. $\delta^{13}C$ ‰$_{VPDB}$	$\delta^{18}O$ ‰$_{VPDB}$ Calc @ 25° C	Av. $\delta^{18}O_{fluid}$ ‰$_{VSMOW}$	Mean Δ_{47} ‰	St. Dev. Of Δ_{47}	n	St. Err. Of Δ_{47}	Av. T from Av. Δ_{47} °C
Brachiopods	Becsie Fm.	15	1.29	-3.72	9.44	0.498	0.104	3	0.060	96.5
Brachiopods	Lousy Cove Memb.	0	0.05	-3.78	2.98	0.575	0.028	3	0.016	51
Brachiopods	Becsie Fm.	16.65	0.61	-3.70	4.01	0.563	0.026	2	0.019	57.1
Brachiopods	Lousy Cove Memb.	2	0.02	-3.48	4.61	0.558	0.010	2	0.007	59.6
Brachiopods	Lousy Cove Memb.	7.2	0.23	-3.67	5.67	0.542	0.008	2	0.006	67.9
Brachiopods	Lousy Cove Memb.	4.8	-0.04	-3.67	3.43	0.570	0.008	2	0.006	53.2
Inter-reef brachiopods	Laframboise Memb.	12.51	3.87	-2.42	6.06	0.553	0.015	2	0.010	62
Brachiopods	Lousy Cove Memb.	4.5	0.22	-3.39	7.39	0.525	0.045	2	0.032	78.1
Rugose Coral Outer	Laffarmboise Memb.	14	3.08	-3.48	8.38	0.513	0.059	3	0.034	86.2
Rugose Coral Outer	Laframboise Memb.	14.1	3.02	-3.35	8.98	0.507	0.034	3	0.019	89.9
Rugose Coral	Laframboise Memb.	13.9	3.80	-2.82	4.66	0.566	0.013	2	0.009	55.5
Rugose Coral	Laframboise Memb.	13.6	3.59	-2.96	7.32	0.531	0.004	2	0.002	74.4
Rugose Coral	Laframboise Memb.	13.8	2.59	-5.33	1.59	0.572		1		52.2
Trilobite Spine	Becscie Fm.	14.6	0.25	-3.64	5.85	0.541	0.050	3	0.029	69
Trilobite Plate	Lousy Cove Memb.	1.3	0.34	-4.30	2.94	0.568	0.002	2	0.002	54.1
Trioobite Plate	Lousy Cove Memb.	2	0.23	-3.94	6.17	0.533	0.012	2	0.008	73.4
Tabulate Coral	Laframboise Memb.	14.1	2.23	-3.76	5.58	0.542	0.030	3	0.018	67.9
Tabulate Coral	Laframboise Memb.	13.5	2.33	-4.55	3.03	0.564		1		56.3
Void Cement - White Calcite	Lousy Cove Memb.	1.3	0.65	-5.11	5.06	0.532	0.010	3	0.006	73.9
Void Cement - Darker Calcite	Lousy Cove Memb.	11.9	2.37	-4.25	2.43	0.575	0.010	3	0.006	50.6

Void Cement - Darker Calcite	Lousy Cove Memb.	1.3	0.25	-4.07	4.45	0.552	0.000	2	0.000	62.4
Whole Rock Sample	Laframboise Memb.	14.6	1.61	-3.77	11.26	0.477	0.005	2	0.004	112.3
Crystalline Grainstone	Becscie Fm.	14.8	1.77	-4.71	5.25	0.535	0.032	2	0.023	72.4
Inter-reef Micrite	Laframboise Memb.	13	3.95	-2.54	4.96	0.565	0.025	3	0.014	55.7
Inter-reef Micrite	Lafamrboise Memb.	13.9	2.94	-3.04	2.66	0.588	0.045	3	0.026	44.6
Micrite	Becscie Fm.	21.5	-0.03	-3.91	7.06	0.523	0.014	3	0.008	79.6
Micrite	Losy Cove Memb.	5.7	0.50	-3.66	4.82	0.553	0.012	3	0.007	62.1
Micrite	Lousy Cove Memb.	11.7	1.99	-4.13	6.67	0.525	0.036	2	0.025	78.3

Table 5. 3 Clumped isotope results of the Anticosti sample set measured on the MIRA mass spectrometer.

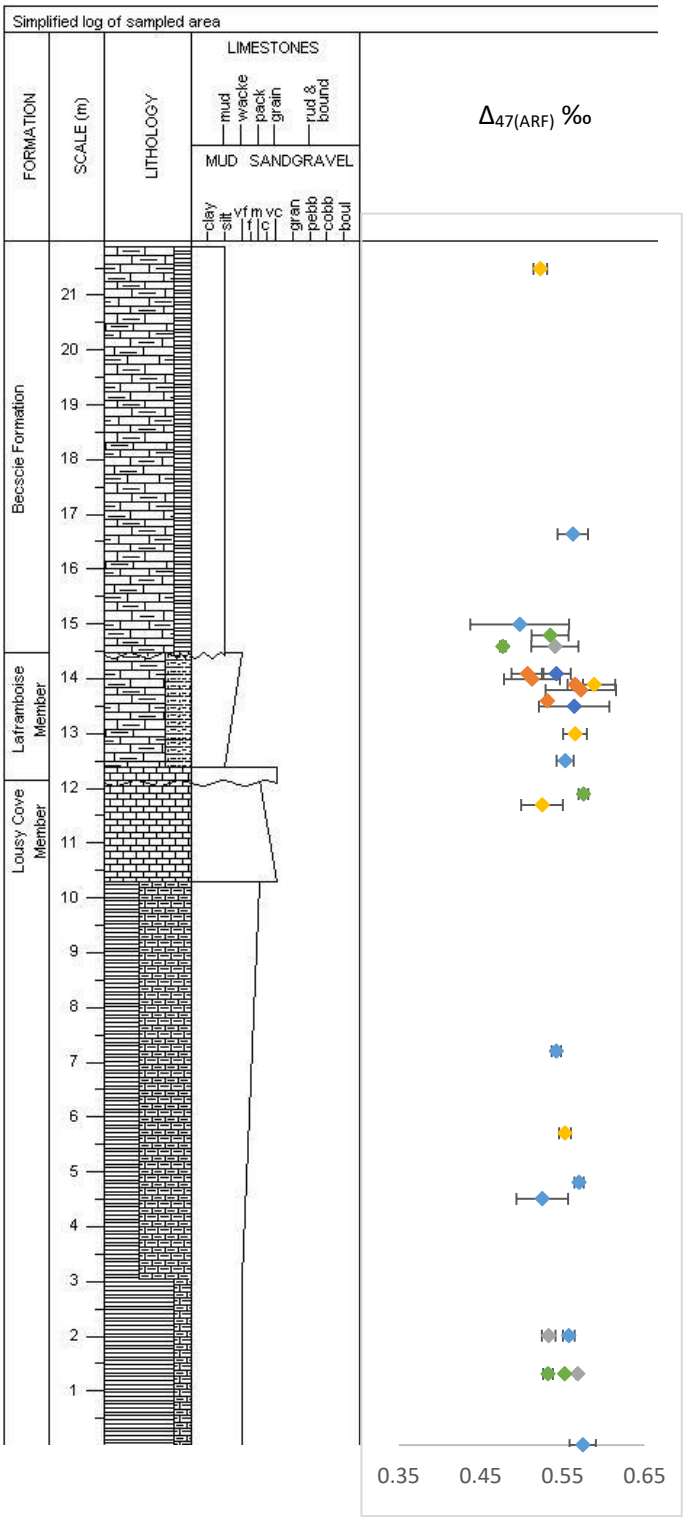

Figure 5.17 Clumped isotope values plotted according to their stratigraphic location.

The average Δ_{47} values measured for this sequence on Anticosti are plotted as a function of their stratigraphic position in Figure 5.17, with error bars representing standard error. The transect position is measured in metres above the start point (0 m) at the upper end of the Lousy Cove member. The samples are colour coded with the same scheme as in the bulk isotope graphs. The clumped isotope values range from 0.47 ‰ to 0.59 ‰. There is no clear trend within the dataset, except that the values remain relatively constant throughout. There are no variations that could represent changing conditions at the end-Hirnantian similar to those seen in the $\delta^{13}C$ and $\delta^{18}O$ data. Any variation is within the measurement error. As sampling was focussed in an attempt to identify a change in temperatures surrounding the final end-Ordovician glaciation, there are fewer samples in the area prior to and after this event.

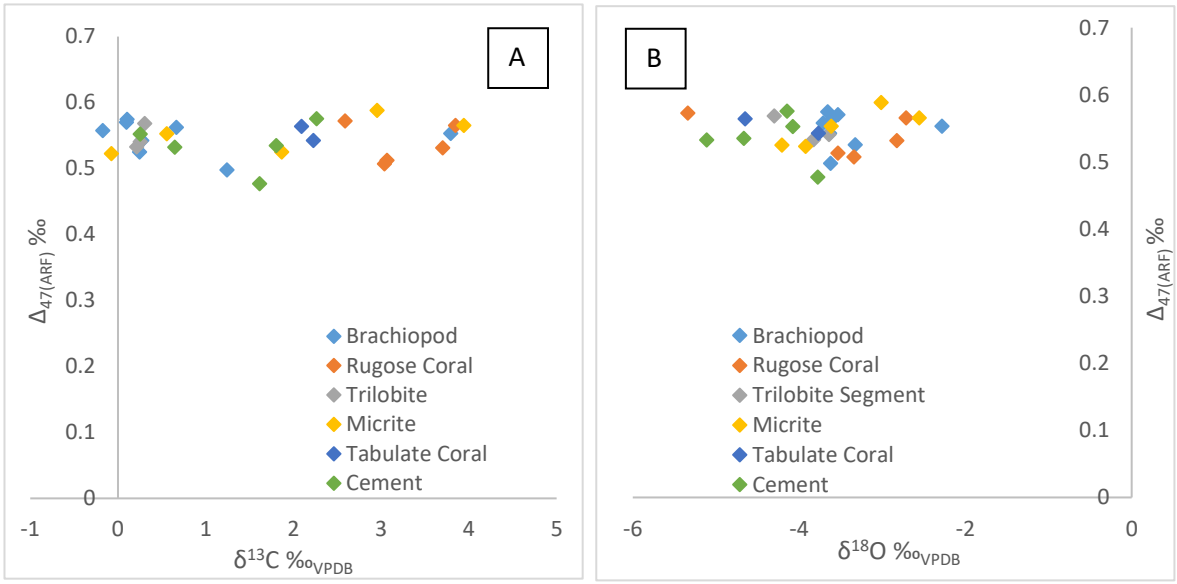

Figure 5.18 The clumped isotope values and bulk stable isotope values measured on MIRA are plotted against one another. There appears to be no overall trends between the different materials.

The clumped isotope Δ_{47} values are plotted against the bulk isotope $\delta^{18}O$ and $\delta^{13}C$ values measured at each transect point according to sample type in Figure 5.18. There appears to be no covariation between Δ_{47} and the Anticosti bulk isotope values. There is no variation according to the type of material. The clumped isotopes generally remain at a constant value (within measurement error) compared to the variation seen in the bulk isotope measurements.

5.3.4 Trace Elements

Averaged trace element data for each material type analysed using laser ablation ICPMS are given in Table 5.4. The significance of these variations are explored in Section 5.4.1.2.

	Na	Mg	Fe	Mn	Sr	K	n
	ppm	ppm	ppm	ppm	ppm	ppm	
Brachiopod average	9069	2990	635	109	732	762	15
Trilobite average	3296	4886	2628	332	938	125	8
Cement average	2299	4848	2311	350	707	406	13
Rugose Coral average	8686	5733	1335	227	617	835	15
Micrite/Matrix average	906044	75040	29559	1920	2171	-17843	29

Table 5.4 Average trace element values for the various materials in this study, and the number of analyses.

5.4 Discussion

5.4.1 Evidence of diagenesis

5.4.1.1 Textural study

Thin section observations show that skeletal remains in limestone have varying degrees of preservation, from well preserved calcites, e.g. brachiopods, to diagenetically altered former aragonite or Mg-calcites e.g. gastropods, trilobite and echinoderm grains. Former gastropod shell walls are missing but chambers retain their shape, completely filled with drusy spar cements. This demonstrates that aragonite dissolution occurred before significant compaction. Brachiopod shells show the best evidence for good preservation. The shells retain their original fibrous calcite texture in the thick secondary layer (Fig. 5.19) and punctae are clear in some of the specimens under CL (Fig. 5.20a). Brachiopod CL response is dull brownish, contrasting with cements in associated shelter porosity (Fig. 5.20) which luminesces bright orange. Dull to no CL response is typical of skeletal calcites that have not suffered diagenetic alteration.

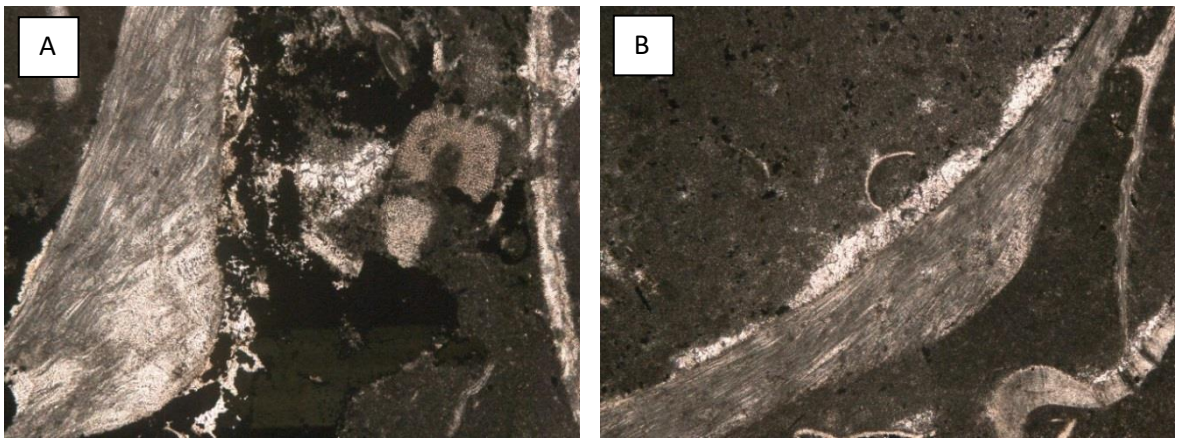

Figure 5.19 A is 0 m bioclastic packstone x4 magnification PPL showing fibrous brachiopod structure. B is 0 m bioclastic packstone x4 magnification PPL showing fibrous brachiopod structure and shelter porosity.

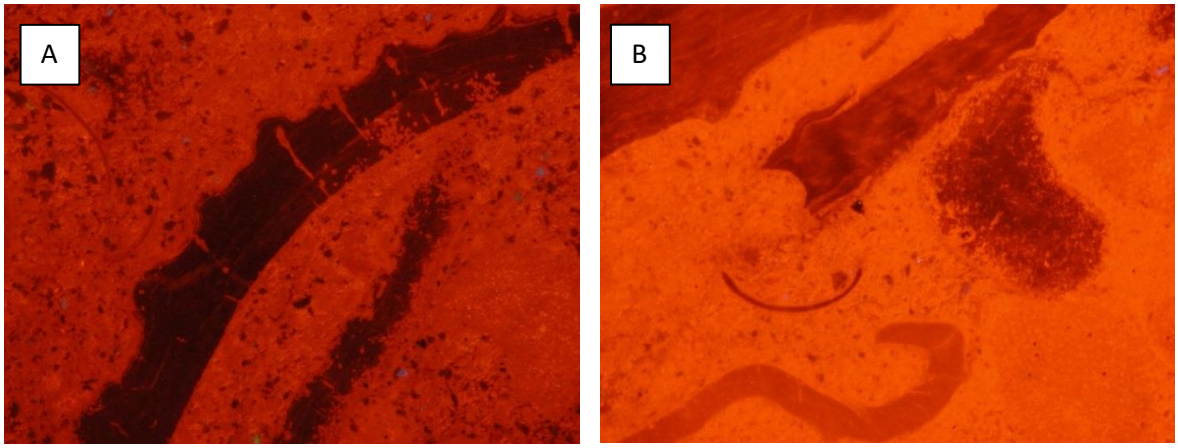

Figure 5.20 A is 0 m bioclastic packstone CL showing darker brachiopod fragments. B is 0 m bioclastic packstone CL showing darker brachiopod fragments.

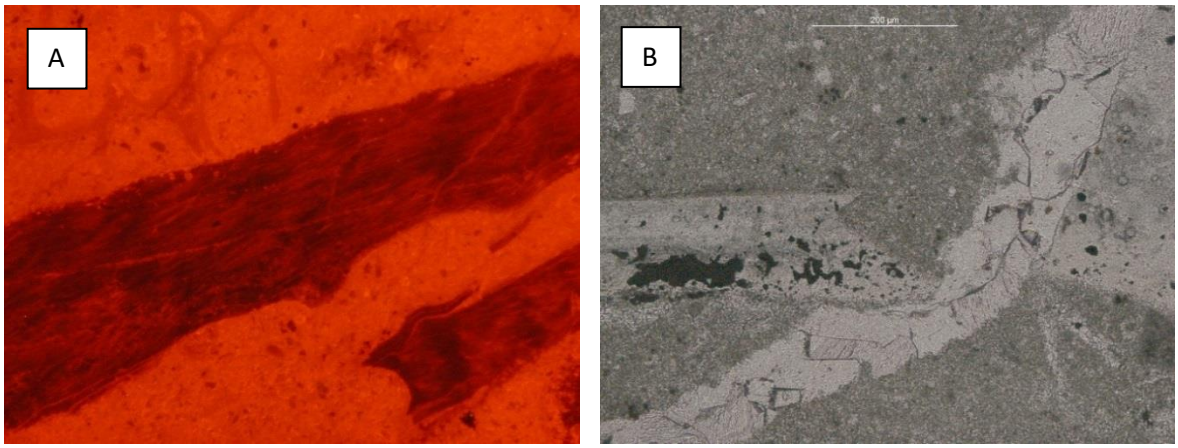

Figure 5.21 A is 0 m bioclastic packstone CL showing veinlets of orange within brachiopod shell. B is 0.6 m bioclastic wackestone x10 magnification PPL showing a broken brachiopod fragment with vein running through it.

Some of the brachiopod shell fragments have a bright orange rim under CL, but as primary shell layer preservation is quite rare (Horowitz and Potter, 1971), these rims are most likely thin layers of cement between the shell secondary layer edge and the matrix. Some shells are broken, sometimes with vein-filling mosaic crystals precipitating within the fracture space (Fig. 5.21); there is, however, no evidence of cement-filled veinlets penetrating the well-preserved brachiopod shells. Interestingly, despite the good preservation, brachiopod material shows no difference in Δ_{47} compared to other fossil material, which suggests either the clumped isotope signature has been changed without any serious textural alteration, or the samples were contaminated with more matrix than was assumed (see sampling protocol).

Trilobite thoracic segments, many with a distinctive 'shepherds crook' shape are quite common within thin sections (Fig. 5.22a and 5.20b) and some show the distinctive canals perpendicular to the shell surface as noted by Cayeux (1916). Although there is some discussion in the literature, trilobite calcite was likely formed as low magnesian calcite (LMC) (Wilmot & Fallick 1989) and has brighter orange luminescence relative to brachiopod shells, but not as bright as the cements of matrix luminescence (see Figure 5.20b). The trilobite material stains red in thin section, suggesting a low iron content. There is no other evidence of pervasive alteration and the luminescence response is ambiguous.

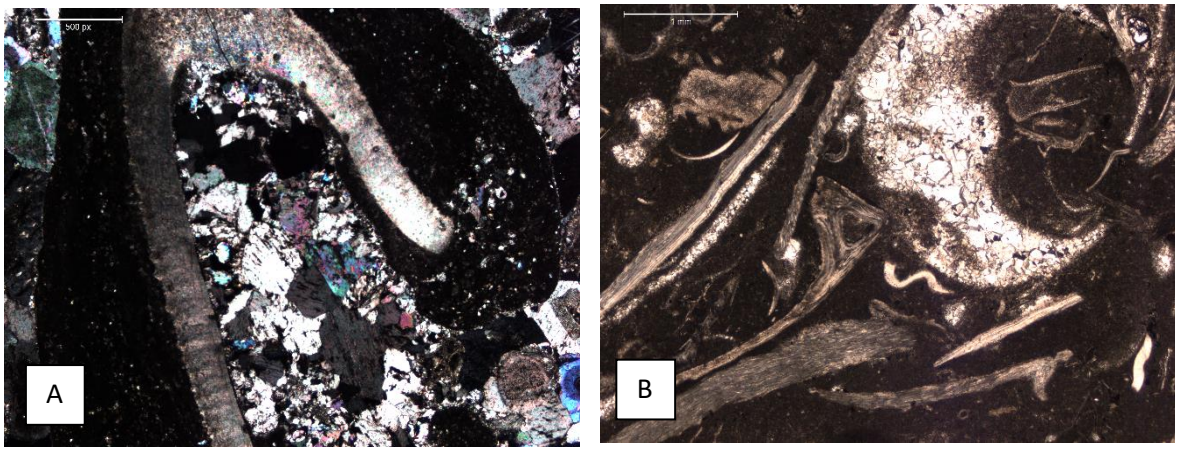

Figure 5.22 A shows 12 m x2.5 magnification XPL showing a trilobite thoracic segment, with sparry calcite area below. B shows 0 m bioclastic packstone x2.5 magnification PPL showing a fossil debris including a trilobite thoracic segment in the lower section of the picture.

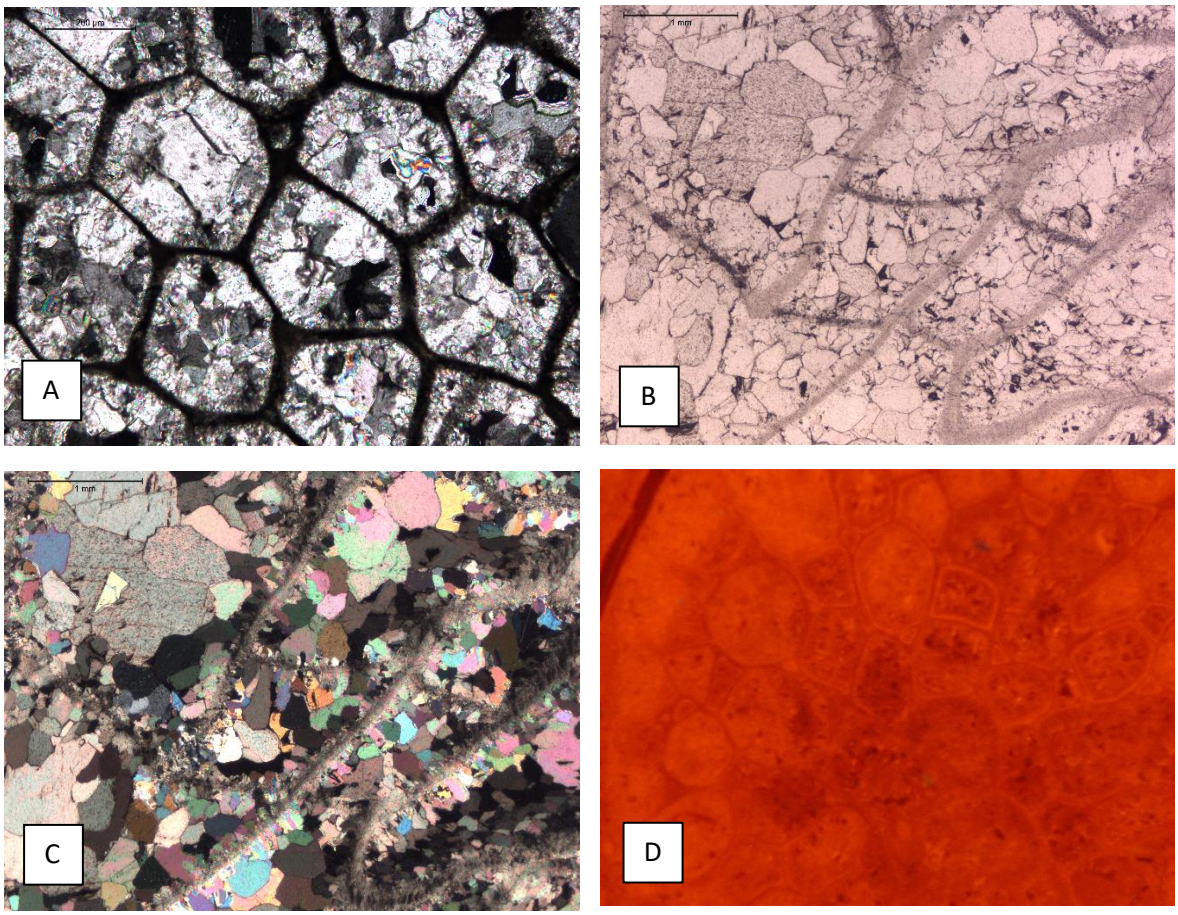

Figure 5. 23 A is 3 m x10 magnification XPL showing rugose corals infilled with sparry calcite. B is coral sample x2.5 magnification PPL showing original rugose coral walls have finer calcite compared with the sparry calcite infills. C is Reef coral sample x2.5 magnification XPL showing same coral B. D is rugose coral under CL showing bright septal walls.

Whilst the rugose corals are largely un-compacted, in thin section it is clear that all inter septal cavities have been fully cemented by drusy spar (Figure 5.23). Rugose coral septal and wall calcite material has much brighter orange CL colour than the brachiopod and trilobite material, which is circumstantial evidence of more pervasive diagenetic alteration. Inter-septal cementation is most pervasive in the central area, which has quite dark CL response. As the coral septal and wall material are both thin, and arguably altered/contaminated with spar cement, it is likely that isotopic data will largely reflect a diagenetic trend rather than depositional conditions.

Carbonate mudstones and the matrix of the wackestones and packstones are essentially micritic with patches of microspar variably present (Fig. 5.22). Under CL, the micritic matrix luminesces bright orange (Fig. 5.20 and 5.21a), suggesting that it has been pervasively altered at some stage during diagenetic events. The micrite contains minor amounts of detrital quartz (dull brown CL) and feldspar (blue CL) silt grains. Some of the micritic carbonates have microbial textures forming oncoids or encrusting surfaces (Figure 5.24). Microbialites are typically associated with

encrusting flat-lying gastropods and/or serpulid worms. Void spaces in microbial layers, which may have been gas- or fluid-filled are now cemented by sparry calcites. Small rhombic dolomite crystals are present, but uncommon, showing bright orange under CL but no zonation. These dolomites do not appear to show replacement relationships and are probably detrital in origin. There is hydrothermal dolomitisation in Lower Ordovician deposits of the Anticosti Basin (Lavoie et al. 2005) so they could be derived from this source. Pyrite appears in the majority of thin sections and is mostly associated with micritic fabrics.

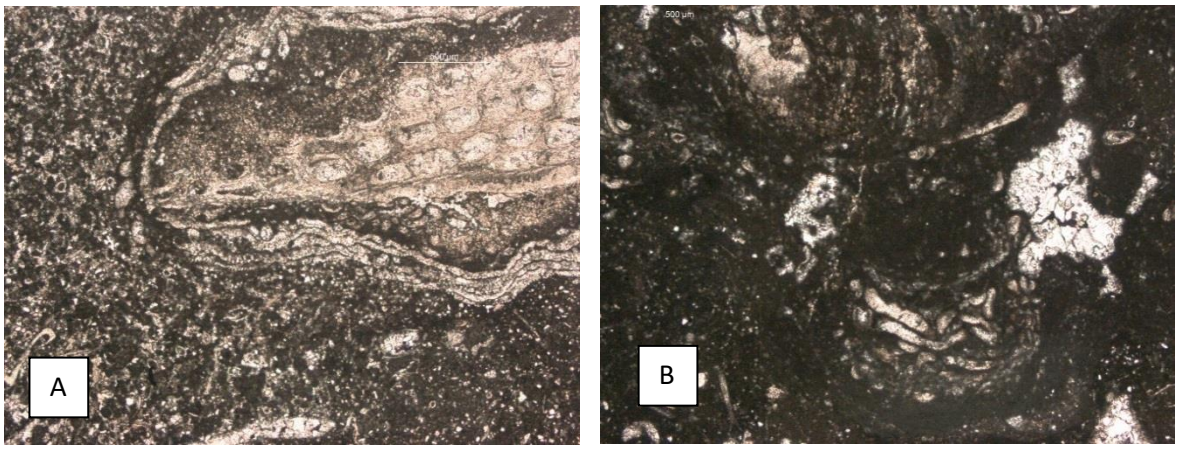

Figure 5.24 A is 13 m bioclastic wackestone x2.5 magnification PPL showing microbial tubes encrusting onto a coral fragment. B is 13.98 m bioclastic wackestone x2.5 magnification PPL showing microbial tubes with light and dark sections.

Most of the samples contain either vein-filling (Figure 5.25a and b) or void-filling cements as described above (for example 5.21b). These cements are also visible in hand specimen, appearing either as patches of cloudy calcite crystals or as rims around voids, and were targets for clumped isotope 'diagenetic' samples (Figure 5.22a and 5.19). Crinoid-rich grainstones show evidence of syntaxial calcite spar overgrowths (Fig. 5.25c and d) and some void-filling spars have geopetal fabrics. These are typically basal micrite inclusion-rich neomorphic spars, sometimes with ghosts of former laminae, defined by an upper dusty line marking the former sediment floor surface, with clear calcite spar above, filling former open space.

Overall these samples present features that suggest some diagenesis has affected much of the matrix and some of the skeletal grains. This means that derived clumped isotope temperatures will, at least in part reflect these events, probably suggesting that temperature will be higher than those formed in purely depositional conditions.

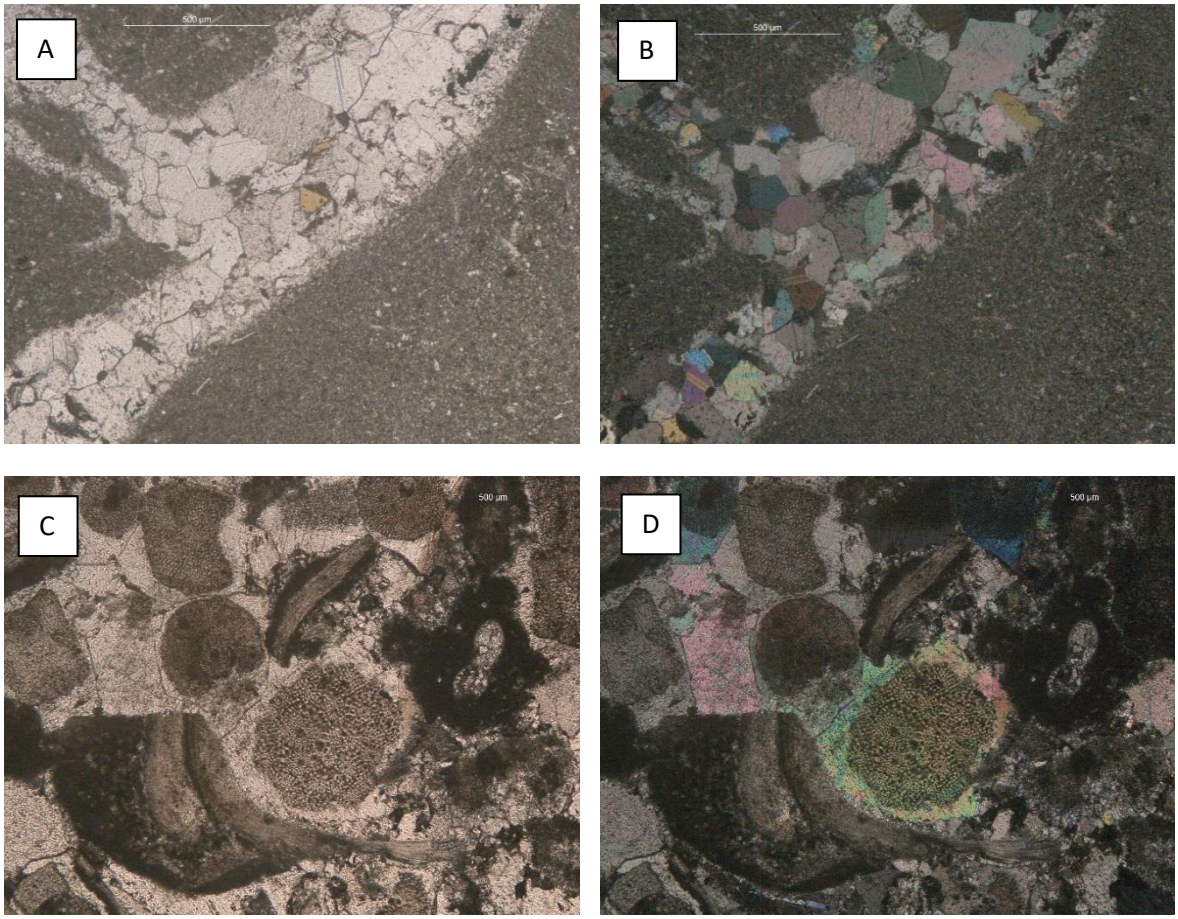

Figure 5.25 A is 0.6 m bioclastic wackestone x4 magnification PPL showing sparry calcite vein. B is 0.6 m bioclastic wackestone x4 magnification XPL showing sparry calcite vein. C is 12 m syntaxial overgrowth of crinoid grain PPL. D is 12 m syntaxial overgrowth of crinoid grain in XPL – going into extinction as one grain.

5.4.1.2 Trace Elements

Trace element data was used to help constrain the extent of diagenetic alteration in limestone and fossil samples. In general diagenesis of calcite typically increases manganese and iron content, and depletes strontium and magnesium (Brand & Veizer 1981; Shields et al. 2003). Trace element data can be used comparatively, relative to the extensive published data (Brand et al. (2003)) ranges of both fossil and modern skeletal carbonates.

It is thought that 200 ppm Mn or less is indicative of a well-preserved modern brachiopod (Brand et al. 2003). The Anticosti brachiopod calcite averages 109 ppm Mn, suggesting they are well preserved (see also Azmy et al. 1998a). Similarly, non-altered brachiopod calcites have Fe contents below 800 ppm according to (Qing & Veizer 1994), whilst Shields et al. (2003) suggest a value <600 ppm is more representative of a non-diagenetically altered brachiopod. Brand et al. (2003) indicate

that modern well-preserved brachiopods have an Fe content <200 ppm. Overall, there is some spread in the Anticosti brachiopod data, but the average value is 635 ppm Fe, around an acceptable level for fossil material. Anticosti brachiopod material shows a range in Sr values but the average 733 ppm (see also Azmy et al. (1998b)) is again similar to published values for a well-preserved brachiopod (less than 2000ppm (Shields et al. 2003; Qing & Veizer 1994)). These values, combined with the petrography and CL confirm that brachiopod calcite is the best target to retrieve an original Ordovician seawater isotopic and temperature signal. However, clumped isotope temperatures derived from these brachiopods are much higher than likely ocean temperatures. This suggests the clumped isotope signal is likely to have been corrupted by a process that leaves both trace element contents, bulk isotopes and petrography relatively unaltered.

The trace element geochemistry of trilobite skeletal material is not as well-documented as brachiopod geochemistry. Brand (2004) did some isotopic and geochemical analysis of Palaeozoic carbonates which included trilobite material. His Mn and Mg values are very close to the Anticosti averages in Table 4. However, the Anticosti trilobite Fe values (average 2628 ppm) are much higher than those considered by Brand (2004) to be well-preserved, which were less than 1000 ppm. Their study concluded that trilobite material is comparable to brachiopod material for the preservation of seawater isotope compositions, and the Anticosti samples show comparable isotopic values in both brachiopods and trilobite calcites which supports this suggestion. The elevated Fe contents in this study may suggest there has been some diagenetic affect, which is not uncommon in the early diagenetic stabilisation of Mg calcites (Richter and Füchtbauer, 1978). However, the trilobite material stains red, suggesting a lower Fe content and no diagenetic change from high Mg calcite.

Work on Devonian limestone by (Popp et al. 1986) showed that corals, micritic material and sparry cements had lower Sr values than brachiopods present in the same section. The Anticosti data (Table 5.4) show similar relationships for these materials except for the micrite Sr, which is considerably higher than in other components. Corals and micrite material are also considered to have higher Mn values than brachiopods (Popp et al. 1986), which is seen in the Anticosti samples. As already shown by petrography, it is likely that the majority of coral material has been either replaced by a secondary cement, or contaminated by a cement during sampling suggesting that ‘coral’ samples are essentially diagenetic sparry calcite samples. Barring Na and K, Table 5.4 indicates that the averaged values for the other trace elements are quite similar between rugose corals and cement. Both the corals and sparry cements luminesce strongly, which suggests the corals have undergone some diagenetic alteration. During stabilisation of depositional calcites and aragonites the usual trend under open system conditions is depletion of Sr as Mn increases (Veizer

1983). However, for Anticosti material the observed relationship is reversed for rugose corals, cements and micrites (Fig. 5.26).

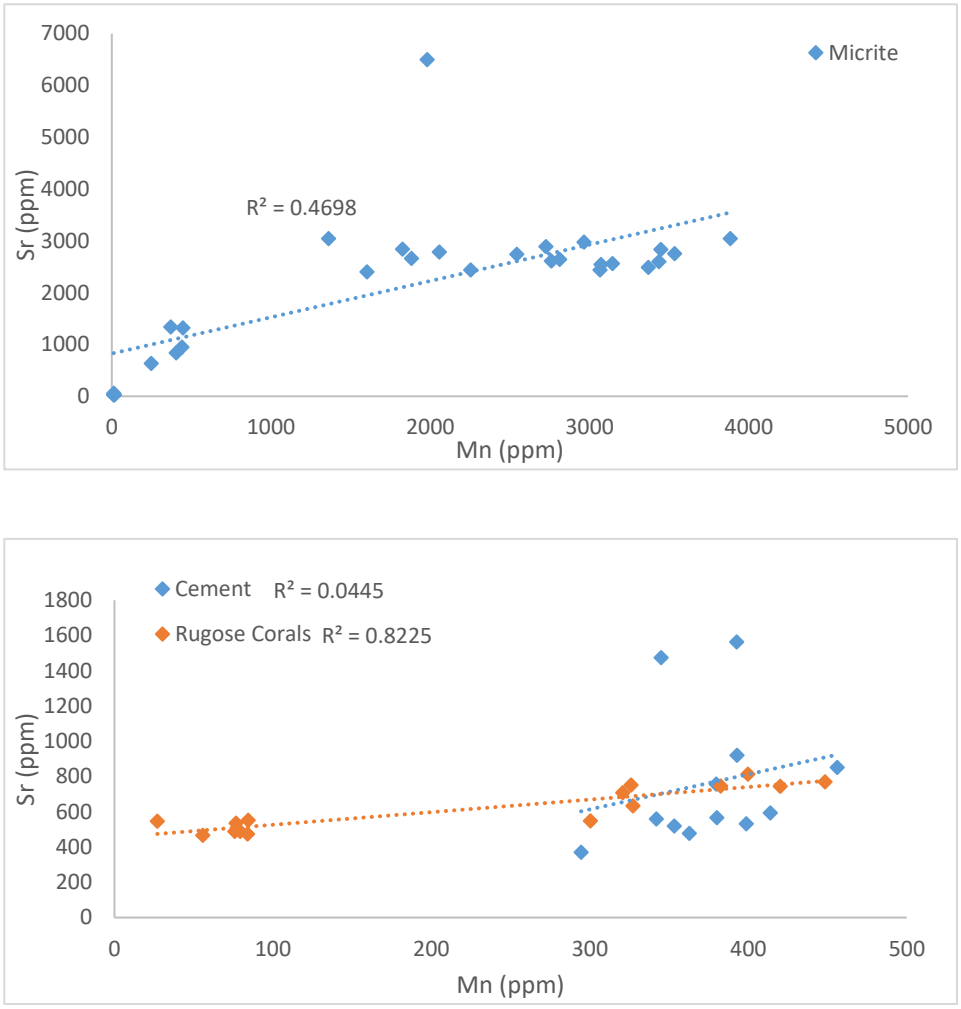

Figure 5.26 Plotting the diagenetic relationships between trace element values retrieved from the Anticosti study material.

The rugose coral data show a fairly strong positive relationship between Mn and Sr (R^2 = 0.82), as does the micrite data (R^2 = 0.47). This the opposite trend from what is expected during diagenesis. The cements show a less clear relationship. This data might suggest that early diagenesis was under relatively closed conditions, with aragonite dissolution releasing Sr to pore fluids which was then incorporated into neomorphic micrites and spars. Notwithstanding this the high Mn values (Miller 1988) explain the bright luminescence of the micrites and other diagenetically altered calcites.

5.4.2 Clumped Isotopes

A key aim of this study is to assess the possibility of using clumped isotope compositions of sedimentary carbonates and associated biogenic components as a proxy for Earth surface temperatures in the geological past. The end-Ordovician Hirnantian glaciation represents a major climatic shift that may be possible to study using clumped isotopes. Anticosti was chosen as a case study due to its well-defined stratigraphy and well-preserved geological record (See Section 5.1 Introduction). The findings from this study have been broken down into the sections below so that each area of information can be discussed before a final overall understanding is reached.

5.4.2.1 Earth Surface Temperatures

The temperatures recovered by clumped isotope analysis of samples from the sequence on Anticosti cover a wide range (42 °C to 112 °C). These temperatures cover a range that is far higher than the modern ocean temperature range for tropical regions (approximately 22 °C to 32 °C (National Oceanic and Atmospheric Administration Ocean Climate Observation Program, data from July 2016)). These retrieved temperatures are highly unlikely to support marine life in the Palaeozoic (Veizer & Prokoph 2015). These elevated temperatures are strong evidence to suggest that the original marine clumped isotope signature has been overprinted. As noted in Figure 5.16, there is no significant variation in Δ_{47} value throughout the end-Ordovician glaciation event, suggesting no record remains preserved of possible temperature changes during this time. In terms of the different types of material analysed (micritic material compared to fossil and cements), there is also no significant temperature variations. For example, brachiopod material ranges from 51 °C to 96 °C, and cement material has a similar range from 50 °C to 112 °C. The large range in values suggest there is a range of partial resetting in the Δ_{47} values. To help understand the partial resetting of the clumped isotopes, the derived temperatures ($T_{\Delta 47}$) are plotted as a function of the isotopic composition of water that is in equilibrium with the carbonate in Figure 5.27.

Clumped isotope analysis allows us to calculate a fluid composition with which the calcite would have been in equilibrium with during formation. This can be calculated independently from the temperature of the fluid. Kim & O'Neil (1997) defined the low temperature oxygen isotope fractionation between water and calcite as:

$$1000ln\alpha(Calcite - Water) = 18.03(10^3 T^{-1}) - 32.42 \qquad \text{(Equation 5.1)}$$

where T (temperature) is in degrees Kelvin and α is the fractionation factor between the calcite and the fluid. Using this equation, it is possible to calculate the composition of the fluid with which the

calcium carbonate of the Anticosti samples was in equilibrium with and therefore potentially precipitated from. These values are shown in Table 5.3. Fluid $\delta^{18}O$ is standardised to VSMOW. The relationship between oxygen isotopic composition of the carbonate, the oxygen isotope composition of the fluid and the Δ_{47} calculated temperature is displayed in Figure 5.27. The isopleths in this figure are contours of constant calcite $\delta^{18}O$ values. They represent curves of oxygen isotope composition for water in equilibrium with the indicated $\delta^{18}O$ of the calcite. These curves are as a function of temperature, and are calculated using the isotopic equilibrium equation defined by Kim & O'Neil (1997) (Sheppard 1986; Gregory et al. 1989; Eiler 2011).

The isotopic composition of fluids in equilibrium with carbonate sample from Anticosti are all positive and lie in the range of 1.6 ‰ and 11.3 ‰. The lowest recorded temperatures of 40 °C to 50 °C are in equilibrium with fluids having an isotopic composition of 1.5 ‰ to 3.4 ‰ rising to 12.3 ‰ for the highest reported temperature of 112 °C. Samples from Anticosti plot in a band of $\delta^{18}O_{calcite}$ values between approximately 26 $‰_{VSMOW}$ to 28 $‰_{VSMOW}$. This trend is characteristic of diagenetic evolution of an isotopic system under closed or near-closed conditions (Eiler 2011). Overlying the plot are vectors which represent evolution under open and closed conditions.

Open system conditions are characterised by large water/rock ratios. A carbonate system that undergoes a temperature increase under open system conditions will have its oxygen isotope composition buffered by the composition of the formation fluid. For marine fluids this would be close to 0 ‰, and for meteoric fluids this would be <0 ‰. As the temperature increases, the oxygen isotope composition of the carbonate evolves towards a more depleted value. This trend was seen within modern borehole measurements taken from the Gulf Coast (Sheppard 1986). Isotopic exchange under open system conditions likely occurs by dissolution/re-precipitation processes.

Sheppard (1986) also noted that modern formation fluids measured from other basins (for example the Michigan basin) remain close to their initial formation values as the temperature increases. These fluid isotope values plot along a narrow range of calcite equilibrium values. The calcite curves of constant value are roughly parallel to the subsurface change in the isotopic composition of the water as a function of temperature. This suggests that in geological examples, the curving line of constant calcite and plotted fluid values can be extrapolated back to the original surface fluid composition (Gregory et al. 1989). Under closed system conditions, the water:rock ratio is low, and the oxygen isotope composition of the system is buffered by the rock. As the temperature rises, the carbonate isotopic composition is invariant, or nearly invariant, whilst the fluid evolves towards a more enriched $\delta^{18}O$ value. This is reflected in the modern fluids that were measured in the basin systems in Sheppard (1986).

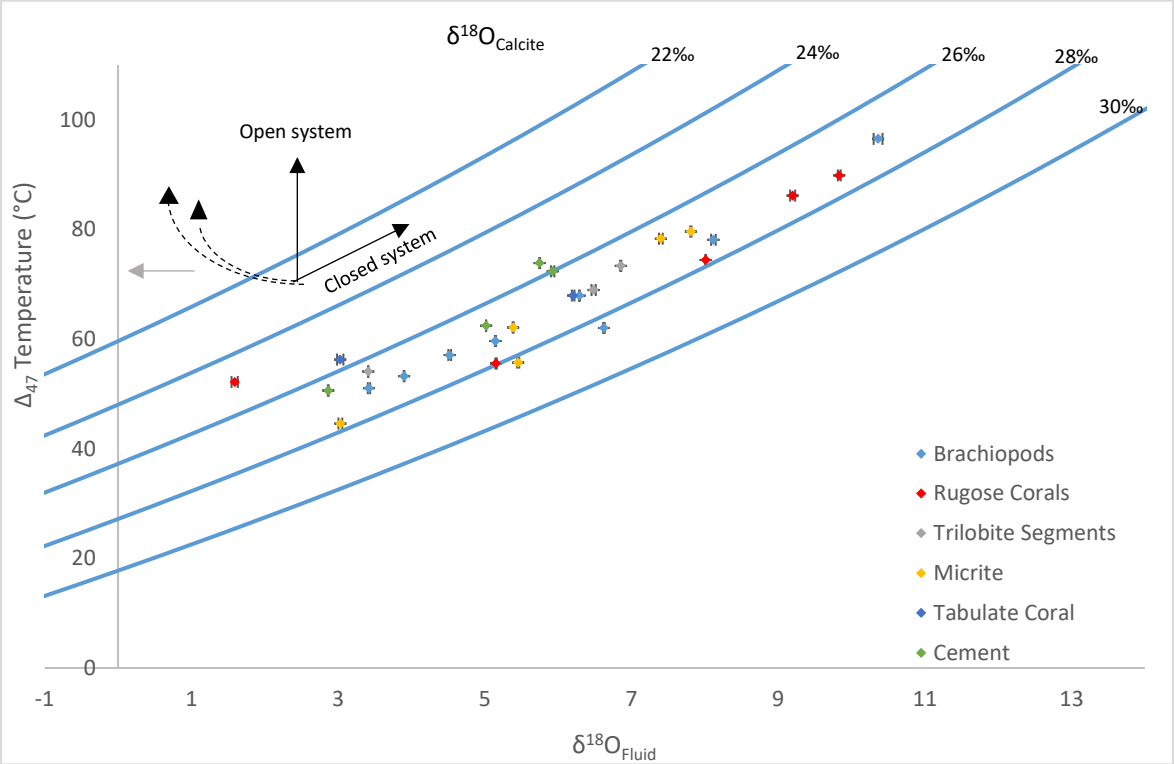

Figure 5.27 Anticosti fluid and Δ47 derived temperatures showing closed-system evolution of the Anticosti basin. Fluids are reported vs VSMOW.

It is clear from the plot in Figure 5.27 that the end-Ordovician/Silurian sequence sampled from Anticosti has evolved under closed or near-closed system conditions. The samples plot within a curving trend suggesting a near-invariant oxygen isotope composition whilst the isotopic composition of the fluid becomes more enriched as the temperature has increased. The clumped isotope signature has undergone resetting or partial resetting towards values consistent with diagenetic temperatures whilst the bulk isotope values have not been substantially altered.

The range of resetting temperatures rises up to approximately 100 °C, therefore reflecting the temperatures experienced during diagenesis. If the maximum burial depth is assumed using the maximum likely sediment to be added to the section after the sampled sequence (see Burial History Section 5.1.7), and a geothermal gradient of 25 °C per 1 km is assumed, the maximum temperature the material could have been exposed to was 88 °C (assuming a start temperature of 20 °C). This is in keeping with the range of clumped isotope temperatures retrieved in this study, and with the Conodont Alteration Index measured in McCracken and Barnes (1981), which suggested temperatures no more than 90 °C.

5.4.2.2 Ocean Fluids

The cement calcite crystals include vuggy crystal growths into voids (see figure 5.13). There are also veinlets present within the samples but they are too small for accurate drilling to produce the amount required for clumped isotope analysis. The oxygen isotopic fluid composition calculated for these samples should be a direct representation of the fluid composition from which the cements precipitated. The fluid values calculated from the other materials (fossils and micritic material) can only suggest a notional fluid value, as the calculated value represents how this material interacted with fluid.

The temperatures derived from analysis of clumped isotopes are not representative of marine depositional conditions. This lack of an original marine signal is also suggested by the enriched fluid oxygen isotopes. Modern tropical ocean isotopic composition ranges between 0 ‰ to 1.5 ‰ (Global Seawater Oxygen-18 Database). The values calculated for Anticosti in this study are far more enriched than the modern ocean. This again suggests this is not the original fluid composition, as a positive ocean isotopic composition would suggest unfeasibly hot temperatures for seawater.

As the calcite trend shown in Figure 5.27 reflects the evolution of the ocean fluid as the sequence was buried deeper, it is therefore possible to extrapolate back to the original isotopic value of the seawater. Veizer & Prokoph (2015) suggest that the early Palaeozoic oceans had a depleted isotopic composition between -4 ‰ and -6 ‰. For the samples measured in this study, at tropical seawater temperatures between 20 °C to 30 °C, this suggests a seawater oxygen isotope value of -2 ‰ to -4 $‰_{VSMOW}$, very similar to the range in Veizer & Prokoph (2015).

5.4.2.3 Implications for Bulk Isotopes

The implication of identifying that the clumped isotope signature has been altered raises the question of whether the bulk isotope record has also been overprinted with a diagenetic signal. In figure 5.26, it is clear that the Anticosti Basin has evolved under closed system conditions. This means that the bulk isotope composition should be buffered by the isotopic signal of the rock, and not by the fluid isotope composition. Therefore, as the basin evolves, the oxygen isotope composition of the sequence remains constant and records an original environmental signal.

A second suggestion that the original bulk isotopic composition has been preserved is the presence of the carbon isotope excursion at the end of the Hirnantian glaciation event. The $\delta^{13}C$ values clearly show a background constant value prior to the end-Hirnantian glacial event, after which there is a clear peak during the interglacial recorded in the Laframboise Member and the start of the Becscie Formation. The $\delta^{18}O$ of the carbonate is near uniform, with a small excursion

located in the same geological sequence as the carbon isotope excursion. As these excursions have been retained in the bulk isotope record, it is unlikely they have been overprinted by diagenetic processes, and therefore retain original environmental indicators. Further discussion of these environmental record preserved in the bulk isotopes will be outlined later in this discussion, but for now this raises the question of what post-depositional process could cause the clumped isotope signal to be reset whilst retaining an original bulk isotope signature.

5.4.2.4 Evolution of Clumped Isotopes

By whatever method the system has evolved, the original bulk isotope system has been preserved to a certain extent, whereas the clumped isotope signature has been altered to varying degrees. For the bulk isotopes to remain unaltered, diagenesis has occurred under a low water to rock ratio within a closed system, in one of the scenarios outlined below.

5.4.2.4.1 Solid state diffusion reordering

Clumped isotope signals can be altered by post-depositional events, typically through solid-state reordering. This is essentially a reordering of the distribution of bonds between carbon and oxygen when temperatures are elevated during diagenetic alteration. This can occur with little or no interaction with the phase that surrounds the crystal, and therefore can preserve the bulk isotope composition. The clumped isotope record is altered at the lattice level, whereas the oxygen isotope value is altered in terms of whole grains. The oxygen can diffuse through the crystalline carbonate and change the proportions of ^{13}C-^{18}O bonding. This occurs in a 'closed' system where the bulk isotopes are buffered by the surrounding rock (Eiler 2011). Passey & Henkes (2012) suggested that different carbonates will be more or less susceptible to bond re-ordering, depending on the types of lattice defects present along with features of the carbonate itself, such as at grain boundaries. Further work by Henkes et al. (2014) suggest that original brachiopod temperatures were preserved when buried to 100 °C as a maximum for not more than 10^8 years. If kept within these parameters, a brachiopod is unlikely to undergo solid-state diffusion. At 160 °C, they predicted that the clumped isotope signal would be completely reordered. They also suggested that the bulk chemistry may control a crystal's resistance to re-ordering. The trace element composition implies ionic impurities, which can create defects (Henkes et al. 2014).

Veizer & Prokoph (2015) suggest that as the clumped isotopes can be altered at the lattice level by processes such as solid state diffusion by altering the ^{13}C-^{18}O bonds, there is no recrystallization of the grain. The bulk isotopes can act as closed system at the grain level. This would mean that any optical and chemical attributes are retained whilst the clumped isotopes are

reset. The Anticosti samples appear to reflect a situation very similar to this. On the whole, the petrographic appearance of the fossils suggests good to moderate preservation, and the trace elements for the brachiopod calcites are not far from those expected in a well preserved sample.

As already discussed, the burial history of Anticosti is not fully understood, but according to suggested sediment thicknesses, it is likely to have been buried to a depth where temperatures are reaching approximately 90 °C if we take the maximum value for sedimentation (see Burial History section). The length of burial time before uplifting is also not well known, but again is likely to be in excess of 10^8 years (if uplift started during the Jurassic, this would be approximately 180 Ma – see Burial History Section 5.1.7). The elevated clumped isotope temperatures in this study are on average lower than the 100°C limit defined by (Henkes et al. 2014), but do not reflect an original ocean temperature. This shows that the clumped isotope signal has been altered, but it is unknown whether this could be through solid state diffusion and reordering, as Anticosti does not entirely fit the outlined parameters. The bulk isotope values combined with the clumped isotope temperatures indicate a closed, rock-buffered system during diagenesis, preserving the bulk isotope composition of the calcite. This is demonstrated by the fluid phase (e.g. the sparry calcite infills) having a very similar oxygen isotope composition to the rest of the components of the rock. The clumped isotope signal is altered, but when combined with the information concerning the burial history, it does not seem likely that solid state diffusion and reordering is entirely responsible for the elevated temperature record.

5.4.2.4.2 Grain growth and recrystallization

Grain growth and recrystallization are typical of metamorphic rocks, where grain growth is driven by the high surface energy of fine grained rocks. The extent to which this happens under diagenetic conditions is difficult to ascertain. Many sediments show evidence of grain boundary dissolution and re-precipitation, where less soluble minerals grow at the expense of the more soluble minerals around them. This occurs through processes such as pressure solution along the grain boundary. The solution of mineral grains occurs at the point of contact, and is then re-precipitated on a free surface. Features such as fossil fragments show no sign of deformation of the fragments whilst this pressure solution mechanism occurs (Weyl 1959). It is possible that the fine-grained micritic material within the Anticosti samples could be preferentially dissolved and re-precipitated as overgrowths on the larger grains. This process would be similar to grain growth in metamorphic systems that involves grain boundary migration. As the material dissolved is re-precipitated locally, there would be no change to the overall bulk isotope composition recorded in

the calcite. However, there is the potential for re-distribution of the ^{13}C-^{18}O bonding, therefore altering the clumped isotope temperature recovered.

5.4.2.4.3 Dissolution and re-precipitation

Weyl (1959) also noted a second mechanism of solution alteration. This is local recrystallization of sedimentary material caused by differences in aspects such as crystal size and mineralogy. An example is the difference between the solubility of aragonite and calcite. This creates a concentration gradient within the solution which causes an increased dissolution of the more soluble phase (aragonite) whilst increasing the precipitation of the more stable and less soluble phase (calcite). Again, this is material dissolved locally and then re-precipitated within the same system, thereby no overall changes in chemical composition can occur (Weyl 1959). The bulk isotope composition is preserved, whereas the clumped isotope record (depending on the distribution of ^{13}C-^{18}O bonds) could be altered.

5.4.2.5 Comparison with other studies

There have been some previous isotopic studies of the geological sequence recorded on Anticosti. These include both conventional bulk isotopic studies and one clumped isotope study. Bulk isotope results within this study are similar to the values published in previous studies. This will be discussed later in Section 5.4.3. The clumped isotope measurements that have been previously made are published in Finnegan et al. (2011), and the results of this study contrast with the published work. Finnegan et al. (2011) sampled similar fossil material (brachiopods, rugose corals and trilobite material) and derived clumped isotope temperatures from 28 °C to 49 °C from material within the same formations as this study. The range of temperatures from the western outcrops on Anticosti are shown in full in the supplementary data of the paper, and are also displayed in Figure 5.28. Some material was removed from the data suite as it was identified to be altered through diagenesis (see Figure 5.28 caption for outline of this). The data that was later removed is displayed in blue on the graph, and the orange data is what was used in the publication. They identified a temperature decrease during the final event of the end-Ordovician glaciation, with a return to warm temperatures at the very end of the Hirnantian stage. A change of 5.4 °C is recorded within these periods.

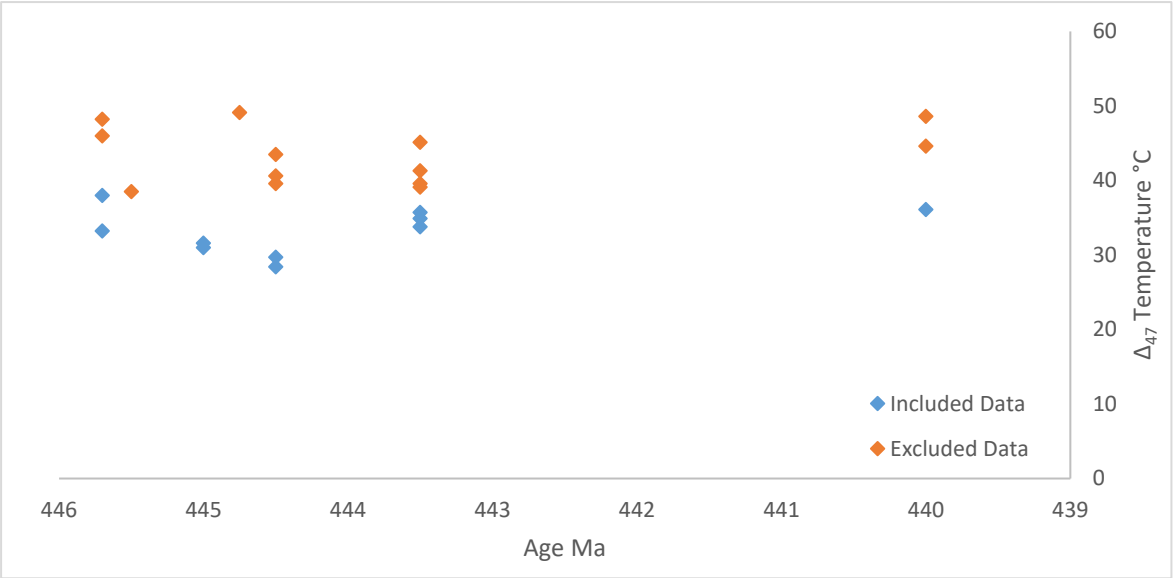

Figure 5.28 Re-plotted clumped isotope derived temperature data from Finnegan et al (2011). Blue is data falling within their preservation parameters (defined by PC1 results and Δ_{47} values), whereas orange is data that appears altered.

Whilst the published data show a low temperature comparable to today's tropical ocean, the dataset when taken as a whole shows a range of temperatures similar to the lower end of the temperatures measured in this study. Finnegan et al. (2011) used the lowest temperature samples within the respective time intervals to form a basis for trend lines. Whilst some of the individual analyses in this study have produced derived temperatures similar to the temperatures of Finnegan et al. (2011) (see Appendix V), these low temperatures disappear when data points are removed as they show effects of contamination on Δ_{48} and Δ_{49}. Averaging the repeated analyses also removes the lowest and highest single measurements. It is possible that the data used in Finnegan et al. (2011) showed no contamination effects on Δ_{48} and Δ_{49}, and this method was not used as a basis for removal of contaminated material. They do not state whether any analyses were removed from the dataset due to contamination on the clumped isotope results. Samples were only excluded on the basis of textural and trace element analysis.

The data included in Finnegan et al. (2011) is predominantly rugose coral material, as it appeared to be the most well-preserved. They were unable to extract well-preserved brachiopod and trilobite material from the Laframboise Member. This again contrasts the findings of this study, as the rugose corals sampled here appear to be recrystallized and spar filled, therefore contaminated during sampling. The brachiopod and trilobite data appears optically the best preserved. When all of the data from the Finnegan et al. (2011) study is combined (Figure 5.29), the spread of values at each stratigraphic interval could be reflecting a range of partial resetting effect similar to the interpretation in this study, rather than a shift in temperature. Veizer & Prokoph

(2015) suggest that habitat palaeotemperature ranges are from 14° to 32° for brachiopods. The data published in the supplementary information of Finnegan et al. (2011) are at the upper end and outside this range, similar to the temperatures retrieved in this study. This greater range of temperatures again suggests there has been resetting of the clumped isotopes.

It is worth considering the effect of the temperature calibration used to derive a temperature from the Δ_{47} value. At this point in time, there are many different temperature calibrations published, and calibrations are very varied (for a full discussion on this subject see Chapter 4). When temperatures are derived using the UEA calibration, it has the effect of increasing the temperatures calculated from the Finnegan et al. (2011) study due to the different gradient. The difference in slope between different temperature calibrations means that the range of temperatures calculated from the Δ_{47} value will be different for each calibration used.

A second difficulty in comparing the Finnegan et al. (2011) data with this study is that at the time of publishing, the data was not projected onto the Absolute Reference Frame (Dennis et al. 2011) whereas the data in this study is. The data from the Finnegan et al. (2011) study cannot be projected onto the ARF as the working reference gas composition used to analyse the samples at that time is unknown. If the data could be projected onto the ARF, it would likely reduce the amount of scale compression, and therefore increase the range of Δ_{47} values recorded.

Finnegan et al. (2011) also calculated the oxygen isotopic composition of the water with which their calcium carbonate samples would have been in equilibrium with. The values for the same sequence as this study are plotted with respect to the clumped isotope derived temperature in Figure 5.29. This figure shows the data from this study in red, and the Finnegan et al. (2011) study in blue. The values calculated fall at the lower end of the range of my data, and plot within the 26 ‰ to 30 ‰ contour lines, again similarly to the data in this study. The values again follow the vector that defines closed system diagenesis. Their fluid isotope values are more depleted than the values in this study, but still more positive than the values for the ancient ocean suggested by Veizer & Prokoph (2015). However, if their data was interpreted as a diagenetic trend, then following the trend back to between 20 °C and 30 °C would indicate an ocean composition of between -1 ‰ and 1 ‰.

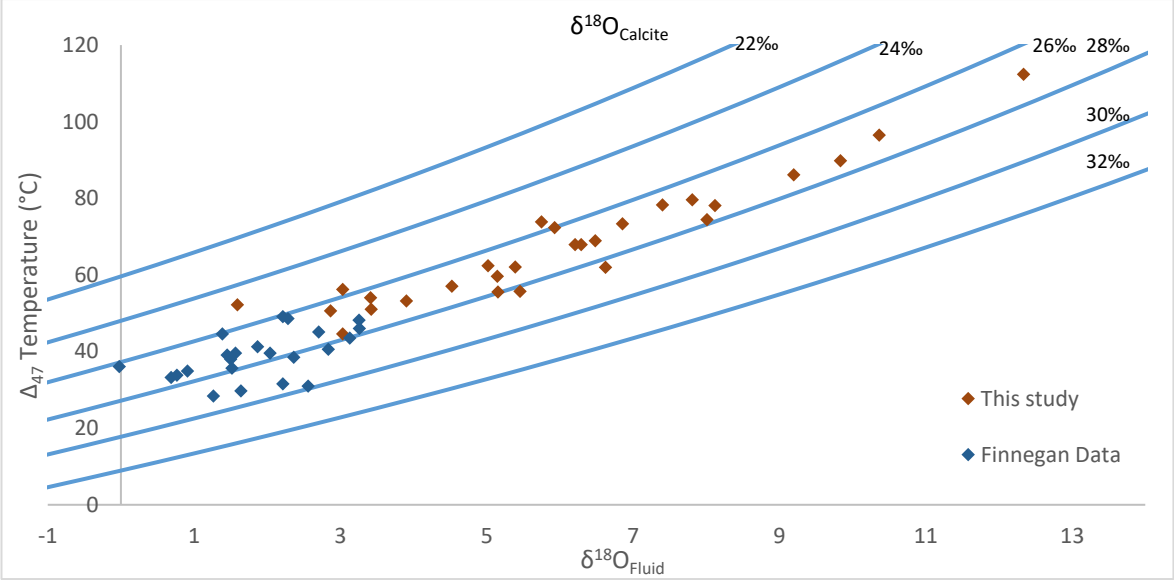

Figure 5.29 The relationship between Δ_{47} derived temperatures and the calculated fluid isotopes are displayed for both the data in this study, and the data taken from the supplementary information of Finnegan et al (2011). Isopleths of constant δ18Ocalcite are displayed in blue.

Finnegan et al. (2011) suggest that their enriched fluid isotopes are part of an overall enrichment between the mid-Katian to the end of the Rhuddanian stage, reflective of the growth of ice sheets prior to the final glaciation event. Within this period with enriched oxygen isotopes, the Hirnantian glaciation can be identified as a peak, followed by a drop during the final Laframboise interglacial period. This does suggest that they can recognise a change in the fluid composition that is controlled by the growth of ice sheets. However, the choice of data again includes only those with the lowest Δ_{47} values to be included in calculating the fluid isotopes. Due to the partially reset nature of the clumped isotopes on Anticosti, it is possible that the peak in temperature in Finnegan et al. (2011) after the end Ordovician glaciation event may not be as well-defined as they demonstrate.

5.4.3 Environmental signals in conventional bulk Isotopes

5.4.3.1 Oxygen isotopes on Anticosti

The samples analysed in this study show a $\delta^{18}O_{carbonate}$ small positive excursion during the Laframboise Member deposited at the very end of the Ordovician period. Other workers have also identified this excursion on Anticosti Island: (Darrel G.F. Long 1993; Azmy et al. 1998b; Brenchley et al. 2003; Jones et al. 2011; Finnegan et al. 2011) for example. As outlined in Section 5.3.1, there is a clear drop towards a more negative value in the final section of the Lousy Cove Member, before the $\delta^{18}O_{carbonate}$ rises to a small peak for the duration of the Laframboise member. This sequence is

very similar to that found by Jones et al. (2011) at the western end of Anticosti. The positive shift of 2‰ seen in this study is also visible in material analysed by Young et al. (2010b) (Figure 5.30).

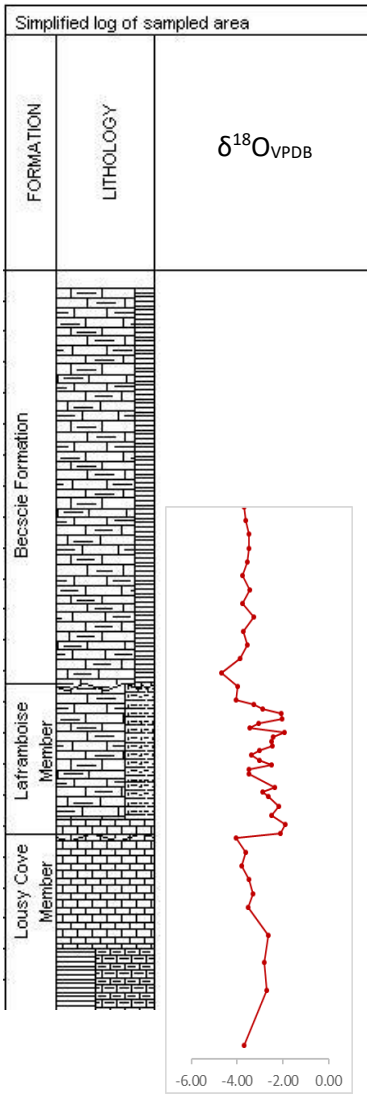

Figure 5.30 $\delta^{18}O_{VPDB}$ from Young et al (2010) showing a clear oxygen isotope excursion through the Laframboise Member on Anticosti.

Whilst the Anticosti $\delta^{18}O_{calcite}$ record in this study appears to be similar to some published work, it differs slightly to the data presented in Finnegan et al. (2011a). The positive excursion in Young et al. (2010a) is slightly larger, ranging almost 3 ‰ from the start of the Hirnantian to the peak of the excursion. They also do not identify the dip in oxygen values immediately before the peak, although this could be a due to a lower sampling frequency and a more compressed timescale in comparison to the data analysed for this study.

5.4.3.2 Environmental signal in oxygen isotopes

Overall, negative $\delta^{18}O_{calcite}$ values are expected throughout the Phanerozoic. Most recently reviewed in Veizer & Prokoph (2015), there is a consistent trend in fossil material, such as brachiopods, to give a negative carbonate $\delta^{18}O_{calcite}$ value, that rises throughout the Phanerozoic until reaching the present day value of approximately 0 ‰. If we suppose the fluid isotope composition has not changed through geological time, it would suggest the early oceans would be hot, potentially reaching up to 60°C, far above what is considered to support marine biological communities. The alternative is that the oxygen isotope signal of the seawater has evolved through time, through oxygen in seawater exchanging with rocks at mid-ocean ridges (For further discussions see Azmy et al. (1998b) and Veizer & Prokoph (2015) and references therein.

It is well documented that the $\delta^{18}O_{calcite}$ record is complicated to interpret, as it reflects changes in both ocean temperature and oxygen isotopic composition (e.g. Veizer et al. 1986). The positive $\delta^{18}O_{calcite}$ excursion recorded on Anticosti would usually be expected during a glacial period. However, the stratigraphy on Anticosti during this excursion is representative of a marine transgression and rising sea level (Laframboise Member of the Ellis Bay Formation). The peak of the Hirnantian glaciation event is represented by the erosional unconformity at the base of the Laframboise Member. The Laframboise Member itself is considered to be a transgressive deposit during a time of maximum ice sheet coverage (Ghienne et al. 2014; Desrochers et al. 2010).

Ghienne et al. (2014) correlated the end-Ordovician sequence stratigraphy from Anticosti, with the Anti-Atlas sequence in Morocco. They suggest that some amounts of material are missing from the Anticosti geological sequence, representing possibly subaerial periods that may have lead to removal of material. The carbon isotope signal may only be recorded in disjointed records ((Ghienne et al. 2014) see below), and therefore it is possible that the oxygen isotope record may be similarly disjointed. This makes it harder to ascertain if a whole peak has been resolved from the sequence, and the oxygen peak residing over a transgressive period raises the question of how completely the oxygen peak is preserved, and what the $\delta^{18}O$ signal is recording.

5.4.3.3 Carbon isotopes on Anticosti

A key find from the bulk isotope analysis of the Anticosti dataset has been identifying the carbon isotope excursion occurring at the end of the Hirnantian. The excursion has been noted in other studies of the strata on Anticosti and one example is displayed in Figure 5.31. The Hirnantian carbon isotope excursion is a globally recorded feature, seen in strata from Estonia, Morocco and Scotland for example. Figure 5.31 shows data from Young et al. (2010b) re-plotted against the corresponding stratigraphy. The peak shows a similar flat-topped shape to that identified in this

study, with some irregularities appearing towards the end. The rise in $\delta^{13}C_{VPDB}$ is of a similar amplitude, approximately 4 ‰, with an initial rise and shoulder on the rising arm at the top of the Lousy Cove Member.

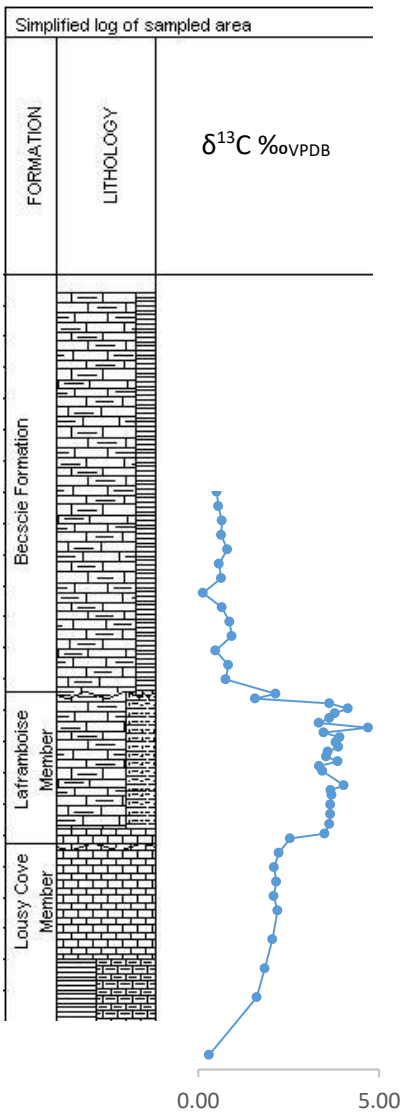

Figure 5.31 $\delta^{13}C$ data taken from Young et al (2010) demonstrating the carbon isotope peak.

The rise up to the peak at the beginning of the Laframboise Member is steeper than the equivalent point in this study, and the return to background levels after the excursion is also more rapid. A similarly shaped peak to that in Figure 5.31 is also presented in the carbon data shown in Desrochers et al. (2010). This dataset shows a rise in carbon by approximately 4 ‰, and a sharp rise and fall to the peak. A flat top to the peaks is also displayed here along with similar background

$\delta^{13}C_{VPDB}$ levels of 0 ‰. These are just two examples of $\delta^{13}C_{VPDB}$ records analysed from materials on Anticosti, but the others also show a very similar relatively flat topped peak with a similarly sized positive shift, and steep sides (e.g. Long (1993)).

5.4.3.4 Environmental signal in carbon isotopes

Enriched $\delta^{13}C$ values recorded in carbonates are indicative of a change in the marine carbon cycle. This is either due to enhanced burial of organic matter that is isotopically light, or due to increased productivity (Munnecke et al. 2010 and references therein). Carbon isotopes are less likely to be affected by diagenetic changes as pore fluids contain little carbon to re-equilibrate the isotopic composition of the rock. There is still some discussion as to the causes of the end-Ordovician carbon isotope excursion.

The $\delta^{13}C$ record on Anticosti shows a positive excursion within the Laframboise Member. This is a transgressive deposit during the glacial maximum of the glacial sequence. Due to the hiatuses in the Anticosti sequence, it is unlikely the whole of the carbon isotope record is preserved (Ghienne et al. 2014). They suggest that the excursion is not restricted to the final low order glacial package, but could also be a feature within the second glacial cycle. The excursion recorded during the final glacial event records the change from extensive glacial conditions to a warmer de-glacial environment, reflected in the reefs of the Laframboise member. The peak is therefore associated with a deglaciation (Ghienne et al. 2014).

Organic matter has a strong control over the $\delta^{13}C$ values, but vascular land plants had not evolved at this time, and the bryophytes that were present are not considered to have a significant global contribution (Munnecke et al. 2010). Kump et al. (1999) put forward one possible hypothesis for a carbon isotope excursion. They suggest that the relationship between increased weathering of silicate rocks caused a decline in atmospheric pCO_2, which lead to global cooling. This encouraged the growth of ice sheets. During the glaciation, the rate of silicate weathering then started to decline, allowing an increase in carbon dioxide until a level was reached that allowed warming to begin. They state that the positive $\delta^{13}C$ excursion was caused by weathering of carbonate platforms when sea levels were at their lowest (during the most extensive glaciations). This theory is not related to any increased burial of organic carbon (Kump et al. 1999).

Ghienne et al. (2014) argued that this scenario could be discounted, as each positive excursion in the end Ordovician glaciations occurs in the highstand system tracts when sea levels were rising. This is contrary to the weathering hypothesis. They suggest an alternative explanation that the excursion is caused by changes in deep water productivity and carbon sequestration. Brenchley (1994) suggests that a fall in polar sea temperatures would trigger down-welling currents

away from the poles. This would produce strong circulation in the cool bottom waters, eventually causing a new pattern of circulation bringing nutrients to the surface. This generates high productivity and therefore sedimentation of carbon with high $\delta^{13}C$ values, causing the excursion. CO_2 levels would decrease in the atmosphere as there would be a drawdown of carbon dioxide, which in turn promotes glaciation. They suggest that the major ice cap development is restricted to the Hirnantian, with warmer and stratified oceans before and after this time (Brenchley 1994; Brenchley et al. 2003).

This 'productivity' model suggests that the glaciation and isotopic excursion should be simultaneous (Brenchley et al. 2003) but this is not supported in the rock record or by the positioning of the isotope excursion. The lowest sea level point occurs immediately prior to the excursion in both $\delta^{13}C$ and $\delta^{18}O$. Ghienne et al. (2014) suggest that each glacial cycle throughout the Ordovician is not necessarily connected to an individual isotopic excursion. The 'productivity' model is a realistic explanation, as long as the isotopic excursion is not tied to the facies. This is because, on Anticosti, the final glaciation occurs prior to the carbon excursion. The scenario of deep carbon storage is a likely explanation, but it must be restricted to a basinal event, rather than a global one (Ghienne et al. 2014).

5.5 Closing discussion and conclusions

This study on the end-Ordovician of Anticosti Island has generated a suite of geochemical and petrographic observations that can be drawn together to understand the development of the basin and the environment during this glaciation event. By studying the material in thin section and measuring the trace element content it is possible to observe a range of preservation states. Brachiopod and trilobite material appears to be well preserved, whereas rugose corals show clear re-precipitation textures. There are also veinlets and void filling calcite cements present of vuggy and sparry calcite, which is proof of post-depositional precipitation of calcite.

The oxygen isotope values are consistent with other Late Ordovician calcite values (Veizer & Prokoph 2015). Whilst this could be that the oxygen isotope values on Anticosti are reflecting an early diagenetic signal, it is not far from what is considered the norm for calcite of this age. The carbon isotope values appear to be well preserved also. They are again comparable to other studies, and preserve an excellent isotopic excursion. Whatever diagenetic process that has effected the clumped isotopes has not altered the bulk isotopic record. The similarity in bulk isotope signal between original fossil material and diagenetic precipitates suggest they have been produced from the same original fluid, in a closed diagenetic system.

The clumped isotope analyses show that whilst the bulk isotopes have likely been preserved, the clumped isotope signal has been reset and displays a range of diagenetic temperatures up to approximately 100 °C. This is in direct contrast to the Finnegan et al (2011) study. They were able to retrieve and original ocean temperature signal using similar materials as this study for clumped isotope measurements. Their full temperature range reaches up to nearly 60 °C, which is too hot for a marine ocean. However, they used only the lowest Δ_{47} derived temperatures to show the changes during the end-Ordovician glaciation. There is no discussion as to the evolution of the basin and the likely diagenetic overprinting of the clumped isotopes to produce elevated temperature values. The procedure for altering the clumped isotope record is occurring at the grain scale within the carbonate lattice, rather than wider scale dissolution of the carbonate. The mechanism cannot be defined in this study, but is most likely to be solid state diffusion, grain growth and recrystallization, dissolution and re-precipitation or a potential combination of all three.

Whilst the clumped isotope data has not preserved an original surface temperature, the geochemical analysis of the Anticosti sequence has indicated how the system has evolved under closed system conditions. It has also allowed us to place limits on the ocean isotopic composition by tracing back the calculated compositions to a temperature more likely for a tropical ocean. This study has indicated that whilst clumped isotopes could not be used to retrieve an original ocean temperature, they are an excellent tool for understanding basin development over geological timescales.

Chapter 6 – Conclusions and future work

The application of clumped isotopes as a palaeothermometer is still within the development phase. This is reflected by the continued improvement in instrumentation, sample preparation methods and calibration. This thesis is a contribution towards the development and improvement of clumped isotope analysis, and attempts to answer the question of whether the technique can be applied to geological material in order to understand Earth surface conditions in the past. Here I summarise the key findings of my research and possible future directions.

6.1 Developing and improving the accuracy and precision of clumped isotope measurements at UEA

There are several methodological challenges to making measurements of clumped isotopes at a high enough precision and accuracy for robust palaeotemperature measurements. Chapters 2 and 3 outline the key issues. The MIRA instrument is a high sensitivity mass spectrometer that is capable of making accurate and precise measurements of clumped isotopes in CO_2. The long term and short term means and standard deviation for the carbonate standards and calibration gases have a good precision.

In terms of the mass spectrometry, there are two main issues that are inherent to the equipment used for measurements. One is the dependency between Δ_{47} and δ^{47}, the so-called non-linearity of the majority of mass spectrometers. The design of MIRA is such that the likely cause of this non-linearity (the generation of secondary electrons) is prevented, and the measurement of 1000 °C heated gases and water equilibrated gases shows that MIRA remains linear over long periods of time.

The second key challenge to making clumped isotope measurements is the scrambling and recombination of the CO_2 analyte gas within the source of the mass spectrometer. This ultimately causes scale compression, altering the measured Δ_{47} value. Within the published literature, there is still some discussion as to the cause of this scrambling. During my PhD, we noted that there is often a large reduction in scale compression on MIRA immediately after the source has been exposed to the atmosphere during maintenance work. The standard measurements evolve over one to two weeks before the scale compression settles close to 1.3. We feel there is a strong possibility that the presence of water vapour within the source after this exposure to atmosphere prevents the change in distribution of bonds within the CO_2, reducing the scale compression. Whilst there needs to be more strenuous testing of this hypothesis, it is a step in the right direction towards a better understanding of this system.

The preparation methods for carbonates during clumped isotope analysis varies between each of the laboratories. In this study, I have used the standard McCrea-type offline reaction method at 25 °C. Other laboratories use variations of this at higher temperatures, and use a variety of techniques. There are problems associated with each of these techniques that still require detailed study. Key issues that perhaps still need to be resolved or standardised include the length and temperature of the reaction of carbonate with phosphoric acid, the removal of water from the product CO_2 and the removal of contaminants. The identification of contaminants and setting boundary values for the identification of uncontaminated samples has been a key find of this study. The effect of contaminants, such as chlorinated compounds, can be clearly seen in the Δ_{48} and Δ_{49} values of the measured carbonates and has an effect on the Δ_{47} value. This study has shown that not only is the vacuum preparation line at UEA capable of removing contaminants such as organic material, we have been able to identify another key contaminate in the form of chlorinated compounds, and identified its effect on clumped isotope measurements.

6.2 Developing a clumped isotope temperature calibration for the MIRA instrument

By measuring the clumped isotope signals of carbonate material precipitated at a known and or controlled temperature, we can understand the relationship between Δ_{47} and temperature. In this thesis I used a combination of inorganic and biogenic material from a range of temperatures to produce a temperature calibration. The linear regression between Δ_{47} and temperature is very similar to the theoretical relationship calculated by Guo et al. (2009) for calcium carbonate reacted at 25 °C. One temperature calibration can be applied to both inorganic and biogenic material across a range of temperatures.

6.3 Application of the clumped isotope technique to a geological case study

One of the most exciting uses and the most widely developed application for clumped isotope measurements is the use of the technique as a palaeothermometer. The conventional carbonate-water oxygen isotope thermometer is limited in its geological application as we cannot know the oxygen isotope composition of the fluid. Clumped isotope measurements allow us to independently calculate a temperature of formation without requiring knowledge of the fluid isotope composition. It is also possible to calculate a likely formation fluid isotope composition from geological material.

This study applies the clumped isotope palaeothermometer to material collected from the Ordovician/Silurian deposits on Anticosti Island, with an aim to re-construct marine temperature and fluid isotope changes during a major glaciation event. Whilst there was good preservation of

the geological material, and apparent preservation of environmental trends in the oxygen and carbon isotopes, the clumped isotopic signal had been reset. The material appears to present an early diagenetic trend of elevated temperatures, whilst the oxygen isotope signal of the carbonate remained constant. This is likely to represent diagenesis within a closed system, where the rock has buffered the composition of the fluids with no influx of water to change the oxygen isotope composition. The clumped isotopes have been altered due to diagenetic processes occurring at the grain boundary, and so record the elevated burial temperatures.

6.4 Future directions for clumped isotope measurements

There is more development required before measurements of clumped isotopes perhaps reach their full potential. There is a wide variation in methodologies for preparation and measurements of the clumped isotopes recorded in carbonate minerals, and this needs to be further standardised between laboratories. The range of different temperature calibrations published by different working groups is a direct reflection of this, especially as the majority of laboratories measure a very similar Δ_{47} value for Carrara marble. As this is an extremely pure carbonate, issues such as the removal of contaminants have less of an effect, suggesting this may be a reason for much of the discrepancies between laboratories.

Projecting data onto the absolute reference frame (Dennis et al. 2011) has done much to remove the effects of mass spectrometry issues such as scale compression. However, non-linearity remains an issue across the majority of laboratories, with variations in the methods used to correct the issue. Standardisation of correction methods would improve future clumped isotope work. This will be aided by the development of new instruments such as MIRA, the Nu-Instruments Perspective and the Thermo-Finnegan 253 Plus which have been designed to eliminate non-linearity in clumped isotope measurements. Further improvements to the sensitivity of mass spectrometers would decrease the measurement time for samples, improve the mass spectrometer precision and ultimately reduce the sample size required for analysis.

The clumped isotope palaeothermometer has huge potential for understanding geological processes. An attractive application is its potential to unlock Earth surface temperatures in the geological past. However, there is a need for further experimental and theoretical studies to improve the understanding of the kinetics of resetting in different geological environments. There has been some work prior to this study which has suggested that original clumped isotope temperatures can be retrieved from ancient geological material (Finnegan et al. 2011b; Came et al. 2007). However, more recent discussions have suggested that this may not be possible (Veizer & Prokoph 2015), and the case study of Anticosti in this project also suggests it may not be possible.

Clumped isotopes appear to be more susceptible to diagenetic alteration than the conventional oxygen and carbon isotope records. The Anticosti case study shows that the Earth surface clumped isotope temperatures were not preserved, and were overprinted by a diagenetic signal that needs detailed study. Diagenetic processes such as dissolution-reprecipitation and solid state diffusions require more investigation at lower diagenetic temperatures. Extrapolation of high temperature data towards the lower temperature environment may not be the most appropriate way to understand the resetting process. More serious investigation is required to determine whether clumped isotope signals of this age can be preserved, and need to be investigated on a case by case basis. This is because geological systems vary hugely, and no single rule is likely to apply. Whilst the Earth surface temperatures have not been preserved in the Anticosti material, the analyses have given us insight into the geological development of the Anticosti Basin. Understanding how geological systems have been developed, in terms of their burial depth and the fluid compositions recorded in the carbonate, may be important for other geological applications.

Bibliography

Achab, A. et al., 2011. Chitinozoan biostratigraphy of a new Upper Ordovician stratigraphic framework for Anticosti Island, Canada. *Bulletin of the Geological Society of America*, 123(1-2), pp.186–205.

Achab, A. et al., 2013. The end-Ordovician chitinozoan zones of Anticosti Island, Québec: Definition and stratigraphic position. *Review of Palaeobotany and Palynology*, 198, pp.92–109.

Affek, H.P. et al., 2008. Glacial/interglacial temperature variations in Soreq cave speleothems as recorded by "clumped isotope" thermometry. *Geochimica et Cosmochimica Acta*, 72(22), pp.5351–5360.

Azmy, K. et al., 1998. Oxygen and carbon isotopic composition of Silurian brachiopods : Implications for coeval seawater and glaciations. *Geological Society of America Bulletin*, 110(11), pp.1499–1512.

Bernasconi, S.M. et al., 2013. Background effects on Faraday collectors in gas-source mass spectrometry and implications for clumped isotope measurements. *Rapid Communications in Mass Spectrometry*, 27(5), pp.603–612.

Bertrand, R., Heroux, Y. & Heroux, W.O.N., 1987. Chitinozoan, graptolite, and scolecodont reflectance as an alternative to vitrinite and pyrobitumen reflectance in Ordovician and Silurian strata, Anticosti Island, Quebec, Canada. *AAPG Bulletin*, 71(8), pp.951–957.

Bevington, P.R. & Robinson, D.K., 1992. *Data Reduction and Error Analysis for the Physical Sciences, 2nd edn.*,

Bordet, E., Malo, M. & Kirkwood, D., 2010. A structural study of western Anticosti Island, St. Lawrence platform, Québec: a fracture analysis that integrates surface and subsurface structural data. *Bulletin of Canadian Petroleum Geology*, 58(1), pp.36–55.

Brand, U., 2004. Carbon, oxygen and strontium isotopes in Paleozoic carbonate components: An evaluation of original seawater-chemistry proxies. *Chemical Geology*, 204(1-2), pp.23–44.

Brand, U. et al., 2003. Geochemistry of modern brachiopods: Applications and implications for oceanography and paleoceanography. *Chemical Geology*, 198(3-4), pp.305–334.

Brand, U. & Veizer, J., 1981. Chemical diagenesis of a multicomponent carbonate system - 2: Stable isotopes. , 51(3).

Brenchley, P.J., 1994. Bathymetric and isotopic evidence for a short-lived late Ordovician glaciation in a greenhouse period. *Geology*, 22(4), pp.295–298.

Brenchley, P.J. et al., 2003. High-resolution stable isotope stratigraphy of Upper Ordovician sequences: Constraints on the timing of bioevents and environmental changes associated with mass extinction and glaciation. *Bulletin of the Geological Society of America*, 115(1), pp.89–104.

Came, R.E. et al., 2007. Coupling of surface temperatures and atmospheric CO2 concentrations during the Palaeozoic era. *Nature*, 449(7159), pp.198–201.

Came, R.E., Brand, U. & Affek, H.P., 2014. Clumped isotope signatures in modern brachiopod carbonate. *Chemical Geology*, 377, pp.20–30.

Cayeux, L. (1916). *Introduction a l'etude petrographique des roches sedimentaires,* 524 pp. Imprimerie nationale: Paris.

Chi, G. et al., 2010. Downward hydrocarbon migration predicted from numerical modeling of fluid overpressure in the Paleozoic Anticosti Basin, eastern Canada. *Geofluids*, 10(3), pp.334–350.

Coplen, T.B., 2007. Calibration of the calcite–water oxygen-isotope geothermometer at Devils Hole, Nevada, a natural laboratory. *Geochimica et Cosmochimica Acta*, 71(16), pp.3948–3957.

Copper, P., 2001. Reefs during the multiple crises towards the Ordovician-Silurian boundary: Anticosti Island, eastern Canada, and worldwide. *Canadian Journal of Earth Sciences/Revue Canadienne des Sciences de la Terre*, 38(2), pp.153–171.

Defliese, W. & Lohmann, K., 2015. Non-linear mixing effects on mass-47 CO2 clumped isotope thermometry: Patterns and implications. *Rapid Communications in Mass …*, (February), pp.901–909.

Defliese, W.F., Hren, M.T. & Lohmann, K.C., 2015. Compositional and temperature effects of phosphoric acid fractionation on Δ47 analysis and implications for discrepant calibrations. *Chemical Geology*, 396, pp.51–60.

Delabroye, A. et al., 2011. Phytoplankton dynamics across the Ordovician/Silurian boundary at low palaeolatitudes: Correlations with carbon isotopic and glacial events. *Palaeogeography, Palaeoclimatology, Palaeoecology*, 312(1-2), pp.79–97.

Dennis, K.J. et al., 2011. Defining an absolute reference frame for “clumped” isotope studies of CO2. *Geochimica et Cosmochimica Acta*, 75(22), pp.7117–7131.

Dennis, K.J. & Schrag, D.P., 2010. Clumped isotope thermometry of carbonatites as an indicator of diagenetic alteration. *Geochimica et Cosmochimica Acta*, 74(14), pp.4110–4122.

Desrochers, a et al., 2012. Regional stratigraphic, depositional and diagenetic patterns of the interior of St. Lawrence Platform: the Lower Ordovician Romain Formation, Western Anticosti Basin, Quebec. *AAPG Memoir 98 Great American Carbonate Bank*, 98, pp.525–543.

Desrochers, a, 2006. Rocky shoreline deposits in the lower Silurian (upper Llandovery, Telychian) Chicotte formation, Anticosti island, Quebec. *Canadian Journal of Earth Sciences*, 1214, pp.1205–1214.

Desrochers, A. & Gauthier. (2009) *Carte geologique de l'ile d'Anticosti*

Desrochers, A. et al., 2010. A far-field record of the end Ordovician glaciation: The Ellis Bay Formation, Anticosti Island, Eastern Canada. *Palaeogeography, Palaeoclimatology, Palaeoecology*, 296(3-4), pp.248–263.

Dietzel, M. et al., 2009. Oxygen isotopic fractionation during inorganic calcite precipitation - Effects of temperature, precipitation rate and pH. *Chemical Geology*, 268(1-2), pp.107–115.

Dietzel, M. & Usdowski, E., 1996. Coprecipitation of Ni2+, Co2+, and Mn2+ with galena and covellite, and of Sr2+ with calcite during crystallization via diffusion of H2S and C02 through polyethylene at 20°C: Power law and Nernst law control of trace element partitioning. *Chemical Geology*, 131(1-4), pp.55–65.

Eagle, R. a et al., 2010. Body temperatures of modern and extinct vertebrates from (13)C-(18)O bond abundances in bioapatite. *Proceedings of the National Academy of Sciences of the United States of America*, 107(23), pp.10377–10382.

Eagle, R. a. et al., 2013. The influence of temperature and seawater carbonate saturation state on 13C-18O bond ordering in bivalve mollusks. *Biogeosciences*, 10(7), pp.4591–4606.

Eiler, J.M., 2007. "Clumped-isotope" geochemistry-The study of naturally-occurring, multiply-substituted isotopologues. *Earth and Planetary Science Letters*, 262(3-4), pp.309–327.

Eiler, J.M., 2011. Paleoclimate reconstruction using carbonate clumped isotope thermometry. *Quaternary Science Reviews*, 30(25-26), pp.3575–3588.

Eiler, J.M. & Schauble, E., 2004. 18O13C16O in Earth's atmosphere. *Geochimica et Cosmochimica Acta*, 68(23), pp.4767–4777.

Emiliani, C. (1955). Pleistocene Temperatures. *The Journal of Geology, 63,* 538-578.

Epstein, S. et al., 1953. Revised Carbonate-Water Isotopic Temeprature Scale. *Geological Society of America Bulletin*, 64, pp.1315–1325.

Fernandez, A., Tang, J. & Rosenheim, B.E., 2014. Siderite "clumped" isotope thermometry: A new paleoclimate proxy for humid continental environments. *Geochimica et Cosmochimica Acta*, 126, pp.411–421.

Fiebig, J. et al., 2015. Slight pressure imbalances can affect accuracy and precision of dual inlet-based clumped isotope analysis. *Isotopes in Environmental and Health Studies*, (April), pp.1–17.

Finnegan, S. et al., 2011. The magnitude and duration of Late Ordovician-Early Silurian glaciation supp. *Science (New York, N.Y.)*, 331(6019), pp.903–906.

Ghienne, J.-F. et al., 2014. A Cenozoic-style scenario for the end-Ordovician glaciation. *Nature Communications*, 5, p.4485.

Ghosh, P. et al., 2006. 13C–18O bonds in carbonate minerals: A new kind of paleothermometer. *Geochimica et Cosmochimica Acta*, 70(6), pp.1439–1456.

Ghosh, P. et al., 2007. Calibration of the carbonate "clumped isotope" paleothermometer for otoliths. *Geochimica et Cosmochimica Acta*, 71(11), pp.2736–2744.

Ghosh, P., 2013. Rapid Uplift of the Altiplano Revealed Through 13 C- 18 O Bonds in Paleosol Carbonates Prosenjit Ghosh. , 511(2006).

Grauel, A.-L. et al., 2013. Calibration and application of the “clumped isotope” thermometer to foraminifera for high-resolution climate reconstructions. *Geochimica et Cosmochimica Acta*, 108, pp.125–140.

Gregory, R.T. et al., 1989. Oxygen isotopic composition of carbonate concretions from the lower Cretaceous of Victoria, Australia: implications for the evolution of meteoric waters on the Australian continent in a paleopolar environment. *Earth and Planetary Science Letters*, 92(1), pp.27–42.

Guo, W. et al., 2009. Isotopic fractionations associated with phosphoric acid digestion of carbonate minerals: Insights from first-principles theoretical modeling and clumped isotope measurements. *Geochimica et Cosmochimica Acta*, 73(24), pp.7203–7225.

He, B., Olack, G. a. & Colman, A.S., 2012. Pressure baseline correction and high-precision CO_2 clumped-isotope (Δ_{47}) measurements in bellows and micro-volume modes. *Rapid Communications in Mass Spectrometry*, 26(24), pp.2837–2853.

Hendy, C. H. & Wilson, A. T. (1968). Palaeoclimate Data From speleothems. *Nature, 219,* 48-51

Henkes, G. a. et al., 2013. Carbonate clumped isotope compositions of modern marine mollusk and brachiopod shells. *Geochimica et Cosmochimica Acta*, 106, pp.307–325.

Henkes, G. a. et al., 2014. Temperature limits for preservation of primary calcite clumped isotope paleotemperatures. *Geochimica et Cosmochimica Acta*, 139, pp.362–382.

Horowitz, AS and Potter, PE(1971) Introductory Petrography of Fossils, *Springer-Verlag, Berlin,* 302 pp

Le Heron, D.P. & Dowdeswell, J. a, 2009. Calculating ice volumes and ice flux to constrain the dimensions of a 440 Ma North African ice sheet. *Journal of the Geological Society*, 166(2), pp.277–281.

Hren, M.T. et al., 2013. Terrestrial cooling in Northern Europe during the eocene-oligocene transition. *Proceedings of the National Academy of Sciences of the United States of America*, 110(19), pp.7562–7.

Huntington, K.W. et al., 2009. Methods and limitations of “clumped” CO_2 isotope (Δ_{47}) analysis by gas-source isotope ratio mass spectrometry. *Journal of Mass Spectrometry*, 44(9), pp.1318–1329.

Jones, D.S. et al., 2011. Terminal Ordovician carbon isotope stratigraphy and glacioeustatic sea-level change across Anticosti Island (Quebec, Canada). *Geological Society of America Bulletin*, 123(7-8), pp.1645–1664.

Kele, S. et al., 2015. Temperature dependence of oxygen- and clumped isotope fractionation in carbonates: a study of travertines and tufas in the 6-95°C temperature range. *Geochimica et Cosmochimica Acta*.

Kim, S.-T. & O’Neil, J.R., 1997. Equilibrium and nonequilibrium oxygen isotope effects in synthetic carbonates. *Geochimica et Cosmochimica Acta*, 61(16), pp.3461–3475.

Kluge, T. et al., 2014. Devils Hole paleotemperatures and implications for oxygen isotope equilibrium fractionation. *Earth and Planetary Science Letters*, 400, pp.251–260.

Kluge, T. et al., 2015. Laboratory calibration of the calcium carbonate clumped isotope thermometer in the 25–250°C temperature range. *Geochimica et Cosmochimica Acta*, 157, pp.213–227.

Kluge, T. & John, C.M., 2015. Effects of brine chemistry and polymorphism on clumped isotopes revealed by laboratory precipitation of mono- and multiphase calcium carbonates. *Geochimica et Cosmochimica Acta*, 160, pp.155–168.

Kump, L.R. et al., 1999. A weathering hypothesis for glaciation at high atmospheric pCO2 during the Late Ordovician. *Palaeogeography, Palaeoclimatology, Palaeoecology*, 152(1-2), pp.173–187.

Lavoie, D. et al., 2005. Hydrothermal dolomitization on the Lower Ordovician Romaine Formation of the Anticosti basin: significance for hydrocarbon exploration. *Bulletin of Canadian Petroleum Geology*, 53(4), pp.454–472.

Licciardi, J.M. et al., 1998. Deglaciation of a soft-bedded Laurentide Ice Sheet. *Quaternary Science Reviews*, 17(4-5), pp.427–448.

Loi, a. et al., 2010. The Late Ordovician glacio-eustatic record from a high-latitude storm-dominated shelf succession: The Bou Ingarf section (Anti-Atlas, Southern Morocco). *Palaeogeography, Palaeoclimatology, Palaeoecology*, 296(3-4), pp.332–358.

Long, D.G., 2007. Tempestite frequency curves: a key to Late Ordovician and Early Silurian subsidence, sea-level change, and orbital forcing in the Anticosti foreland basin, Quebec, Canada. *Canadian Journal of Earth Sciences*, 44(3), pp.413–431.

Long, D.G.F., 1993. Oxygen and carbon isotopes and event stratigraphy near the Ordovician—Silurian boundary, Anticosti Island Quebec. *Palaeogeography, Palaeoclimatology, Palaeoecology*, 104, pp.49–59.

Mauviel, A. & Desrochers, A., 2016. A high-resolution , continuous d13C record spanning the Ordovician–Silurian boundary on Anticosti Island , eastern Canada. *Canadian Journal of Earth Sciences*, 53, pp.1–7.

McCracken, A. D. & Barnes, C. R. (1981). Conodont biostratigraphy and paleoecology of the Ellis Bay Formation, anticosti Island, Quebec. *Geological survey of Canada Bulletin, 329,* 51-96

McCrea, J.M., 1950. On the Isotopic Chemistry of Carbonates and a Paleotemperature Scale. *The Journal of Chemical Physics*, 18(6), pp.849–857.

Meckler, a. N. et al., 2014. Long-term performance of the Kiel carbonate device with a new correction scheme for clumped isotope measurements. *Rapid Communications in Mass Spectrometry*, 28(15), pp.1705–1715.

Merritt, D. a & Hayes, J.M., 1994. Factors controlling precision and accuracy in isotope-ratio-monitoring mass spectrometry. *Analytical chemistry*, 66(14), pp.2336–2347.

Miller, J. (1988), Cathodoluminescence microscopy, *in* Tucker, ME., ed., Techniques in Sedimentology: Oxford, UK, Blackwell, p. 86-107

Munnecke, A. et al., 2010. Ordovician and Silurian sea-water chemistry, sea level, and climate: A synopsis. *Palaeogeography, Palaeoclimatology, Palaeoecology*, 296(3-4), pp.389–413.

Murphy, D.M. & Koop, T., 2005. Review of the vapour pressures of ice and supercooled water for atmospheric applications. *Quarterly Journal of the Royal Meteorological Society*, 131(608), pp.1539–1565.

Orth, C.J.C. et al., 1986. Terminal Ordovician extinction: Geochemical analysis of the Ordovician/Silurian boundary, Anticosti Island, Quebec. *Geology*, 14(May), pp.433–436.

Passey, B.H. et al., 2010. High-temperature environments of human evolution in East Africa based on bond ordering in paleosol carbonates. *Proceedings of the National Academy of Sciences*, 107(25), pp.11245–11249.

Passey, B.H. & Henkes, G. a., 2012. Carbonate clumped isotope bond reordering and geospeedometry. *Earth and Planetary Science Letters*, 351-352, pp.223–236.

Petersen, S. V. et al., 2015. The effects of Porapak(TM) trap temperature on d18O, d13C, and D47 values in preparing samples for clumped isotope analysis. *Rapid Communications in Mass Spectrometry*, 30(October 2015), pp.1–10.

Petersen, S. V. & Schrag, D.P., 2015. Antarctic ice growth before and after the Eocene-Oligocene Transition: New estimates from clumped isotope paleothermometry. *Paleoceanography*, p.n/a–n/a.

Petrizzo, D. a., Young, E.D. & Runnegar, B.N., 2014. Implications of high-precision measurements of 13C-18O bond ordering in CO2 for thermometry in modern bivalved mollusc shells. *Geochimica et Cosmochimica Acta*, 142, pp.400–410.

Petrizzo D. & Young, E. (2014). High-precision determination of ^{13}C-^{18}O bonds in CO_2 using the multicollector peak hopping. *Rapid Communications in Mass Spectrometry, 30*

Pinet, N. et al., 2012. Revisiting the Appalachian structural front and offshore Anticosti Basin (northern Gulf of St. Lawrence, Canada) by integrating old and new geophysical datasets. *Marine and Petroleum Geology*, 32(1), pp.50–62.

Pinet, N. et al., 2014. The St Lawrence Platform and Appalachian deformation front in the St Lawrence Estuary and adjacent areas (Quebec, Canada): structural complexity revealed by magnetic and seismic imaging. *Geological Magazine*, 151, pp.1–17.

Popp, B.N., Anderson, T.F. & Sandberg, P. a, 1986. Brachiopods as indicator of original isotopic composition in some Paleozoic limestones. *Bulletin of the Geological Society of America*, 97(October), pp.1262–1269.

Qing, H. & Veizer, J., 1994. Oxygen and carbon isotopic composition of Ordovician brachiopods: Implications for coeval seawater. *Geochimica et Cosmochimica Acta*, 58(20), pp.4429–4442.

Richter, DK and Fuchtbauer H. (1978). Ferroan calcite replacement indicates former magnesian calcite skeletons. *Sedimentology, 25*, 843-860

Rosenheim, B.E., Tang, J. & Fernandez, A., 2013. Measurement of multiply substituted isotopologues (’clumped isotopes') of CO2 using a 5 kV compact isotope ratio mass spectrometer: Performance, reference frame, and carbonate paleothermometry. *Rapid communications in mass spectrometry : RCM*, 27(16), pp.1847–57.

Sami, T. & Desrochers, A., 1992. Episodic sedimentation on an early Silurian, storm-dominated carbonate ramp, Becscie and Merrimack formations, Anticosti Island, Canada. *Sedimentology*, 39(3), pp.355–381.

Santrock, J., Studley, S. a & Hayes, J.M., 1985. Isotopic analyses based on the mass spectra of carbon dioxide. *Analytical Chemistry*, 57(7), pp.1444–1448.

Schauble, E. a., Ghosh, P. & Eiler, J.M., 2006. Preferential formation of 13C–18O bonds in carbonate minerals, estimated using first-principles lattice dynamics. *Geochimica et Cosmochimica Acta*, 70(10), pp.2510–2529.

Schmid, T.W. & Bernasconi, S.M., 2010. An automated method for “clumped-isotope” measurements on small carbonate samples. *Rapid Communications in Mass Spectrometry*, 24(14), pp.1955–1963.

Sheehan, P.M., 2001. The Late Ordovician Mass Extinction. *Annual Reviews in Earth and Planetary Sciences*, 29, pp.331–364.

Sheppard, S.M.F., 1986. Characterization and Isotopic Variations in Natural Waters. *Reviews in Mineralogy*, 16, pp.165–183.

Shields, G. a et al., 2003. Sr, C, and O isotope geochemistry of Ordovician brachiopods: A major isotopic event around the Middle-Late Ordovician transition. *Geochimica et Cosmochimica Acta*, 67(11), pp.2005–2025.

Spencer, C. & Kim, S.-T., 2015. Carbonate clumped isotope paleothermometry: a review of recent advances in CO2 gas evolution, purification, measurement and standardization techniques. *Geosciences Journal*, 19(2), pp.357–374.

Suarez, M.B. & Passey, B.H., 2014. Assessment of the clumped isotope composition of fossil bone carbonate as a recorder of subsurface temperatures. *Geochimica et Cosmochimica Acta*, 140, pp.142–159.

Sumner, K.K. et al., 2015. Assessing Fracture Connectivity using Stable and Clumped Isotope Geochemistry of Calcite Cements. , (phase 1), pp.1–12.

Swart, P.K., Burns, S.J. & Leder, J.J., 1991. Fractionation of the stable isotopes of oxygen and carbon in carbon dioxide during the reaction of calcite with phosphoric acid as a function of temperature and technique. *Chemical Geology: Isotope Geoscience section*, 86(2), pp.89–96.

Tang, J. et al., 2014. Evaluation of kinetic effects on clumped isotope fractionation (Δ47) during inorganic calcite precipitation. *Geochimica et Cosmochimica Acta*, 134, pp.120–136.

Tang, J., Köhler, S.J. & Dietzel, M., 2008. Sr2+/Ca2+ and 44Ca/40Ca fractionation during inorganic calcite formation: I. Sr incorporation. *Geochimica et Cosmochimica Acta*, 72(15), pp.3718–3732.

Thiagarajan, N., Adkins, J. & Eiler, J., 2011. Carbonate clumped isotope thermometry of deep-sea corals and implications for vital effects. *Geochimica et Cosmochimica Acta*, 75(16), pp.4416–4425.

Tripati, A.K. et al., 2010. 13C–18O isotope signatures and "clumped isotope" thermometry in foraminifera and coccoliths. *Geochimica et Cosmochimica Acta*, 74(20), pp.5697–5717.

Tripati, A.K. et al., 2015. Beyond temperature: Clumped isotope signatures in dissolved inorganic carbon species and the influence of solution chemistry on carbonate mineral composition. *Geochimica et Cosmochimica Acta*, 166, pp.344–371.

Urey, H.C. et al., 1951. Measurement of Paleotemperatures and Temperatures and the Southeastern United States. *Bulletin of the geological society of America*, 62(April), pp.399–416.

Urey, H.C., 1947. The thermodynamic properties of isotopic substances. *Journal of the Chemical Society (Resumed)*, (582), p.562.

Veizer, J., 1983. Chemical diagenisis of carbonates: theory and application of trace element technique. *Stable Isotopes in Sedimentary Geology*, pp.1–100.

Veizer, J., Fritz, P. & Jones, B., 1986. Geochemistry of brachiopods: Oxygen and carbon isotopic records of Paleozoic oceans. *Geochimica et Cosmochimica Acta*, 50, pp.1679–1696.

Veizer, J. & Hoefs, J., 1976. The nature of O18/O16 and C13/C12 secular trends in sedimentary carbonate rocks. *Geochimica et Cosmochimica Acta*, 40(11), pp.1387–1395.

Veizer, J. & Prokoph, A., 2015. Temperatures and oxygen isotopic composition of Phanerozoic oceans. *Earth-Science Reviews*, 146, pp.92–104.

Wachter, E. a & Hayes, J.M., 1985. Exchange of oxygen isotopes in carbon dioxide-phosphoric [correction of phosporic] acid systems. *Isotope geoscience*, 52, pp.365–374.

Wacker, U. et al., 2014. Empirical calibration of the clumped isotope paleothermometer using calcites of various origins. *Geochimica et Cosmochimica Acta*, 141, pp.127–144.

Wacker, U., Fiebig, J. & Schoene, B.R., 2013. Clumped isotope analysis of carbonates: comparison of two different acid digestion techniques. *Rapid communications in mass spectrometry : RCM*, 27(14), pp.1631–42.

Wang, Z., Schauble, E. a. & Eiler, J.M., 2004. Equilibrium thermodynamics of multiply substituted isotopologues of molecular gases. *Geochimica et Cosmochimica Acta*, 68(23), pp.4779–4797.

Weyl, P.K., 1959. Pressure solution and the force of crystallization: a phenomenological theory. *Journal of Geophysical Research*, 64(11), p.2001.

Wilmot, N. V & Fallick, a E., 1989. Original mineralogy of trilobite exoskeletons. *Palaeontology*, 32(2), pp.297–304.

Yoshida, N. et al., 2013. Precision and long-term stability of clumped-isotope analysis of CO2 using a small-sector isotope ratio mass spectrometer. *Rapid communications in mass spectrometry : RCM*, 27(1), pp.207–15.

Young, S. a. et al., 2010. Did changes in atmospheric CO2 coincide with latest Ordovician glacial–interglacial cycles? *Palaeogeography, Palaeoclimatology, Palaeoecology*, 296(3-4), pp.376–388.

Zaarur, S., Affek, H.P. & Brandon, M.T., 2013. A revised calibration of the clumped isotope thermometer. *Earth and Planetary Science Letters*, 382, pp.47–57. Available at:

Appendices

Appendix I

150505	‰	S.E.
δ45	0.113	0.002
δ46	3.874	0.001
δ47	3.504	0.007

150508	‰	S.E.
δ45	0.124	0.002
δ46	3.907	0.006
δ47	3.559	0.009

150513	‰	S.E.
δ45	0.129	0.001
δ46	3.944	0.002
δ47	3.587	0.007

150519	‰	S.E.
δ45	0.120	0.002
δ46	3.960	0.001
δ47	3.531	0.006

150520	‰	S.E.
δ45	0.196	0.001
δ46	4.253	0.002
δ47	3.979	0.006

150521	‰	S.E.
δ45	0.184	0.002
δ46	4.237	0.002
δ47	3.971	0.005

150522	‰	S.E.
δ45	0.184	0.001
δ46	4.335	0.002
δ47	4.039	0.005

150527	‰	S.E.
δ45	0.132	0.003

140801	‰	S.E.
δ45	0.111	0.001
δ46	3.872	0.002
δ47	3.518	0.005

140805	‰	S.E.
δ45	0.078	0.001
δ46	3.851	0.002
δ47	3.445	0.005

140807	‰	S.E.
δ45	0.104	0.002
δ46	3.901	0.002
δ47	3.523	0.004

141002	‰	S.E.
δ45	0.085	0.001
δ46	3.855	0.001
δ47	3.443	0.004

141003	‰	S.E.
δ45	0.141	0.002
δ46	4.019	0.001
δ47	3.667	0.005

141007	‰	S.E.
δ45	0.099	0.001
δ46	3.795	0.001
δ47	3.447	0.005

141008	‰	S.E.
δ45	0.113	0.001
δ46	3.827	0.001
δ47	3.488	0.006

141009	‰	S.E.
δ45	0.108	0.001

δ46	4.103	0.003	δ46	3.695	0.001
δ47	3.767	0.007	δ47	3.363	0.005

UEACMST data from two periods, showing a δ^{47} standard error of less than 0.008 ‰ in every analysis.

Appendix II

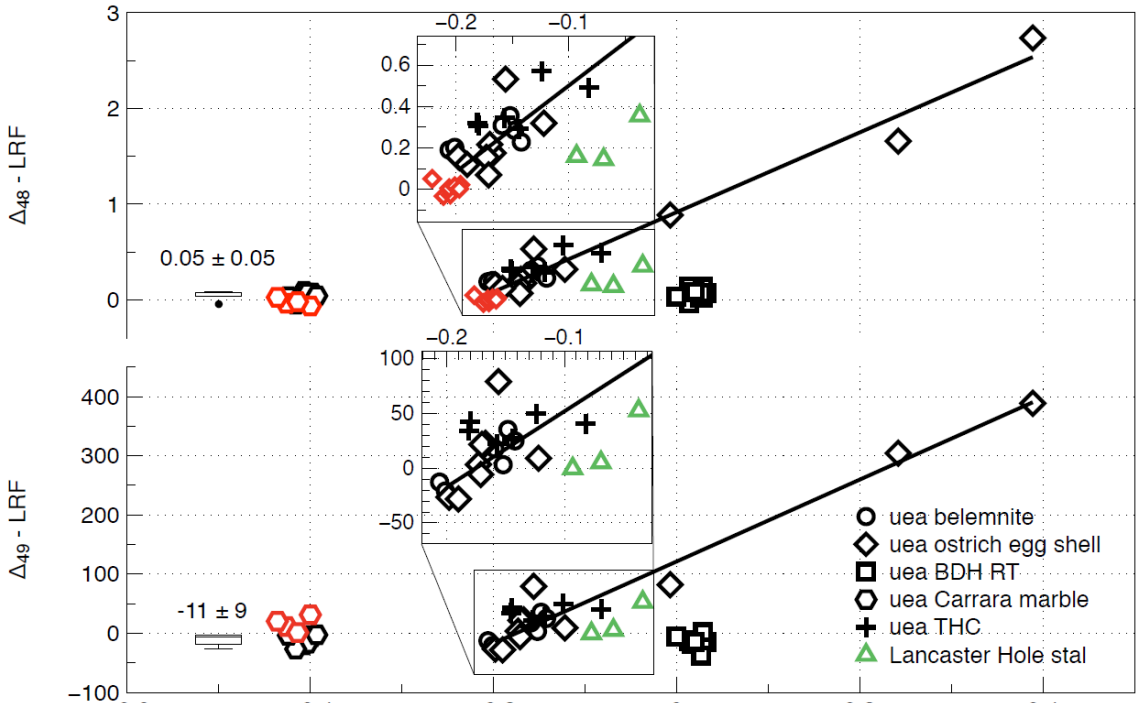

Overall contamination trends identified between $\Delta_{47(wrg)}$ and $\Delta_{48(wrg)}$ and $\Delta_{49(wrg)}$. The gradient of this line is shown in Chapter 3 Section 3.6.

Appendix III

File Name	δ13Cvpdb	δ18Ovsmow	Δ47	Δ48	Δ49	
MIRA_160111_BDHequilRT-1	2.080	33.733	0.053	0.175	57.828	
MIRA_160111_BDHequilRT-2	2.080	33.724	0.026	0.159	42.700	
MIRA_160111_BDHequilRT-3	2.074	33.718	0.044	0.084	31.615	
MIRA_160112_BDHequilRT-1	2.079	33.729	0.052	0.123	55.283	
MIRA_160112_BDHequilRT-2	2.073	33.717	0.047	0.091	42.040	
MIRA_160112_BDHequilRT-3	2.078	33.716	0.042	0.085	27.087	
MIRA_160113_BDHequilRT-1	2.079	33.725	0.033	0.059	35.692	
MIRA_160113_BDHequilRT-2	2.079	33.727	0.042	0.058	29.014	
MIRA_160113_BDHequilRT-3	2.078	33.716	0.031	0.109	33.738	
MIRA_160114_BDHequilRT-1	2.080	33.739	0.015	0.093	30.310	
MIRA_160114_BDHequilRT-2	2.079	33.729	0.041	0.085	18.388	
MIRA_160114_BDHequilRT-3	2.079	33.719	0.051	0.102	36.083	
MIRA_160115_BDHequilRT-1	2.081	33.737	0.036	0.005	28.574	
MIRA_160115_BDHequilRT-2	2.052	33.687	0.058	0.534	475.778	
MIRA_160115_BDHequilRT-3pp	2.042	33.645	0.009	0.047	19.525	
MIRA_160118_BDHequilRT-1	2.078	33.743	0.026	0.145	47.137	
MIRA_160118_BDHequilRT-2	2.077	33.735	0.036	0.143	45.754	
MIRA_160118_BDHequilRT-ppRT1	2.068	33.663	0.023	-0.057	-3.372	
MIRA_160202_BDHequilRT-1	2.078	33.731	0.010	0.120	34.843	
MIRA_160202_BDHequilRT-2	2.083	33.730	0.038	0.163	16.285	
MIRA_160202_BDHequilRT-3	2.076	33.717	0.035	0.141	34.392	
MIRA_160203_BDHequilRT-1	2.072	33.730	0.045	0.097	11.223	
MIRA_160208_BDHequilRT-1	2.104	33.751	0.018	0.336	-6.749	
MIRA_160208_BDHequilRT-2	2.109	33.747	0.046	0.200	-16.862	
MIRA_160209_BDHequilRT-1	2.110	33.753	0.008	0.079	-56.108	
MIRA_160209_BDHequilRT-2	2.107	33.753	0.010	0.076	-27.266	
MIRA_160209_BDHequilRT-3	2.110	33.747	0.008	0.067	-25.512	
MIRA_160209_BDHequilRT-4	2.107	33.736	0.012	0.116	-20.190	
MIRA_160210_BDHequilRT-1	2.109	33.761	-0.027	-0.026	-87.990	
MIRA_160210_BDHequilRT-2	2.107	33.763	-0.009	0.102	-47.923	
MIRA_160210_BDHequilRT-3	2.107	33.759	-0.016	0.081	-48.533	
MIRA_160210_BDHequilRT-4	2.101	33.752	0.007	0.042	-56.752	
MIRA_160210_BDHequilRT-5	2.103	33.747	0.037	0.002	-51.797	
MIRA_160211_BDHequilRT-1	2.113	33.783	0.014	0.209	-28.546	
MIRA_160211_BDHequilRT-2	2.103	33.763	0.009	0.095	-25.350	
MIRA_160211_BDHequilRT-3	2.098	33.754	-0.005	0.044	-37.463	
						Valve on reference gas changed
MIRA_160212_BDHequilRT-1	2.113	33.788	-0.060	0.048	-46.502	
MIRA_160212_BDHequilRT-2	2.101	33.776	-0.020	0.048	-45.110	
MIRA_160215_BDHequilRT-1	2.113	33.782	-0.107	-0.455	-187.565	
MIRA_160215_BDHequilRT-2	2.105	33.782	-0.076	-0.151	-105.478	
MIRA_160215_BDHequilRT-3	2.103	33.785	0.001	-0.089	-100.919	

MIRA_160216_BDHequilRT-1	2.104	33.790	-0.009	-0.061	-45.859
MIRA_160216_BDHequilRT-2	2.098	33.782	0.016	0.105	-49.473
MIRA_160216_BDHequilRT-3	2.094	33.784	-0.012	-0.037	-38.256
MIRA_160216_BDHequilRT-4	2.094	33.790	0.013	0.054	-37.621
MIRA_160216_BDHequilRT-5	2.093	33.778	0.003	-0.031	-44.618
MIRA_160217_BDHequilRT-1	2.099	33.809	0.002	0.075	-24.350
MIRA_160217_BDHequilRT-2	2.092	33.771	0.009	0.013	-41.213
MIRA_160217_BDHequilRT-3	2.104	33.800	0.011	-0.038	-24.859
MIRA_160217_BDHequilRT-4	2.097	33.789	0.006	0.088	-29.452
MIRA_160219_BDHequilRT-1	2.098	33.794	0.019	0.070	-12.822
MIRA_160219_BDHequilRT-2	2.097	33.784	-0.040	-0.064	-30.623
MIRA_160219_BDHequilRT-3	2.095	33.780	-0.057	-0.028	-46.276
MIRA_160223_BDHequilRT-1	2.103	33.783	0.010	0.059	-5.868
MIRA_160223_BDHequilRT-2	2.096	33.782	0.011	0.067	-37.313
MIRA_160223_BDHequilRT-3	2.093	33.770	0.002	0.114	-28.314
MIRA_160224_BDHequilRT-1	2.102	33.792	0.013	0.156	-25.202
MIRA_160224_BDHequilRT-2	2.098	33.776	0.006	0.074	-20.224
MIRA_160225_BDHequilRT-1	2.106	33.792	-0.003	-0.040	-36.252
MIRA_160229_BDHequilRT-1	2.098	33.776	0.005	0.093	-0.738
MIRA_160229_BDHequilRT-2	2.093	33.773	0.007	0.091	-0.413
MIRA_160301_BDHequilRT-1	2.099	33.790	-0.025	0.091	-24.038
MIRA_160302_BDHequilRT-1	2.084	33.780	0.002	0.003	-19.311
MIRA_160303_BDHequilRT-1	2.088	33.797	0.018	0.103	-7.032
MIRA_160307_BDHequilRT-1	2.097	33.822	-0.027	0.008	-21.284
MIRA_160308_BDHequilRT-1	2.092	33.794	0.002	0.054	-20.773
MIRA_160309_BDHequilRT-1	2.092	33.788	-0.007	-0.018	-32.446
MIRA_160310_BDHequilRT-1	2.090	33.783	0.007	-0.010	-36.961
MIRA_160311_BDHequilRT-1	2.092	33.786	0.013	0.076	-24.901
MIRA_160318_BDHequilRT-1	2.092	33.772	0.009	0.352	-1.109
MIRA_160318_BDHequilRT-2	2.093	33.774	0.005	0.166	-14.606
MIRA_160321_BDHequilRT-1	2.092	33.777	0.004	0.292	0.905
MIRA_160321_BDHequilRT-2	2.092	33.765	-0.009	0.209	-5.213
MIRA_160321_BDHequilRT-3	2.086	33.772	0.018	0.196	-19.516
MIRA_160322_BDHequilRT-1	2.088	33.795	0.014	0.214	-10.486
MIRA_160323_BDHequilRT-1	2.087494	33.78713	-0.01002	0.076305	-17.1703

BDHequilRT data

Appendix IV

Digestion results from two powdered samples from Anticosti. Between 6 % and 7 % of each sample was not calcium carbonate.

	Initial wt of powder		volume of 1 in 4 Acetic Acid		filter wt	filter plus residue		residue		Residue as percentage
RK130811 16.65m	1.10348		20mls		0.12821	0.20612		0.07791		7.06
RK130809 11.7 m	1.26092		20mls		0.12771	0.20612		0.07841		6.22

Appendix V

Finnegan Data

Sample age (ma)	Formation/Member	Material type	Δ_{47} ‰	$\delta^{13}C$ ‰$_{VPDB}$	$\delta^{18}O$ ‰$_{VPDB}$	Temperature °C
445.7	Lousy Cove	Brachiopod	0.553	0.737	-3.455	48.2
445.7	Lousy Cove	Trilobite	0.591	0.135	-3.37	38
445.7	Lousy Cove	Brachiopod	0.561	0.849	-3.071	46
445.7	Lousy Cove	Trilobite	0.611	0.041	-3.272	33.2
445.5	Lafromboise	Brachiopod	0.589	2.25	-2.603	38.5
445	Lafromboise	Rugose coral	0.617	4.834	-1.438	31.6
445	Lafromboise	Rugose coral	0.62	4.184	-0.979	31
444.75	Lafromboise	Tabulate Coral	0.55	3.443	-4.033	49.1
444.5	Lafromboise	Rugose coral	0.585	3.694	-3.13	39.6
444.5	Lafromboise	Rugose coral	0.631	4.059	-0.803	28.4
444.5	Lafromboise	Tabulate Coral	0.571	3.001	-4.589	43.5
444.5	Lafromboise	Rugose coral	0.625	4.468	-0.159	29.7
444.5	Lafromboise	Rugose coral	0.581	3.113	-3.699	40.6
443.5	Becscie	Rugose coral	0.608	1.054	-3.312	33.8
443.5	Becscie	Brachiopod	0.585	1.798	-3.591	39.6
443.5	Becscie	Rugose coral	0.587	2.07	-3.617	39.1
443.5	Becscie	Brachiopod	0.579	2.115	-3.594	41.3
443.5	Becscie	Rugose coral	0.601	2.162	-2.916	35.7
443.5	Becscie	Brachiopod	0.564	2.427	-3.456	45.1
443.5	Becscie	Rugose coral	0.604	0.647	-3.362	34.9
440	Becscie	Rugose coral	0.552	1.335	-4.486	48.6
440	Becscie	Rugose coral	0.599	0.965	-4.527	36.1
440	Becscie	Rugose coral	0.566	1.486	-4.668	44.6

Appendix VI

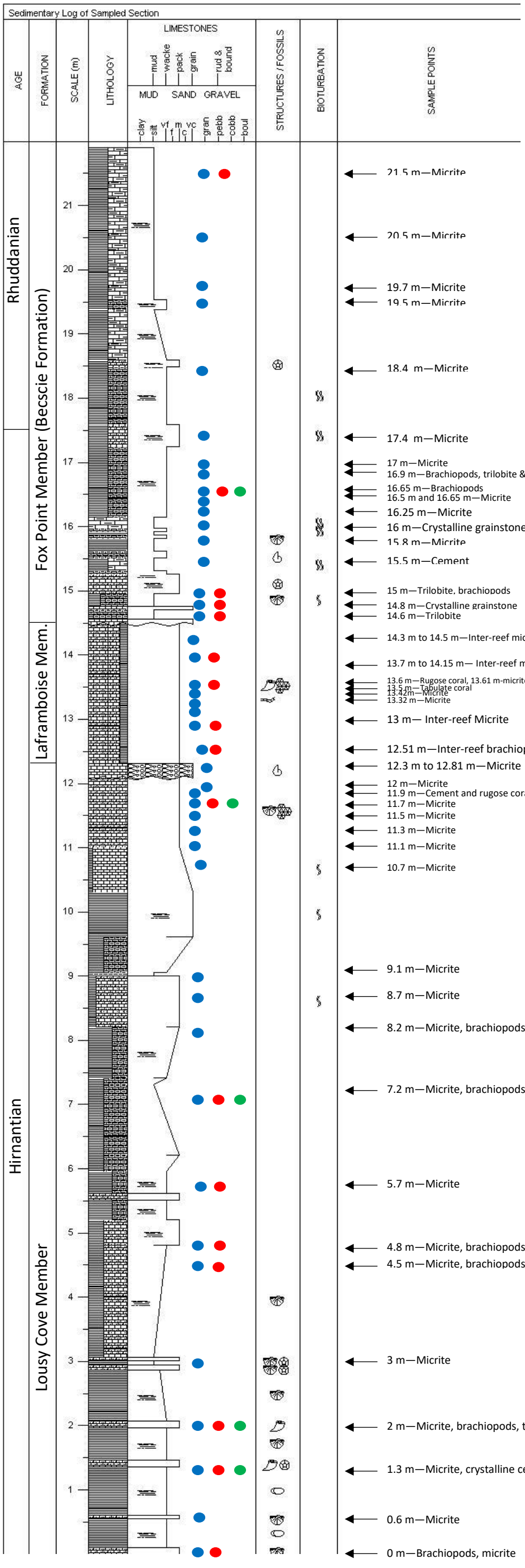

Figure 5.32 Stratigraphic log of the sampled section. The key to symbols is on the previous page. Arrows indicate locations from which samples were taken, with the accompanying text outlining the material types.